Terahertz Airborne Astronomy using a Four Detector High Resolution Spectrometer: 4GREAT

Dissertation
zur
Erlangung des Doktorgrades (Dr. rer. nat.)
der
Mathematisch-Naturwissenschaftlichen Fakultät
der
Rheinischen Friedrich-Wilhelms-Universität Bonn

von
Carlos Alberto Durán Urrutia
aus
Temuco, Chile

Bonn, 20.08.2018

Dieser Forschungsbericht wurde als Dissertation von der Mathematisch-Naturwissenschaftlichen Fakultät der Universität Bonn angenommen und ist auf dem Hochschulschriftenserver der ULB Bonn `http://hss.ulb.uni-bonn.de/diss_online` elektronisch publiziert.

1. Gutachter:	Prof. Dr. Karl Menten
2. Gutachter:	Prof. Dr. Frank Bertoldi
Tag der Promotion:	23.11.2018
Erscheinungsjahr:	2018

Abstract

After the Herschel Space Telescope ceased operations in 2013, the astronomical community has been lacking access to those parts of the terahertz spectrum that are not visible from ground-based observatories. The atmosphere blocks most of the radiation at those frequency bands, even at high geographical altitude facilities like the Atacama desert (> 5000 m altitude), where APEX and ALMA operate. 4GREAT, an extension of the German Receiver at Terahertz frequencies (GREAT) operated aboard the Stratospheric Observatory for Infrared Astronomy (SOFIA), has been developed in response to those needs. This works describes its design, test, commissioning and scientific capabilities.

4GREAT is a heterodyne receiver that comprises four different detector bands and their associated subsystems, which can be simultaneously operated fully independently in one system. All four detector beams are co-aligned on the sky.

The four frequency bands of 4GREAT cover 492–627, 893–1073, 1239–1515 and 2495–2690 GHz respectively. Various astrophysically important spectral lines are observable in each band, and in some cases different transitions of the same species, for example CO, lie in two or more bands of 4GREAT. The very important ground state transitions of various molecules can be observed, including NH_3, $H_2^{18}O$, CH, OH, OH^+, NH, NH_2, and the deuterated isotopologues HDO, and OD, as well as fine structure lines from neutral atomic carbon, [CI], and ionized nitrogen, [NII].

The expanded capabilities of GREAT with 4GREAT are now being used for a variety of spectroscopic studies. Its potential has been demonstrated by an absorption study of two ground state transitions or the methylidyne radical (CH) in diffuse molecular gas. As CH traces the unobservable molecular hydrogen, such observations are of fundamental importance for diffuse cloud astrochemistry.

...una pequeña victoria, para una gran Viktoria.

Contents

CHAPTER 1

Terahertz Astronomy

1.1 Terahertz Astronomy of the Interstellar Medium

The wavelength range of the electromagnetic spectrum between 20 μm and 1 mm is typically called far-infrared (or terahertz) range and mostly traces the cold universe. It is challenging to have access to this frequency window because the atmosphere blocks most of this radiation. This band provides information about various unique radiative processes of ionized, atomic and molecular gas related to astrophysical objects.

Most of the photons in this range are emitted by black body (continuum) radiation with temperatures between 5 and 50 K, which peaks at these frequencies, and gases with temperatures between 10 and 200 K which emit (and absorb) their brightest molecular and atomic lines (Fig. 1.1). They trace the different physical conditions of cold and diffuse material in the form of gas and dust in the Interstellar Medium (ISM), but also from dense regions of molecular clouds, and planets within the Solar System and their atmospheres. Redshifted emission from distant galaxies can also be traced in the terahertz regime.

The ISM is the material in the Milky Way (and in any galaxy) between stars. It contains gas in various phases, and dust, which is made up of graphite and silicon *grains* expelled from aging stars. At optical and UV wavelengths dust in interstellar clouds causes extinction. The absorbed radiation is then reemitted in the THz band (Draine 2010), therefore in the far-infrared cold dust appears in emission. For example the most recent state-of-the-art far-infrared space observatory, Herschel, has provided an unprecedented view on the highly structured distribution of interstellar dust (e.g. André et al. 2014 and Molinari et al. 2014). Terahertz emission and absorption lines from molecules and atoms are not affected by extinction as the corresponding wavelength of their transitions is much larger (50 - 1000 μm) than the average size of dust grains (~0.1 μm). The main focus of this work is however on the gas phase content of the ISM.

Within the ISM there are different physical conditions and compositions (Fig. 1.2), known as *phases of the ISM*. They are described as follows:

* Hot Ionized Medium (HIM). It is a very low density ionized gas superheated by supernova blast waves. It fills the voids between denser components and represents around 50% of the total volume of the ISM. It is also know as *coronal* gas.

* Warm Ionized Medium (WIM). It is made up of gas that is photo-ionized by UV radiation coming from O- and B-Type stars (Kaper 1998). The ionizing stars are found in the proximities of the dense molecular clouds from which they form. The UV photons dissociate the molecules and ionize the atomic hydrogen. Also parts of the WIM are volumes mainly consisting of ionized hydrogen (HII regions) photo dissociation regions or PDRs (Hollenbach and Tielens 1997).

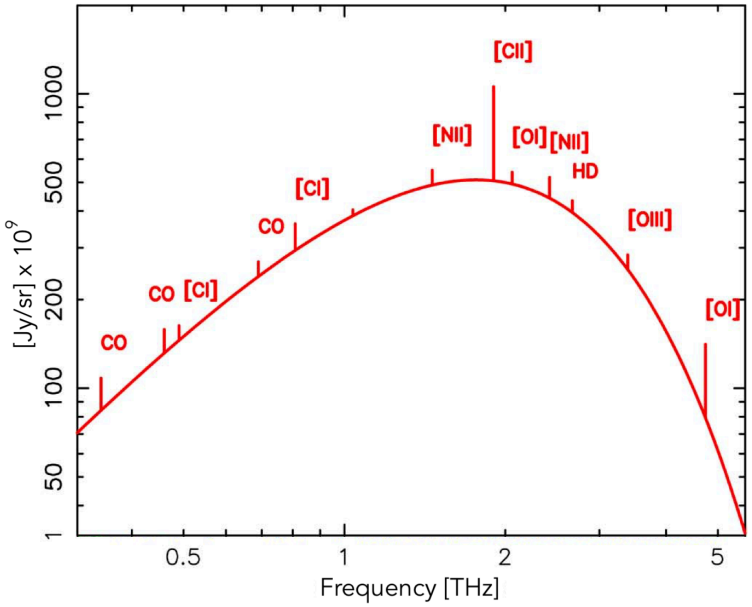

Figure 1.1: Representation of spectral characteristics observed towards an interstellar cloud, featuring a 30 K continuum level. Some important molecular and atomic lines are included. Taken and adapted from Kulesa (2011).

* Warm Neutral Medium (WNM). It is composed of neutral atomic hydrogen at temperatures of up to 10.000 K, and ionized carbon. It occupies about 40 % of the ISM volume.
* Cool Neutral Medium (CNM). Most of the CNM is formed by neutral atomic hydrogen clouds with an approximate temperature of 100 K. In over-densities of the CNM, diffuse molecular hydrogen clouds form.
* Cold Dense Molecular clouds (CDM). These are molecular clouds with temperatures between 10 and 50 K. They are the nurseries of the stars. Giant Molecular Clouds (GMC) contain clumpy CDM with a lower density inter-clump medium.

Table 1.1: Specific characteristics for the ISM of the Milky Way; f_V is the volume filling factor, n_H the density and T_P the phase temperature. Adapted from Walker (2015)

Phase	f_V	n_H [cm^{-3}]	T_P [K]	%H Mass	% Thermal energy in each phase
Coronal (HIM)	0.5	0.004	$> 10^{5.5}$	~0.24	~34
HII (WIM)	0.1	0.3 - 10^4	10^4	~2.4	~11
Warm HI (WNM)	0.4	0.6	~5000	~24	~53
Cool HI (CNM)	0.01	30	~100	~37	~2
Diffuse H_2 (CNM)	0.001	100	~50	~12	~0.3
Dense H_2 (CDM)	0.0001	10^3 - 10^6	10 - 50	~24	~0.4

Although the interstellar medium is highly structured, exchange of components within these phases

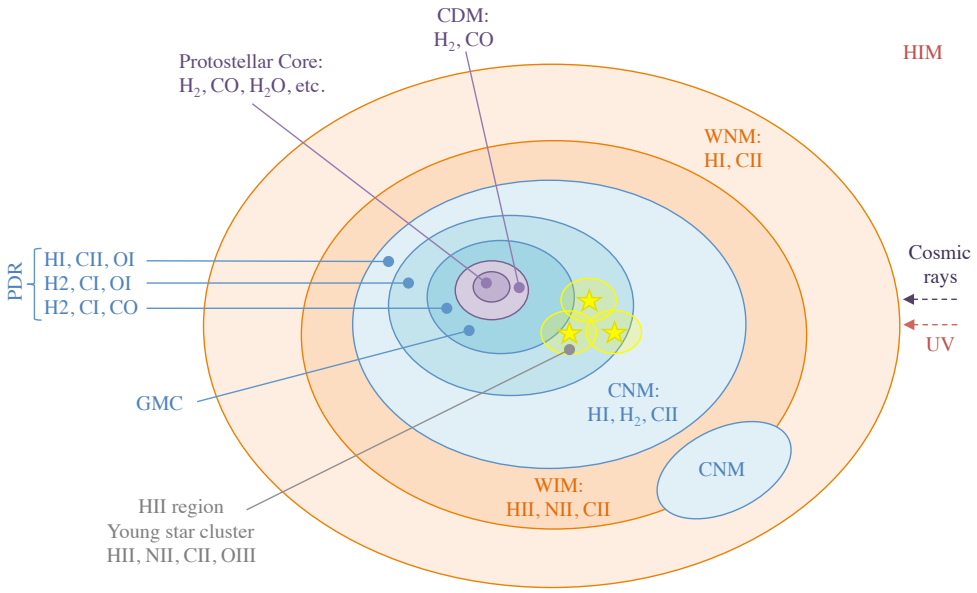

Figure 1.2: Schematic representation of the different phases, physical conditions and characteristic molecular and atomic content within the interstellar medium. Photo dissociation regions (PDR) and their tracers are also indicated. Adapted from Walker (2015)

.

occurs, which is called *interstellar recycling*. For example, there is an intimate relationship between molecular clouds and stars. During parts of its life, a star blows away part of its envelope through stellar winds back to the ISM.

The observable components of the ISM in the terahertz band are mainly the CNM and the CDM, the last of which is composed primarily of molecular hydrogen. However H_2 does not have a permanent electric dipole moment and therefore does not show strong dipole rotational transitions. Because of this and the fact that its rotationally excited levels have energies considerable above the ground state, the bulk of the molecular gas within the ISM remains unobservable for us. There are, however, other species which can be abundant enough to be detected directly and can serve as tracers of hydrogen. The most commonly used tracer is carbon monoxide, but in diffuse clouds CO is under-abundant because it shields itself less efficiently against disassociating UV radiation than molecular hydrogen (Snow and McCall 2006). For these conditions other surrogates should be used, such as the simplest molecules containing hydrogen called hydrides, like OH, HF and CH. Light hydrides have typically their rotational ground state transitions in the THz regime. Their chemical pathways are relatively simple and therefore they can be used as tracers of diffuse molecular hydrogen. In addition, their abundances provide information about the environment where they form (Gerin et al. 2016). CH as a tracer of diffuse H_2 is of particular interest for this work.

The terahertz regime offers other simple tracers of atomic and ionized gas, in particular the bright fine structure lines of oxygen, carbon and nitrogen.

Neutral atomic carbon has two atomic fine structure lines ([CI]); one at 492.16 GHz (Phillips et al. 1980) and the other at 809.34 GHz. Carbon is easier to ionize (11.26 eV) than hydrogen (13.60 eV) and therefore C^+ appears in ionized gas regions, but also in neutral gas where the external Far-UV radiation is not energetic enough to ionize hydrogen but carbon. Singly ionized carbon is only observable in the THz regime (λ158 μm, 1900.537 GHz) and due to its low ionization potential acts as an important coolant for

the diffuse neutral atomic gas in molecular cloud surfaces. To constrain the relative abundance of the different forms of carbon, such as ionized, atomic and molecular, it is of key importance to understand the physical and chemical equilibrium of the different phases of the ISM.

Singly ionized oxygen has a higher ionization potential, just over that of H (13.62 eV) and the [OI] lines at 145 μm and 63 μm are also important agents in the cooling process, in particular in dense PDRs (Hollenbach and Tielens 1997).

Nitrogen has the highest ionization potential of the three elements (14.25 eV), and therefore the [NII] line (at λ205 μm) appears in strongly ionized regions, where the [CII] line will also appear bright. Comparing the relative strengths of [NII] and [CII] emission, it is possible to determine whether the [CII] emission comes from ionized or neutral gas (Walker 2015).

Carbon monoxide is the main and widely used tracer of the dense molecular gas. It also has several transitions that can be observed in the THz band. The mid- to high-J CO lines trace dense and warm gas.

A comprehensive view of all these diagnostics is key to constrain the thermal balance of the ISM and the interaction between the different phases, as the mass and energetics of the ISM are the drivers of the evolution of the Galaxy.

1.2 Terahertz Telescopes

Telescopes or antennae suited for the THz band are of the aperture type, typically using a parabolic (or hyperbolic) main reflector and a secondary mirror. When these two reflectors (mirrors) are conveniently placed, a much bigger effective focal length (Bahner 1967) system can be achieved in a relatively compact configuration that otherwise would be unpractical. Depending on the relative position of the secondary respect to the revolution axis of the main mirror (Fig. 1.3), they can be of the *on-axis* or *off-axis* type. The off-axis telescopes use only a portion of a revolved paraboloid, and the secondary mirror is placed in a way that does not shadow the main reflector. For the on-axis telescope three basic configurations are the most used (Wilson et al. 2009):

- **Cassegrain**. Uses a parabolic main reflector and a hyperbolic subreflector. The focus of the paraboloid coincides with one of the foci of the hyperbola. The focal plane (at the Cassegrain focus) is placed in the revolution axis, and can be in between the two mirrors or behind the main reflector.

- **Gregorian**. Uses a parabolic main reflector and an ellipsoidal subreflector. As for the Cassegrain configuration, both mirror's foci coincide and the focus can be conveniently placed in any point of the telescope axis by choosing proper focal distances.

- **Nasmyth**. It is a variation of the Cassegrain telescope for which the beam is deflected by 90 degrees by an additional mirror. This allows an even more compact configuration for large effective focal lengths. When receiver arrays or cameras are coupled to a Nasmyth telescope, image derotation is required, either optically or by additional software processing.

Variations of these configurations can be built by using different mirrors like the **Ritchey-Chrétien** telescope which is a Cassegrain-like telescope that has both primary and secondary hyperbolic mirrors. When multiple astronomical instruments need to be accommodated, a Cassegrain/Nasmyth system can be built by the use of appropriate tertiary optics.

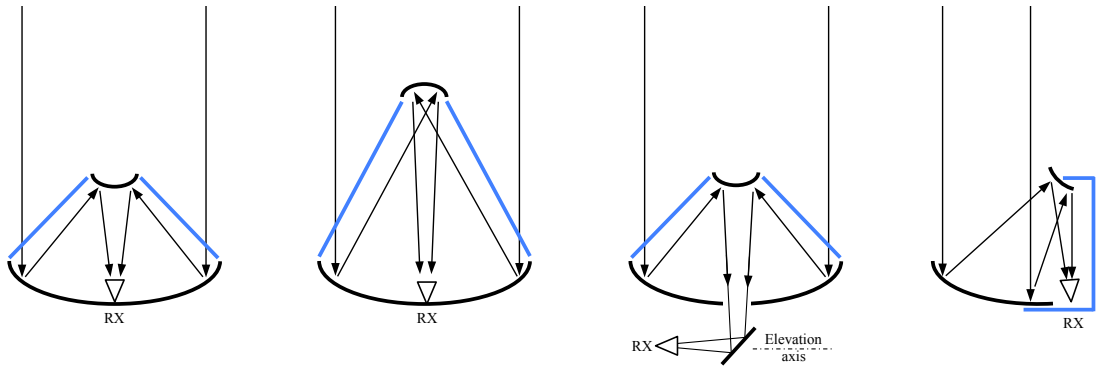

Figure 1.3: Different parabolic reflector types. From left to right: Cassegrain, Gregorian, Nasmyth and Off-axis Cassegrain. The support structures for the secondary mirrors are marked in blue. Adapted from Wilson et al. (2009)

1.2.1 Telescope Key Parameters

The performance of a telescope can be defined through many parameters. Most of these parameters are wavelength dependent, and therefore during the telescope design phase are modeled and accounted for. By the reciprocity principle (Balanis 2005), any optical system (and antenna) designed to *receive* or intercept a radiation field and then focus it into a receiver attached to it, is equally suitable for transmitting radiation originated from a transmitter that replaces the receiver. This makes the analysis more intuitive, as receiving and transmitting concepts can be equivalently used for convenience.

- **Effective focal length and focal ratio (f/D)**. The focal length is the distance in which parallel rays are brought into focus. In other words, it refers to how strong the telescope converges the light into a point. The higher the focal length, the narrower the field of view. The focal ratio, defined as the ratio between the effective focal length and the (effective) aperture, relates the magnification and gain/resolving power of the telescope.

- **Taper**. Astronomical instruments illuminate the optics of a telescope assuming a Gaussian profile. Taper refers to the effective illumination power ratio (Goldsmith 1998) between the center of the mirror (main or secondary) with respect to its edge. It is measured in decibels.

- **Spillover**. It is the percentage of power, emitted by the transmitter, which *spills over* the edge of the reflector and hence is not used to form the (diffraction) beam. In other words, it is the portion of the power measured by a receiver at the focal point that does not come from what is reflected and focused by the telescope optics.

- **Pointing accuracy**. It is directly related to the tracking and control system of a telescope, the alignment between the telescope and the receiver(s), and the mechanical deformations of the telescope optics due to gravitation. This parameter plays a major role, as depending on the receiver beam size (the effective size of the receiver detector beam when projected in the sky through the telescope), a variation of a few arcseconds can lead on a major error with the telescope targeting an object in the sky. The error can be controlled by systematically producing pointing models.

- **Surface accuracy**. Ruze (1966) studied and established a way to quantify the small scale, randomly distributed deviations (mechanical imperfections and deformations) of a mirror from its prescribed

shape, causing randomly distributed phase errors. The surface quality limits the telescope efficiency and the upper operational frequency of the system.

- **Blocking, vignetting and effective aperture.** For on-axis telescopes, the central sub-reflector and its support structure (legs) cause shadowing of the aperture, reducing the effective aperture (Fig. 1.3). Vignetting is the effect of any additional element that limits and frames the beam on the edges of the mirror. The effective aperture differs from the physical aperture due to these two effects.

A complete formal treatment description of the concepts described above is provided in the monograph by Baars (2007).

1.2.2 The Role of the Atmosphere

At terahertz frequencies, the transparency or transmission of the atmosphere is mostly limited by the (amount of) water vapor present in it. Water vapor absorbs the incoming radiation in significant frequency ranges and leaves a number of windows with relatively good transmission. The atmospheric water content decreases exponentially with the geographical altitude. In addition, the presence of other chemical species yield additional absorption lines, called telluric features. Telluric lines in the terahertz windows are coming from ozone (O_3), gaseous oxygen (O_2), carbon dioxide (CO_2), sodium (Cotton et al. 2014) and some other molecules.

Measuring the atmospherical optical depth (τ_{atm}) is important to establish a proper calibration (Guan et al. 2012) and to determine the atmospheric transmission. Depending on the transmission, certain frequencies might be difficult to observe from a specific place or not at all. The use of atmospheric models which rely on precipitable water vapor (PWV) measurements and include the telluric lines is fundamental for far-infrared spectroscopy, in order to avoid introducing spurious features into the astronomical data. Models, such as the ATM (Pardo et al. 2001), ATRAN (Lord 1992) and AM (Paine 2018), are used at different observatories as standard tools.

Ground base observations are strongly affected by the atmosphere. For this reason, the telescope location (site) needs to be as dry (low PWV) and as geographically high as possible (less atmospheric mass and lower pressure, making water absorption narrower). Figure 1.4 shows the situation for the Chajnantor plateau at 5000 m above sea level, and SOFIA flying at 13 km.a.s.l. For example, the Chajnantor[1] site is completely *blind* over 1.6 THz and even SOFIA observations are not completely exempted from the effect of the atmosphere.

1.2.3 Site and Telescope Platform

Ground-based Telescopes

The selection of the location for a telescope, known as *site testing*, is usually a long and systematic process. It implies the instrumental measurement and analysis of atmospheric data over many years (Otárola et al. 2005) of different potential places (candidates).

There are only a few places on the Earth were environmental and geographical conditions, and logistics are suitable to install and operate a THz telescope. Among the most remarkable are:

- The Chajnantor plateau and its surroundings (> 5000 m.a.s.l), in the Chilean Andes, hosts the Atacama Pathfinder EXperiment - **APEX**, (R. Güsten et al. 2006) a 12 m diameter Cassegrain/Nasmyth submillimeter telescope, and the Tokyo Atacama Observatory, **TAO**, of 6.5 m

[1] From local Ckunza language: "Taking-off place"

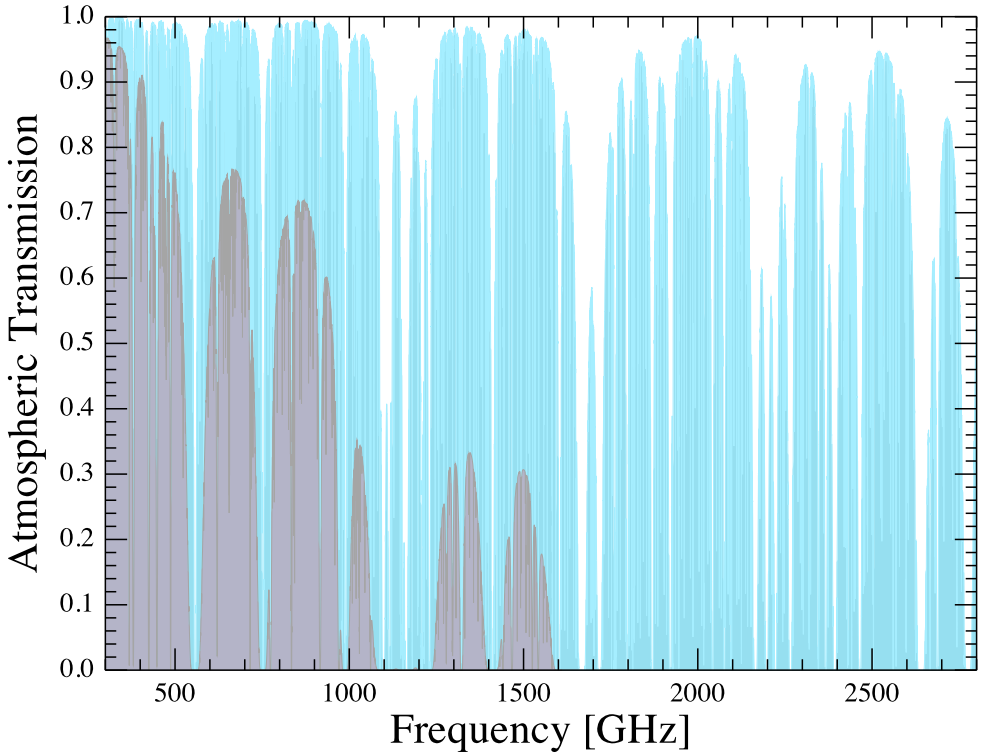

Figure 1.4: Comparison of atmospheric transmission for different observatories: In cyan, SOFIA at 43.000 ft (13.000 m.a.s.l.) and PWV of 10 μm, a typical situation. In gray, APEX (Chajnantor Plateau) at 5000 m.a.s.l. and 200 μm of PWV, which is a rather exceptional condition.

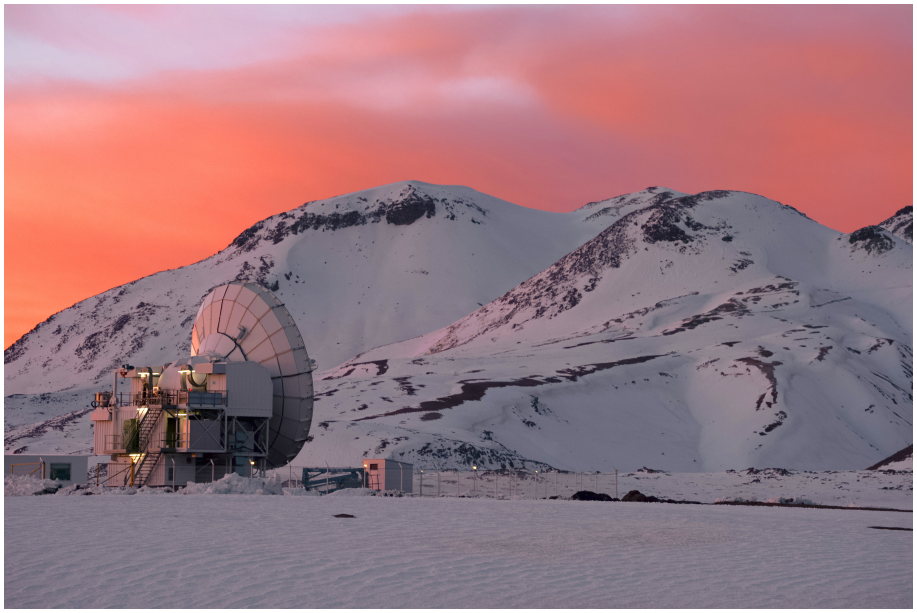

Figure 1.5: The Atacama Pathfinder Experiment (APEX) telescope on a snow covered Chajnantor landscape. Credit: Carlos A. Durán/ESO

and its predecessor, the 1.0 m *miniTAO* (Yoshii et al. 2010) operating in the infrared range, among others. It is also the home place for **ALMA**, the Atacama Large Millimeter Array (Wootten and Thompson 2009).

- Mauna Kea in Hawaii (> 4200 m.a.s.l) hosts several observatories: the James Clerk Maxwell Telescope, **JCMT** (Vanderveen 1989), with a 15 m diameter reflector and the Submillimeter Array or **SMA**, with 8 antennae of 6 m diameter each (Blundell 2004).

- The south pole on the Antarctic plateau (> 3000 m.a.s.l.) also offers an excellent site, being the home of the South Pole Telescope, **SPT**, a 10 m telescope fitting a bolometer camera specially suited for the detection of the SZ-Effect (Gardner et al. 2006) and **AST/RO**, the 1.7 m Antarctic Submillimeter Telescope and Remote Observatory (Stark et al. 2001).

Airborne Telescopes

Strictly speaking, airborne astronomy began in the 1920s (Whiting Dolci 1997). For the next 40 years most of the observations made had solar eclipse studies as scientific goals.

In 1966 the **LearJet Observatory** (Russell 1985) was introduced as a flying infrared observatory. It was initially fitted with a 25 mm thick and 305 mm diameter quartz window which restricted the size of the telescopes and the frequency range for the observations (to $\lambda 5\ \mu$m). In 1968 a 12-inch open-port reflecting telescope was installed in a passenger window enabling a wider infrared window, and with this technical achievement, modern airborne infrared astronomy started. It continued in sporadic operation until 1997. The Learjet observatory accounts for the first observation of the important ISM cooling [CII] line at $\lambda 158\ \mu$m.

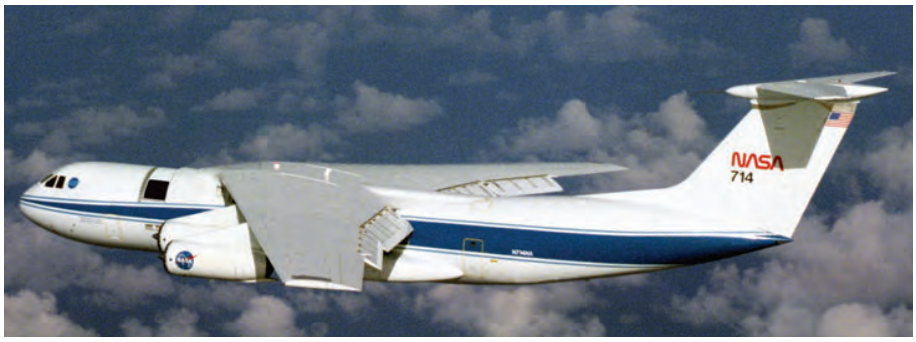

Figure 1.6: The Kuiper Airborne Observatory (KAO), in flight. Telescope door hatch is open in this image. Image taken from Erickson and Meyer (2013)

The Kuiper Airborne Observatory or **KAO** (Erickson and Meyer 2013), a modified Lockheed C-141 plane (NASA N714NA, Fig 1.6) hosting a 36 inch infrared telescope, replaced the LearJet Observatory. It operated between 1971 and 1995 flying up to 15 km.a.s.l. During its life time about 50 specialized scientific instruments were tested and operated on board, spanning different techniques and technologies, including spectrometers (heterodyne, Echelle grating, prism, imaging Fabry-Perot and Michelson) and photometer/camera (high speed CDD[2] and high angular resolution) and their support modules and subsystems. Many of the technologies and procedures developed and matured at KAO are used on SOFIA.

[2] CCD: Charge-coupled device

The Stratospheric Observatory for Infrared Astronomy, **SOFIA**, is a modified Boeing 747SP fitting a 2.7 meters telescope. Currently 8 different scientific instruments are in used at SOFIA (E. C. Smith et al. 2014): EXES (Echelon-cross-Echelle Spectrograph), FIFI-LS (Far-Infrared Field-Imaging Line Spectrometer), FLITECAM (First Light Infrared Test Experiment CAMera), FORCAST (Faint Object InfraRed CAmera for the SOFIA Telescope), GREAT (German Receiver for Astronomy at Terahertz Frequencies), HAWC+ (High-resolution Airborne Wideband Camera) and HIPO (High-speed Imaging Photometer for Occultations). SOFIA is described in more detail in Chapter 2.

Balloon-borne Telescopes

For the last 60 years, balloons have been employed as telescope platforms, beyond their classical use for meteorological measurements. Modern scientific balloons can lift up to 3600 kg and usually reach much higher altitude than airplanes (30 - 50 km.a.s.l.), but require 3-axis active tracking control to compensate the induced motion of the stratospheric winds and the slow rotation and pendulum motion of the balloon. They also need constant communication with a control base. The first balloon-borne telescopes were the **Stratoscope** I and II missions (Kidd 1964). However, it was not until **THISBE**, the Telescope of Heidelberg for Infrared Studies by Balloon-borne Experiments (Lemke 1970), that they started to be used for far-infrared astronomy. Many other experiments in different wavelength regimes have been carried out since then, like the **BOOMERanG** experiment (Balloon Observations Of Millimetric Extragalactic Radiation ANd Geophysics) used to measure the cosmic microwave background (CMB) radiation (Crill et al. 2003).

The Balloon-borne Large Aperture Submillimeter Telescope, **BLAST**, a 2 m telescope equipped with a bolometer array covering the λ250, λ350, and λ500 μm bands (Pascale et al. 2008; Fissel et al. 2010) flew in both hemispheres (from Sweden to Canada and over Antarctica) in three scientific missions. The technology used in the arrays was developed for the Herschel/SPIRE instrument (Griffin et al. 2010).

The Stratospheric Terahertz Observatory or **STO** (Walker et al. 2010) and its successor, the STO2 are both a long duration ballon experiments with a 0.8 m telescope, flying over Antarctica. STO is equipped with two 4-pixel arrays of heterodyne receivers, one tuned for the [CII] line (λ158 μm), and the other for the star formation tracer [NII] (λ205 μm). STO2, has in addition a single pixel neutral atomic oxygen [OI] frequency tuned receiver (4.7 THz).

GUSTO, the Galactic/extragalactic Ultra long duration balloon Spectroscopic Stratospheric THz Observatory is a new mission expected to be launched in December, 2021 (Walker et al. 2018; Martin et al. 2012). Currently under development, it will host a 0.85 m telescope with an expanded version of the STO-2 receiver, counting 8-pixels per frequency. Its goal baseline mission is 100 days of flight over Antarctica, conducting a Galactic plane survey, a Large Magellanic Cloud survey and deep surveys of selected sources.

Space Telescopes

IRAS, the Infrared Astronomical Satellite (Neugebauer et al. 1984) was the first space telescope to perform a survey of the entire sky at infrared wavelengths. Consisting of a 0.57 m telescope its was equipped with detectors covering the λ12, 25, 60, and 100 μm bands and a spectrometer. IRAS operated for about 10 months (in 1983) before being shut down.

It was not until the middle of the 1990 decade that a new mission saw the light. **ISO**, the Infrared Space Observatory (Kessler et al. 1996) had a 1.7 K cooled (superfluid helium) 0.6 m telescope and carried four instruments (ISOCAM, ISOPHOT, SWS and SWS) that allowed for imaging and photometry from λ2.5 to 240 μm and spectroscopy from λ2.5 to 197 μm. ISO was a collaboration between the European

Figure 1.7: Artist's impression of the Herschel spacecraft. Copyright: ESA/ AOES Medialab; background: Hubble Space Telescope image (NASA/ESA/STScI)

Space Agency (ESA), the Japanese Aerospace Exploration Agency (JAXA) and NASA that operated from December 1995 to April 1998.

The **Spitzer** space telescope (Werner et al. 2004), a Ritchey-Chrétien 0.85 m telescope, was launched in August 2003. Its instrumentation is composed by an infrared camera which operates simultaneously in four wavelengths (3.6, 4.5, 5.8 and 8 μm), four 128×128 pixels infrared spectrometer sub-modules which operate at the wavelengths range of 5.3-14 μm and 14-40 μm in low resolution and 10-19.5 μm and 19-37 μm (high resolution), and three detector arrays in the far infrared (128×128 pixels at 24 μm, 32×32 pixels at 70 μm, 2×20 pixels at 160 μm). The mission duration of over 5 years doubled the originally planned life span. Spitzer ran out of its liquid helium coolant in May 2009, but still is continuing to take data with the 3.6 and 4.5 μm channels of the near infrared camera.

The **AKARI** (Murakami et al. 2007) satellite has a 68.5 cm cooled telescope and hosts two focal plane instruments, the Far-Infrared-Surveyor (FIS) and the Infrared Camera (IRC). FIS is an all-sky survey Fourier Transform Spectrometer (FTS) for imaging and spectroscopy, consisting of four detector arrays: 20×2 GeGa detectors, covering the 65 μm, 20×3 GeGa detectors for the 90 μm, 15×3 stressed GeGa detectors for the 140 μm and 15×2 stressed GeGa detectors for the 160 μm wavelength band. IRC, on the other hand, is an all-sky imaging and spectroscopy capable prism and grism[3] instrument equipped with three arrays: a 512×412 InSb detector based array for 2.4, 3.3 and 4.1 μm, a 256×256 SiAs array for 7.0, 9.0 and 11 μm, and a 256×256 SiAs array for 15, 18 and 24 μm wavelength. It was built by the Japanese space agency (JAXA) and operated between May 2006 and August 2007, when its liquid-helium coolant depleted.

The **Herschel** Space Observatory (Pilbratt et al. 2010) is one of the most remarkable space telescopes and of particular relevance for this work. Unlike the aforementioned spacecrafts, which all orbit the Earth, Herschel was transported to the second Lagrangian point (L2) of the Sun–Earth system and orbits

[3] Grism is a combination of a prism and a grating, used for optical filtering.

the Sun with a fixed distance of 1.5 million km from Earth. Herschel is four times larger than any other previous infrared telescope and was aimed to observe the cold and dusty universe. The telescope (Fig. 1.7) is a Cassegrain configuration consisting of a 3.5 m monolithic SiC structure based main reflector and a 0.3 m secondary mirror containing a scattering cone to reduce standing waves. The main reflector was passively cooled below the 90 K. It boards three different highly optimized and complementary instruments, with different technologies: the Photodetecting Array Camera and Spectrometer or PACS (Billot et al. 2006), the Spectral and Photometric Imaging Receiver or SPIRE (Griffin et al. 2010) and the Heterodyne Instrument for the Far Infrared or HIFI (de Graauw et al. 2009). PACS and SPIRE are aimed for large scale imaging at wavelengths of 70, 100, 160, 250, 350 and 500 μm and they operate in parallel, providing also medium resolution spectrometry. HIFI on the other hand offered single-pixel very high resolution spectrometry over the range from 480 GHz (625 μm) to 1910 GHz (157 μm) using different mixers. The PACS spectrometer and the HIFI mixers were cooled to 1.7 K by a thermal link to the onboard helium tank, used as main cryo-coolant, whereas the SPIRE and the PACS bolometers, were cooled down to 300 mK by means of an internal ^{3}He sorption cooler (Duband et al. 1991).

In the coming years new telescopes will be launched. Among the most remarkable are the James Webb Space Telescope or **JWST** (Gardner et al. 2006) for the near (λ0.6 μm) to mid-IR (λ28.5 μm) ranges with its novel 6.5 m gold-coated beryllium reflector with a collecting area of 25 m^2 made up of 18 hexagons. **SPICA** (Roelfsema et al. 2018), the Space Infrared Telescope for Cosmology and Astrophysics, is a proposed mission focused on the mid and far infrared frequency windows. The current concept foresees a 8 K cooled 2.5 m telescope and its instrumentation will include two spectrometers to cover the wavelengths between 12 and 18 μm and 17-230 μm. Additionally SPICA will have instruments for efficient λ30-37 μm broad band mapping, and polarimetric imaging in the λ100-350 μm range. The goal launch year of SPICA is 2022, with an expected mission duration of over 36 months.

Comparison between the Different Telescope Locations

Airborne astronomy allows observation over an exceptionally broad frequency range, with a large fraction of it non-accessible from ground-based facilities. As for ground-based observatories, an airborne observatory permits continuous technical upgrades of its systems and instrumentation (software and hardware), and regularly scheduled and corrective maintenance. However the operational costs are much higher than for a ground based facility. There are also special (aeronautics) safety considerations and limitations in the weight and dimensions of the instrumentation installed. The duration of an observing run (daily observing hours) is also limited.

Space missions offer a much longer observing run with no atmospheric interference, but have much more limited life span for the instrumentation and systems because of the limited amount of coolant. Corrective maintenance is nearly impossible[4]. To over come this, redundancy in critical systems is required, limiting the total amount of weight and size left for instrumentation. A satellite mission usually demands a high investment and years of test and development for every subsystem, to ensure reliable operation in the outer space. Moreover, compared to ground based and airborne telescopes, the amount of instantaneous data output they can transmit is limited by their radio data links.

Ballon based telescopes are intermediate between airborne and and space observatories. While they benefit from a thin atmosphere, their instrument carrying capacity is also restricted. The mission duration is also limited and the absolute trajectory of the ballon is dominated by high altitude winds and local weather. In case of a failure, the mission can be canceled and the telescope recovered. However during landing an important fraction of the onboard equipment can get damaged.

[4] The exception is the Hubble Space Telescope, which has undergone five servicing missions, including the famous (and expensive) correction for the flaw in Hubble's primary mirror. https://www.nasa.gov/mission_pages/hubble/servicing/index.html.

Ground based observatories, when located in high and dry places, offer a platform which is only limited by the the atmospheric transmission and the logistics. Depending on their configuration, they can lodge many instruments, several of which can be potentially used simultaneously, with the suitable optical setup. Preventive and corrective maintenance can be performed as well as systematic technical and operational upgrades.

Table 1.2 provides a comparison between the different telescope locations.

Table 1.2: Telescope characteristics according to their physical location (site)

Site	Atmosphere	Able to update/repair	Access	Observing run	Data rate	Limitations
Ground-based	Thin (altitude)	HW/SW	Always	24/7	High	No
Airborne	Very thin	HW/SW	Daily	Hours (daily)	High	Power/Weight
Balloon	Very thin	HW/SW	Monthly	Weeks	Mid	Power/Weight
Satellite/Space	non-existing	SW	No	Months	Low	Power/Weight

1.3 Receiver Technology for THz Astronomy

Astronomical receivers are complex systems, made up of several subcomponents. They can be classified into two big groups: coherent and non-coherent. Coherent receivers can be tuned to a specific frequency of the electromagnetic spectrum and process the individual frequency components of a selected frequency range, defined as the bandpass. They are of particular interest of this work and therefore we focus on them. Non-coherent receivers, on the other hand, measure the (total) power of the incident electromagnetic radiation by causing a temperature change in some detector material. They are usually non-tunable but sensitive to a broad wavelength range. At (sub)millimeter wavelengths, the most commonly used non coherent detectors have been bolometers. A very extensive study and through review of the receiver technology has been presented by Kooi (2008).

1.3.1 Coherent Detection Systems

The principle behind coherent or *heterodyne* detection is based on *downconversion*. Downconversion is the frequency-shifting of a signal from a high frequency regime to a lower frequency range. The term coherent refers to the fact that the process keeps the amplitude and phase of the processed signal. Downconversion is achieved by multiplying or *mixing* the incoming RF[5] signal with a high precision frequency reference called local oscillator (LO). The result of this process is an amplitude modulated signal (in the time domain) which is decomposed into the sum of two signals: one having a frequency equal to the sum of the frequency of the RF signal and the LO, and another resulting from the frequency difference between LO and RF. This second component, known as intermediate frequency (IF), is of our interest. The other component, of much higher frequency, is discarded or *filtered* as it lies out of the band. The mixing process is described mathematically by the equations 1.1 and 1.2, where $g_{RF}(t)$ corresponds to the RF signal in the time domain, represented here by a sinusoidal signal for simplicity, $g_{LO}(t)$ the LO signal and $g_{IF}(t)$ the (filtered) result from the downconversion.

[5] RF stands for radio frequency. The term has been kept until today for historical convention and used to refer to the high frequency signal on a receiving or transmitting system.

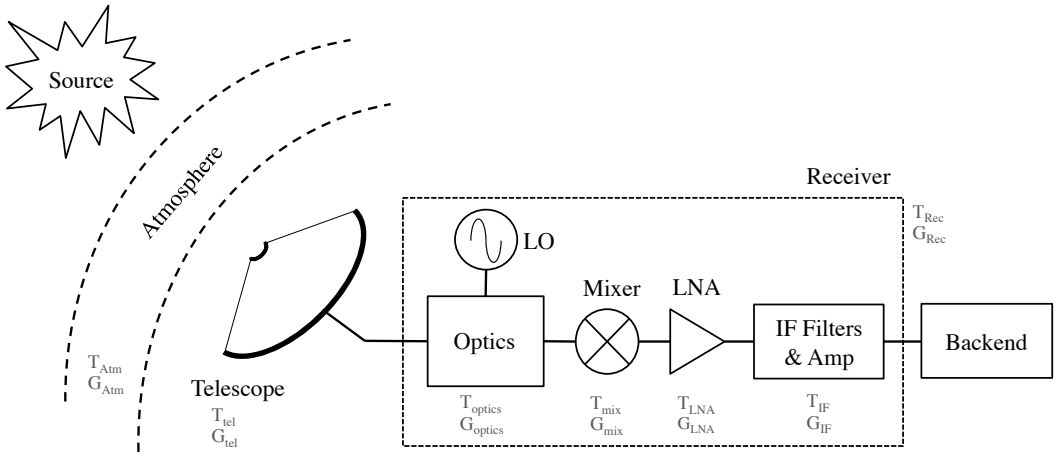

Figure 1.8: General diagram of an heterodyne receiver at Terahertz frequencies. Note that the local oscillator signal is coupled through the optics at this frequency range.

$$g_{RF}(t) \cdot g_{LO}(t) = (V_s \cdot \cos(2\pi \cdot \nu_{RF} \cdot t + \phi_{RF})) \cdot (V_{LO} \cdot \cos(2\pi \cdot \nu_{LO} \cdot t + \phi_{LO})) \tag{1.1a}$$

$$= \frac{V_{RF} \cdot V_{LO}}{2} \cdot [\cos((2\pi \cdot \nu_{RF} + 2\pi \cdot \nu_{LO}) \cdot t + (\phi_{RF} + \phi_{LO})) + \cos((2\pi \cdot \nu_{RF} - 2\pi \cdot \nu_{LO}) \cdot t - (\phi_{RF} + \phi_{LO}))] \tag{1.1b}$$

$$g_{IF}(t) = \frac{V_{RF} \cdot V_{LO}}{2} \cdot \cos(|2\pi \cdot \nu_{RF} - 2\pi \cdot \nu_{LO}| \cdot t \mp \phi_{IF}) \tag{1.2}$$

A negative frequency value for the IF signal expression implies a shift on the phase of 180 degrees, and is not relevant for the amplitude of the signal. However this effect has implications on how the RF signal band is translated into the IF band. Equation 1.2 implies that $\nu_{IF} = \nu_{RF} - \nu_{LO}$ and $\nu_{IF} = \nu_{LO} - \nu_{RF}$ are both valid as IF frequency. In other words, two values for the frequency of the RF signal ($\nu_{1-RF} = \nu_{LO} + \nu_{IF}$ and $\nu_{2-RF} = \nu_{LO} - \nu_{IF}$) could be successfully downconverted to the same IF signal. These two values, or bands for a more general case, are known as *sidebands*. The lower side band or LSB is the one with frequency lower than the LO, while the upper side band or USB, corresponds to the higher value (Fig. 1.9).

In the frequency domain, the downconversion process can be seen as the convolution (Eq. C.7) of the corresponding Fourier transforms (defined as Eq. C.6. and its operator designated by the letter $\mathfrak{F}$) of the RF signal (G_{RF}) and the LO (G_{LO}) as presented in Eq. 1.3.

$$\mathfrak{F}(g_{RF} \cdot g_{LO}) = G_{RF} * G_{LO} \tag{1.3}$$

The mixing process described in the previous paragraphs represents an ideal case for downconversion. In practice, the process is carried out by making use of the non-linear response of an material or a junction of different materials, like a diode. In a diode, the relation among the applied voltage between the anode and the cathode ($V_{ak}(t)$), and the measured current through the diode junction ($I_d(t)$) is highly non-linear and can be described by a polynomial function (Eq. 1.4).

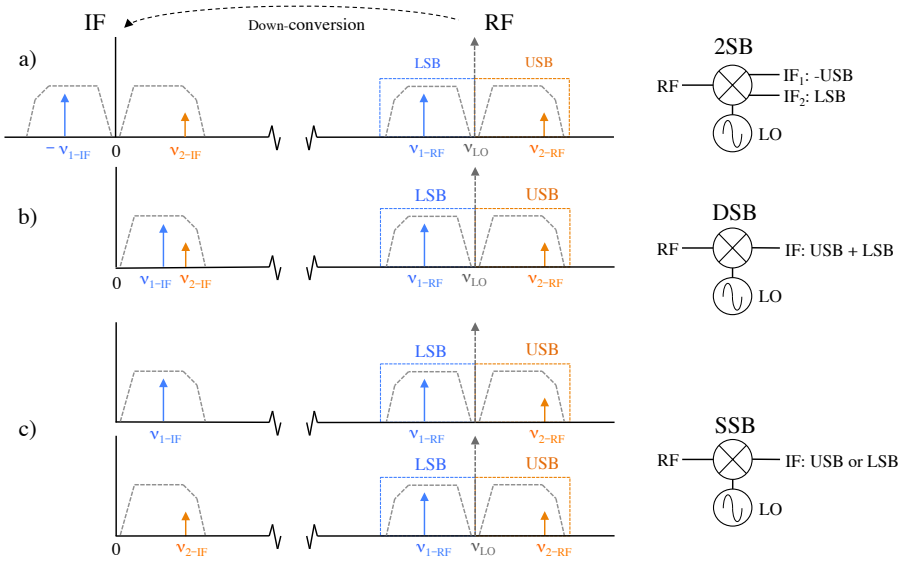

Figure 1.9: Frequency downconversion using different mixing schemes

$$I_d(t) = a_0 + a_1 \cdot V_{ak}(t) + a_2 \cdot V_{ak}^2(t) + a_3 \cdot V_{ak}^3(t) + \ldots \tag{1.4}$$

It is the quadratic term of this equation that is used for mixing purposes. When LO and RF signals are present, this term leads to the Eq. 1.5. When expanding the expression on the right-hand side of that equation, one of the terms equals that in Eq. 1.1.

$$g_{IF}(t) \propto [g_{RF}(t) + g_{LO}(t)]^2 = [V_s \cdot \cos(2\pi \cdot \nu_{RF} \cdot t + \phi_{RF}) + V_{LO} \cdot \cos(2\pi \cdot \nu_{LO} \cdot t + \phi_{LO})]^2 \tag{1.5}$$

The downconversion can be realized in three different ways. These are known as mixing schemes. Depending in the presence or absence of the RF sub-bands (LSB and USB) on the IF, they can be classified on:

* Double side band (DSB)
* Single side band (SSB)
* Dual or two side band (2SB)

The double side band conversion is the simplest and most commonly used mixing scheme. A mixer using a single junction is intrinsically DSB, which implies that not only the signal frequency band appears in the IF but also the *image* band. This case is shown in Fig. 1.9b. The LSB is *back folded* into the IF. This means that the portion of the RF spectrum contained in that sub-band is mirrored and superimposed or added to the down converted side band. Although this scheme is simple, its major drawback comes from the contamination suffered in the signal band (at the IF) by the image band. When dealing with DSB mixers systems, this fact must be accounted when selecting the band/mode and the LO tuning frequency during the astronomical observations, and in the data calibration process. The atmospheric opacity, atmospheric noise (telluric features) and mixer response could be different on the LSB and USB and therefore its contribution to the IF band, introducing spurious features and calibration problems both of which hampers the scientific interpretation of the data.

The SSB scheme filters the image band before performing the mixing process and therefore only the signal band is present in the IF band. The band filtering is not perfect and a small fraction of the radiation from the filtered image band contributes to the noise. High frequency filters can be implemented in different manners. A common way is to use a mixer waveguide back-short, which acts as a (destructive) resonator. The mixer requires mechanical tuning for every LO frequency. The SSB mixers still exhibit the LSB folding feature (Fig. 1.9c).

The 2SB scheme, also known as side band separation, makes the USB and LSB simultaneously and independently available (Fig. 1.9a). More complex in its fabrication, it employs two DSB mixer junctions, power splitters and a 3 dB-90° hybrid couplers (Pozar 2004). The RF band is equally split (in power) and directed to each of the internal mixers. The LO signal is also split and one of the legs shifted in 90°. The output from the first mixing element contains the USB and LSB, while the second mixer yields USB shifted in -90° and LSB in +90°. Both outputs are then shifted in +90° and combined through the hybrid coupler. At the output of the two independent hybrid coupler ports the LSB and USB bands are available. The 2SB scheme requires careful gain balancing between the internal mixers, precise phase shifting of the LO and the signal in the intermediate steps and signal power splitting/combination.

DSB and SSB mixers parameters are compared by Lamb (2000), while Guilloteau (2002) makes a performance assessment of the three mixing schemes using a scientific approach.

Detector Technology

Heterodyne receivers are implemented in different forms for a wide range of applications. Concerning astronomical investigations, there are only few different detector topologies and technologies available as real options. They can be separated in two groups according to the target frequency coverage and the disposition of certain key components in the receiver chain.

The first group makes use of a high frequency low noise amplifier (LNA) placed directly in between the mixer and the free space coupling element (horn) or quasi-optical element. The front end LNA, usually cooled, amplifies the RF signal before getting to the mixer, usually at room temperature. This makes the system very compact. These kind of receivers are suitable for frequencies below 115 GHz. The technology used for the LNA is either High Electron Mobility Transistor (HEMT) or Monolithic Microwave Integrated Circuit (MMIC), while mixers can be implemented using silicon junctions.

For the second group, suitable for frequencies in the THz regime, the mixer connects directly to the horn or the coupling antenna. In addition, the local oscillator signal is injected quasi-optically through the same RF port or through a dedicated input. A LNA can be connected to the mixer IF port. This situation is depicted by Figure 1.8. Superconductor-Insulator-Superconductor (SIS) and Hot Electron Bolometer (HEB) mixers are the primary technologies used for these frequencies, while HEMTs and MMICs are used here as IF band LNAs, at much lower frequency.

Table 1.3 shows an overview of these detector technologies and the specific frequency windows they cover.

A field effect transistor or FET is built upon a *sandwich* of three doped materials. The electric field (voltage) on the gate port (G) of the transistor controls the flow of the carrier source (electrons) from the source port (S) to the drain (D). Small variations on the electric field have a large effect on the current flow from S to D. This makes a FET a good amplifier. The **HEMT** (Mimura et al. 1980) is an enhanced high speed version of a FET. Traditionally made on GaAs substrate, modern HEMTs based on InP reach excellent performance and low noise temperatures, and are easily used in cryogenic environments, as they have very low power dissipation. State of the art receivers, like the ALMA band 1 cartridge (Huang et al. 2016) shown in Fig. 1.10, use two front end HEMTs, one per polarization. The HEMTs are cooled to 15 K and cover the band from 35 to 50 GHz. The mixer (at room temperature) can separate the sidebands

Table 1.3: Current technologies used for astronomical applications.

Abbrev. name	Technology full name	Frequency range [GHz]	IF Band [GHz]	Use	Remark
HEMT	High Electron Mobility Transistor	< 100		FE LNA IF LNA	Cooled Semiconductor
MMIC	Monolithic Microwave Integrated Circuit	< 100		FE LNA IF LNA	Cooled Semiconductor
SIS	Superconductor-Insulator-Superconductor	< 1000	4 - 8(12)	Mixer	Superconductor
HEB	Hot Electron Bolometer	> 900	0 - 4	Mixer	Superconductor

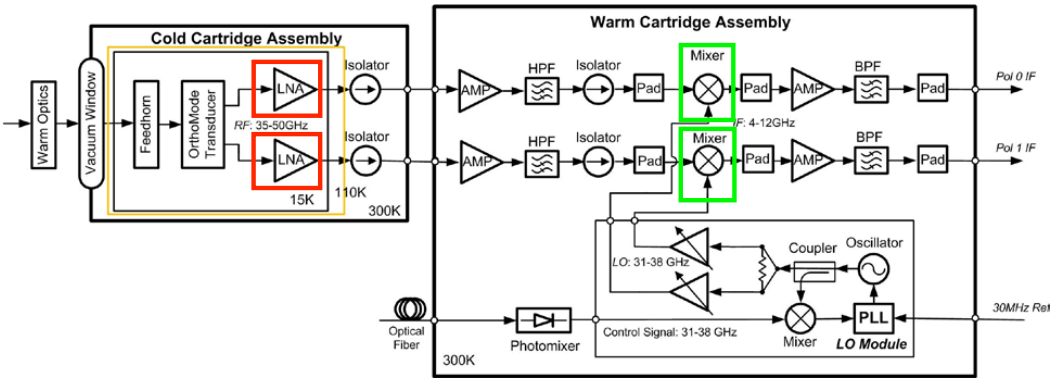

Figure 1.10: ALMA band 1 receiver block diagram. HEMTs, boxed in red, are the first active element and placed just behind the polarization splitter (Orthomode transducer - OMT). Mixers, boxed in green, are at room temperature. Taken and adapted from Huang et al. (2016)

using a more conventional strategy (Pozar 2004).

HEMTs are commonly used at lower radio frequencies, as cryogenic low noise amplifiers. In (sub)millimeter receivers, located after the mixer, they amplify the IF band, adding very low noise temperature to the receiver temperature (T_{Rec}).

MMICs (ibid.) integrate HEMTs into a more compact layout. Here all the active and passive elements are fabricated on a single semiconductor wafer (crystal). With this, the variabilities and tolerances of the lumped components that are integrated in the design are much more controlled and therefore performance dispersion between amplifiers implemented using this way is much lower. This is particularly useful when many compact low noise amplifier system are required either for a multi-pixel receiver or for multiple individual receivers working together. The ALMA Band 2+3 cartridge (Cuadrado-Calle et al. 2017), covering from the 67 to 116 GHz, uses MMICs as front end LNAs. Excellent MMICs covering the band from 0 to 10 GHz that are suitable for cryogenic environments are commercially available.

A good description of the design and characterization process of HEMT and MMIC amplifiers has been given by Risacher (2005).

The Superconductor-Insulator-Superconductor tunnel junction mixers or **SIS** can be defined in a single sentence as *single quasiparticle photon assisted tunneling detectors* (Wilson et al. 2009). A SIS junction consists of a superconducting layer, a thin insulating layer and another superconducting layer (Fig. 1.11).

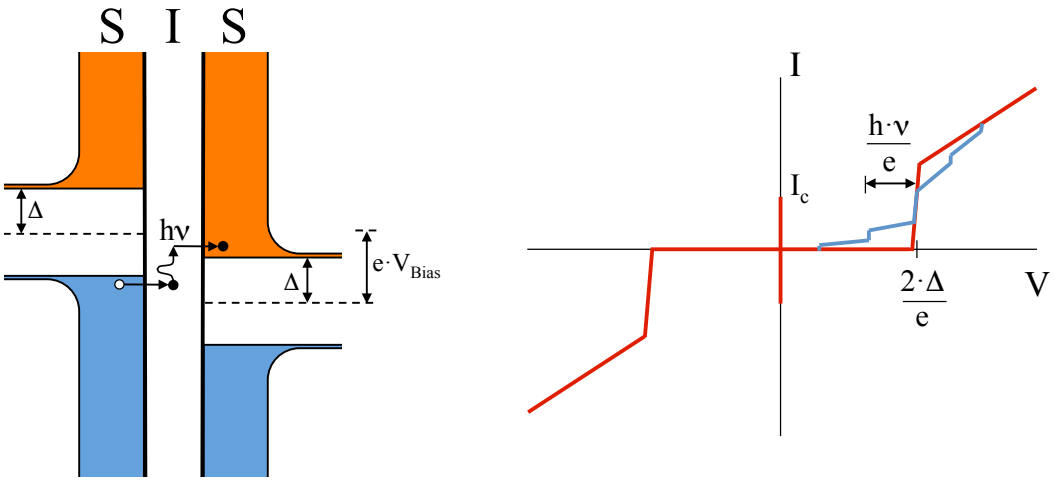

Figure 1.11: SIS Mixer. Left: Energy band scheme. The gap between the filled (blue) and the empty states (orange) is 2Δ, the Copper pair binding energy. Right: I-V Curve. Curve in red corresponds to an unpumped mixer, that in blue, with LO power on.

The principle of an SIS junction can be understood in the framework of the Bardeen-Cooper-Schrieffer (BSC) theory of superconductivity (Kadin 1999). In the superconducting (S) material, the gap between the energy band with filled states and that with unfilled states is 2Δ. In a superconducting material, electrons bind together forming quasi-particles named Cooper pairs. A quasiparticle with an energy $|E| < \Delta$ on the left side superconductor cannot tunnel into the right superconductor. Only when the voltage (V_{Bias}) applied to the junction is large enough, quasiparticles will have the energy to overcome the gap and a current will flow from the left to the right superconductor. Above the energy gap ($V_{Bias} > V_{gap} = 2\Delta/e$) the filled state from the left semiconductor and the unfilled state from the right semiconductor line up and current flows linearly with respect to the applied voltage. If the applied bias voltage has a value just below V_{gap}, an incoming photon increases the energy of the quasi particle allowing it to tunnel. This effect is known as photon-assisted tunneling. When an LO signal is injected, photon steps appear on the I-V curve, spaced by $h\nu/e$, and photon-assisted tunneling follows the LO signal. For a fixed bias voltage, an increase on the LO power implies an increase of the current.

The tunneling of the Cooper pairs causes the Josephson effect, which manifests in two ways. The first is the appearance of a DC current in absence of a bias voltage. The second, the AC Josephson current, appears as oscillations (at ≈ 484 GHz/mV for Niobium-Aluminumoxide-Niobium mixers), resembling features similar to the photon steps (known as Shapiro steps). To suppress the Josephson effect, different techniques can be employed. The most common technique is to apply an external magnetic field parallel to the junction by using superconducting magnets. There poses an inherent risk of a residual magnetic flux when the DC voltage used to generate the magnetic field is switched off. This issue, known as trapped flux, is solved by temporary heating up the mixer to take it out of the superconducting regime.

SIS mixers have many advantages. They have very low noise, close to the quantum limit ($h\nu/k$), have fast response time, reflected in the IF bandwidth, have high conversion gain (IF output power to RF input power ratio), can be tuned over a large frequency range (>20%) and require relatively low LO power to be pumped, usually between 1 and 10 μW (Belitsky 1999). However, they often present problems with output impedance mismatch with the IF LNA, inducing standing waves and requiring the use of an isolator.

The Hot Electron Bolometer or **HEB** mixer is based on the bolometric principle. HEBs are (mainly)

temperature dependent resistive devices (R = 20 - 200 Ω). They are built using a superconducting bridge ($\sim 1 \times 0.1$ μm) held by two normal contact pads. The contact pads are part of an antenna used to couple the LO and RF radiation from the mixer horn or waveguide (Fig 1.12 left.).

$$P_{HEB} = \frac{[V_{LO} \cdot \cos(2\pi \cdot \nu_{LO} \cdot t) + V_{RF} \cdot \cos(2\pi \cdot \nu_{RF} \cdot t)]^2}{2 \cdot R_o} \tag{1.6}$$

HEB mixers, as SIS, also require setting a working point with a bias voltage, V_{bias}. When $V_{bias} = 0$, the HEB bridge behaves like a short circuit (in superconductivity). As V_{bias} is raised, the Cooper pairs on the bridge start to brake up and the device no longer behaves like a superconductor. This is called the *transition region*. When V_{bias} is high enough and all the pairs are broken, the HEB behaves like a resistor (*normal region*). To efficiently operate the HEB as a mixer, it is biased in a way that the combination of V_{Bias}, LO power and temperature (cryogenics) make the mixer to work in the transition region. At this point, and in the presence of an RF signal, the central part of the bridge (known as *hotspot*) is heated to its critical temperature (when superconducting is no longer supported) and goes into the normal state, while the adjacent portions of the bridge remain superconducting. The time varying heating associated with the LO and RF signals (Eq. 1.6) modulate the extension of the hot spot, and therefore the bridge conductivity at the IF frequency. The IF response is determined by the thermal properties of the material.

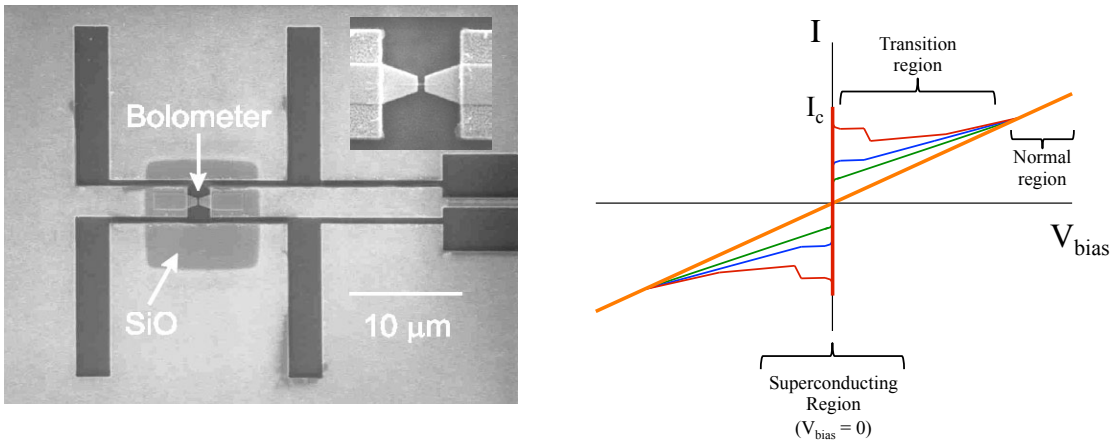

Figure 1.12: HEB mixer. Left:Nb HEB mixer circuit with a twin-slot antenna. Right: I-V curve with different LO levels, from no LO power applied (red) to a fully over-pumped mixer (orange). Taken and adapted from McGrath et al. (2002)

Modern HEBs are based on Nb, NbN and/or NbTiN. They are low noise mixers, and the state-of-the-art devices are able to reach frequencies as high as 4.7 THz (Büchel et al. 2015), with IF covering the 0.2 to 4 GHz band.

The LO power has a strong effect on the shape of the I-V curve (Fig. 1.12 right). For a specific V_{bias}, the more LO power gets to the HEB, the lower the current (I_B) through the junction. This feature is of particular use for determining the optimum operational point of a HEB. The mixer LO power requirements run from 0.1 to 0.5 μW, depending on the material.

A drawback of HEBs is that they can suffer from the direct detection effect (Cherednichenko et al. 2007), which is the dependence of the HEB parameters (bias point) on the RF input.

Local Oscillator Sources

Another fundamental component of an heterodyne receiver is the local oscillator source. LOs must be frequency (phase) and power stable. Noise modulates the amplitude ($a_n(t)$) and the phase ($\theta_n(t)$) of the LO signal (Eq. 1.7).

$$V_{LO} = (1 + a_n(t)) \cdot \cos(2\pi\nu_{LO} \cdot t + \theta_n(t)) \tag{1.7}$$

LO noise has a strong influence on narrow spectral lines. While the amplitude terms of the noise manifests in form of spurious features on the spectrum, the phase noise broadens lines. The astronomical data is usually processed in terms of radial velocity. Equation 1.8 relates frequency and velocity (i.e., the Doppler effect of an astronomical source), with Δv being the velocity difference with respect to the rest frequency (ν_0) of the source being studied. Given equation 1.8, the lower the rest frequency, the more the frequency noise affects the line width measurement of a narrow line.

$$\Delta v = \frac{\Delta\nu}{\nu_0} \cdot c \tag{1.8}$$

The selection of an specific type of LO depends on requirements on the signal power, frequency range, LO stability and form factor (physical dimensions). Different technologies can fulfill these requirements, however the most used ones in modern sub-mm and THz astronomical receiver systems are:

* Gunn oscillators
* Solid state multiplication stages chains.
* Quantum cascade laser (QCL)
* Photonics oscillators

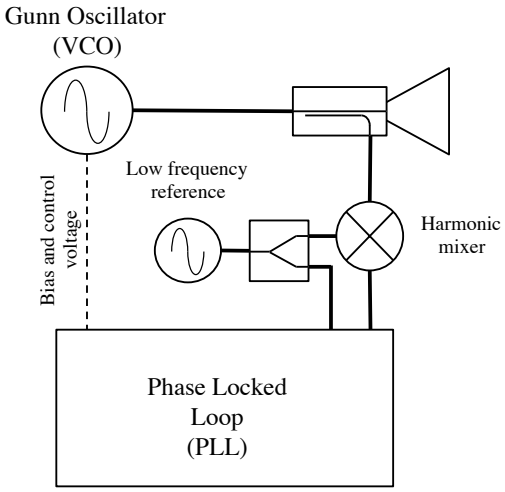

Figure 1.13: Gunn diode based local oscillator scheme. Key elements are the Gunn VCO, a directional coupler, harmonic mixer and the PLL. See text for details.

The **Gunn oscillator** is based on the Gunn (1963) effect. It refers to microwave current oscillations in homogeneous samples of n-type material subjected to high voltage electric fields. The discovery allowed

the construction of the first solid state sources of microwave power (Gunn diodes). Gunn oscillators are able to cover a wide tunable range and have been used in astronomical receivers for more than 30 years (Carlstrom et al. 1985). They can reach frequencies as high as 1.5 THz, however at that frequency the output power is lower than 1 μW (Gružinskis et al. 1998), restricting their use mostly to the sub-mm range, were power level reaches the 100 mW.

The frequency of oscillation is controlled by a DC bias voltage (the Gunn diode is a voltage controlled oscillator) and in some cases by an additional mechanically tunable resonator cavity. This kind of oscillator has a free running frequency (when the control voltage is equal to zero) around which it can be tuned. Gunn oscillators are complex, as the control voltage requires a closed control loop usually using a phase locked loop or PLL (Best 2003). The noise on the DC bias line has direct impact on the signal phase noise. Figure 1.13 displays a possible implementation of a Gunn LO. Note the main components: the Gunn voltage controlled oscillator, the PLL, the low frequency external reference oscillator and the harmonic mixer. The harmonic mixer performs heterodyne mixing between a sample of the output signal from the LO and a high harmonic of the reference oscillator and provides a low frequency feedback signal for the PLL. The PLL *locks* to the reference and the oscillator control voltage is related to the phase difference between the reference and the low frequency feedback signal.

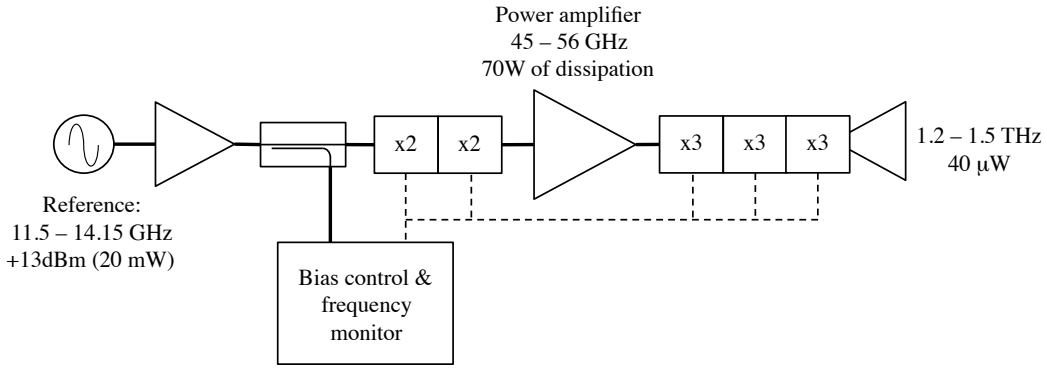

Figure 1.14: Solid state multiplication chain. The reference input is multiplied by many stages to get to the desired frequency. Adapted from VDI

Solid state multiplication chains LOs require a stable low frequency reference signal, which then passes through a series of *multiplication stages*. The reference is typically generated by a controllable analog or direct-digital synthesizer (Vankka and Halonen 2010), allowing tuning of the LO. The multiplication stages can be active or passive and exhibit a non-linear response (Eq. 1.4). The output signal from each stage is composed of different order harmonics of the input signal. By appropriate filtering, only wanted harmonics are selected for the next stage. As power is split among the different components, the efficiency of the multiplication stage depends on the selected harmonic. Figure 1.14 shows a dual *doubler* (×2) and three *triplers* (×3) stages configuration, which yields a total multiplication factor of 108. In between the last doubler and the first tripler an amplification stage is required as the signal power is not high enough to bias the tripler. In terms of conversion efficiency, a system like this reaches at most 2%.

The performance of solid state LO chains has increased significantly over the last years (Crowe et al. 2009; Pearson et al. 2011) while their form factor has decreased, allowing a much easier integration into astronomical systems. They easily deliver 25 μW at 1.9 THz (Table 1.4) and by actively cooling some of the chain components, their individual conversion efficiencies are increased and with this the output power (Risacher et al. 2016a).

Table 1.4: Solid state LO power delivered at different frequencies. Adapted from specification sheets for LO sources provided by VDI

Power [μW]	Frequency [THz]
600	0.5
350	1
80	1.5
25	1.9
5	2.5

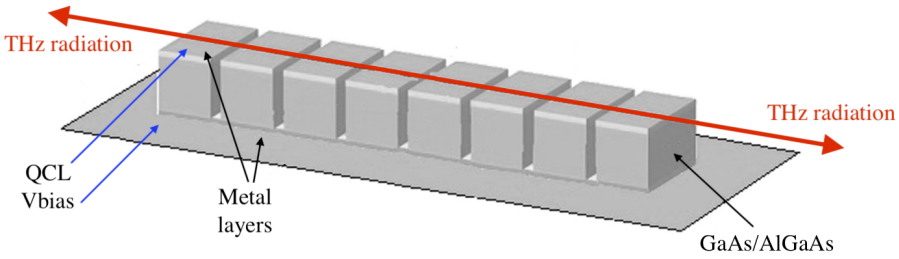

Figure 1.15: QCL Bragg reflector. Adapted from Cui et al. (2013)

Quantum cascade lasers or QCL (Faist et al. 1994) are modified versions of laser diodes. Laser diodes rely on transitions between energy bands in which conduction electrons and valence band holes recombine across the band gap. The band gap determines the emission wavelength, and depends on the specific semiconductor material used. A QCL is created by using layers of material with varying composition deposited on a substrate. This way a *superlattice* with a number of energy sub-bands is created. By choosing an appropriate material and controlling the thickness of the inversion layer, the coarse frequency of the laser emission can be selected. Slots on the material, separated at $\lambda/2$ allow constructive and destructive interference on the different THz tones (Cui et al. 2013). This structure, known as Bragg reflector (Fig. 1.15), behaves like a periodic antenna. The QCL oscillator requires careful control of the current and the temperature of operation as the precise oscillation frequency depends on these two parameters.

The QCL can operate in pulsed and continuous mode. The latter is chosen when a QCL is used as a LO for a heterodyne receiver system in the range from ~1 to 10 THz, with power as high as 100 μW at 4.7 THz (H. Richter et al. 2015). QCL devices are commercially available[6] to wavelengths of μm as light sources for mid-IR applications such as molecular gas analysis.

Photonics oscillators are electro-optical frequency down conversion devices. Two near-infrared single-mode laser beams are combined and amplified into a single mode optic fiber that illuminates the photomixer with an orthogonal polarization to the *finger structure*. (See Fig. 1.16). The photomixer is DC biased and the incident laser beams generate electron-hole pairs, creating a current proportional to the optical intensity. The short lifetime of the electrons in the photomixer allows that the current follows the optical intensity instantaneously, and with this the frequency difference between the two lasers. The photomixer is part of a microstrip antenna used to emit the signals' frequency difference (LO).

Photomixers have been demonstrated to provide a reliable local oscillator reference for heterodyne systems (Cámara Mayorga et al. 2012). Currently the LO power they are able to deliver is limited to 10

[6] https://www.hamamatsu.com/jp/en/1006.html

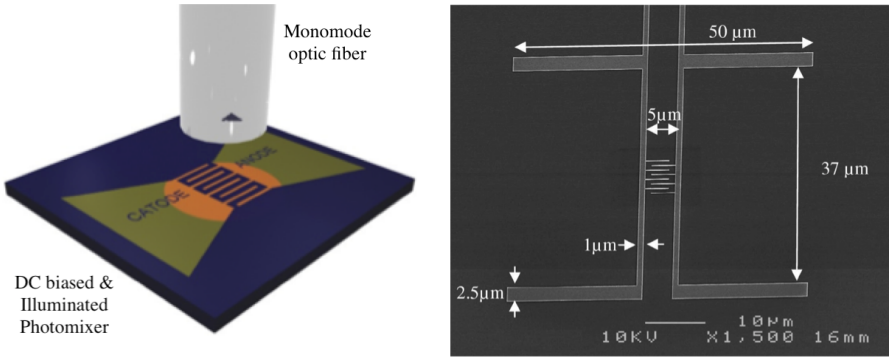

Figure 1.16: Left: A photomixer (the inter-digit structure) illuminated by two lasers (in orange) transmitted on a monomode optic fiber simultaneously. Right: SEM of a photomixer used to provide 1 THz of LO reference. Taken and adapted from Cámara Mayorga et al. (2012) and Cámara Mayorga (2008)

μW, however they can be tuned over a very wide range of frequencies, are very stable and can be packed in a relatively compact system.

Heterodyne Receiver Performance and Figures of Merit

$$T_{rms} = \frac{T_{sys}}{\sqrt{\tau_{int} \cdot \Delta\nu}} \tag{1.9}$$

The minimum detectable signal (T_{rms}) by an heterodyne system is directly related to the integration time (τ_{int}), the receiver bandwidth ($\Delta\nu$) and the system temperature (T_{sys}) by Eq. 1.9. The maximum integration time depends on the stability and the intrinsic noise of the receiver. A measurement of the **Allan variance** (Ossenkopf 2008) can be used to determine the maximum integration time (Allan time) for which Equation 1.9 holds.

The Allan variance test has two versions: the total power or radiometric and the spectroscopic measurement. For heterodyne systems these tests are performed while a LO signal is applied and the receiver is *looking* at a temperature stabilized blackbody reference signal.

In the radiometric measurement test, the power on a (wide) spectral range is monitored while an integration takes place. Non correlated white noise power decreases with integration time. At a certain point the internal noise, composed by the (correlated) drift noise and the flicker or $1/f$ noise of the systems dominates and the noise power increases again. It is this *knee* in the noise power that determines the radiometric Allan time.

In the spectroscopic measurement, deviations on the power level between two arbitrary (binned) spectral channels of the IF are analyzed. The goal of this test is to check on frequency dependent variations of the IF band response, which would influence the continuum level of the astronomical data.

The system temperature (T_{sys}) depends on the temperature and transmission of the Earth's atmosphere at the telescope site and the observed frequency, the telescope (optics) temperature, and the **receiver noise temperature** or T_{Rec}. The atmospheric temperature and the telescope temperature are accounted for as a frequency dependent intensity, equivalent to an antenna temperature $T_{A,sky,\nu}$ (Guan et al. 2012).

$$T_{sys} = T_{Rec} + T_{A,sky} \tag{1.10}$$

The receiver noise temperature, T_{Rec}, represents the noise contribution of all the single components (Figure 1.8) of the heterodyne system condensed into a unique number.

In astronomical systems, T_{rec} (and therefore the T_{sys}) is commonly derived by using the Y-factor method (Pozar 2004). The Y factor is calculated by measuring the total power (per spectral channel on the IF) while the receiver alternately points to two different (conveniently called hot and cold) calibrated temperature black bodies (Fig C.1). These black bodies are usually called *loads*. With the Y-factor, calculated as the P_{hot} / P_{cold} (Eq. C.1) and knowing the physical temperatures of the loads, the receiver temperature is computed by Eq. 1.11. This value usually includes all the contributions from the receiver optics (the common part to both loads paths), mixers, amplifiers, filters, passive components and the backend.

$$T_{Rec} = \frac{T_{hot} - Y \cdot T_{cold}}{Y - 1} \tag{1.11}$$

A good a priori estimate of the receiver temperature, useful during the design phase of a receiver, can be calculated by knowing the individual noise temperatures of each subcomponent, and using equations C.3 and C.4 (See appendix C).

1.3.2 Backends

Backend is the generic name given to the part of the astronomical system used for signal processing and display. There are various technologies and types of backends, but in general they can be grouped in two big families: total power detectors and spectrometers.

Total power detectors integrate the entire power available over the detector bandwidth, for a determined time (integration time). In this sense, they are signal phase independent and only the signal power information is of relevance. The spectrometers, on the other hand, deliver the information of signal amplitude (power) and phase for a specific number of discrete frequencies over the backend band (channels).

Total power backends

The simplest version of a total power detector can be realized by using a diode and a resistor-capacitor (RC) network, where the voltage available in the RC network is proportional to the incoming power. The voltage is then digitized by using an analog to digital converter (ADC) and the detector time response (and sampling rate) is set by the RC network time constant. Although they are conceptually simple, total power backends require a careful implementation. They can be used during particular astronomical observing modes (total power maps) or when determining the system temperature.

Spectrometers

Spectrometers measure the power spectral density (PSD) of an incoming signal and its phase over their working band. The resolution of the spectrometer is given by the amount of spectral channels over the frequency range they cover. The incoming signal phase is of particular interest for interferometric astronomy systems.

A particular application of the Wiener-Kinchin principle describes two ways of obtaining the PSD (Proakis 2007) of a time varying signal (g(t)), which offers two different ways for building spectrometers. One path uses the squared modulus of the calculated Fourier transform of the signal (G(ν)), while the other computes the autocorrelation of the signal ($R_{g,g}$(t)) and then obtains the Fourier transform in a sequential way (Fig. 1.17).

Spectrometers can be used as total power detectors by binning the spectral channels together. The most common types of spectrometers are:

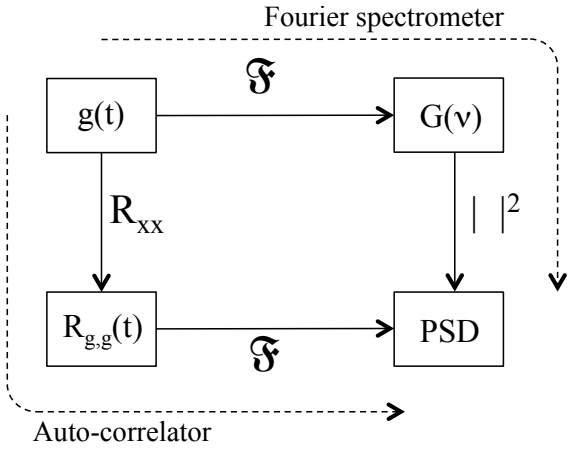

Figure 1.17: Wiener-Kinchin principle. Two different ways to compute signal PSD.

* Filter banks
* Correlators and Autocorrelators
* Acusto-optic spectrometers (AOS)
* Fast Fourier spectrometers (FFTS)
* Chirp transform spectrometer (CTS)

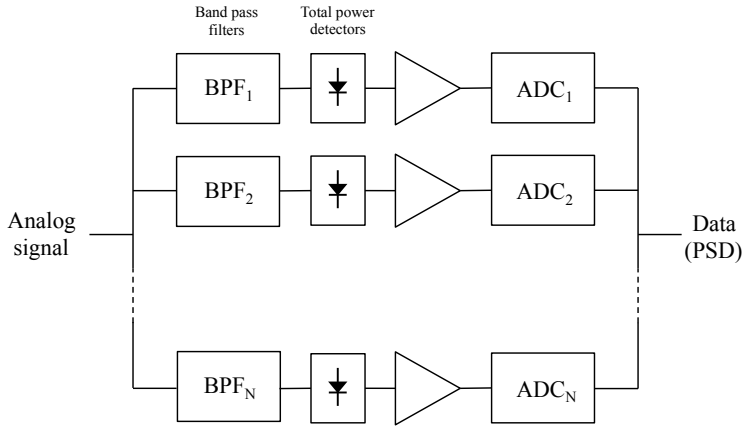

Figure 1.18: One of the many filter bank spectrometer realizations: Each spectral channel consists of a bandpass filter, a total power detector and an analog to digital converter.

Strictly speaking, a **filter bank** spectrometer is made up of many filtered narrow band total power detectors (Fig. 1.18). The response of the individual sub-band filters requires fine tuning in order to provide a total flat band of the system.

The **correlator** takes its name from its core mathematical operation, the correlation function. Beyond the formalisms, correlation accounts for the similitude (index) between two different signals. When the

two input signals of the correlator are (almost) identical, the result of the correlation operation is the same input signal, but without the uncorrelated noise content. The Fourier transform applied to the clean signal then provides the signal spectrum (modulus and phase). In this configuration, the correlator works as an **autocorrelator** (Fig. 1.19). Depending on the way the correlation function is implemented, the correlator is said to be analog or digital. Correlators are of particular interest for astronomical interferometry.

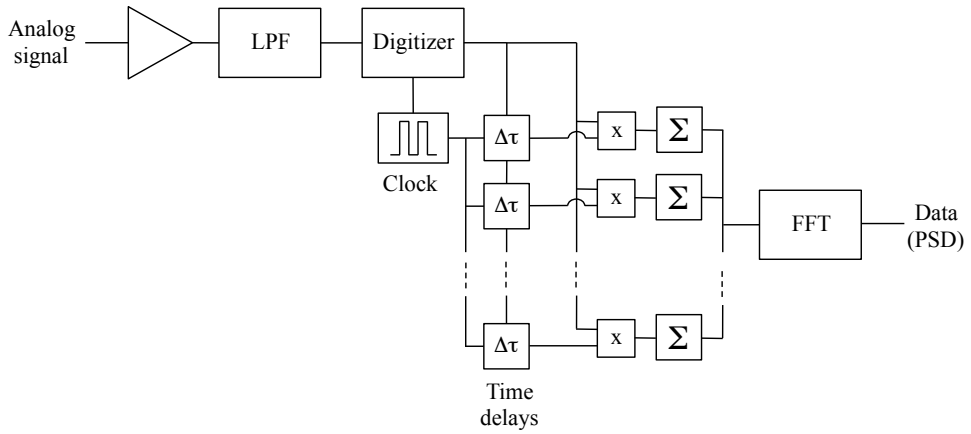

Figure 1.19: Classical scheme of an autocorrelator.

The key element of the **AOS** is a piezoelectric transducer called Bragg cell (Schieder et al. 2003). When applying an AC voltage to the cell, it creates sound waves in the material (glass or quartz), and periodically spaced structures appear in the cell, separated in proportion to the frequency of the applied voltage. The cell is illuminated using a collimated light source, like a laser, and diffracts the passing light due to the cell structures. The diffracted light is projected over an array of optical sensors (CCD), yielding the input signal spectrum. The AOS provides a good trade off between resolution and bandwidth. AOS were the dominant spectrometers for many years. A good example is the WBS (Siebertz et al. 2007) used with Herschel/HIFI instrument (de Graauw et al. 2009).

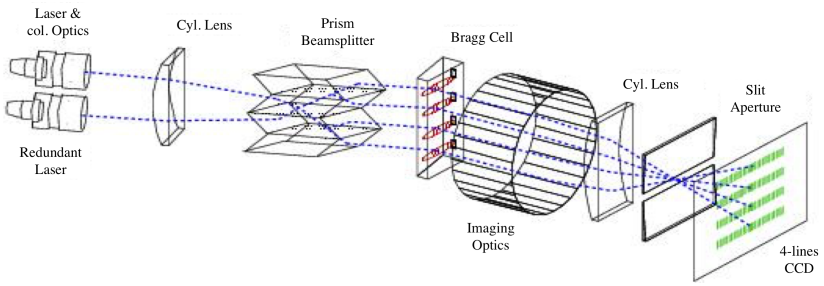

Figure 1.20: The AOS used by the Herschel/HIFI instrument: the wide band spectrometer (WBS). Taken from Siebertz et al. (2007)

Based on the Fast Fourier transform, a computer efficient version of the discrete Fourier transform or DFT (Cooley and Tukey 1965), FFT spectrometers (**FFTSs**) have become the first choice for compact and robust spectrometers. This technology has rapidly evolved in the last 10 years (Klein 2017) thanks to faster ADCs, more powerful processors and better algorithms. The core component of a modern FFTS is the Field Gate Programable Array or FPGA. In it the digital filtering, the fast Fourier transform and other

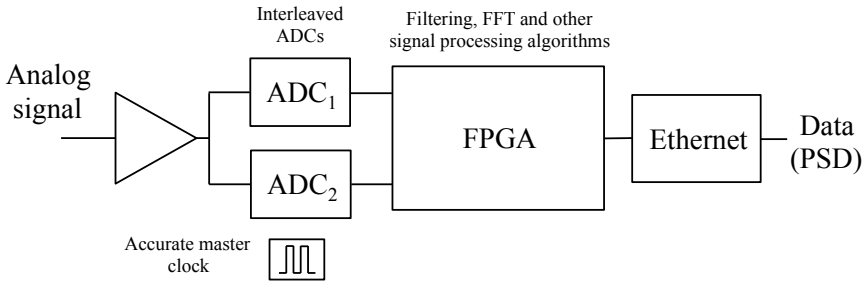

Figure 1.21: A Fast Fourier transform spectrometer scheme. Adapted from Klein et al. (2012)

part of the algorithm are programmed and embedded. By using sampling interleaving technique (Fig. 1.21), higher frequency bandwidths up to 4 GHz, have been achieved.

The **CTS** uses the chirp transform as processing principle (Villanueva 2004). A chirp signal varies its frequency up or down over time in a defined *sweep time*. The chirp signal acts as a variable frequency sweeping mathematical base, that when multiplied with the incoming signal and integrated over a time interval yields a correlation index (transform), directly related to the instantaneous frequency of the chirp base. The frequency dependent index provided by the transform corresponds to a representation of the signal spectrum. The major limitation of this system comes from its restricted resolution-to-bandwidth ratio.

CHAPTER 2

The Stratospheric Observatory For Infrared Astronomy and the German REceiver at Terahertz Frequencies

2.1 The Stratospheric Observatory for Infrared Astronomy: SOFIA

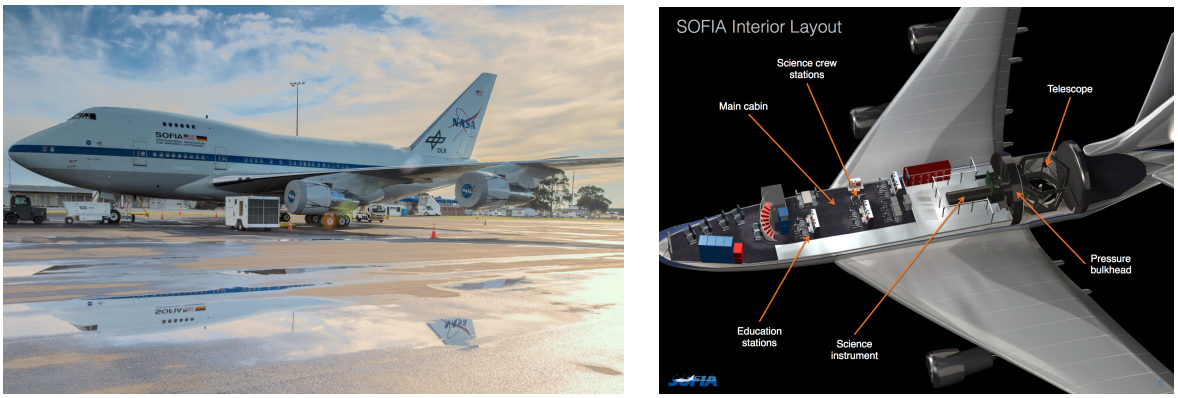

Figure 2.1: SOFIA aircraft, a Boing 747SP. Right: internal layout.

SOFIA is a joint airborne observatory of the National Aeronautics and Space Administration, USA (NASA) and the German Aerospace Center (DLR). Consisting of a 100 inch diameter (2.7 m physical, 2.5 m effective) infrared telescope mounted on a highly modified Boeing 747SP aircraft, SOFIA is able to reach altitudes higher than 42.000 ft (13.000 m) during normal operation campaigns. This makes SOFIA the ideal platform for observations in the far infrared and sub-millimeter regime as it flies at an altitude where residual atmospheric water vapor content is very low. Typical precipitable water vapor (PWV) values reach around the 10 μm.

2.1.1 SOFIA Platform: NASA747

The SOFIA aircraft, or NASA747, is built on a former commercial Boeing 747SP airliner jumbo jet built in 1977. The 747SP (Special Performance) is a shortened variation of the standard Boeing 747-100 of that time which allows longer flight span and reaching higher altitudes. SOFIA has been extensively modified

(1997-2007) in its fuselage and avionics systems to fit the telescope and the additional subsystems to provide support to scientific instrumentation.

Thanks to these significant modifications, a part of the cabin is separated into the telescope cavity by a pressure bulkhead (Fig. 2.1). The telescope cavity is at external pressure and a hatch side door of 5.5 by 4.1 meter opens during flight exposing the telescope. The door opening follows the position of the telescope elevation allowing an unvignetted operation range from 23 to 58 degrees elevation. The telescope door is flanked by body humps which serve as its guiding rails, and ensure a smooth aerodynamic transition (Young et al. 2012a) reducing turbulence during observations.

SOFIA is operated and maintained by NASA, the Universities Space Research Association (USRA) and the Deutsche SOFIA Institut (DSI) at the Armstrong Flight Research Center (AFRC) in Palmdale, California, USA, making this facility its regular home base. Scientific flights usually take off and land from/to the AFRC. During the yearly southern hemisphere deployment the aircraft flies to the international Christchurch Airport, in Christchurch, New Zealand, making this location the SOFIA seasonal base.

2.1.2 The Telescope and its Optical Design

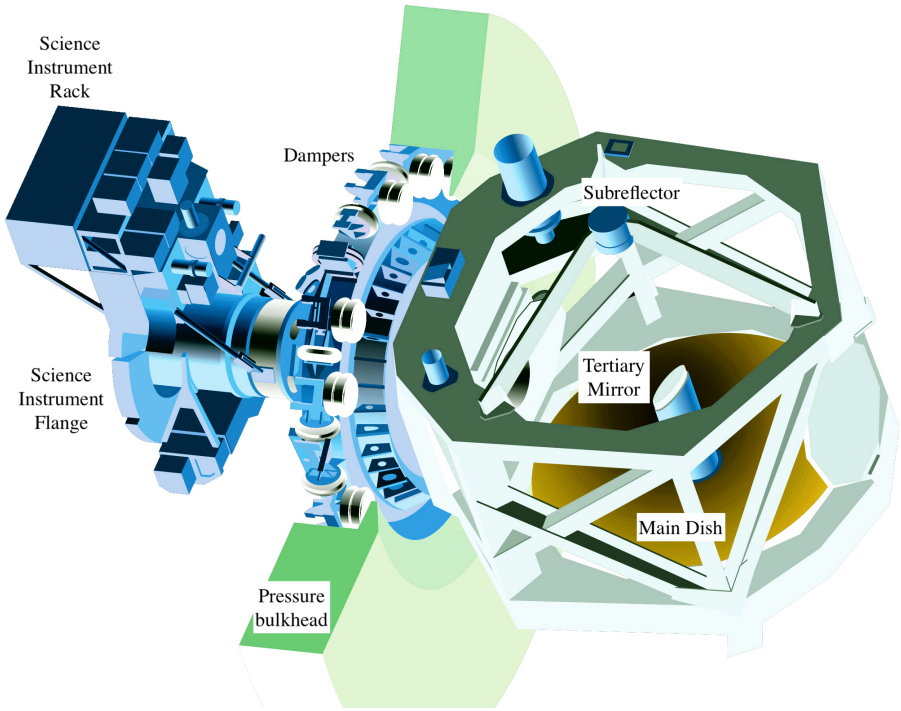

Figure 2.2: 3D model of the Telescope. Adapted from Young et al. (2012b)

The SOFIA telescope is a 17 ton Nasmyth-Cassegrain telescope, mounted on a 1.2 m diameter spherical hydrostatic bearing. It is composed of a 2.7 m diameter parabolic main reflector (M1), a 350 mm hyperbolic secondary (M2) and two tertiary mirrors. Given the size of the secondary mirror, only 2.5 m of the main reflector is illuminated in favor of ± 4 arcmin of chopping throw at a maximum frequency of 20 Hz. The first tertiary mirror, M3-1, is a 310 mm effective diameter gold coated high pass dichroic filter (Winnewisser et al. 1998) acting as 90 degrees mirror for the infrared (IR) and sub-millimeter (Sub-mm) radiation, while the second tertiary mirror, M3-2 located beneath M3-1, deflects the visible

Table 2.1: SOFIA important optical parameters. Taken from Krabbe (2000)

Parameter	Value	Remark
Nominal focal length	49141 mm	Total equivalent
Telescope diameter	2500 mm	Effective diameter
Primary focal length (M_1)	3200 mm	
Primary conic constant	-1	Paraboloid
Primary center hole	420 mm	
Secondary diameter (M_2)	352 mm	
Secondary conic constant	-1.298	Hyperboloid
e	2754 mm	As defined by Bahner (1967)
e+g	6849 mm	As defined by Bahner (1967)
Scattering Cone	73.66	Conic. Used by GREAT
Blockage factor	0.1408	Calculated as M2/M1
Blockage factor f_b	0.209	Calculated as cone/M2

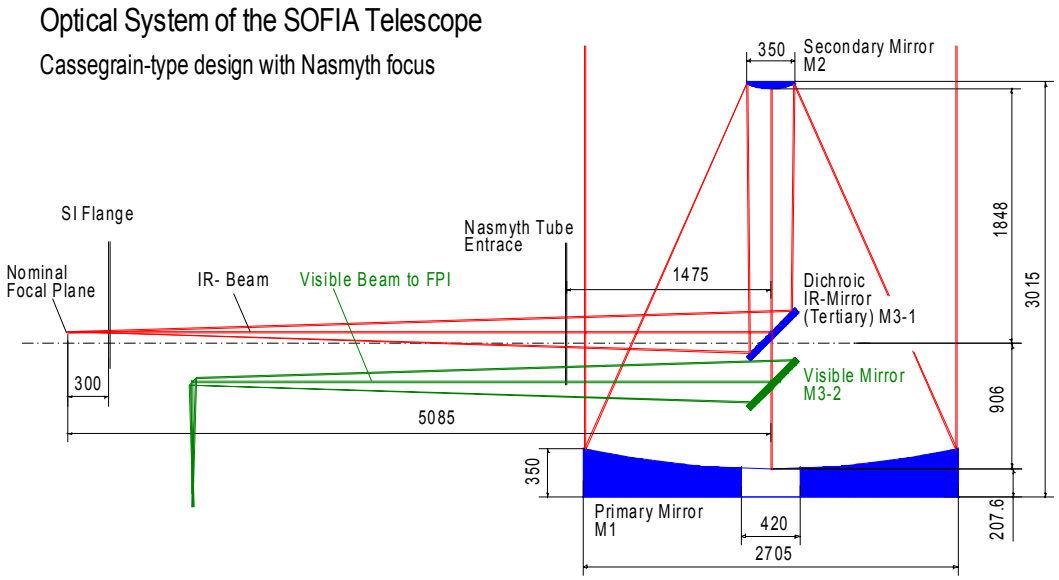

Figure 2.3: Signal path and key distances in the SOFIA telescope optics (Krabbe 2000)

beam to a CCD guide camera used for tracking, the Focal Plane Imager (FPI). There are two other acquisition and guiding cameras, the Wide Field Imager (WFI) and the Fine Field Imager (FFI). The IR / Sub-millimeter beam (or simply *telescope beam*) passes through the telescope bearing and is focused into a focal plane (FP), as illustrated in Fig. 2.3.

Different scientific instruments (SIs) can be operated on the SOFIA telescope, one at a time. Instrumentation and telescope masses are counterweighted and balanced such that during flight the active tracking system keeps the telescope on target with minimum effort. Key components of the tracking system are the three fiber optic gyroscopes that maintain an inertial reference frame. A vibration isolation system, consisting of pressurized rubber bumpers, is also a fundamental part of the telescope tracking.

They are radially and axially arranged between the telescope drive and the bulkhead.

The instrument nominal focal plane is located at 6933 mm from the secondary mirror and 300 mm behind the SI mounting flange (Fig 2.2). The position of the focal plane can be adjusted by the sub-reflector which is mounted on an hexapod. Table 2.1 provides details of the telescope optics.

2.2 The German REceiver at Terahertz frequencies: GREAT

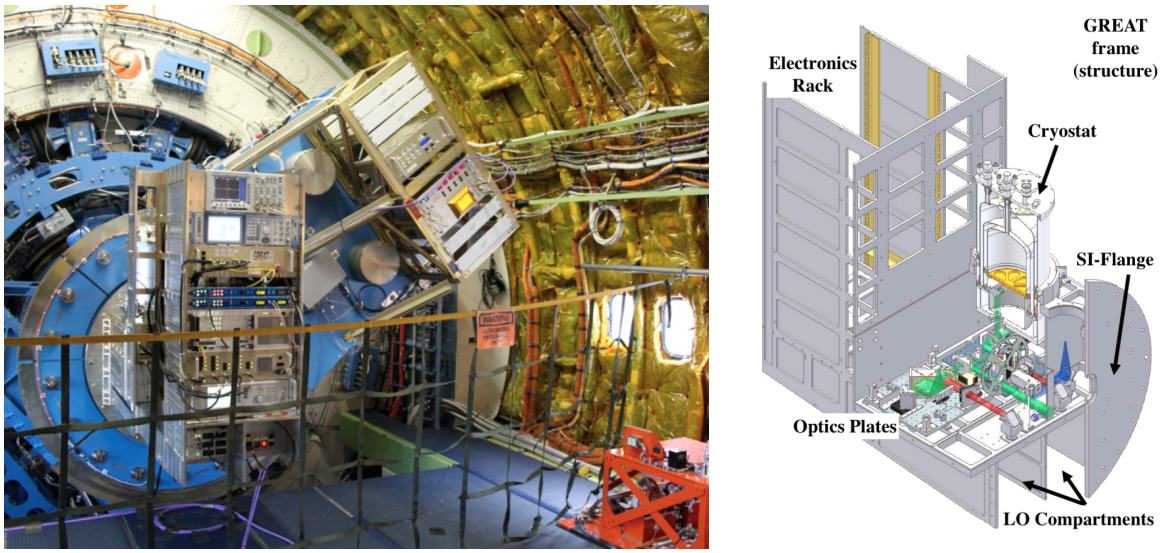

Figure 2.4: Left, GREAT installed in SOFIA. Right, GREAT structure with some of the GREAT submodules indicated. Taken from Heyminck et al. (2012)

The German REceiver at Terahertz frequencies, GREAT (Heyminck et al. 2012) has been conceived as a highly modular dual-color heterodyne instrument for high resolution far-infrared (FIR) spectroscopy. It has been specially designed for SOFIA and built by the Max-Planck-Institut für Radioastronomie (MPIfR) and the KOSMA (Universität zu Köln), in cooperation with the MPI für Sonnensystemforschung (MPS) and the DLR Institut für Planetenforschung (DLR-Pf). GREAT saw its first light on April 1^{st}, 2011.

2.2.1 Scientific Goals and Requirements

GREAT was designed targeting a series of astrophysical lines of interest (see Table 2.2) spread over a wide frequency range. Many of these lines are only visible from airborne/balloon or space telescopes due to strong atmospheric absorption at these frequencies. One of the objectives for GREAT was to achieve the widest intermediate frequency (IF) bandwidth possible (over 3 GHz), with high resolution (< 100 kHz). These requirements immediately set the condition of making GREAT a modular system as technically no single detector nor local oscillator source can cover the entire range spanning from 1.2 to 4.7 THz at the sensitivities and responses required. Modularity allows the exchange (and constant upgrade) of frequency specific components while most of the system remains installed on-board.

Table 2.2: GREAT channels general specifications and some of the astrophysical lines of interest per band. $T_{Rec-2011}$ and $T_{Rec-2015}$ refer to performance achieved in 2011 and 2015. Adapted from Risacher et al. (2016a)

RX	LO	RF tuning [GHz]	$T_{Rec-2011}$ DSB [K]	$T_{Rec-2015}$ DSB [K]	Astrophysical lines (examples)
L1	$L1_a$	1252-1392	1000-1750	500	CO(11-10), CO(12-11), OD, SH, H_2D^+, HCN
	$L1_b$	1417-1520			[NII], ^{13}CO(13-12), HCN, HCO^+
L2	L2	1815-1910	1500-4000	700	NH_3(3-2), OH(21/2), CO(16-15), [CII]
M	M_a	2507-2514	3000	1500	OH(23/2)
	M_b	2670-2680	-	-	HD(1-0)
H	H	4745 ± 4	-	800	[OI]

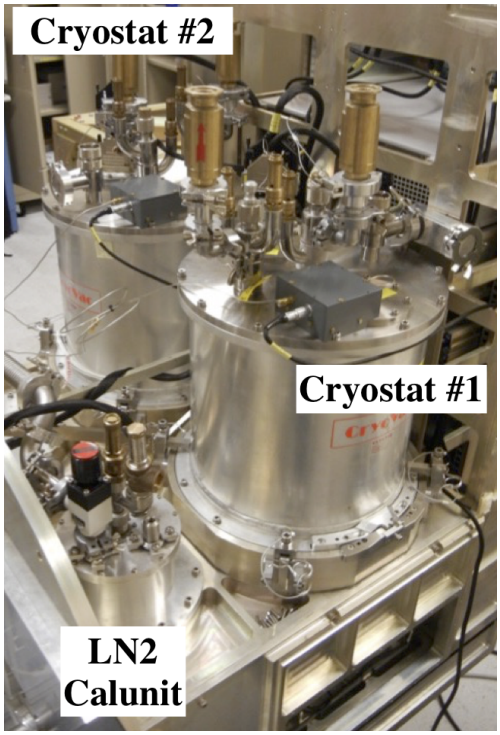

Figure 2.5: Two GREAT single pixel liquid cooled channels and the LN_2 Calunit cold load mounted on the GREAT structure.

2.2.2 GREAT and its modular approach

GREAT is composed of several modules and subsystems, out of which the desired *flight configuration* is set-up. Some of the modules are *common*, meaning that they are part of all the different flight configurations. Others are specifically installed for the desired scientific cases to be studied.

The biggest common module is the mechanical support structure that interfaces the telescope and provides precise and reproducible positions for each submodule. The GREAT structure is able to hold two individual cryostats or *channels* at the same time. Each channel contains a single pixel detector. The structure also hosts the respective channel frequency references or local oscillator (LO) modules, placed

underneath and carries the optics plates, located in the optics compartment. The optics plates contain common and channel specific optical components. A calibration unit (*Calunit*) is also common. The calunit is composed of a room temperature load and a 77 K liquid nitrogen cooled load and the respective beam switching optics. Front-end control electronics, bias electronics and support modules are also placed on the rack-like part of the structure (see Fig. 2.4).

A co-rotating counterweight rack is also attached to the telescope and lodges parts of the common intermediate frequency processor (IF) and the digital spectrometer (FFT) backend processor.

A third rack, the PI Rack, is located away from the telescope inside the cabin at the science crew station location (Fig. 2.1). The PI rack contains additional electronics modules, e.g. control computers, an acusto-optical spectrometer (AOS), a chirp transform spectrometer (CTS) and the main IF processor.

Single Pixel Receivers

GREAT channels are single pixel Hot Electron Bolometer (HEB) detectors. There are 4 channels in total, accordingly named as L1, L2, M and H (Table 2.2). Each detector is contained in an independent liquid nitrogen (LN_2 at 77K) and liquid helium (LHe at 4K) cooled cryostat, with hold times of over 20 hours. Cryogenic liquids refill is required daily, with a last top-up performed shortly before take-off. The cryostats are all of the same design and have been manufactured by Cryovac in Germany (Fig 2.5).

The HEB detectors have been developed by KOSMA (Pütz et al. 2012) and are waveguide coupled. They are connected through a bias-T to a CITLF4 cryogenic amplifier (CalTech CMT) without isolator in favor of the gain. In order to reduce the intrinsic noise and increase the sensibility, the detectors need to be cooled down below 6 K. For this reason, they are thermally connected to the 4 K LHe bath reservoir. The LHe tank is large enough to keep the detectors cold for over 20 hours.

All four cryostats have a similar wiring interface in terms of detector bias, amplifiers, temperature sensors and IF output. On top of each channel a pre-amplifier and bias interface module is installed.

Local Oscillators

The local oscillator source is specific for each channel. There are in fact 6 LO sources. All L1, L2 and M local oscillators are based on cascaded solid-state multiplication stages or *chains* (Crowe et al. 2009). Starting from a reference frequency coming from a controllable synthesizer, the signal is filtered and then multiplied by the respective chain to the required LO tone. The L1 channel detector can be tuned over a very wide frequency range from 1200 to 1500 GHz. A similar situation is valid for the M band, ranging from 2520 to 2680 GHz. To make use of the wide frequency coverage of these mixers, each of these channels requires two LO sources. This gives the subscript *a* (lower sub-band) and *b* (upper sub-band) to the channel LO denomination.

The H channel, on the other hand uses a totally different technology: A Quantum Cascade Laser (QCL). This LO has been developed and built by DLR-Pf in Berlin (H. Richter et al. 2015). The LO provides a narrow coverage of ± 4 GHz around the [OI] line.

Optics Plates and LO Coupling

The optical design of GREAT is based on Gaussian beam telescopes, using only reflective elements. Each single pixel channel has its own specific optical bench or *optics plate*. The incoming signal beam is divided in two sub-beams to illuminate each of the optics plates by using a wire-grid or a frequency specific low pass dichroic filter (Winnewisser et al. 1998; Ade et al. 2006), according to the channel configuration. On the optics plates specific optical components are mounted that are required to direct and

focus the telescope beam into the corresponding cryostat window, and finally the detector. Although the specifications for these components vary channel to channel, the basic modules and the optical approach is common. It is also a task of these optics plate to combine the telescope beam with the local oscillator beam.

Power delivered by the GREAT LO sources is relatively weak and therefore the use of a Martin Puplett interferometer as diplexer (Lesurf 1981) is required. These kind of diplexers are able to couple almost all the power from the LO with the telescope beams, regardless of the polarization. However they limit the intermediate frequency band of the mixers, increase the receiver temperature and require (mechanical) tuning for the central IF frequency. Later, the use of diplexers was dropped in favor of beam splitters using a wire-grid, thanks to significant improvements in the LO solid state chain technology and increase on the power delivered. This explains the dramatic performance improvement (in terms of receiver temperature) shown in Table 2.2.

A very good description of the optics of GREAT (single pixels) for SOFIA is provided by Wagner-Gentner et al. (2004) and Wagner-Gentner (2007).

Intermediate Frequency Processor

GREAT has been equipped with two IF processors. One processor couples to the AOS / CTS spectrometers, while the another to the FFT spectrometer. The IF modules have total power detection submodules and remotely controlled attenuators for optimal power level ranging for the spectrometers. In addition, the IF processors have a remotely controlled synthesizer used for internal mixing and with this, provide specific base band shifting according to the respective spectrometer requirements or base band coverage configuration.

Backends

GREAT was originally equipped with three different spectrometer technologies. All of the three spectrometers were operating at the same time given their specific advantages and drawbacks, and scientific needs. The first kind of spectrometer, the AOS (Horn et al. 1999) developed by KOSMA, provides a bandwidth of 1 GHz per module, with a resolution of 1.6 MHz. With 4 AOS modules and the correct IF processor setup, this covers the entire IF band of the mixers. The second kind of spectrometer, the CTS, was specially built for GREAT by the MPS (Villanueva and Hartogh 2004). It has higher resolution (56 kHz), particularly useful to resolve spectral details, but limited in bandwidth to 220 MHz. GREAT was equipped with two units, one for each channel. The third type of spectrometer is based on the fast Fourier transform principle. Named AFFTS (Klein et al. 2006), it provides 1.5 GHz of bandwidth per module with a resolution of 212 kHz. Each GREAT channel was connected to one AFFTS board.

After 2012, the evolution of the FFT spectrometers lead to a new generation, the XFFTS (Klein et al. 2012) that provides an instantaneous bandwidth of 2.5 GHz and 65536 spectral channels (44 kHz in frequency resolution), making it the preferred option for the observation campaigns with GREAT since then.

2.2.3 GREAT Extends into Arrays: upGREAT LFA and HFA

GREAT, being in constant evolution and development, incorporates state of the art systems, including detectors along with signal processing systems and support modules. A major improvement came in 2015 and 2016 with the addition of two multi-pixel channels: The upGREAT Low Frequency Array (LFA) and the High Frequency Array (HFA). They represent an important update of GREAT as to exploit scientific

capabilities, technical and technological limits had to be pushed forward. Some of the main components of upGREAT LFA and HFA are presented in Fig. 2.6, and their specifications listed in Table 2.3.

In practice upGREAT implied substantial updates of the IF processor and backend, the addition of new optical elements and new local oscillators systems. The software and data pipeline also required a major revision as the data throughput increased dramatically. The use of closed cycle pulse tube coolers also represented a major improvement compared to the cryo liquid filled single pixels as no daily maintenance is required.

The upGREAT LFA has been fully commissioned during a total of 5 flights in May and December 2015 (Risacher et al. 2016b).

Table 2.3: upGREAT LFA and HFA specifications. The receiver temperature values shown here correspond to an average of all the mixers in the array. The frequency coverage of each array is limited by the local oscillator range.

Characteristics	LFA	HFA
Mixer technology	Waveguide feed-horn antenna coupling, NbN HEB on Si membrane	Waveguide feed-horn antenna coupling, NbN HEB on Si membrane
Manufacturer	KOSMA	KOSMA
Array layout	Dual polarization 2×7 pixels in an hexagon layout with a central pixel	7 pixels (mixers) in an hexagonal layout with a central pixel
Band [THz]	1.81 - 2.07	4.745 ± 0.004
IF Band [GHz]	0.2 - 4	0.2 - 4
T_{Rec} DSB [K]	<1000	<1500
Cooling	Closed cycle pulse tube	Closed cycle pulse tube

upGREAT LFA

The upGREAT LFA compromises two sub-arrays of 7 pixels each, coupling to orthogonal polarization. The mixers are Hot Electron Bolometers (HEB) fabricated by KOSMA (Pütz et al. 2015). The HEB element is made up of 3.5 nm layers of NbN deposited over a 2 μm Si substrate and is able to cover the band from 1.9 to 2.5 THz thanks to the use of a single-side waveguide probe antenna and transmission lines matching circuits. A spline smooth walled horn (Granet et al. 2004) couples the incoming radiation to the mixer waveguide probe. The horn has been fabricated using electro-forming by RPG. Many batches of LFA mixers were produced to ensure uniformity among the units in the same subarray.

The IF output of the HEB is directly connected to a SiGe cryogenic low noise amplifier (LNA) CITLF4 from CMT. The LNA provides between 35 and 40 dB of gain with nose temperature of 4-5 K. This unit also includes a bias-T for the mixer biasing. The output of the LNA is connected to a Miteq AFS4 room temperature low noise amplifier through stainless steel coaxial lines, to minimize thermal conductivity.

The bias-Ts are connected to the bias pre-amplifier boards located outside the cryostat through low thermal conductivity Phosphors-Bronze wires and a vacuum tight feed through connector.

The LFA allows better and more efficient observing strategies: a $17.5' \times 12.5'$ sized map of the [CII] line from the Horse Head Nebular was obtained as science demonstration on December 11^{th}, 2015. It

required just four hours of observing time (Risacher et al. 2016b). For comparison, a similar map using (single pixel) Herschel/HIFI would have taken over 50 hours.

upGREAT HFA

The 7 mixers of the HFA are based on the GREAT H channel detector. Also consisting of NbN HEB elements (Büchel et al. 2015), the horn is a scaled version of the smooth walled horn used in the LFA.

As for the LFA, each mixer IF is connected directly to a respective CITLF amplifier and AFS4 warm amplifier. Mixer bias-Ts are also connected to their respective bias pre-amplifier boards.

Similarly to the LFA cryostat, the HFA could host an additional 7 pixels in a second sub-array. However, plans for such upgrade in the near future are pending adequate funding.

Local Oscillators for the upGREAT Arrays

The upGREAT LFA with its two polarization requires that the LO source provides sufficient power to illuminate 14 detectors in total. Achieving this with a single solid state chain (20 μW of output power at room temperature) was not possible and therefore two chains for the same frequency range are accommodated in the same LO compartment, using the same reference. In addition, the last passive tripler of each chain is cooled down to 80 K using a Stirling cooler which is contained in a small cryostat including also part of the LO optics. Under these conditions, the output power reaches up to 40 μW per chain. In a first version of the LO optics both LO beams had orthogonal polarization and were combined by a wire-grid to be directed through a common beam path to the LFA optics plate. However, this approach was later changed to two independent LO beam paths, meaning one LO beam per sub-array. The splitting of each LO beam into 7 sub-beams is performed by using a Fourier phase grating mirror (U. U. Graf and Heyminck 2001) mounted on the optics plate. The common LO reference approach initially used was also substituted by two independent synthesizers, allowing individual tuning of the subarrays, and with this better use of the total LFA bandwidth.

The upGREAT HFA array is pumped by a redesigned GREAT H channel QCL LO (H. Richter et al. 2017). For this new incarnation, the *HFA QCL LO*, substantial changes have been made on the system: different coupling optics, a more powerful QCL chip, different tuning range of -1.5 to 6 GHz around

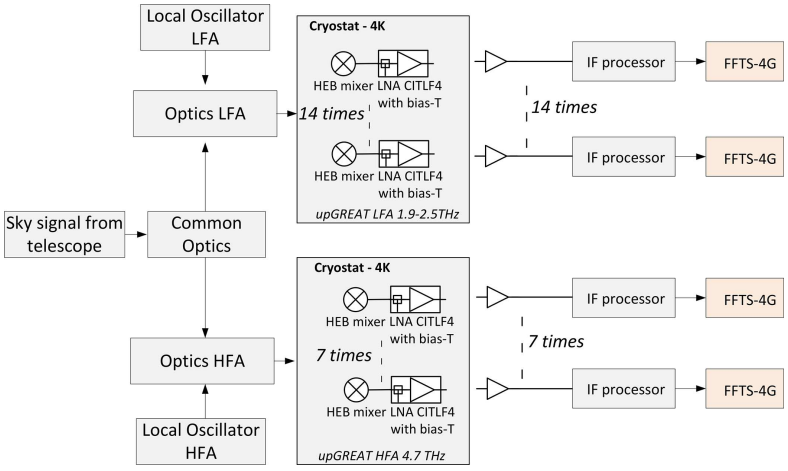

Figure 2.6: General layout of HFA and LFA configuration. Some of their specific modules are identified. Taken from Risacher et al. (2016a).

the [OI] line rest frequency (4745.8040 GHz), more self contained stand-alone design, better shielding and fully remote controllability. The amount of power (over 100 μw) is now high enough to pump the 7 pixels of the upGREAT HFA array. As for the LFA, the HFA LO beam is also split in 7 sub-beams using a Fourier phase grating mirror.

upGREAT Optics Plates

Each LFA and HFA have also their respective optics plate. There is one fundamental difference for the array optics plate with respect to that of the single channels. As mentioned before, the LO beam has to be split and then combined with the signal (sub) beams before illuminating every single pixel of the array. The splitting is done by using independent Fourier phase grating mirrors, while the combination is achieved by using a wire-grid as beam combiner. The relative angle of the grid in respect to the polarization of each beam gives the signal to LO coupling ratio.

A wire-grid in the common optics beam path of the LFA optics plate separates the two polarizations. With two independent LOs, one per subarray, the LFA plate has two phase gratings and beam combiners. The LFA LO beams follow a path from the LO source to the plate such that tilts of LO signal polarization are introduced due to mechanical constraints. To compensate for this effect, a small K-mirror is installed on the plate, before the corresponding LO phase grating. All this makes the LFA optics plate very tight and crowded.

The HFA, with only one polarization, follows the same optical strategy. However, the surface quality of the reflective elements can cause significant losses, given the increased number of mirrors in comparison to the GREAT H channel. After some in-house tests, the final mirror design was presented to Kugler who built and gold-platted the elements, offering high reflectiveness.

New Bias electronics

A new bias electronics crate contains 21 bias boards. These boards are compatible with the upGREAT arrays and backward compatible with the single pixel channels. They are controlled remotely trough a private ethernet network and provide and read the bias voltage and current. One card interfaces one pre-amplifier module for a single mixer.

New IF Processor for upGREAT

A completely new IF processor was installed with upGREAT. It consists of a main controller and 21 (22) individual cards, each of which covers the entire range from 0-4 GHz. The cards are also equipped with total power detector modules and variable attenuators like their predecessors, but lack the internal mixing capability. In addition they provide band pass compensation or *equalization*, accounting for the mixer IF response and the active and passive elements in the IF path of each pixel.

New Spectrometers for upGREAT

Similarly, a new more compact, robust and powerful spectrometer came up. The MPIfR's continuously active development of FFT spectrometer technology lead to a new generation called FFTS4G (Klein 2017). Being able to cover 4 GHz of bandwidth per card, and with a maximum resolution of 61 kHz (65536 spectral channels), the FFTS processor is made up of 21 FFTS4G boards; one per pixel.

2.2.4 Cryostat and Cooling

The cryostat for upGREAT is mechanically compatible with and partially based on the single pixel standard cryostat. The major difference is the cooling mechanism, which also mechanically constrains the location of the detectors. It has been designed at the MPIfR and built by Cryovac.

The cooling is provided by a closed cycle dual stage pulse tube refrigerator. The unit, model PTC-406C, is manufactured by Transmit. This model delivers 0.8 W of cooling power at 4.2 K for its second stage while its first stage handles 10 W at 45 K when paired with a Sumitomo CSA-71A air cooled cryo-compressor. The pulse tube cooling stages are thermally connected to plates through copper braids, to minimize mechanical vibrations. These stage plates (named for convention 4 K and 77 K plates) offer the structural mounting for the receiver components. Concentric cylinders acting as radiation stage shields are connected to the stage plates. In between, fiberglass cylindrical separators act as spacers and provide additional mechanical support.

A Zitex G104 foil, mounted on the cover of the 77 K radiation shield, works as infrared radiation filter, while frequency specific vacuum windows are placed on the outer vacuum wall of the cryostat.

2.3 Optics of GREAT and SOFIA

The effective diameter for each optical component designed for GREAT has been constrained by a $5 \times w$ (beam width, see Eq. A.1) criterion. This implies that the design dimension of each component is related to the beam size at the component (at the target frequency). In general, the optics design of all the GREAT channels produces a beam waist located close to the position of the cryostat windows and the infrared filters to minimize their sizes. This limits the heat load on the cold stages caused by infrared radiation.

Table 2.4 offers a synoptic view of the relevant optical parameters of each GREAT channel, including LFA and HFA. The beam size (HPBW) depends on the frequency, and thus can vary significantly between the low and the high frequency limits of the channel. For the arrays, the separation of the beams on the sky is given by the *plate scale* of the SOFIA telescope and the physical separation of the beams in the SOFIA focal plane. The latter results from the separation in the mixer focal plane, inside the cryostat, and the optics magnification factor. The plate scale is defined as the inverse of the telescope nominal focal length (Table 2.1). For the nominal SOFIA optics (Fig 2.3), 1 mm of spacing maps as 4.2" on sky.

Table 2.4: GREAT Optics specifications. Numbers in parenthesis indicate frequency in THz. Data taken from Risacher et al. (2016a) and Wagner-Gentner et al. (2004)

Parameter	LFA	HFA	L1	L2	M	H
Edge Taper [dB]	13	13	14	14	14	14
Beam waist@FP_{SOFIA} [mm]	2.4 (1.9) 1.7 (2.5)	1.0	3.97 (1.2)	2.51 (1.9)	1.87 (2.7)	1.017
Beam spacing@FP_{Mixer} [mm]	12	10.5	-	-	-	-
Beam spacing@FP_{SOFIA} [mm]	8	3.5	-	-	-	-
HPBW ["]	15.5 (1.9) 11.8 (2.5)	6.3	21.3 (1.3) 19.6 (1.5)	15	11.4 (2.51)	6.4
Pixel spacing on sky ["]	34.0	13.8	-	-	-	-

2.3.1 Taper and Blockage

The scattering cone used at the subreflector during GREAT campaigns has a diameter of 72 mm and projects a blockage shadow f_b = 72/350 (0.205) over the main reflector. This blockage affects the effective aperture of the telescope and the way GREAT couples optically in favor of minimizing standing waves. The SOFIA telescope is illuminated by the upGREAT arrays using an edge taper with a value of 13 dB. This represents a good tradeoff between the number that maximizes the aperture efficiency (10 dB), and where the main beam efficiency peaks (14 dB) with the current blockage factor (Fig 2.7). The optics for the single pixel channels was designed with a 14 dB edge taper.

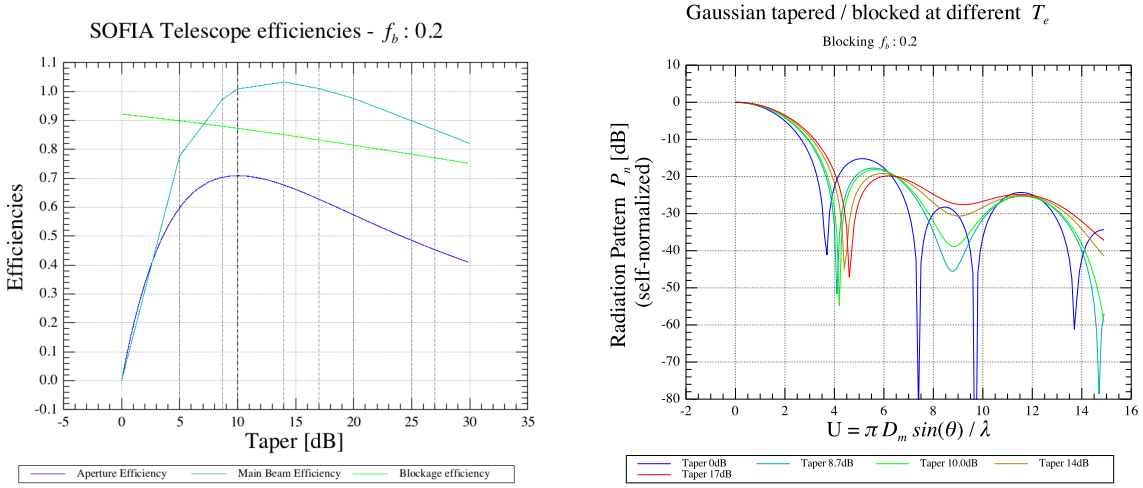

Figure 2.7: Telescope efficiencies and radiation pattern of the SOFIA telescope when coupled with GREAT optics. See text for details.

2.3.2 The GREAT De-rotator

Along with the extension of GREAT by the upGREAT arrays, an image de-rotator, or *K-Mirror*, was built and installed. The K-mirror, which works like a reversion prism (W. Smith 1966), consists of 3 optical quality flat mirrors, a motorized rotary stage and the controller. It compensates for the sky rotation by keeping the pixel patterns of the arrays fixed on the astronomical sources or provides pixel rotation according to the observing strategies. While the K-mirror adds 319.66 mm to the telescope beam path, the physical position of the instrument focal plane remained the same with respect to the SI flange and therefore the distance between the focal plane and the sub-reflector increased from 6933 to 7253 mm. This distance difference is easily compensated by the telescope sub-reflector hexapod focusing (Krabbe 2000). When in focus, the effective focal length of SOFIA increases from 49141 mm (Table 2.1) to 51421 mm (Bahner 1967). With this, the new plate scale is 4.02" per mm. The addition of the K-mirror is fully compatible with the single pixel GREAT channel optics.

CHAPTER 3

The 4-channels German REceiver at Terahertz Frequencies Extension: 4GREAT

The addition of the upGREAT Low Frequency Array (LFA) (Risacher et al. 2016a) and the High Frequency Array (HFA) to the modular GREAT, offers new scientific opportunities to the interested SOFIA communities. However, while these instruments increase the scientific yield of SOFIA by spatial multiplexing, there is also a strong demand for a complementary instrument that spans a wider frequency range. 4GREAT has been developed in response to these needs. The instrument operates simultaneously four state-of-the-art detectors at science-driven frequencies between 0.5 and 2.7 THz.

3.1 Design Drivers and Requirements

Since Herschel ceased operations in 2013, astronomers were lacking access to those parts of the terahertz spectrum that are not visible from ground-based observatories, as much of these frequency ranges are blocked by earth atmosphere, even at high dry sites like the Chajnantor Plateau in Chile, the sites of APEX and ALMA (Figure 1.4).

As the flight spares SIS mixers of the Herschel/HIFI instrument (de Graauw et al. 2009; Jellema 2015; de Graauw et al. 2010) for the bands 1 (480-640 GHz) and 4 (960-1120 GHz) were still available, the first design draft of **4GREAT (4G)** considered the integration of these two detectors into a modified (upGREAT like) closed-cycle cryostat, that would also make use of the GREAT infrastructure. However, with the appropriate choice of dichroic filters and making use of both polarizations, up to four channels (mixers) could be operated in parallel, all co-aligned on sky. The integration of these 2 additional mixers like the (back then) existing GREAT L1 (1252-1520 GHz) & M (2500 (M_a) - 2700 (M_b) GHz) single channel detectors (Heyminck et al. 2012) into such closed cycle cryostat completed the scene.

Some different configurations were initially considered (R. Güsten 2015) and discussed at that time in terms of scientific goals (subsection 3.1.1), constrained by available detectors, local oscillator sources feasibility, and optical configurations. Three basic options were discussed and brainstormed and by September 2016 the design and development of 4GREAT started based on the goal configuration listed in Table 3.1.

3.1.1 Scientific Opportunities

SOFIA provides a unique platform and offers scientific perspectives which can not be done from ground based facilities (Fig 1.4).

Table 3.1: 4GREAT Goal specifications and some of the scientific lines of interest. The entire line catalog can be seen on table J.1

Channel	Detector	LO Frequency [GHz]	Some of the lines of interest
4G-1	HIFI Band 1	492 - 635	[CI], CH, $H_2^{18}O$(110-101), NH_3, CO(5-4)
4G-2	HIFI Band 4	892 - 1100	CO(8-7), CO(9-8), CS(19-18), $H_2^{18}O$(2-1)
4G-3	GREAT L1	1200 - 1500	NH, [NII], CO(11-10), ^{13}CO(13-12), H_2D+
4G-4	GREAT M-HD	2500 - 2700	OH, HD

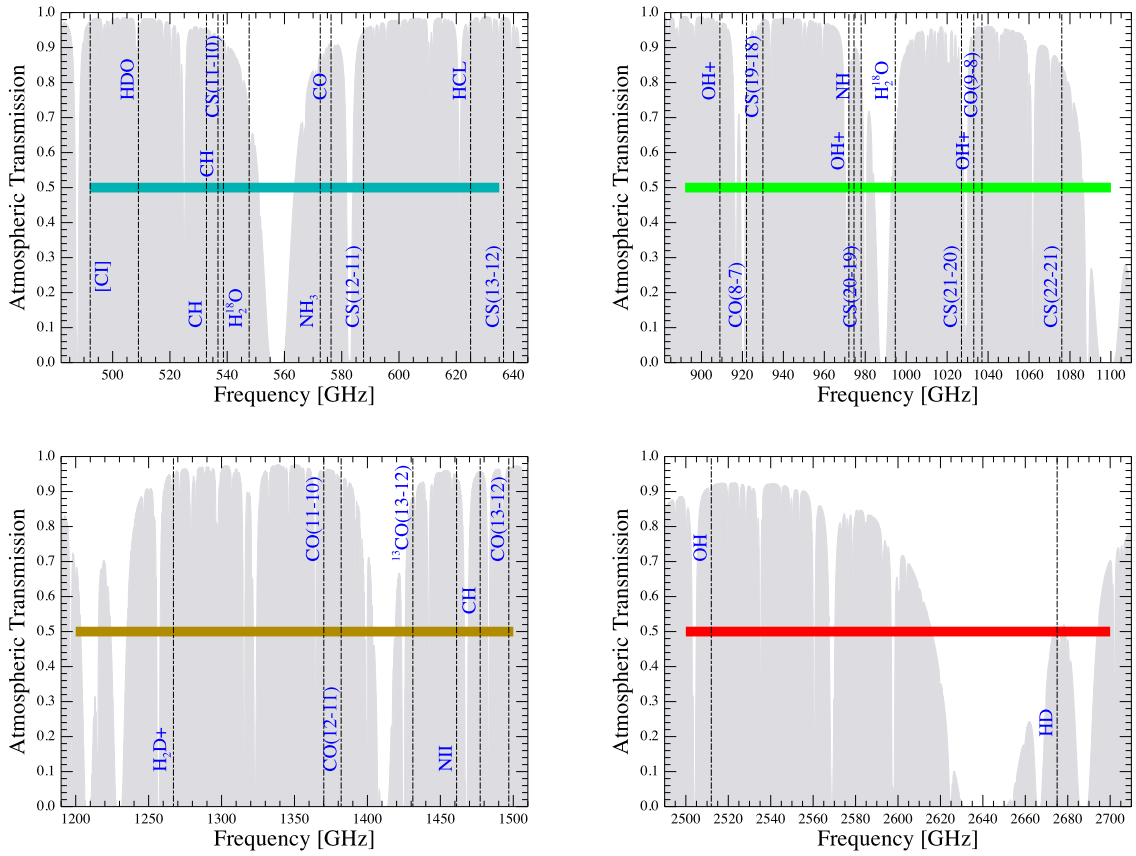

Figure 3.1: Some selected astrophysical lines of interest per band. Underlaid in gray, the atmospheric transmission for a PWV of 10 μm, a typical SOFIA flight at an altitude of 43.000 ft. Top: 4G-1 and 4G-2, Bottom: 4G-3 and 4G-4. The color bars represent the goal LO coverage.

There is a set of attractive astrophysical lines of interest (LOI) with the major ground-state transitions of important molecules, like NH_3, $H_2^{18}O(1_{10}\text{-}1_{01})$, CH, HCL, HDO which are to be observed using the 4GREAT channel 1 (4G-1). The 4GREAT channel 2 (4G-2) covers a wealth of ground-state transitions of important molecules; in particular hydrides: the HDO (111-000) line, of relevance for cometary studies, lines of HNCO in the 900-910 GHz range, the three fine structure lines of the OH^+ ground state transitions at 909, 972 and 1033 GHz, ground state transitions of NH and NH_2 in the 950-1000 GHz range, H_3O+, and the low lying water line $H_2^{18}O(2_{02}\text{-}1_{11})$. Most of the transitions and molecules are

unique to this band. 4G-3 will continue with the work performed by GREAT L1 on the detection of four transitions of the CO ladder and in particular on the [NII] line, a key transition on interstellar medium cooling processes. CH at 204 μm in this same band complements the CH transition at 559 μm (4G-1) and 149 μm (upGREAT LFA). 4G-4, integrating the detector from GREAT-M, has the mission of detecting two important molecules: OH and HD. HD is of particular relevance in tracing molecular hydrogen and constraining the cosmological Deuterium abundance. OH on the other hand plays an important role in the so called oxygen chemistry.

Figure 3.1 and table 3.1 summarize the frequency coverage and some of the lines of interest. The entire line catalog can be seen on table J.1

3.1.2 Technical Constraints and Design Challenges

During the specification and design phase several constraints were identified. Some of these pushed the specifications and boundaries of SOFIA/GREAT and required a much more innovative approach.

The opto-mechanics of GREAT and SOFIA constrained the design of 4G in different manners, in particular due to the wide range of the low frequency 4G-1 channel (Table 3.1). These are discussed in more detail by this chapter and in particular in the optics section (3.5).

Constraints also came from operational facts. GREAT as a whole can not exceed certain weight and volume boundaries given by technical tolerances and stated in the interface design documents of the SOFIA telescope. In addition every single module of GREAT must adhere to very strict airplane safety requirements.

To ensure best performance of in particular for the 4G-1 mixer, which requires the lowest operating temperature possible, the thermal load of the system had to be carefully addressed. This is described in section 3.3.1.

There were also some technical limitations that arose during the mechanical design and construction of individual components. The most important goals and challenges are listed on Table 3.2.

Table 3.2: 4GREAT design constraints and goals

Performance	∗ Lowest receiver noise temperature, with highest possible stability
Optics	∗ Simultaneous operation with upGREAT HFA ∗ 4 different frequency bands observed simultaneously co-aligned on sky ∗ Beam separation by frequency & polarization ∗ Telescope taper, coupling and beam blockages ∗ Optics for signal and 4 LO sources ∗ 4G-4 LO very low power
Cooling	∗ 4G-1 mixer requiring the lowest possible operating temperature ∗ Closed cycle coolers to operate independent of cryogenic logistics, also on deployment missions
Size and Weight	∗ Limited space in the GREAT structure ∗ Very limited space inside cryostat ∗ Allocating 4 solid state LOs ∗ Maximum Weight: 600 kg., including the GREAT frame, within the envelope defined GREAT airworthiness certification
Operation	∗ 4 LOs tunable independently at same time ∗ 4 reference synthesizers / attenuators

3.2 Modules of 4GREAT

4G is not a single piece of hardware but a system made up of many modules and its associated interface and control software. There are four clearly distinguishable parts:

* 4GREAT receiver (cryostat)
* Local oscillator upper unit (LO-U): Hosting the 4G-1 and 4G-2 LO chains and optics
* Local oscillator lower unit (LO-D): Hosting the 4G-3 and 4G-3 LO chains and optics
* Optics plate

These four modules are installed on the GREAT structure/frame along with additional support and control modules also used by upGREAT, which include a calibration unit, mixer bias controller and LO base synthesizers. Figure 3.2 shows the disposition of 4GREAT modules. They are individually described through the next sections.

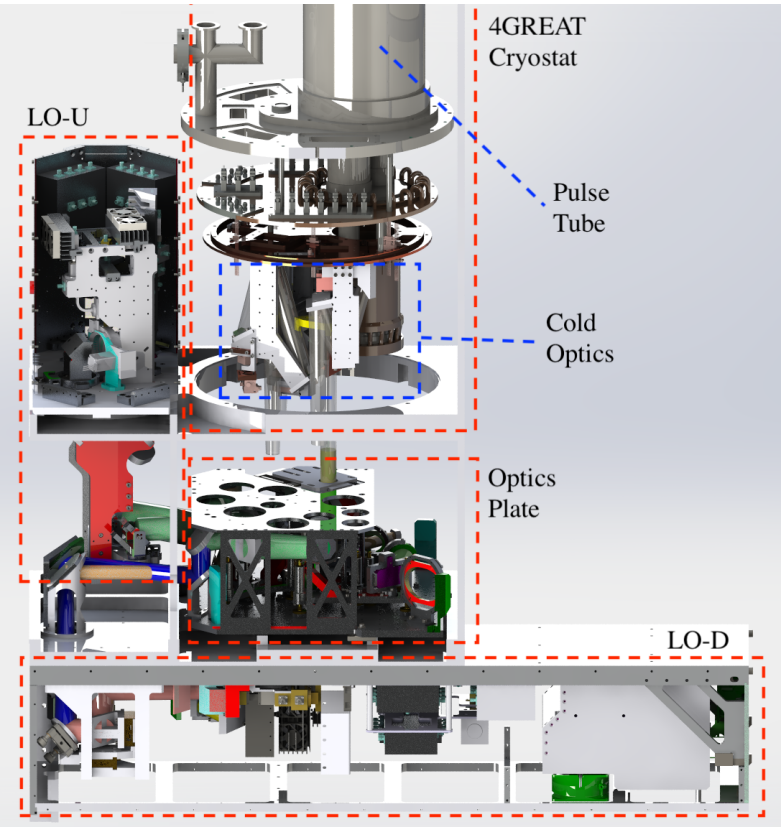

Figure 3.2: The different modules of 4GREAT. Framed in segmented lines each of the four main modules. In blue, some important submodules. GREAT mounting frame not fully shown for better visualization.

At the frequency regime that all four 4G channels operate, LO coupling and injection to each detector is done (quasi-) optically (Fig. 1.8). This means that the optics inside the 4G cryostat have to be compatible with the optics from the LO source and the signal path.

3.3 The 4GREAT Receiver

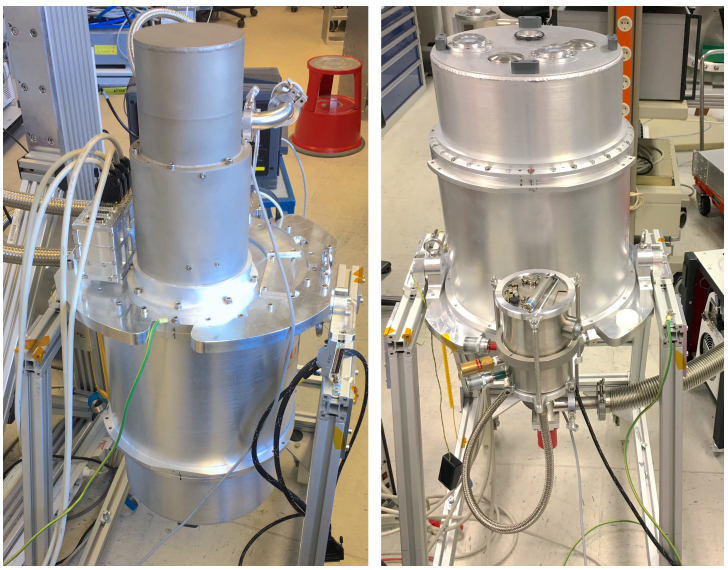

Figure 3.3: 4GREAT receiver cryostat on the laboratory stand. On the right image, 4G is upside-down and the pulse tube rotary valve and vacuum windows can be seen.

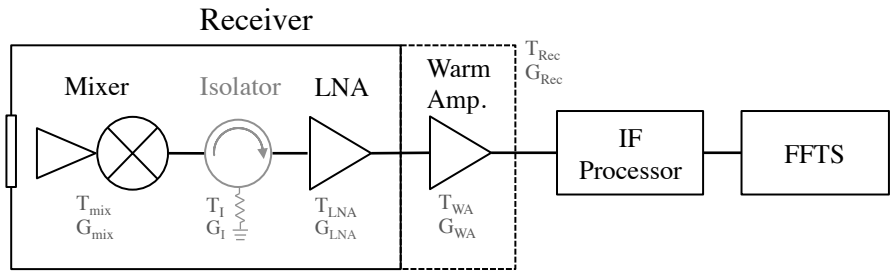

Figure 3.4: 4GREAT Receiver Components per channel (boxed). 4G1 and 4G2 use an isolator between their respective mixers and LNA, can be omitted for the HEB mixers channels in favor of minimizing losses.

In general the term *receiver* is colloquially used to make reference to a cryostat containing detectors and associated electronics. Although not strictly correct, it helps to make the distinction between a fully populated and complete vessel and the cryostat (Section 3.6).

As said before, 4G is in fact a four channels receiver, or in other words, four fully independent receivers contained in one system. Each channel is built using the same kind of elements: a vacuum window, an infrared filter (subsection 3.5.1), cold focusing optics (see section 3.5), a mixer (subsection 3.3.1), a ferrite isolator (only for 4G-1 and 4G-2), a low noise amplifier (LNA) and an external warm amplifier (subsection 3.3.2). Figure 3.4 shows the disposition of most of them. There are also temperature sensors, wiring interfaces and electronics for biasing the detectors.

3.3.1 Detectors

Although all four detectors are double side band mixers (Fig 1.9), they are coming from two different technology families: SIS and HEB.

These two families coincidently also correspond to different detector genesis: The 4G SIS mixers were originally developed for the Herschel/HIFI instrument, while the HEBs used by 4G were designed and built for GREAT.

The detectors for Herschel/HIFI were developed by different research institutes following directives and specifications given on the instrument specification documents. As they were built to fit two polarizations per band into the focal plane unit (FPU) of HIFI, two mixers were boarded per band. For each HIFI band *qualification models* (QM) mixers were provided during the selection and tests processes. Once the proposed model was accepted, final *flight* versions were built. These are known as *flight models* (FM) and *spare flight models* (FS). QM and FM/FS are fully compatible and interchangeable for each channel in any regard.

The HEB mixers were developed and produced by the *Kölner Observatorium für Submm Astronomie (KOSMA)* group for GREAT L1 and M single channel bands but also for L2 (Pütz et al. 2012) and H (Büchel et al. 2015). The mixer designs are therefore specific for this instrument. The M-band mixer uses a novel design of horns embedded in a clamp and then attached to a mixer block. The HEB mixer blocks are mechanically more compact than the SIS mixers as they do not require heaters or magnets.

4G-1 SIS Mixer

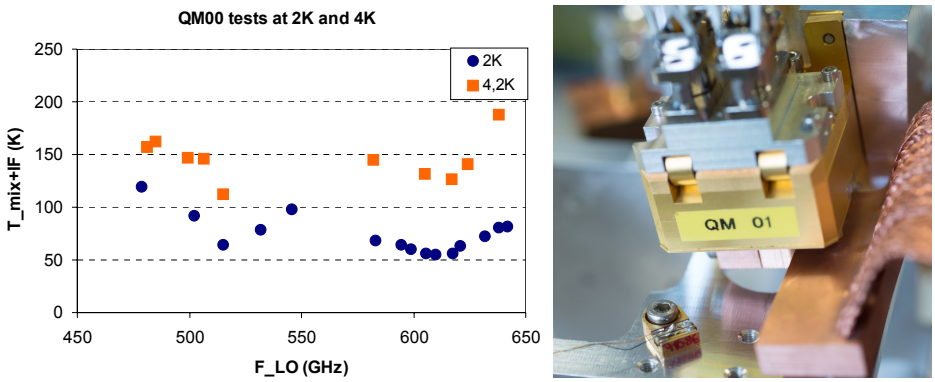

Figure 3.5: 4G-1. Left: QM s/n 00 noise temperature measured when mixer block is at 4.2K and 2K (Delorme 2016). Right: QM-01 was used for the 4G-1 channel during the tests phase. Its horn is thermally connected to the pulse tube 2nd stage at 4K through a copper clamp.

The 4G-1 mixer is a waveguide unit without mechanical tuning elements. Developed by *Laboratoire d'Etudes du Rayonnement et de la Matière en Astrophysique et Atmosphères*, LERMA, in Paris, France (Krieg et al. 2002; Delorme 2016), the detector element is made up of a pair of SIS tunnel junctions with Nb superconductors and an integrated RF matching circuit. The coupling to the optical beam is performed through a waveguide corrugated horn. The SIS elements are mechanically and thermally attached to the horn, and all encased in a *bracket* or block.

The mixer unit (block) is equipped with the necessary bias circuitry and heaters and electromagnets to remove trapped magnetic flux, along with the corresponding interface connectors and IF output connector.

Table 3.3: 4G-1 SIS mixer specifications

Manufacturer	LERMA	
Model type	FM/FS	
Serial	FS02	
Technology	SIS	Dual junction
Type	DSB	
Band [GHz]	480-640	Design specification
IF band [GHz]	4-8	
Side-band ratio	0.5 ± 0.1	As defined by Higgins et al. 2014
Horn	Corrugated	See Table 3.12
Noise temperature $T_{\text{Mixer-SSB}}$ [K]	100	see text and Fig. 3.5

The design of the optics, mechanical components, electrical interfaces and preliminary tests for 4G-1 were performed using the HIFI-band1 qualification model QM-01. Just before the commissioning of 4GREAT, a spare flight model (FS02) was integrated. This is therefore the mixer commissioned, characterized and used for this work. Table 3.3 displays its relevant parameters.

An interesting characteristic shared by all the mixers of this design, either FM/FS and QM, is their strong temperature dependence in regard to its performance (Fig. 3.5 left). This is given by the fact that the SIS elements are thermally attached to the horn, and not to the casing block. As the mechanical fixations and references are part of the casing, they also serve as standard thermal links. To overcome this issue, the horn was additionally clamped, and thermally linked to the pulse tube cold head, as seen on figure 3.5 right pane.

4G-2 SIS Mixer

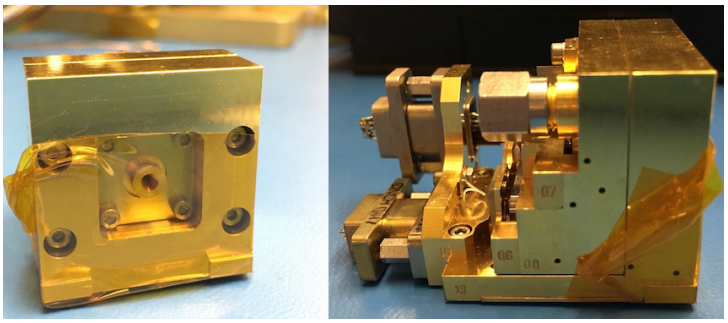

Figure 3.6: 4G-2 Mixer is a special version of a QM for HIFI-band4 produced by SRON. See text for details.

The mixer was developed by SRON, the *Netherlands Institute for Space Research*, also as part of the development for HIFI, and to be the band 4 detector. As for 4G-1, it employs a corrugated horn, a RF matching circuit and twin SIS tunnel junctions made of $Nb/Al_2O_3/Nb$ with Al and NbTiN top and bottom electrodes respectively. In fact the design follows the same directives as for 4G-1 in terms of mechanical references and envelope volumes, but with the obvious differences given by the target frequency range.

SRON has provided the MPIfR two detectors: a flight spare mixer, FM10 (Junction SIS 21-14 G32) and a modified qualification model Q4H1 (Junction SIS 21-19 F31). The FM10 detector was integrated

Table 3.4: 4G-2 Mixer specifications

Manufacturer	SRON	
Model type	QM	Modified
Serial	Q4H1	Junction 21-19 F31
Technology	SIS	Dual junction
Material	NbTiN	
Type	DSB	
Band [GHz]	960-1120	Design specification
IF band [GHz]	4-8	
Side-band ratio	0.5	As defined by Higgins et al. 2014
Horn	Corrugated	See Table 3.12. Δz = +1.65 mm
Noise temperature $T_{\text{Mixer-SSB}}$ [K]	350	

into the APEX 1 THz Receiver (de Lange et al. 2006) and successfully commissioned in 2009 (Leinz et al. 2010). 4G-2 makes use of the Q4H1 version. There is however a difference between the FM-10 and Q4H1. As SRON also built HIFI-band 3 mixers (de Lange et al. 2003), the Q4H1 is a band 4 sensor and horn mounted in a band 3 bracket (De Lange 2016). This has an impact on displacing the horn waist position with respect to the absolute mechanical references (FM-10) of the mixer by 1.65 mm. Such feature was properly accounted and makes the optical and mechanical design of the optics for this channel exclusive for this particular mixer and is not directly replaceable by any other QM or FM/FS built. Although the design specifications for HIFI band 4 mixer targets the band from 960 to 1120 GHz (Jackson et al. 2002), each mixer has a wider range. In fact, to make use of this feature and include more scientific cases, the local oscillator source used for 4G-2 runs from 892 to 1085 GHz (see Table 3.10 for details).

4G-3 HEB Mixer

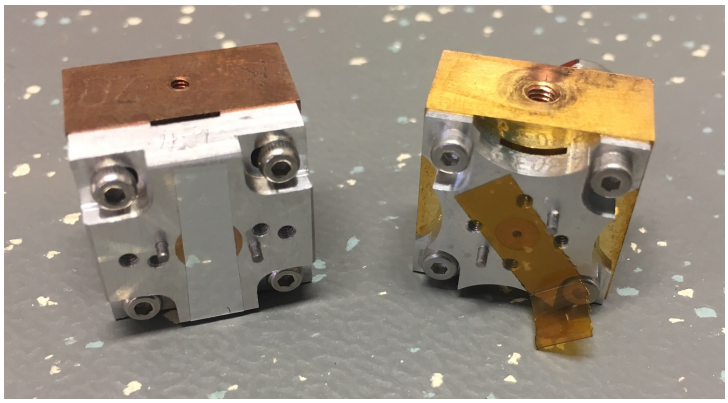

Figure 3.7: HEB mixers used by 4G. From left to right, 4G-3 and 4G-4. Horns apertures are covered for handling.

The base technology used by the mixer integrated into 4G-3 has its origins back to 2004 (Muñoz et al. 2004) when a 1.25 - 1.5 THz NbTiN hot electron bolometer mixer was developed for the *CO N+*

Deuterium Observations Receiver, CONDOR (Wieching 2007), by the KOSMA team (Muñoz et al. 2006). In November 2005, CONDOR was successfully commissioned on APEX and so, the technology was proved to be effective.

The mixer for GREAT L1 is built using a corrugated horn which is held by an aluminum clip into a copper mixer block (Fig. 3.7). The mixer only has a coaxial sma connector for the IF output which is also employed to supply the bias voltage through an external *bias-T*. The employed bias-T is consolidated with the LNA in a single module (subsection 3.3.2). 4G-3 detector characteristics are summarized in table. 3.5.

Table 3.5: 4G-3 Mixer specifications

Manufacturer	KOSMA	
Technology	HEB	
Material	NbTiN	
Type	DSB	
Band [GHz]	1200 - 1500	Design specification
IF band [GHz]	0.2 - 2.5	Mixer rolloff
Side-band ratio	≈ 0.5	
Horn	Corrugated	
Noise temperature $T_{\text{Mixer-DSB}}$ [K]	550	@ IF 1.0 GHz

4G-4 HEB Mixer

There are two generations of this detector. The first version is a 2.5 THz NbTiN HEB element suspended on Si_3N_4 developed for the GREAT M channel (Pütz et al. 2011). It makes use of novel scaled custom spline-profile conical feed (Granet et al. 2004) which was micro-machined by RPG, under the specifications of the KOSMA team (Rabanus et al. 2006). The 4G-4 mixer (Fig. 3.7) corresponds to the second generation that was also used by the GREAT M channel. It is a NbN HEB mixer and has been optimized to cover the band from 2.52 to 2.68 THz (Pütz 2016), including the HD line at 2.675 THz. This gives the *"HD"* suffix: M-HD. Both generations are opto-mechanically compatible. 4G-4 also requires an additional biasing module (bias-T), just like 4G-3.

3.3.2 Isolators, LNA and Warm Amplifiers

Its a feature of an SIS mixer that its output impedance can be far from 50 Ω and therefore when a low noise amplifier is connected directly to its output, oscillations and standing waves can arise. To overcome this problem two approaches can be taken. An impedance matching network can be placed between the SIS and LNA, with the drawback that the output impedance of the mixer might not be uniform over its IF band. In addition, the insertion loss can be considerable. A second way is the use of a ferrite isolator. 4G-1 and 4G-2 employ isolators provided by Ferrite-Quasar (see table 3.8). The chain of components is depicted in Figure 3.4.

HEB mixers are less prone to suffer from this feature and therefore the connection between mixer and LNA is direct and can be as short as possible to minimize losses.

The LNA output IF signals are then further amplified by room-temperature low noise amplifiers from Miteq mounted externally, on top of the receiver; there is one per channel.

Table 3.6: 4G-4 Mixer specifications

		Remarks
Manufacturer	KOSMA	
Model type	M-HD	
Serial	6.101.39	
Technology	HEB	
Material	NbN	
Type	DSB	
Band [GHz]	2520 - 2675	Design specification
IF band [GHz]	0.2 - 4	
Side-band ratio	≈ 0.5	
Horn	Smooth walled	
Noise temperature $T_{\text{Mixer-DSB}}$ [K]	850	

Table 3.7: 4GREAT cryogenic and warm low noise amplifiers specifications. LNA specifications and performance numbers are obtained under device cooling at the indicated physical test temperatures.

Low Noise Amplifier	4G-1	4G-2	4G-3	4G-4
Manufacturer	LNF	LNF	CalTech CMT	CalTech/CMT
Model	LNF-LNC4-8C	LNF-LNC4-8C	CITLF4	CITLF4
Frequency band [GHz]	4 - 8	4 - 8	0 - 4	0 - 4
Gain [dB]	39	39	36	36
Gain flatness [dB]	±0.5	±0.5	± 3	±3
Noise temperature [K]	2.1	2.1	< 7	< 7
Physical test temp. [K]	5	5	16	16
Serial	348Z	344Z	517L	629L
Warm LNA	All Channels			
Manufacturer	L3 Narda Miteq			
Model	AFS3-00100800			
Frequency Band [GHz]	0.1 - 8			
Gain [dB]	30 min.			
Gain flatness [dB]	1.5 max.			
Noise temperature [K]	225.7 max			
VWSR in / out	2:1 max / 2:1 max			
P1dB out [dB]	10 min.			

Table 3.8: 4G-1 and 4G-2 isolator by Ferrite-Quasar. Specifications at 77 K

Model	Range [GHz]	Insertion loss [dB]	Isolation [dB], min	VSWR max
3CCC60-1	4 - 8	0.4	18	1.30

3.3.3 Mixer Bias Pre-amplifier Interface

An additional module is attached externally to the receiver: The mixer bias pre-amp box interface (Fig. 3.3). Made up of four independent cards, this module safely interfaces the bias connectors of each mixer (or the bias-T in the case of the HEB mixers) through a 62-pin D-sub vacuum feedthrough connector with the main bias electronics control unit. It provides amplification for the weak bias monitor signals and filters the mixer bias voltage. The bias control and monitor uses the 5-wire scheme (Fig. 3.8) described by Jackson et al. 2002.

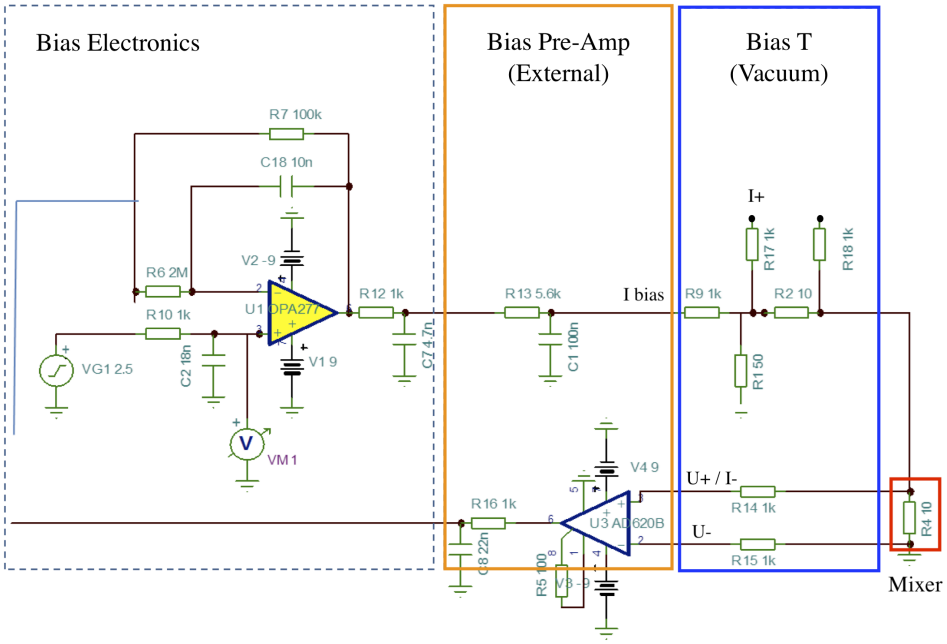

Figure 3.8: Electrical diagrams for the HEB mixer biasing. Bias boards are in the bias electronics module. The bias pre-amplifiers sit on top of the cryostat, and the bias-T are placed as closed as possible to the HEB mixer, providing also ESD/EMI protection (not shown here).

3.3.4 Temperature Monitoring

A total of 8 temperature sensors (diodes) have been installed inside the receiver. Four of them have been attached to each cold optics group, while the other 4 are distributed on key spots (Table 3.9). When the receiver is in the laboratory, all 8 sensors are monitored by an external Lakeshore LS 218 display, while during flight only the first four are read by the GREAT electronics, displayed by the frontend software and stored in a data base.

3.4 Local Oscillators: LO-U and LO-D

The development of solid state local oscillator sources (Crowe et al. 2009) or *chains* up to 3 THz has improved in the last 5 years. By cascading multiplication stages and high frequency power amplifiers, these signal sources have output power in excess of 20 μW, even at 2 THz. The small form factor of the multiplication chains allow to conveniently combine them and provide wide range LO sources. At this

Table 3.9: Temperature sensors installed inside the 4G cryostat

Number	Model	Location	Use
1	DT-670	77K plate (1st stage)	In-flight/lab
2	DT-670	4K plate (2nd stage)	"
3	DT-470	4G-1 cold tower	"
4	DT-670	4G-2 cold tower	"
5	DT-670	4G-3 cold tower	Lab only
6	DT-670	4G-4 cold tower	"
7	DT-670	Pulse tube 4K plate	"
8	DT-670	4K plate -2nd sensor	"

power regime LO coupling can be done by simpler methods (see subsection 3.5.2) instead of using a Martin-Puplett interferometer (MPI) as diplexer (Lesurf 1981).

VDI provided the LO sources for the four channels of 4G. Its only the 4G-4LO (local oscillator for 4G channel 4) which requires a MPI to couple all the available LO power and combine it with the astronomical signal, as power at this frequency range is rather low (Table 3.11).

3.4.1 LO-U Chains

LO-U hosts the two *low frequency* channels local oscillators: 4G-1LO and 4G-2LO. Each LO chain requires a power supply and an external reference signal. Such signal comes from the synthesizer box of GREAT (independent for each LO).

The LO sources have a relatively wide frequency coverage (> 21%), which can not be served by a single multiplication chain and therefore the sources are composed of two subchains with their respective power amplifiers and control electronics. The signals from the subchains are combined by a waveguide diplexer before the last multiplication stage and its horn. Each subchain covers a specific sub-band of the LO. The LO control electronics monitors the input reference signal and switches *on* or *off* each subchain by biasing the corresponding multiplication modules and its power amplifier according to factory settings. The boundary between the two subchains is seen as a *gap* on the chain output power (Fig. 3.9) and have been defined to match a strong atmospheric absorption feature.

Table 3.10: LO-U solid state LO chains specifications

Channel	Chain	Factor	Range [GHz]	Output power (μW)	Horn
4G-1LO	AMC 563	×48	495 - 628	> 300	Diagonal WM-380
4G-2LO	AMC 581	×72	892 - 1085	> 100	Diagonal WM-250

3.4.2 LO-D Chains

The 4G-3LO is also made up of two subchains, just as the local oscillator sources for 4G-1 and 4G-2. However 4G-4LO is different as it is a single (sub)chain, which makes it even more compact. Table 3.11 presents some of the characteristics of each the chains in the LO-D, while figure 3.10 displays the respective output power plots. The LO-D also hosts all the LO power supplies, not only for 4G-3LO and

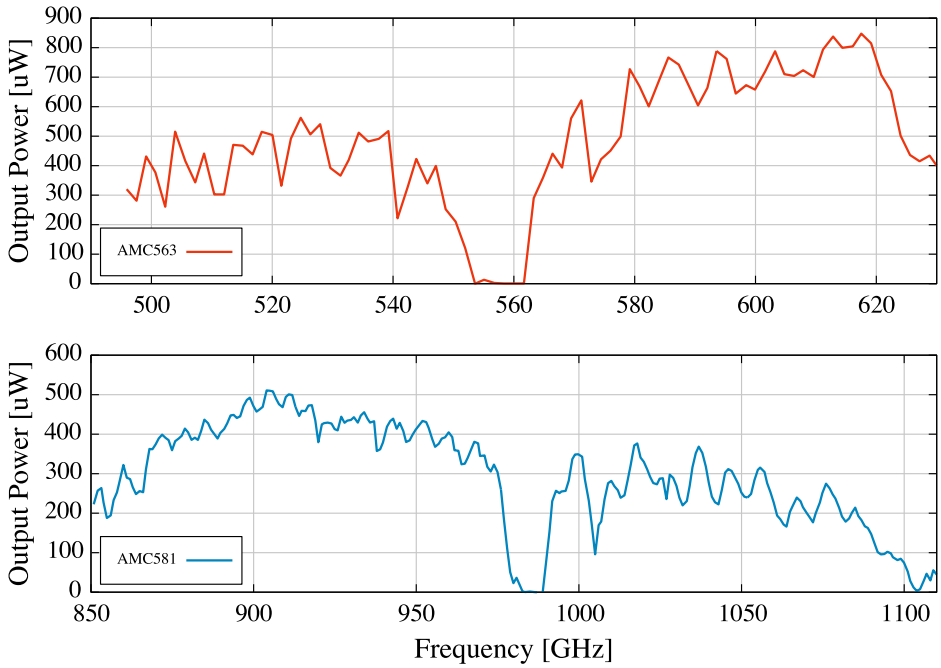

Figure 3.9: Output power of 4G-1LO (AMC 563) and 4G-2LO (AMC 581) chains. Power measurements were performed by VDI using an Erikson power meter directly connected to each chain (no horn attached)

Table 3.11: LO-D Solid state LO chains specifications.

Channel	Chain	Factor	Range [GHz]	Output power (μW)	Horn
4G-3LO	AMC 627	×108	1240 - 1525	> 30	Diagonal WM-165
4G-4LO	AMC 616	×216	2480 - 2695	> 3	Diagonal WM-86

4G-4LO, which are internally connected to the respective chain, but also for 4G-1LO and 4G-2LO. This is realized by two external cables interconnecting the LO-D with LO-U.

3.5 Optics

Perhaps the most critical part of the whole receiver system mechanical design is the optics. It is strongly constrained by different factors (Table 3.2), including the SOFIA telescope but also the cryostat geometry.

The 4G optics consists of the cold optics inside the cryostat, the optics plate, where the splitting of the telescope beam into the 4 signal beams and superposition with the LO beams is done, and dedicated LO optics for each of the LO chains, grouped in the LO-D and LO-U. In general, a multiple Gaussian beam telescope (appendix. A.3) approach was taken to make the system as frequency independent as possible, with the only exception of the 4G-3LO.

The fixed optical parameters given by the characteristics and properties of key elements, like mixer horns and local oscillator sources, oblige the design to be approached from three different but simultaneous directions. The design process begins using the beam waist size (w_0), position waist (z_0) and curvature radius (R) from the detector horn (Table 3.12) as input values for the cold optics and part of the optics plate elements. At the same time, the design of the LO optics, based on the LO source horn parameters,

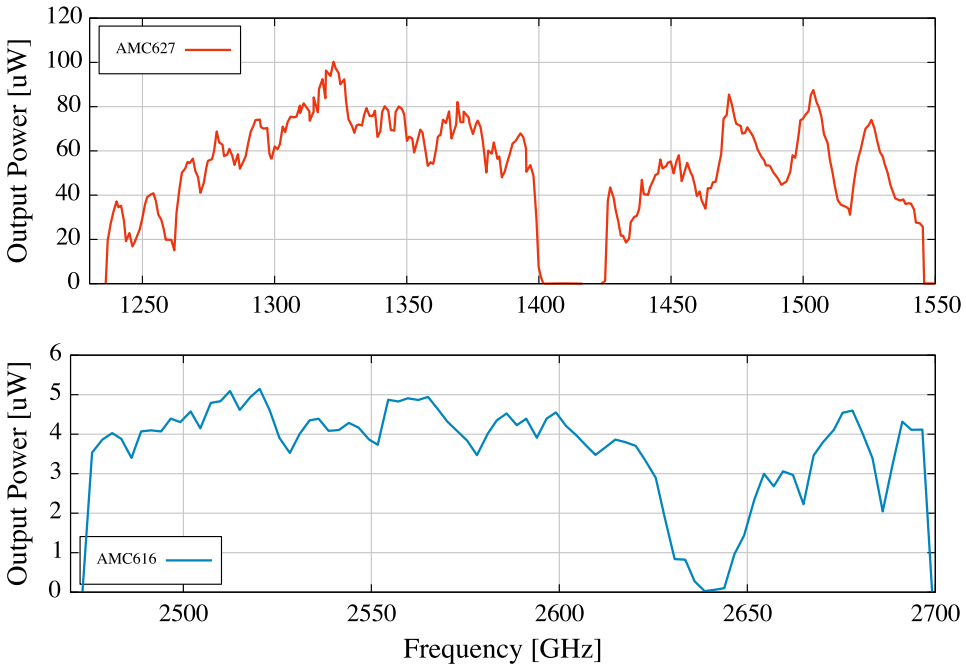

Figure 3.10: Output power for 4G-3LO (AMC 627) and 4G-4LO (AMC 616). Power measurements were performed by manufacturer directly coupling an PM5 VDI Erikson power meter (no horn). Note the water absorption of 4G4-LO chain at 2.64 THz

matches the optics plate and the cold optics. The position of the focal plane and the selected edge taper set the focal plane beam waist. The optics design uses the focal plane waist and position as output parameters, matching them too. Figure 3.11 depicts the steps on the design workflow.

Table 3.12: 4G mixer horn specifications per band. R_h is the horn length, a is the horn aperture (radius), w_0 is the waist, and z_0 is the position of the waist measured from the horn aperture.

Band	Type	f_c [GHz]	R_h [mm]	a [mm]	w_0 [mm]	z_0 [mm]	Reference
4G-1	Corrugated	560	15.4	2.50	1.15	7.6	Jellema (2015)
4G-2	Corrugated	1040	8.3	1.36	0.62	4.2 (+1.65)	Jellema (2015)
4G-3	Corrugated	1350	4.382	0.59	0.344	0.7421	U. Graf (2016)
4G-4	Smooth Walled	2500	-	-	0.239	1.008	Rabanus et al. (2006)

3.5.1 Signal Optics and Signal Path

4GREAT, with 4 co-aligned channels, requires that the signal beam is split and focused into each detector. However, the first optical element in the beam path is a low pass dichroic filter, provided by QMC, used to separate the beam between the upGREAT HFA and 4G. Such dichroic (named D-HFA4G), with a cut-off frequency above 3 THz, is located at the focal plane of GREAT inside the optics plates compartment, and attached to the HFA optics plate (Figure 3.12 low).

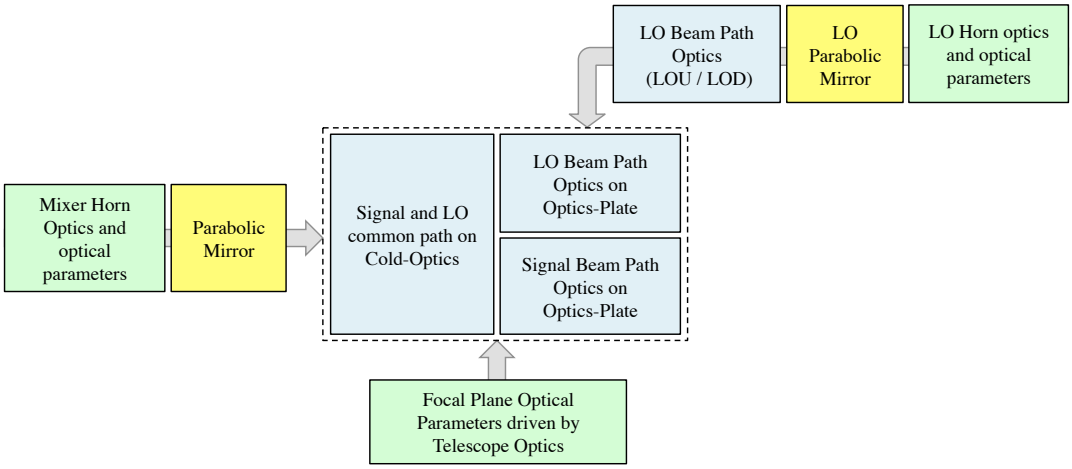

Figure 3.11: Optics design workflow: modules in green represent pre-existing conditions, in yellow the directly designed components and parts in blue were iterated and optimized several times.

Each of the 4G channels signal optics is made up of the same kind of elements, but dimensioned for their respective frequency ranges (Fig. 3.12). Some of these elements are common to two or even all of the channels. The 4G-4 optics has some additional components.

The next element that the signal encounters, after D-HFA4G, towards the mixers is an ellipsoidal (active) mirror, which is common to all 4 channels: M4G. This mirror focuses and deflects the beam to a first wire-grid (WG-VH) which separates the beam into two polarizations. Each of the new beams (horizontal and vertical) is then refocused by another active mirror (M3-13 or M3-24). The mirror couple M4G and M3-13/M3-24 form the first Gaussian beam telescope of each channel. The horizontal and vertical beams are filtered by independent low pass dichroic filters (D-13 and D-24), yielding now 4 different beams: horizontal-low (4G-1), horizontal-high (4G-3), vertical-low (4G-2) and vertical-high (4G-4). The beams are then reflected on a flat/active (F2/M2) mirrors group which provides 4 degrees of freedom for the optical alignment, independently. The 4G-4 beam however has a LO coupling grid before the flat/active group. The beams now go through the respective LO coupling grids (diplexer for 4G-4) and polarization cleaning grid (in line with the mixer polarization), before illuminating the corresponding cryostat vacuum window (W). Inside the cryostat, the beams pass through an infrared filter (IR) located on the 77 K shield and reach the cold optics. The cold optics is composed by an active mirror (M1), a flat mirror (F1) and a parabolic mirror (M0) in front of the respective detector horn. The M2/M1 mirror couple form the second Gaussian beam telescope on the beam path of every channel.

A detailed description of the key parameters of each optical element (per channel) can be found in the tables of the appendix E, while the unfolded optics plots for the respective central frequency of each channel can be seen in the appendix F.

Cold Optics

Each of the 4 mixers is mounted on a block that also contains part of the channel optics and the LNA (Fig. 3.13). These blocks or *cold towers* contain the paraboloidal mirror M0, located in front of each mixer horn, the flat mirror (F1) and the M1 ellipsoidal mirror of the corresponding channel. The cold towers have been designed in such way that they offer a large contact surface for thermal link with the 4 K plate, while keeping deformations under control and making the cold optical group alignment free.

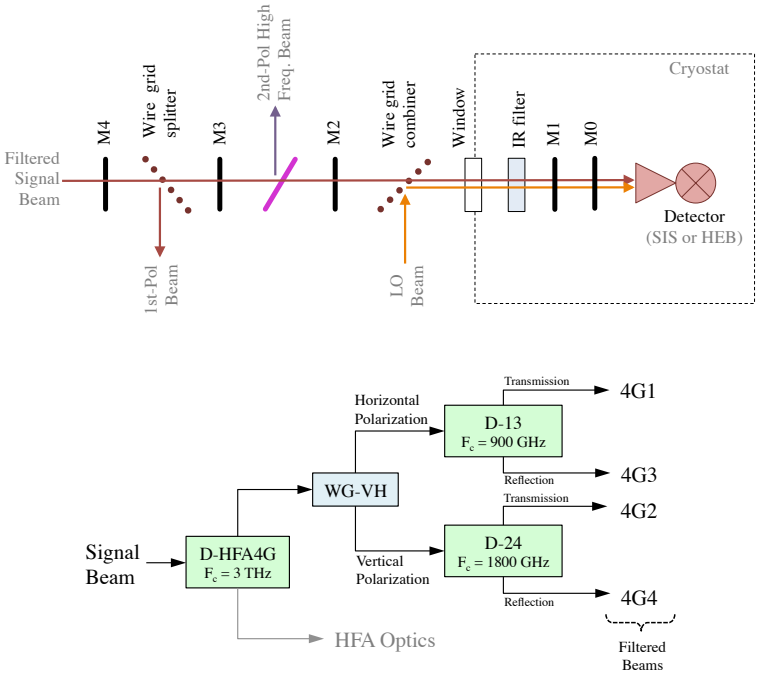

Figure 3.12: Up: Simplified diagram of signal optics for a single channel. Low: Signal beam splitting scheme.

Because of the low frequency and hence large beam size of 4G-1, the cold tower for this channel is much larger than the others, constraining the position of the other cold towers. The mixer on this tower is also conveniently placed in an elevated position, just in front of the pulse tube cold finger plate for a direct thermal clamping (see subsection 3.3.1).

Windows and Filters

Because of the wide frequency range and the different central frequencies of the four channels, the cryostat vacuum RF window is optimized and customized specifically for its channel (Fig. 3.14). Windows for 4G-1 and 4G-2 are made up of quartz with anti-reflection coating (A/R) and were manufactured by QMC. They actually correspond to the same kind of technology used by ALMA on their receivers. Tydex provided the A/R silicon windows for 4G-3 and 4G-4. Figures 3.15 and 3.16 show the transmission of each window, while the average values over the bands are 96.74% for W-1, 94.72% for W-2, 85.25% for W-3 and W-4 has 90.01%.

As for the IR filter, the same material is used for the four channels. The filters are composed of a porous foil of Polytetrafluoroethylene (PTFE) of 100 μm of thickness known commercially as Zytex G104. Although there were some measurements on the transmission properties of different thickness of Zytex (Benford et al. 2003), the sub-mm and FIR range data was not available. However new measurements performed at the MPIfR (Heiter 2017) confirmed their suitability for the above frequency regimes. Simulations and estimations of the heat load and temperature distribution profile (Lamb 1992) were performed under different filter configurations. This subject is developed in more detail in the appendix D.

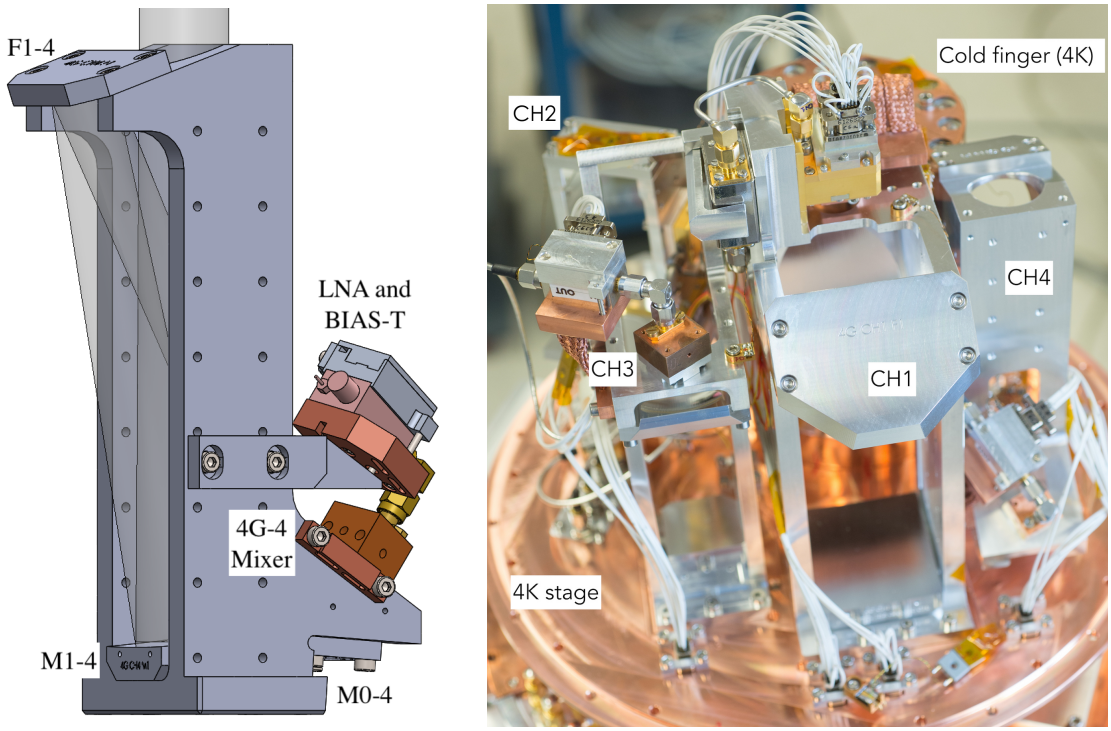

Figure 3.13: Cold optics. Each cold tower mounts a paraboloidal (M0), a flat and an ellipsoidal mirror (M1), along with the corresponding mixer and cold LNA amplifier. Left: 4G-4 cold tower. Right: All four 4G towers on the 4K plate.

Table 3.13: Transmission of the 4GREAT vacuum windows and IR filters. (*) See appendix D

Windows	W-1	W-2	W-3	W-4
Min (%)	93.16	92.89	79.15	86.35
Max (%)	98.08	95.91	92.33	93.79
Average (%)	96.74	94.72	85.25	90.01
Filter	IR-1	IR-2	IR-3	IR-4
Average (%)	91.73*	97.95	98.15	94.73

3.5.2 LO Optics

The LO-U optics, hosting 4G-1LO and 4G-2LO, has a very particular design as these LO frequencies require larger optical elements. Due to the location of the LO-U in the auxiliary calibration unit port (Fig. 3.17), its components are placed on an *extension branch* that sticks into the GREAT structure and then couples to the upper level of the optics plate (Fig. 3.21). Each of the LO output beams is mapped to its respective mixer input beam by two Gaussian beam telescopes (4 active mirrors). The first Gaussian beam telescope is located inside/at the LO-U. The second Gaussian beam telescope is formed by an active mirror on the upper optics plate level and the corresponding *M1* inside the cryostat. The upGREAT-LFA, with its two polarization arrays, fits two LO chains in the LO compartment by tilting one of the LO beams. The design of 4GREAT LO-D with 4G-3LO and 4G-4LO follows the same approach and uses most of the optical components already installed in the GREAT structure for the LFA-LO, to ensure

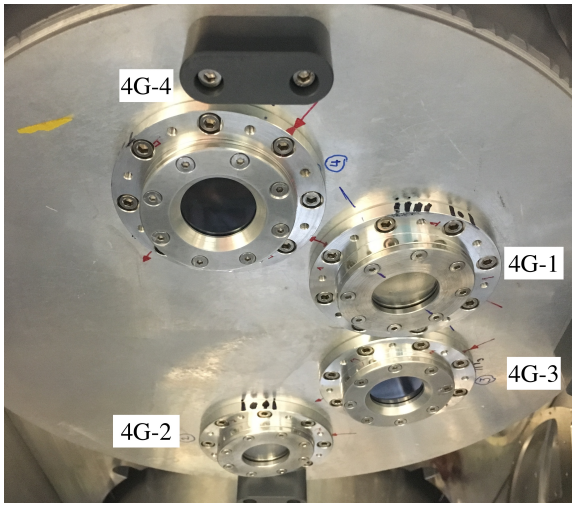

Figure 3.14: Cryostat vacuum windows: all four bands are visible

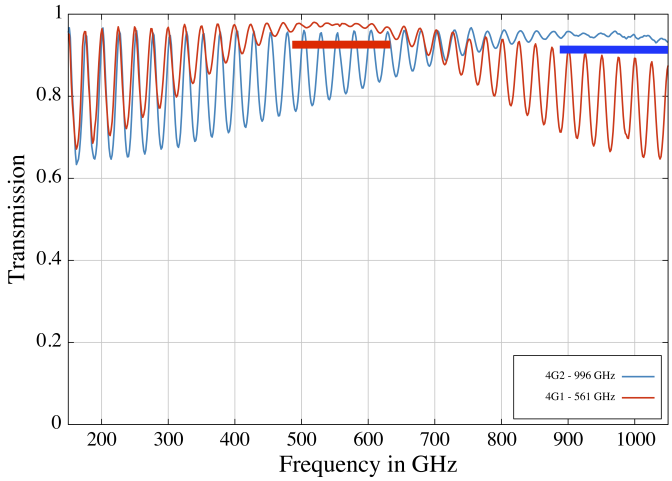

Figure 3.15: FTS transmission for 4G-1 and 4G-2 windows. Solid bars represent the channel frequency coverage

that modularity of GREAT remains intact. This constrains the optics of the 4G-3LO to only three active mirrors and introduces a minor frequency dependence. The LO optics for 4G-4 uses four active mirrors (2 Gaussian beam telescopes).

Each LO beam is shaped by elements which are placed at different positions, under different temperature and pressure conditions and therefore proper interfaces between these areas are required, without affecting the beam. This is realized by vacuum windows.

The unfolded optics plots for all four LO beams can be seen in detail in Appendix F.

Optics in LO-U

LO-U optics is made up of two fully independent optic paths, each of them illuminated by their corresponding chain. The only common element both channels share is the controller for the LO attenuator.

All 4G-1LO optical elements from the LO source horn to the 4G-1 Mixer are described by their

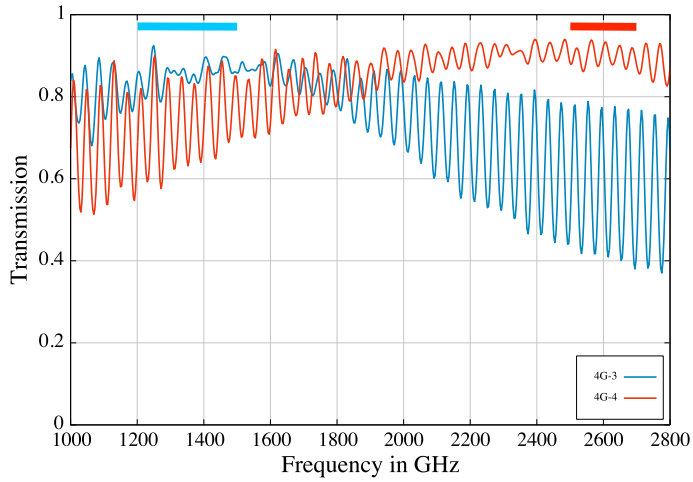

Figure 3.16: Window transmission for 4G-3 (blue) and 4G-4 (red) windows. Solid bars represent the channel frequency coverage.

Table 3.14: LO diagonal horns specifications from VDI. Parameters w_0 and z_0 are calculated from the aperture and horn length for the central frequencies (Goldsmith 1998).

Channel	Model	f [GHz]	Aperture [mm]	R_h [mm]	w_0 [mm]	z_0 [mm]
4G-1LO	WM-380	500-700	2.4	24	0.998	1.404
4G-2LO	WM-250	750-1100	1.6	16	0.657	1.312
4G-3LO	WM-164	1100-1700	1.1	5.9	0.417	1.215
4G-4LO	WM-86	2200-3250	0.56	3.1	0.215	0.588

parameters and listed in table E.8. The elements that are located in the LO-U are those between the Horn-LO1 and the F3-LO1 (included). The alignment of the LO beam can be modified by mechanical adjusters available in two elements: M4-LO1 and F3-LO1. M4-LO1 can be rotated around its axis, and because it is an active mirror, it has the effect of deflecting the beam out of its axis and changing the beam focus. This is in fact a composed effect: a tilt plus a shift of the beam at any position after the mirror. F3-LO1, a flat mirror, can be tilted, tipped and position shifted and with this controls linear displacements and compensates angular deflections. In between M4-LO1 and F4-LO1 a vacuum window is placed (Fig. 3.17). This window is identical to the one used by the 4G-1 channel (see subsection 3.5.1) and it is also provided by QMC.

The design philosophy for the optics of 4G-2LO is pretty similar. Table E.9 lists all the elements and those on LO-U are in between Horn-LO2 and F4-LO2. In the same manner, M4-LO2 and F4-LO2 are adjustable, and the results over the LO beam are similar as for 4G-1LO. As for the vacuum window, it is a copy of the one used in the cryostat for 4G-2.

Optics in LO-D

LO-D hosts also two local oscillator chains (subsection 3.4.2) and their respective optics. Tables E.10 and E.11 list all the elements included in each of the LO beam paths. The elements from Horn-LO3 to W-LO3 are all included in the LO-D. The mirrors M3-LO3/F4-LO2 represent the adjusting points for the

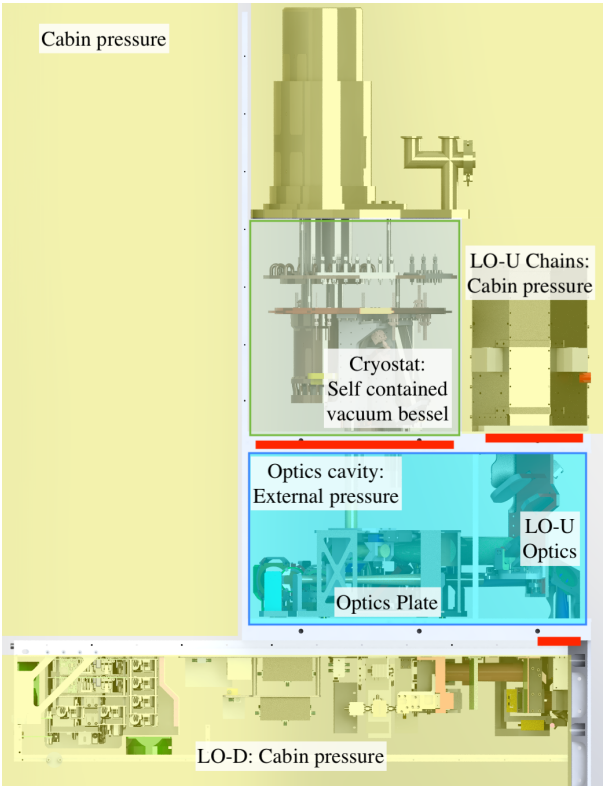

Figure 3.17: GREAT pressure boundaries. Most of the optics are at external pressure. Required pressure interfaces (windows and seals) are highlighted in red

beam alignment. Similarly, 4G-4LO elements contained in LO-D are those from Horn-LO4 to W-LO4 and the LO adjusting beam group is made up of M4-LO4 and F6-LO4.

The fact of having two LO sources, in which one has almost exactly the double of the frequency of the other, made the use of a unique vacuum window for both beams (required between the LO-D and the GREAT structure) not feasible. Either one of the beam is fully optimized and the other resonates, or the antireflection coating is optimized for some other frequency in between the two bands, having some reflection in both bands. In order to overcome this problem a specially designed window holder fits the two vacuum windows (W-LO3 and W-LO4), following the angles of the two beams axes (Fig. 3.18).

LO Coupling

Table 3.15: LO and signal coupling per channel. Method and power percentage are indicted. Grid intrinsic losses are not included.

Channel	Method	Effective wire angles	Signal	LO	Comment
4G-1LO	Wire-grid	9.153°	90.5 %	4.7 %	
4G-2LO	Wire-grid	12.625°	90.6 %	4.6 %	
4G-3LO	Wire-grid	11.241°	92.5 %	3.7 %	
4G-4LO	M-P Int.	45°/45°	100 %	100 %	Table 3.16

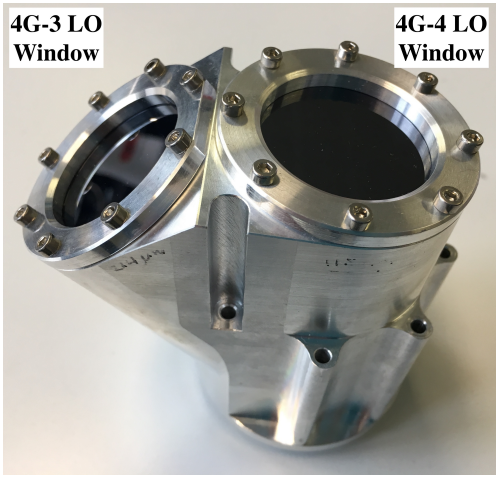

Figure 3.18: LO-D dual vacuum window holder designed at the MPIfR. It is colloquially called *Y-Win*.

The 4G-1LO, 4G-2LO and 4G-3LO signal coupling is performed by wire-grids working as combiners. The free standing grids are made up of gold plated 10 μm wires with 30 μm of pitch and are attached to an ellipsoidal frame. The grids are placed in between the respective M2 mirror and the corresponding channel window, in the upper level of the optics plate (Figure 3.19 a-c). The frame is positioned at 45°, while the angle of the wires controls LO (in reflection) to signal (in transmission) ratio according to their respective polarizations and the mixer polarization (see Table 3.15). This is a simple method which requires good quality grids, but could introduce modulations in the signal due to microphonic effect for big effective diameter wire grids.

$$\lambda_{IF} = \frac{4 \cdot (L_l - L_s)}{2 \cdot M - 1} \tag{3.1}$$

4G-4LO uses a MP interferometer. This unit has been dimensioned such that its short leg has 30 mm (L_s) and the long tunable leg runs from 55.5 to 84.5 mm (L_l) which translates on an IF tunable range from 1.37 to 2.94 GHz, according to the equation 3.1, with $M = 1$. The use of a M-P interferometer as diplexer (Lesurf 1981) allows the coupling of all the available LO power (rather low in the case of 4G-4LO) at the input of the diplexer, along with the signal, in the same polarization of the mixer, in spite of a casted and narrow IF signal band from the mixer and relatively high T_{Rec}, in particular to the edges of the IF band.

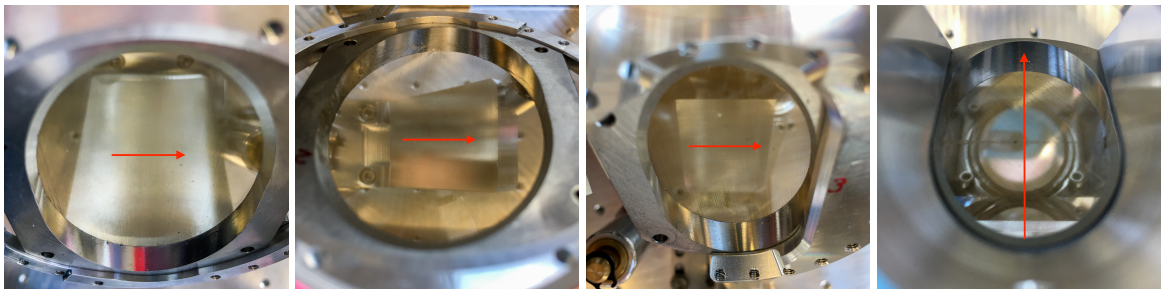

(a) 4G-1 (b) 4G-2 (c) 4G-3 (d) 4G-4 Diplexer

Figure 3.19: LO signal coupling per channel. The red arrow indicates the mixer polarization direction. M2-1, M2-2 and M2-3 are visible and one of the roof top mirrors of the 4G-4 diplexer on panel d)

Table 3.16: Martin Puplett interferometer, used as diplexer, to combine LO and signal in 4G-4: Optical elements specifications

Element	Name	$\measuredangle$ [°]	ϕ [mm]	Comment
Wire grid	WG-DIPL	45	25	
Roof-top mirror	RT-SH	45/45	29.8	Turns pol. short leg
Roof-top mirror	RT-LO	45/45	32.5	Turns pol. adjustable long leg

LO Attenuators

As mixer response to LO signal is not uniform over its RF band, LO power is required to be adjusted by using *optical* attenuators. Three different types of attenuators were designed and built.

* Eccentric rotary grid
* Concentric rotary grid
* Rotary variable pupil

Eccentric grids have been already used by GREAT whereas concentric grids and a rotary variable pupil were used for the first time. The concentric grids attenuators (10 μm wire / 30 μm pitch) are motor driven and are placed in the path of the LO signal and require a terminator for the reflected power. By rotating them, the effective angular difference between the beam polarization, the attenuator wires, the LO coupling grids and the cleaning grids determines the attenuation factor. The control and motor interface has been designed and built by KOSMA, while the grids are built at the MPIfR. The rotary pupil has been conceived as part of this work. It is covered by SiC to absorbed the unwanted portion of the power. The pupil truncates the beam perpendicular to the beam polarization, and varies continuously form 0 to 100% in a 140° range (Fig. 3.20)

Figure 3.20: 4G-1 LO Attenuator: rotary variable pupil, a.k.a. *Ying-Yang Wheel*

3.5.3 Optics Plate

The optics plate contains most of the *warm optics* components of the four channels. It is placed just below the receiver cryostat inside the optics compartment of the GREAT structure (Fig. 3.2). Optical elements

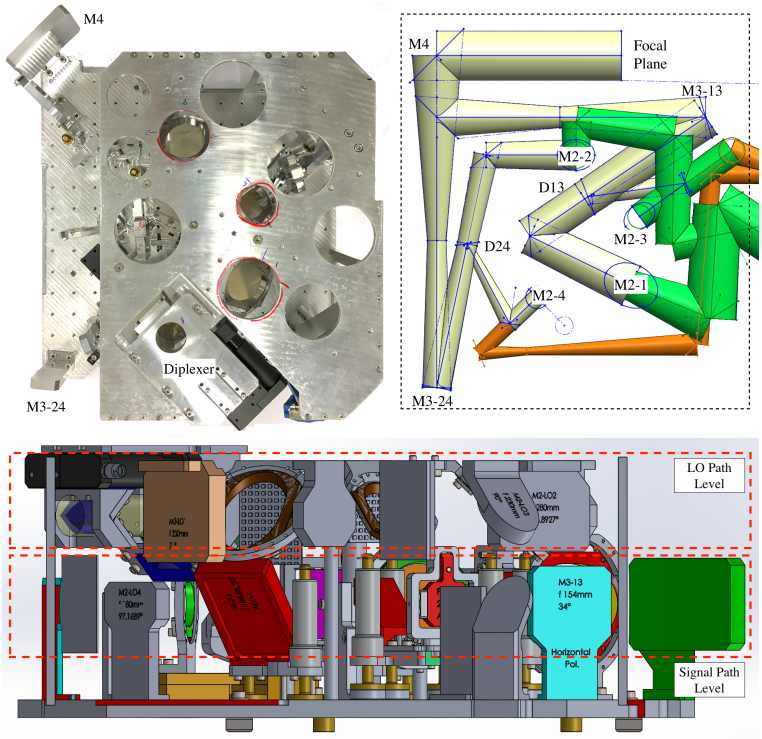

Figure 3.21: Optics Plate. Top: optics plate and signal (gold) / LO beams (green and orange). Bottom: CAD side view of the optics plate: Red dashed lines frame the two optical planes. Some non critical elements have been omitted in the figure for better visualization.

are positioned on two levels spaced by 50 mm, in between the upper and lower module plates. The lower level consists of signal beam related elements for all channels plus some components of 4G-3LO and 4G-4LO, while the upper one is used entirely by LO signal elements and the 4G-4 diplexer (Fig. 3.21). All the elements of the signal beam path on the optics plate are properly described and designated in tables E.4, E.5, E.6 and E.7, while similar elements for the LO signal beams are presented in tables E.8, E.9, E.10 and E.11.

The signal beam alignment and adjustment groups (M2/F2) for each channel are hosted on the optics plate. They provide 4 degrees of freedom, and are driven by screws and locked by counter or side locking screws. The M2-4 element is attached to the M-P diplexer. To adjust the mirror position, the whole group needs to be displaced.

As the adjustment or *alignment* process requires the removal and reinstallation of the plate, it is referenced to an end-stop corner inside the optical compartment.

The LO coupling grids are mounted on holders and secured by clips. The holders are attached to the upper cover of the optics plate, allowing $\pm 15^{\circ}$ of physical rotation of the grids on their planes, and with this, varying the percentage of signal and LO coupling (Goldsmith 1998). See table 3.15.

Two key components on the optics plate are the dichroic filters D-13 and D-24. Being low pass filters, they do not change the direction of the beam for their respective pass frequency band (4G-1 and 4G-2), but act as a flat mirror for the beam in reflection (4G-3 and 4G-4). The transmission and reflection of these filters are presented in figure 3.22. On average the transmission over the band for 4G-1 is 97.89% and for 4G-2 is 95.86%, while the reflection is 93.33% for 4G-3 and 91.5% for 4G-4.

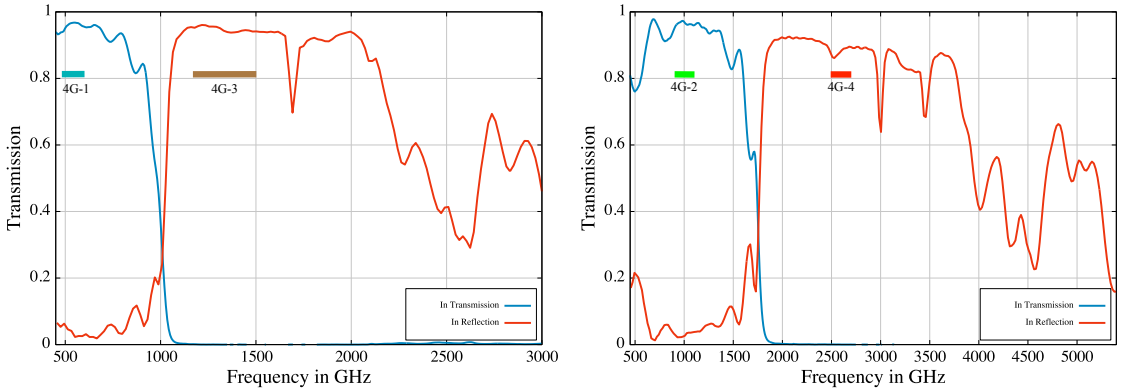

Figure 3.22: Optics Plate Dichroic filters transmission and reflection curves as provided by QMC. Left: D-13. Right: D-24. Color bars on each plot signal the channel frequency coverage.

3.6 Cryostat and Cooling

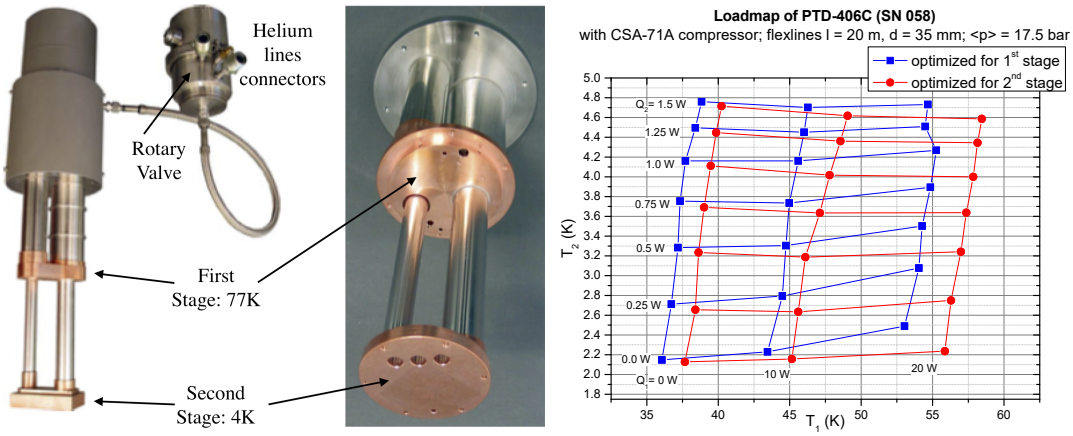

Figure 3.23: Two views of the PTD406 pulse tube and its thermal load map

Following the same cooling scheme employed in the upGREAT LFA and HFA (Risacher et al. 2016b), 4G uses a two stage pulse tube (PT) closed-cycle cooler (Radebaugh 2000). The PT is a PTD-406C model from Transmit. The cooler is made up of a rotary valve and a main body that provides the two cooling stages (Fig 3.23 left panel). The rotation frequency of the rotary valve is controlled by an external mains variable frequency drive (VFD) unit. The mains frequency can be adjusted to make changes on the performance and operation point of the PT. The nominal electrical frequency goes between 28 and 32 Hz that is reflected as a pulse tube rotational frequency of 1.12 (28/25) and 1.28 (32/25) Hz respectively. The cooler has been operated with different He compressors, all with similar performance. When 4GREAT is in the laboratory, it uses either a Sumitomo F50 (7 kVA) water cooled or a CNA-31C (6.5 kVA) air cooled compressor, whereas while in operation in SOFIA, it employs a Cryomech CP2870 (7.5 kVA) water cooled unit. The change of the compressor is accounted by adjusting the VFD frequency. The cooler load map is shown in the Figure 3.23 and also available in full size in the appendix H.

The cryostat has been manufactured by Cryovac according to the GREAT consortium specifications and is a copy of the upGREAT arrays cryostats. It is made up of three sub-containers, one inside the

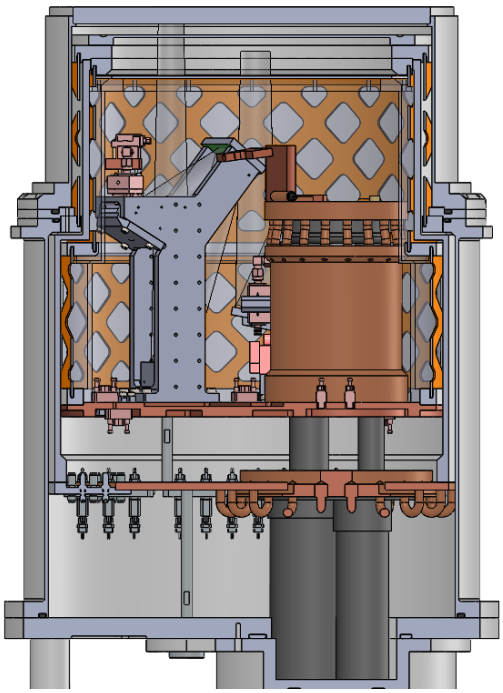

Figure 3.24: 4GREAT cryostat side cut out. 4K and 77K shields and the outer shell are visible. The cold tower of 4G-3 can also be seen.

other. The 4 K shield is composed by an oxygen-free copper circular plate, called the 4 K plate, and a polished aluminum cylinder. The detectors and optics cold towers are attached to the 4 K plate. The 4 K shield is all contained into a 77 K shield, also made up of a copper plate (77 K plate) and a polished aluminum cylinder. The 77 K shield is finally contained inside the cylindrical vacuum vessel which is assembled from three basic parts: a circular plate (cover), a cylinder and a cylindrical cover, where the vacuum windows are attached (Figs. 3.24 and 3.27). The 4 K and 77 K shields are thermally connected to the second and first stage of the pulse tube respectively. To keep the cryo-shields and vacuum vessel thermally isolated among them, there are two light weight cylindrical separators made up of plastic reinforced fiber glass or GFK (Glasfaserverstärkter Kunststoff). These separators also serve as structural support and mounting references. Because of the general size constraints of GREAT and the structure allowed envelope (Heyminck et al. 2012) the whole pulse tube sticks into the cryostat. This makes that the PT second stage cold plate is displaced into the volume enclosed by the 4 K shield, reserved for the detectors and cold optics. The thermal link between the cold plate and the 4 K plate is done through a copper cylinder and copper braids, while the 77 K shield is linked to the pulse tube 1st stage using copper braids only.

3.7 Intermediate Frequency Processor

The intermediate frequency processor connects the IF output from each of the channels of 4G to their respective backend processor (Figure 3.4). Its function is to filter and adjust the power level of the signal and compensate the frequency response of the mixer IF and amplifiers (LNA) for the spectrometer. It was entirely designed and built by the MPIfR.

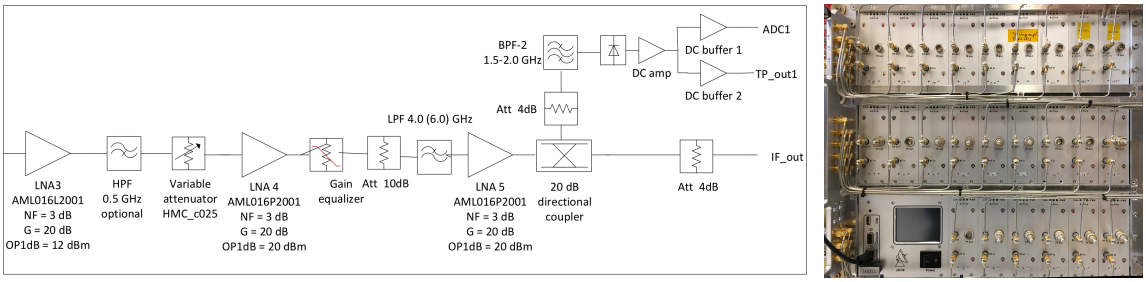

Figure 3.25: IF Processor. Left: General schematics. Right: Crate with 24 channels and controller modules.

The IF processor is made up of 24 independent channels or modules, all controlled by a single interface module which can be remotely commanded (Fig. 3.25 left). 22 modules are identical and configured to cover the base band from 0-4 GHz (Fig. 3.25). The other two have been fit with different filters and amplifiers to cover the 4-8 GHz range required for the SIS IF bands of 4G. The same IF processor is used by 4G and the upGREAT LFA and HFA

All the IF modules are internally equipped with a total power detector which integrates over their entire band. The signal total power is used by the internal auto leveling feature and is also particularly useful during channel characterization and optimization laboratory tests by using the mixer conversion curves.

Table 3.17: Specifications for the IF processor modules used by 4GREAT. The SIS and HEB IF modules differ only by the input filter and the internal equalizer.

	4G-1	4G-2	4G-3	4G-4	Remarks
Input range [GHz]	4-8	4-8	0.1-4	0.1-4	
Noise temp [K]	300-10000	300-10000	300-10000	300-10000	0-30 dB Int. Attn.
Gain [dB]	57	57	57	57	
Variable Attn. [dB]	±15	±15	±15	±15	Manual / Auto.
Input Power [dBm]	-20 ±10	-20 ±10	-20 ±10	-20 ±10	
Output Power [dBm]	+4	+4	+4	+4	

3.8 Backend: Fast Fourier Transformer Spectrometer

The Fast Fourier Transform spectrometer (FFTS) technology has been successfully available since 2006 (Klein et al. 2006) as a development tested and installed at the APEX Telescope, as many other subsystems (Durán 2018). Its first multi band generation, the AFFTS processed 1.5 GHz bandwidth with 8k spectral channels boards on an interface crate.

Just like the IF processor, the FFTS is made up of a main controller and several independent channels. A backend computer interfaces the controller using custom control software and a LabView custom frontend application is used for real time data visualization and diagnostics.

Currently the FFTS system used by GREAT is equipped with 11 dual input 0-4 GHz 64 k (65536) spectral-channels capable boards, named dFFTS4G (Klein 2017) and 3 single input 4-8 GHz 64 k spectral-channels capable (resolution of 61 kHz) boards known as FFTS4G. Under this configuration, it offers 22 independent channels suited for 0-4 GHz and three for the band from 4-8 GHz, as these make

use of the 2nd Nyquist band. DSB observations produce a natural fold-back in the spectrum and the FFTS takes this into account and delivers data in the right sequence. 4G HEB channels (4G-3, 4G-4) are connected to a single dFTTS4G dual input card, while the SIS channels, 4G-1 and 4G-2, are individually connected to independent FFTS4G boards. Table 3.18 summarizes the configuration, while the whole FFTS system can be seen in figure 3.26.

When the FFTS operates its extended configuration of 21 simultaneous channels (for upGREAT LFA and HFA) the resolution is reduced down to 16k (16384) spectral-channels (244 kHz) as this is largely enough for scientific purposes in terms of *velocity* resolution (0.036 km/s at 2 THz and 0.015 km/s at 4.7 THz) at that regime.

Table 3.18: Specifications for the FFTS processor modules used by 4G.

	4G-1	4G-2	4G-3	4G-4	Remark
Model / Version	FFTS4G	FFTS4G	dFFTS4G*	dFFTS4G*	(*) Dual input card
Bandwidth [GHz]	4 - 8**	4 - 8**	0 - 4	0 - 4	(**) 2nd Nyquist band
Max. resolution [Ch]	64 k	64 k	64 k	64 k	Spectral-channels
Module ID	25	26	21	22	Internal sequence

Figure 3.26: GREAT FFT Spectrometer, with 27 independent backend channels. In the image, the 12 dual input dFFT4GS and and three single input FFTS4G boards are visible. Card ID is assigned from left to right, starting from the bottom sub-crate.

3.9 Design Performance Estimations

The receiver temperature is the classical figure of merit for receivers in this regime and therefore having an estimation beforehand is fundamental for the design process. Another key number is the thermal heat load, that determines the operational temperature of the detectors. This is particularly critical for the 4G-1 mixer (section 3.3.1), given its physical temperature performance dependence. The optics performance, estimated by distortion and coupling, allows the early detection and rectification of potential problems. Finally an estimation of the telescope illumination and beam propagation is important, as some previously existing optical elements (of GREAT and the SOFIA telescope) limit the (lower) frequency of 4GREAT

and its optical design.

3.9.1 Receiver Temperature

Table 3.19: Receiver temperature for all channels. 4G-4 has extra optical elements due to the diplexer.

	4G-1	4G-2	4G-3	4G-4	Remarks
$T_{\text{Mixer-DSB}}$ [K]	50	175	550	850	See Tables on section 3.3.1
T_{Optics} [K]	100.87	93.6	135.49	140	See appendix G
$T_{\text{Rec-DSB}}$ [K]	130	298	963	1500	Calculated using equation C.5

The receiver temperature depends directly on the physical temperature of the optics and the inherent noise temperature of the mixer (T_{Mixer}) which is scaled by the *gain* (losses) of the optics. The rest of the contributions coming from the isolator, LNA and Warm amplifier are scaled by their gains too. It is therefore the optics and mixer performance (plus the first LNA) that play a key role.

The main contribution of the optics comes from components at *room temperature*: those on the optics plate plus the dichroic filter D-HFA4G. The temperature contribution of each element (T_e) is estimated by using equation C.3 which takes into account the gain/transmission/reflectivity. Tables G.1, G.2, G.3 provide details for 4G-1. 4G-2 and 4G-3 while 4G-4 (Table G.4) considers the case when its diplexer is tuned. IR filter temperatures considered here correspond to an average over the profile (Appendix D).

The estimated receiver temperature have been calculated using the equation C.5 and the characteristic noise temperatures of the individual components of each channel, and are listed on table 3.19.

3.9.2 Heat Load

Table 3.20: Estimated heat load on the cooler stages and operation temperature points

Heat source/link	1^{st} stage [mW]	2^{nd} stage [mW]	Remarks
Wires	191	4	Temp. & Mixer bias and temp.
Coaxial lines	378	11	IF lines
Cryogenic LNAs	–	34	All channels
Thermal bridge: GFK	448	28	
Thermal bridge: GAS	51	10	Vacuum at $\times 10^{-5}$ HPa
IR filter (B.B. radiation)	759	10	See appendix D
Radiation from 300 K	16021	2	
Radiation from 77 K shield	–	8	
Total	17848	107	
Operation temperature [K]	55	2.45	See appendix H

During the design phase of 4G, a heat load simulation was performed in order to estimate the cryo-cooler operation points. Several factors have been identified and taken into account as main contributors of heat, either acting as active sources or by conduction/radiation.

While active element contributions of heat (q_{act}) can be directly estimated, conductive contributions (q_{cond}) are calculated using the equation 3.2, where l and A correspond to the length and section of the conductor and ΔT the temperature difference. The thermal conductivity (k) is a property of the material and depends also on the temperature (Fig. D.4). For this estimate, the average over the temperature difference range has been considered.

The effect of an infrared filter (subsection 3.5.1), its thermal profile and back radiation contribution requires a careful treatment (Lamb 1992; Benford et al. 2003), and is described in more detail in the appendix D. For the case of the estimations in this work, the filter effective average temperature is taken into account, and then modeled as a uniform black body using the Stefan Boltzmann law (Eq. 3.3), just like the rest of the contributions between stages (Behrens et al. 1997). The value of the emissivity for each material (ϵ_x) has been taken from Ekin (2006)

$$q_{cond} = \frac{k}{l} \cdot A \cdot \Delta T \tag{3.2}$$

$$q_{rad} = 5.67 \cdot 10^{-8} \frac{A_1 \cdot \left(T_1^4 - T_2^4\right)}{\frac{1}{\epsilon_1} + \frac{A_1}{A_2} \cdot \left(\frac{1}{\epsilon_2} - 1\right)} \tag{3.3}$$

The Table 3.20 lists and brakes down all heat contributions from the most important sources. After a careful optimization and using the total estimated heat per stage and the load map of the pulse tube (Appendix H), super-low operational temperatures are reached.

3.9.3 Optics Distortions and Gaussian Coupling

There are two useful parameters to estimate the distortion of an active optical element (Goldsmith 1998). The beam distortion (U), as defined by equation 3.4, is calculated taking into account the incidence angle of the beam (θ_i), the beam width on the active element (w_m) and the focal length of the mirror (f). This sets an implicit dependance on the frequency through w_m, however the element focal lengths have been selected to be large enough to make variations negligible over U. The second parameter used defines the fraction of power in the reflected beam that is in the fundamental Gaussian beam mode (K_f). This can be directly calculated from U. A criterion of $K_f \geq 0.99$, together with the constraint for the effective diameter (D) of the mirrors being a minimum of $4w$ ($5w$ for our case), conditions the beam incidence angle to be $\theta_i \leq 45^\circ$ for $f/\mathrm{D} \geq 1.0$ and $\theta_i \leq 30^\circ$ for $f/\mathrm{D} \geq 0.5$.

$$U = \frac{w_m \cdot \tan\theta_i}{f \cdot 2\sqrt{2}} \tag{3.4}$$

$$K_f = 1 - U^2 = 1 - \frac{w_m^2 \cdot \tan^2\theta_i}{8 \cdot f^2} \tag{3.5}$$

Table 3.21 presents the values for the active elements on the signal beam path of 4G-1. The parameters have been calculated for the center of the frequency band, as the optics targets that value. Tables E.1, E.2 and E.3 in appendix E show the details for 4G-2, 4G-3 and 4G-4. The calculated distortion parameters do not take into account the surface quality of the active element, as defined by Ruze (1966).

Table 3.21: 4G-1 Active mirrors distortion and Gaussian main mode coupling.

Mirror	f [mm]	U	K_f [%]	f/D
M0-1	47.65	0.0302	99.9091	1.3539
M1-1	250.0	0.002	99.9996	4.796
M2-1	188.85	0.0158	99.9752	4.488
M3-1	154.0	0.0056	99.9969	3.857
M4-1	195.0	0.0176	99.969	4.017

Performance of M4-G over all Four Bands

M4-G is a common optics ellipsoidal mirror for all four channels of 4G (Fig. 3.21). For this reason, its has to be able to act as a fixed focal mirror for all frequencies. Table 3.22 shows the different geometric values calculated for M4 when optimized for every band, however M4-G was built based on the geometry determined for 4G-1, requiring the largest aperture for this low-frequency channel. The different curves can be compared by their punctual radius of curvature R_{curv} at the contact point of the beam axis and the percentage of the effective area of the mirror used by the different bands. The net effect is negligible. A sketch of all superposed pattern ellipsoids listed on table 3.22 can be seen in figure B.1 in the appendix B.

Table 3.22: M4-G geometrical parameters as defined in appendix B.1. Numbers correspond to the optimum values for each band, and how they are represented on the effective curvature radius of the beam over the mirror.

Parameter	4G-1	4G-2	4G-3	4G-4
λ [mm]	0.535	0.301	0.222	0.115
w_{01} [mm]	3.702	3.707	3.709	3.709
w_{02} [mm]	8.977	5.309	3.716	3.919
$5w_m$ [mm]	48.54	31.25	26.25	20.91
R_1 [mm]	228.12	300.35	388.96	914.45
R_2 [mm]	1340.32	554.68	390.43	247.64
e	0.8668	0.7377	0.7071	0.8152
a [mm]	784.220	427.517	389.697	581.042
b [mm]	390.997	288.616	275.557	336.490
A_0 [mm]	1359.592	630.780	551.116	947.385
Mirror surface usage [%]	100	41.44	29.25	18.56
Punctual R_{curv}	551.3807	551.1000	551.1082	551.1615
R_{curv} variation [%]	-	0.051	0.049	0.039

3.9.4 Illumination and Propagation

Blockage and Spillover

The 4G-1 frequency range, and in particular its lowest target frequency, impose the limits for apertures and set the minimum admissible effective diameters for optical elements. The focal plane optical waist spans from w_{FP-low} = 10.16 mm at 492 GHz to $w_{FP-high}$ = 7.87 mm for 635 GHz.

At the focal plane, the $5w_{FP-low}$ goes up to the 50.81 mm. As the optics of 4G-1 (the same is valid for every channel and their respective optical elements) considers the biggest required diameter for the lowest admissible frequency, its only the elements in the optical axis towards the main dish of SOFIA that play a role on the blockage.

Table 3.23: Elements on the optical axis, from the GREAT focal plane to the main reflector. The beam considered here corresponds to the 4G-1 beam at its lowest frequency limit.

Element	Beam ($5w$) [mm]	Position (z) [mm]	Aperture (ϕ) [mm]	Remark
Beam measurement wheel	52.625	143.5	50	$4.75w$
Optics compartment wall	53.05	160	60	
GREAT SI flange	62.16	375	130	
GREAT derotator	68.72	484.5	75	
SOFIA tertiary mirror	525.81	5480.2	310	$2.95w$ (98.7% Power ref.)
SOFIA Sub-reflector	693.51	7242.5	350	With edge taper 14 dB

Table 3.23 shows in great details all the elements on the way to the sub-reflector. Some of these elements belong to GREAT while others are part of the SOFIA telescope optics.

The tertiary optics mirror is the element located at 5480.2 mm from the focal plane. it has an effective diameter of 310 mm and is here where the major spillover occurs. As the SOFIA telescope is a Nasmyth focus configuration and the tertiary mirror deflects the beam in 90 degrees, part of the $5w$ beam spills out (1.3%) and does not reach the main reflector. In fact all the channels *see* the telescope compartment cabin walls and this adds to the receiver noise temperature.

Horn Waist Shifting Effect over the Focal Plane

The position (z_0) of the waist (w_0) inside the horns of the mixers and LO sources in 4G, depend on the frequency, and thus has an effect on shifting and scaling the effective beam width (equation A.4) projected over every optical element. This is true as a general rule.

The 4G optics for each channel has been designed targeting the center frequency of the mixer band, which in practice means that geometric distances between elements are set for such. Most of the active mirrors are coupled to form Gaussian beam telescopes (Appendix A.3), which make the system frequency independent, with the sole exception of the first mirror in front of every horn, corresponding to paraboloidal mirrors (M0-n, M0-LOn, n = 1-4). The shift of the waist over this mirror yields a change on the projected beam width w_m. This value then works as input waist of the Gaussian beam telescope chains formed by the other active mirrors and propagated to the focal plane. In other words the net effect is seen as a change of the size of the beam width at the focal plane and therefore the edge taper. This has impact at the low frequency limit in each band in terms of effective apertures and blockage.

3.10 Summary Table

4GREAT integrates four different science frequency driven detectors in a unique vessel, to be operated in parallel with the upGREAT HFA array. This increases the science throughput of GREAT as more bands are observed simultaneously and data from one or more bands can get complemented to constrain

astrophysical parameters and conditions, faster and more efficiently. Table 3.24 offers a summary of the key components and submodules of 4GREAT and their specifications in one glimpse.

Table 3.24: 4G Goal specifications and key components summary table.

	4G-1	4G-2	4G-3	4G-4
RF [GHz]	492-630	892-1100	1200-1500	2490-2700
IF [GHz]	4-8	4-8	0.2-2.5	0.2-4
Mixer type	SIS (DSB)	SIS (DSB)	HEB (DSB)	HEB (DSB)
LNA	LNF-LNC4-8C	LNF-LNC4-8C	CITLF4	CITLF4
LO [μW]	>200	>150	>30	>3.5
LO Coupling	Wire-grid	Wire-grid	Wire-grid	Diplexer
Optics	Plate/Tower/LOU	Plate/Tower/LOU	Plate/Tower/LOD	Plate/Tower/LOD
Taper [dB]	11.86-16.54	12.25-16.09	13.29-14.78	14.35-13.68
T_{Rec} DSB [K]	126	296	1005	1495
IF Processor	IFX 4-8 GHz	IFX 4-8 GHz	IFX 0-4 GHz	IFX 0-4 GHz
Backend	FFTS4G	FFTS4G	dFFTS4G (×1ch)	dFFTS4G (×1ch)

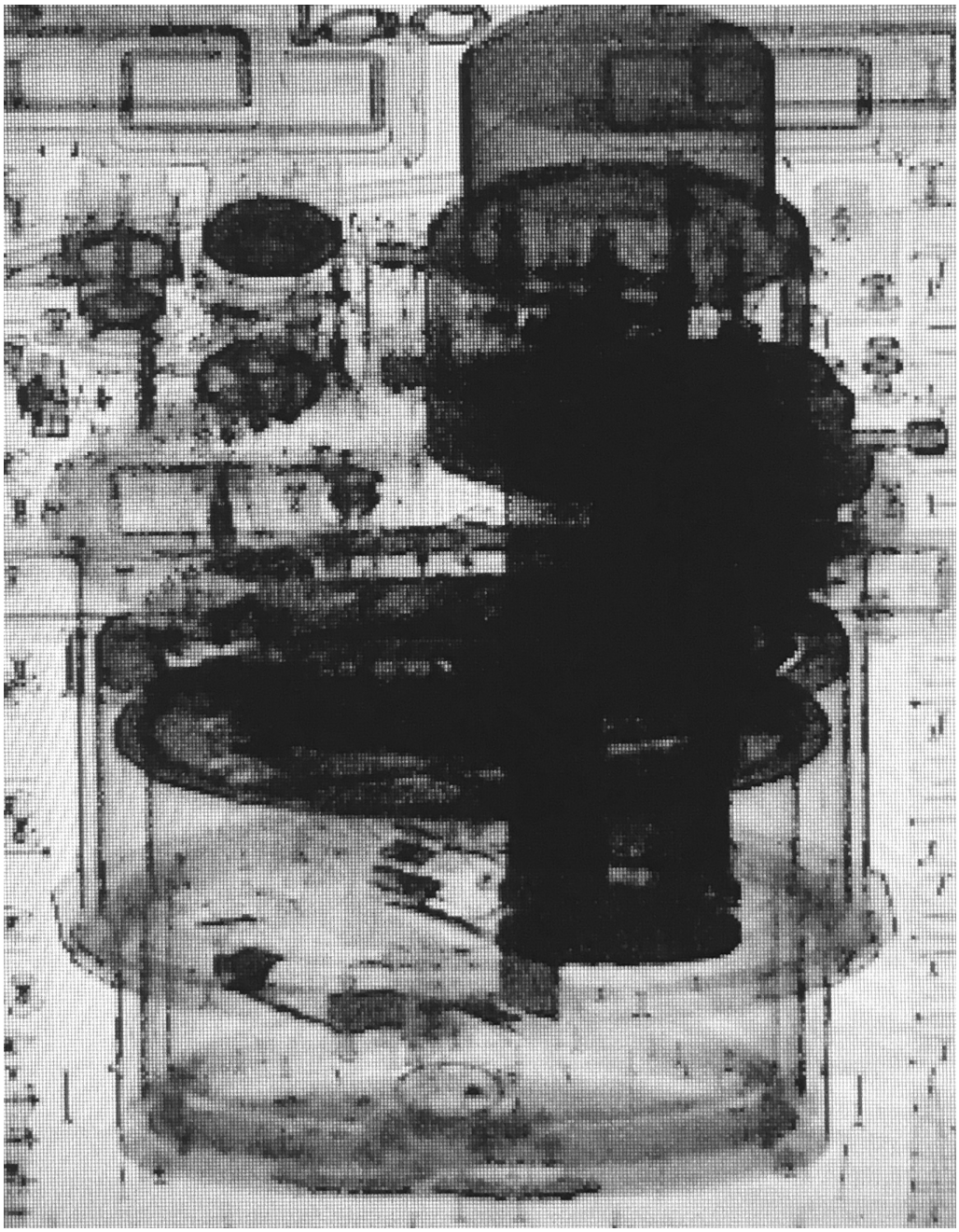

Figure 3.27: X-Ray image of the 4G cryostat in its transport crate. The pulse tube appears as a very dark cylinder. The 4 K and 77 K plates and cylindrical shields can be distinguished. The image has been taken at the Bonn customs office during the security inspection prior to the shipment to Palmdale, California, in April 2017.

CHAPTER 4

4GREAT Tune-up, Characterization and Commissioning

Characterization and commissioning are fundamental processes for any instrument construction. They directly allow to understand the capabilities and limitations, get figures of merit, compare among similar systems and finally help to improve and fine tune the receiver as a whole. 4GREAT has undergone these processes in a sequential way. After finishing the assembly of 4G, an initial tune up and alignment was performed at the MPIfR GREAT-laboratory in Bonn, Germany, followed by tests and re-tune, making it ready for its shipment to the NASA Armstrong Flight Research Center (AFRC) in California, USA. Once there, a realignment using the flight configuration was performed. The installation of 4GREAT in SOFIA and its first light and scientific commissioning of channels 1, 2 and 4 took place in July 2017. The 4G-3 channel employs the L1 single pixel mixer. L1, being a heavily demanded channel, was not ready to be de-commissioned prior to demonstration of the functionality of 4GREAT. 4G-3 is expected to be commissioned during the 2018 SOFIA southern hemisphere deployment.

4.1 Tune-up and Alignment

4.1.1 Optimum Operation Points

Using a heterodyne receiver for scientific purposes on a platform like the SOFIA telescope requires that the instrument is set and operated at its optimum configuration. Although optimizing a receiver requires manipulating many variables, there are a few parameters that have the most impact.

The *bias tables* are populated with the optimum values for mixer bias voltages (V_{bias}) which vary for every admissible frequency of the LO or wanted line-of-interest. Populating the bias tables requires operational readiness of the complete system and at least two parameters are to be optimized: V_{bias} and LO power. In addition, SIS mixers require suppression of the Josephson peak by applying a magnetic field through current ($I_{B-Field}$). This optimization is performed using the mixer conversion (total power) and the IV curves.

4GREAT needs 4 independent bias tables; one per channel. Every 4G channel covers a relatively wide frequency band and therefore populating these tables with sufficient granularity would require a long and demanding use of the LO chains, all in view of their (known) limited life span. Instead, the optimization and fine tuning of every 4G channel is performed on the spot, taking reference values prior to each flight series, focusing on their frequencies requested by the to-be-supported science projects and based on the GREAT line catalog (Table J.1). The LO power, a key player on the bias point selection, varies with the

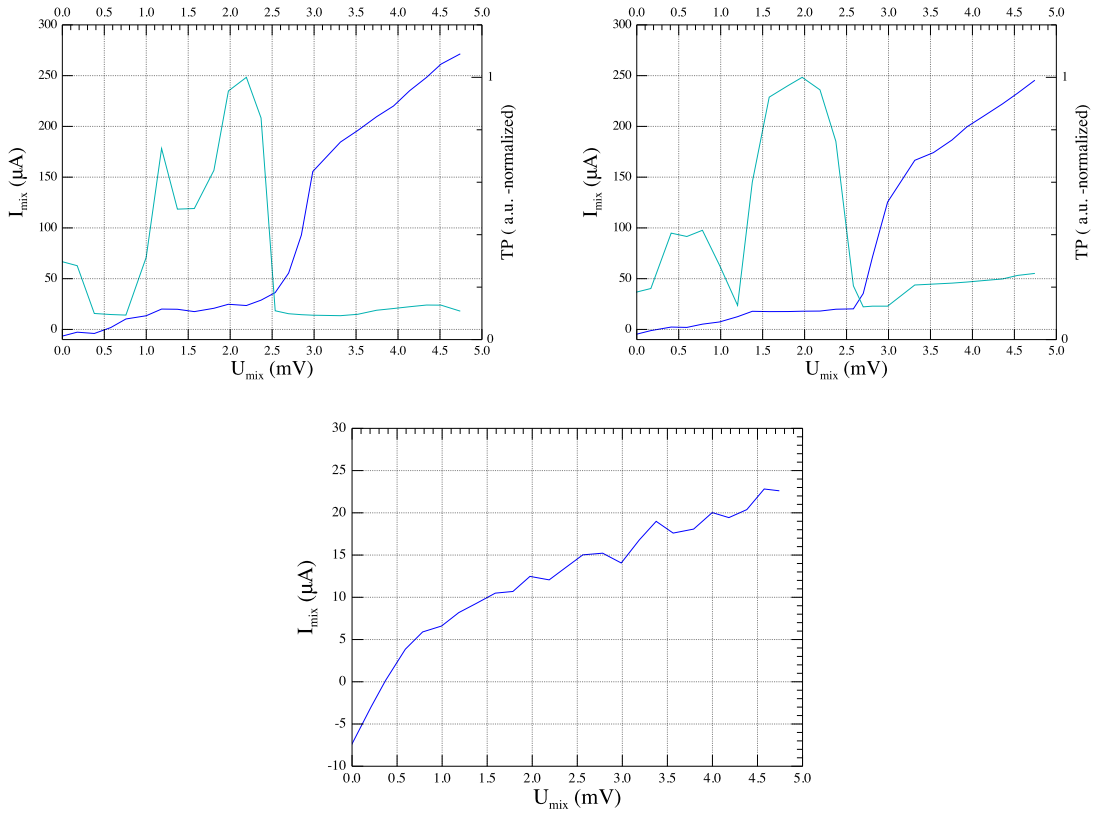

Figure 4.1: Top: I-V and total power mixer curves for SIS. Left: 4G-1 with 15 mA of $I_{B-Field}$ and LO at 520 GHz. Right: 4G-2 curves with 10 mA and LO at 920 GHz. Down: 4G-4 HEB I-V curve pumped at 2515 GHz. V_{mix} and I_{mix} correspond to V_{bias} and I_{bias} respectively.

flight altitude and therefore the mixer bias optimum point. LO power altitude dependence is due to the changes of the pressure and absorption by the residual atmosphere in the aircraft cabin and in the optics compartment, which is at external pressure.

Plotting and analyzing the shape of I-V curves is a powerful tool as it is not only used to get reference values for V_{bias} and the LO power (adjusting the grid attenuators), but allows a quick check of the detectors performance and health.

4.1.2 LO Alignment

Alignment and coupling optimization of the local oscillator signal to each detector is performed by inspecting the I-V curves for each mixer while manipulating specific adjustment elements with the LO attenuators set to maximum transmission. The adjustment elements correspond to groups of mirrors which are mounted in every LO module independently and provide 4 degrees of freedom: tip, tilt and shift on the vertical and horizontal directions. Tables E.8, E.9, E.10 and E.11 indicate them out.

The more LO signal is coupled, the more *pumped* looks the I-V curve. The aspect of a pumped I-V curve is rather different between SIS and HEB. While more LO power implies a higher current mixer I_{bias} at a fixed V_{bias} for the 4G-1 and 4G-2 SIS detectors, 4G-3 and 4G-4 HEB mixers behave the contrary.

LO coupling grid angle plays a key role on the alignment process, and angles determining the coupling of LO versus signal (see Table 3.15) are only changed for diagnostics in case LO signal being too weak.

4.1.3 Individual Channel Alignment

Signal alignment is a very slow iterative process. It makes use of a series of hardware and software tools especially developed or customized for GREAT. Among them, the compact beam measurement wheel (or *Spoked Wheel*) is one of the most remarkable as it remains permanently installed (U. U. Graf 2016). An external 2-axes beam measurement (X-Y) scanner is also an important laboratory tool. A final manual illumination verification once GREAT is in place in SOFIA aircraft is a standard procedure. The alignment process can be described by the following steps:

1. Alignment to the focal plane
2. External alignment using X-Y Scanner
3. Beam propagation (by software) to the sub-reflector
4. Installation of GREAT at SOFIA
5. Verification of the beam position at the sub-reflector

Steps one to three are repeated iteratively according to the results and making adjustments on the alignment optics groups based on the results of the ABCD matrix method (Goldsmith 1998) analysis. The final step is used to validate pointing offsets and the impact of the installation on the alignment, maximize the coupling to the center of the subreflector and check the co-alignment between the channels.

Alignment to the Focal Plane

The alignment to the focal plane is performed by using the internal spoked wheel, together with the internal chopper wheel, while the receiver signal path looks into the cold load of the calibration unit. By rotating the spoked wheel, each spoke casts a shadow on the signal path while a total power profile is recorded. After fitting the data (Fig. 4.2) our customized software calculates the position and angle of the beam axis at the focal plane. The plate to sky ratio at the focal plane, including the *K-mirror* additional path, is 1/51421 [mm/mm] (See section 2.3). This means that a lateral parallel displacement of 1 mm on the axis projects an offset on the sky of 4.055".

External Alignment

The external alignment uses the internal chopper wheel and the external X-Y scanner as main tools. This scanner consists of a large piece of Eccosorb absorber at room temperature mounted on a vertical/horizontal motorized holder. The Eccosorb plate acts a blackbody and is big enough to cover the entire beam using $5w$ criterion, even towards the limits of the axes of the scanner. The center of the plate mounts a perforated scattering cone with optics pointing towards a bucket containing a piece of absorber damped in liquid nitrogen, also mounted on the motorized holder. By sweeping vertically and horizontally and capturing total power counts from each channel at 20 different X-Y coordinates, the beam position and intensity map can be constructed. Once the alignment has succeeded, a high resolution map is taken. Beam maps are of particular use when checking the geometry of the beam. Beam distortions, like asymmetric beams or coma/sidelobes can be easily seen (and corrected) before

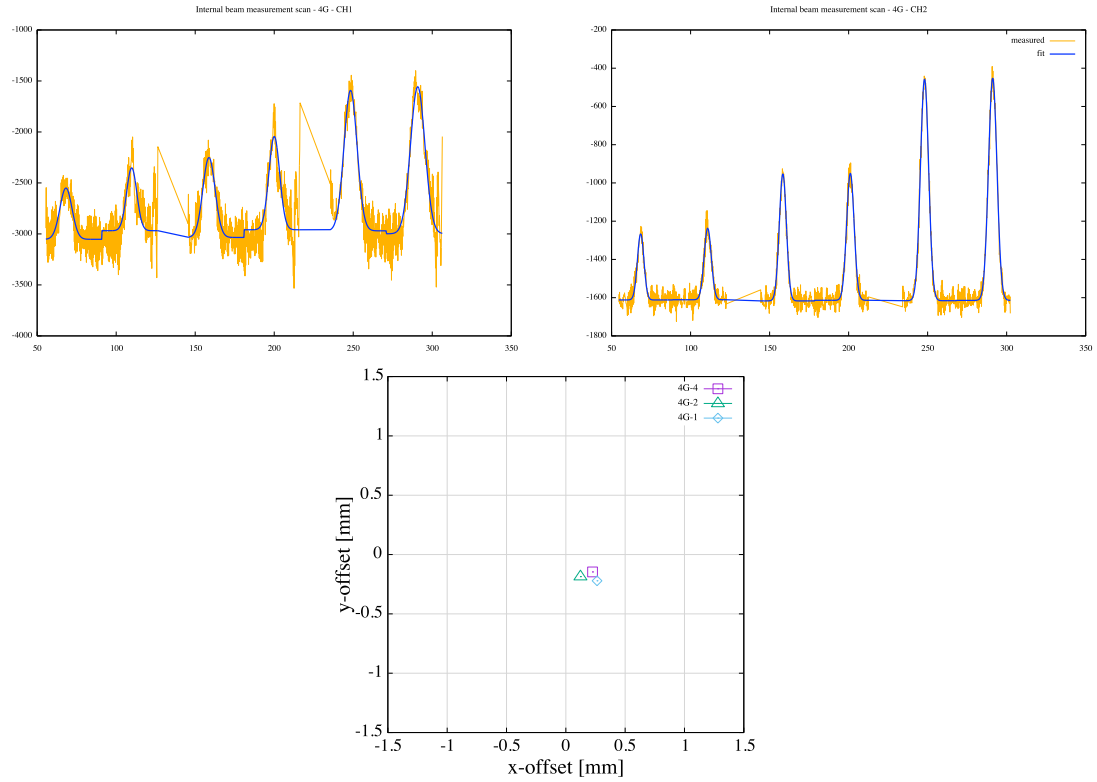

Figure 4.2: Top: spoked wheel beam profile measurements for 4G-1 and 4G-2. The horizontal axis represents angles while vertical axis is in arbitrary units. In blue, the data fit. Bottom: position of the center of the beams at the focal plane. An offset of 1 mm corresponds to 4" on sky.

installing the receiver on board SOFIA. Figure 4.3 shows the beam maps for three channels of 4G during the alignment phase in the laboratory at the AFRC in California, USA. The 4G-4 beam looks distorted due to an optical imperfection on the diplexer. This issue was later fixed.

Propagation to the Sub-reflector

With the information of the beam position in the focal plane and the external alignment, and using customized scripts, the position of the center of the beams projected on the secondary mirror of SOFIA can be calculated. Figure 4.4 shows an actual plot after an alignment run. This information is also used for channel co-alignment verification, which is key for astronomical sources, in particular for those making use of the simultaneous scientific capabilities of the 4G channels, either among them or in combination with the HFA array.

Alignment Verification

The final alignment verification is a procedure that can only be performed with the instrument mounted in the aircraft by directly *paddling* over the telescope sub-reflector. In this procedure portions of the secondary mirror of the telescope at predefined positions are covered with a small rectangular (8×25 cm) paddle of Eccosorb damped in LN_2 (77 K). Variations in the total power level for the selected channel are then correlated to the positions of the paddle and an estimation of the beam can be constructed (Fig. 4.5).

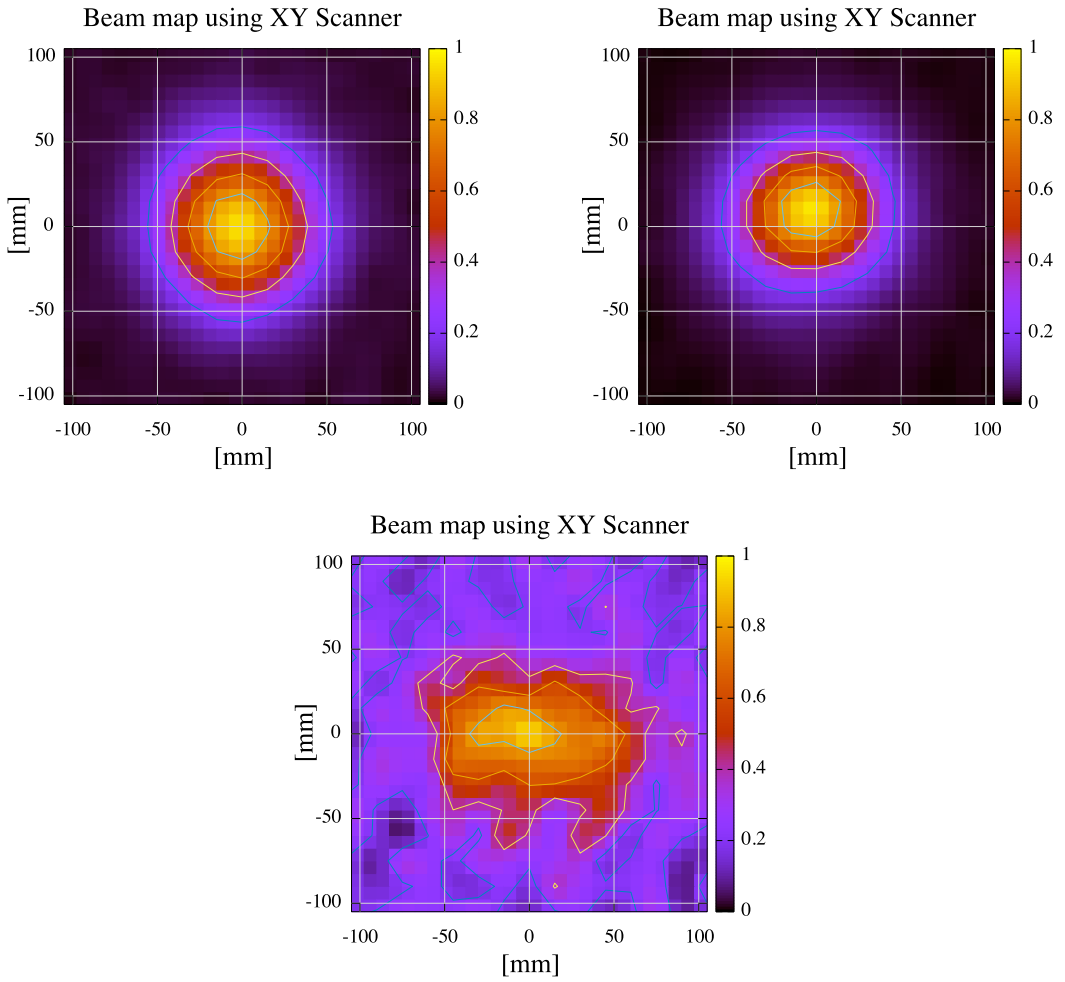

Figure 4.3: Beam measurement for 4G-1 (top-left), 4G-2 (top-right) and 4G-4 (bottom), using an external beam scanner. Test performed during the channels alignment using the flight configuration at the AFRC, USA. The horizontal and vertical axes refer to displacement of the scanner in mm. See text for details.

4.2 Laboratory Tests and Characterizations

4.2.1 Receiver Temperature

Receiver temperature T_{Rec} measurements were performed individually for each channel. The test environment used the spare system calibration unit, IF processor and FFTS backends. An external LN_2 calibration load was used for cross-reference the temperature scale of the internal load. The backend allows a measurement over the entire receiver IF (per channel). Values presented here are DSB.

Measurements were performed for 4G-1 and 4G-2 with and without the D-HFA4G beam splitting dichroic filter. The differences on the receiver temperature for both cases are in the order of what is estimated in section 4.4.4. The 4G-4 receiver temperature over IF band is modulated by the effect of the diplexer IF central frequency tuning (1.37 to 2.94 GHz) and only the usable portion is displayed. The measurement was performed using the dichroic in place.

As for 4G-3, T_{Rec} it was measured without having the dichroic in place. The mixer noise temperature

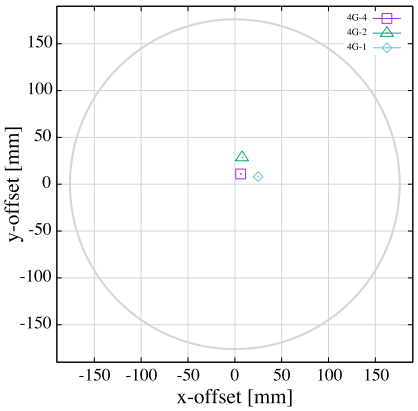

Figure 4.4: Propagation of the beam centers positions to the subreflector using data from internal and external beam measurements. The gray circle represents the contour of the subreflector.

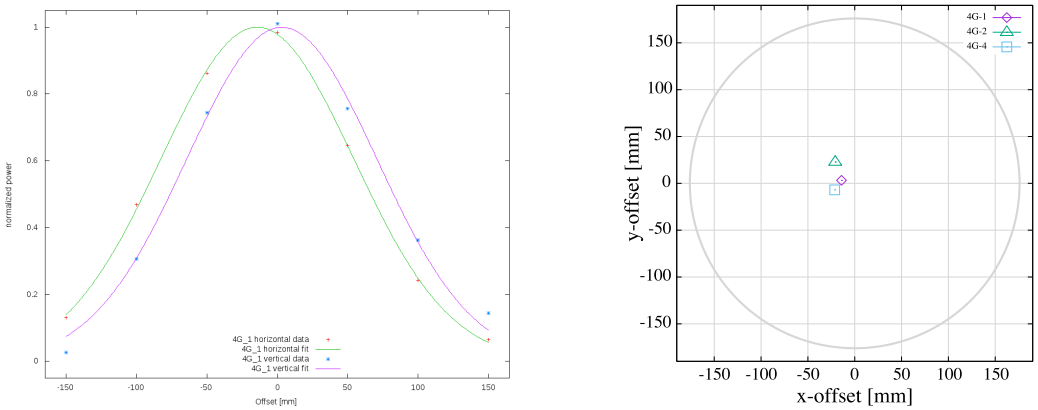

Figure 4.5: Left: 4G-1 Actual beam illumination over SOFIA sub-reflector, measured using a paddle at 77 K. Right: position verification of the beams axes for 4G-1, 4G-2 and 4G-4.

roll-off happens at IF of 2.5 GHz (Fig. 4.6).

4.2.2 Stability and Allan Variance Tests

The stability of a receiver can be characterized by various indicators. Inspection and simple trend analysis of the total power curve recorded over a significant amount of time (>100 minutes) of each channel, while system is properly biased and the LO pumped at laboratory conditions, provides useful information as it allows to see the influence of short and mid term time constants, like environmental temperature changes and thermal stabilization of components and modules.

Receiver stability has to do also with insensibility to mechanical vibration and tilts of the telescope. A telescope inclination test simulation was performed at the MPIfR GREAT-laboratory by tilting the whole GREAT structure while 4G and HFA were in operation (mixers biased, LO pumped and channels pointing to a calibration cold load unit). Figures 4.7 and 4.8 show the mixer current and the total power per channel recorded over 160 seconds during a 20 degrees tilt excursion over 20 seconds. This kind of change on the inclination of the instrument would corresponds to a telescope rewind or source change. Mixer currents show small variations mostly attributable to mixer bias electronics readout, however the

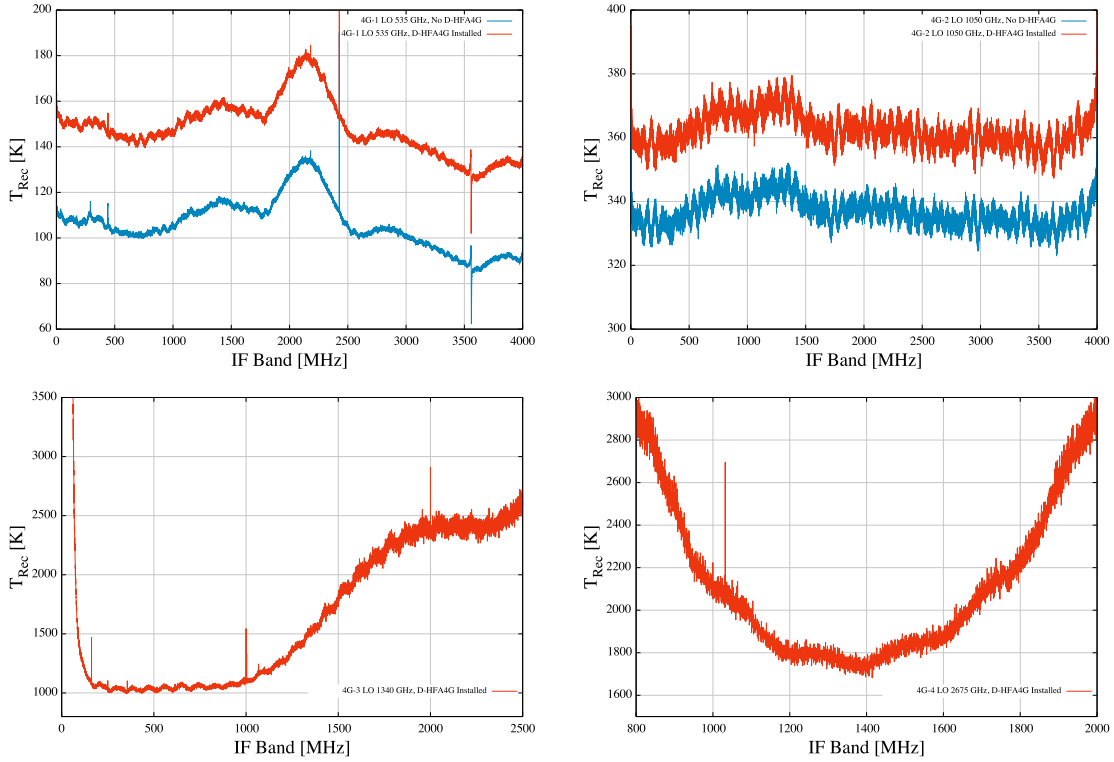

Figure 4.6: T_{Rec} over the IF band for all 4G channels. Top: 4G1 and 4G2. Bottom: 4G-3 and 4G-4

effect of the change on the tilt is not noticeable. The inclination change has a visible effect on total power levels (Fig. 4.8), in particular for the HEB channels. Nevertheless changes were limited to ±3 % on the total level. After the tests, inspection of the system revealed that IF cables were the one causing most of the effect, as they bend and change phase. Dependency on the tilt and vibration can come from different sources as LO, optics in LO, optics plate and receiver, bias electronics, signal references, coaxial lines and detectors their selves.

The minimum detectable signal temperature ΔT_{min} depends directly on the T_{Rec}, bandwidth $\Delta\nu$ and the integration time t, as described by the *Radiometer* equation 4.1. An Allan variance (AV) test provides a way of measuring the maximum integration time t_{max} between phases of a system (Ossenkopf 2008) or receiver and consequently the minimum detectable signal. Its this integration time which depends directly on the stability of the receiver.

$$\Delta T_{min} = \frac{T_{rec}}{\sqrt{\Delta\nu \cdot t}} \tag{4.1}$$

AV tests were performed for every single channel under laboratory conditions. This implies stabilized room temperature, IF processor and FFTS modules warm (See subsection 4.4.5) and no other radiation sources active than those required by the receiver components. Tests were run with the upGREAT HFA active as both HFA and 4G fly together as a combination of frequencies bands.

Two t_{max} indicators can be estimated from the AV tests, depending on how data is binned and processed. On one hand, *total power* AV measurements take into account one individual wide spectral channel, yielding the total power AV time (t_{TP}). On the other hand *spectroscopic* AV, makes use of two spectral channels to calculate the spectroscopic AV time (t_S). The two spectral channels comparison aims to

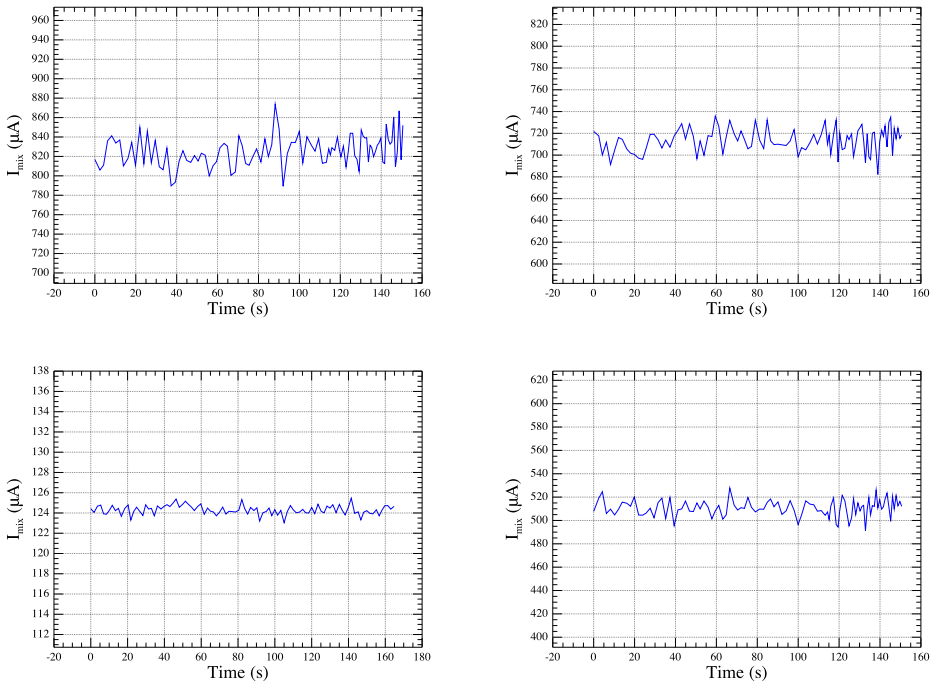

Figure 4.7: Mixer currents recorded during telescope tilt simulation of 20 degrees in elevation.

detect variations on the receiver IF band. Estimated Allan times are listed for each 4GREAT band on table 4.1, while plots for the total power and the spectroscopic AV can be seen in detail in appendix I, Figs. I.1, I.2, I.3 and I.4.

Table 4.1: Allan Variance times. See appendix I for detailed plots for each 4GREAT band.

	4G-1	4G-2	4G-3	4G-4	Remark
Total power AV time t_{TP} [s]	54.5	42	41	46	Average on two spectral channel
Spectrometric AV time t_S [s]	110	135	180	111	Using two spectral channels
LO frequency [GHz]	520	920	1300	2673	

4.3 Commissioning and Science Verification

4GREAT has been commissioned during the 4th southern deployment of SOFIA in Christchurch, New Zealand. The verification of geometry and determination of bore-sight, beam and coupling efficiencies were performed for 4G-1, 4G-2 and partially for 4G-4 on the GREAT cycle 5-H flight #09 *Hamlet* (Flight ID 2017/07/11 #418). Together with the commissioning of 4G, the HFA/4G configuration of GREAT was also tested and accepted. As for 4G-3, the de-commissioning of GREAT L1 and transfer of its detector to 4GREAT was planned for late 2017. The commissioning of 4G-3 will take place during the SOFIA southern deployment in June 2018.

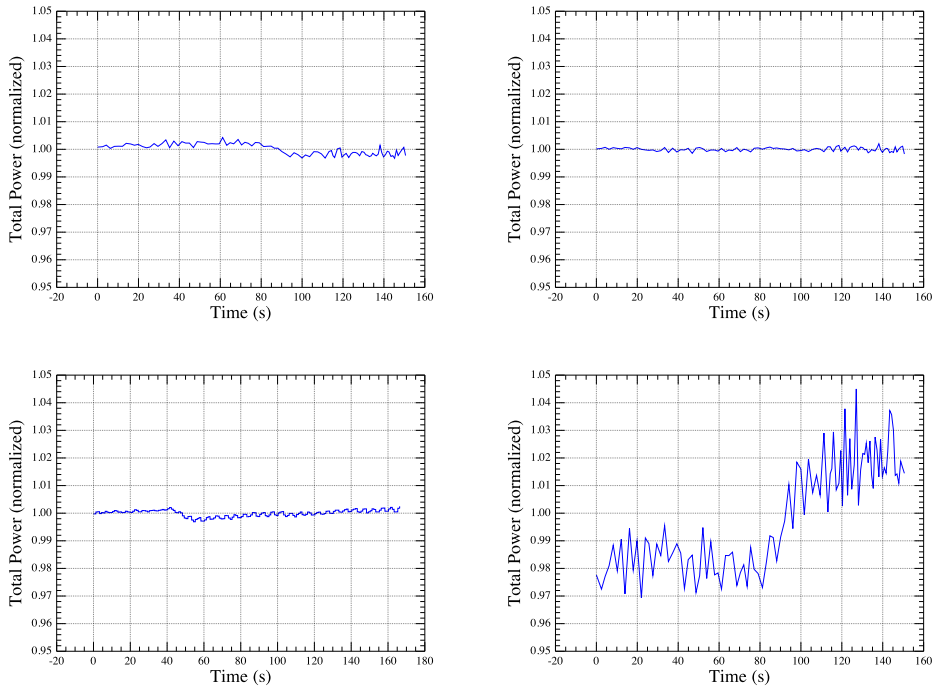

Figure 4.8: Total power recorded during telescope tilt simulation. The tilt was triggered at different times for each channel. Values have been normalized to its average.

4.3.1 Receiver Temperature on Board

After GREAT is installed on board SOFIA, receiver temperature scans are performed. During scientific observations T_{Rec} is also obtained for each channel periodically. This information is fundamental for the online-calibration of the data, performed by the *KOSMA-control* observing software and its *kalibrate* module. Figure 4.9 shows three single side band over-the-band measurements, for 4G-1, 4G-2 and 4G-4. The particular shape of 4G-4 derives from the IF response of the diplexer. The careful selection and tuning of the IF frequency is fundamental as it allows to avoid mixer features and spurious introduced by LO as well as avoiding atmospheric features from the image band in favor of the lowest receiver temperature.

4.3.2 Bore-sight, Beam Size and Efficiencies

The bore-sight, beam size and efficiencies are typically determined using planets, making either a cross-scan (CS) or an On-the-Fly map (OTF). Each spectrum of the CS (Fig. 4.11) or OTF is reduced independently and we measure the continuum emission of the planet by integrating over a frequency range that is free of line emission of absorption and falls into the lowest noise part of the spectrum. This way one temperature value per coordinate is obtained. With this information a profile or beam map can be constructed which is then fitted with a typically Gaussian curve. The peak of this curve gives the position offset or bore-sight against the optical cameras of SOFIA. The width shows the beam convolved profile of the planet, in case of the planet being an extended source. Its this fitted curve which is then de-convolved from the planet profile leading to the measured beam size. For an unresolved source (much smaller than the estimated beam size), the width of the Gaussian curve directly provides the beam. Every time the

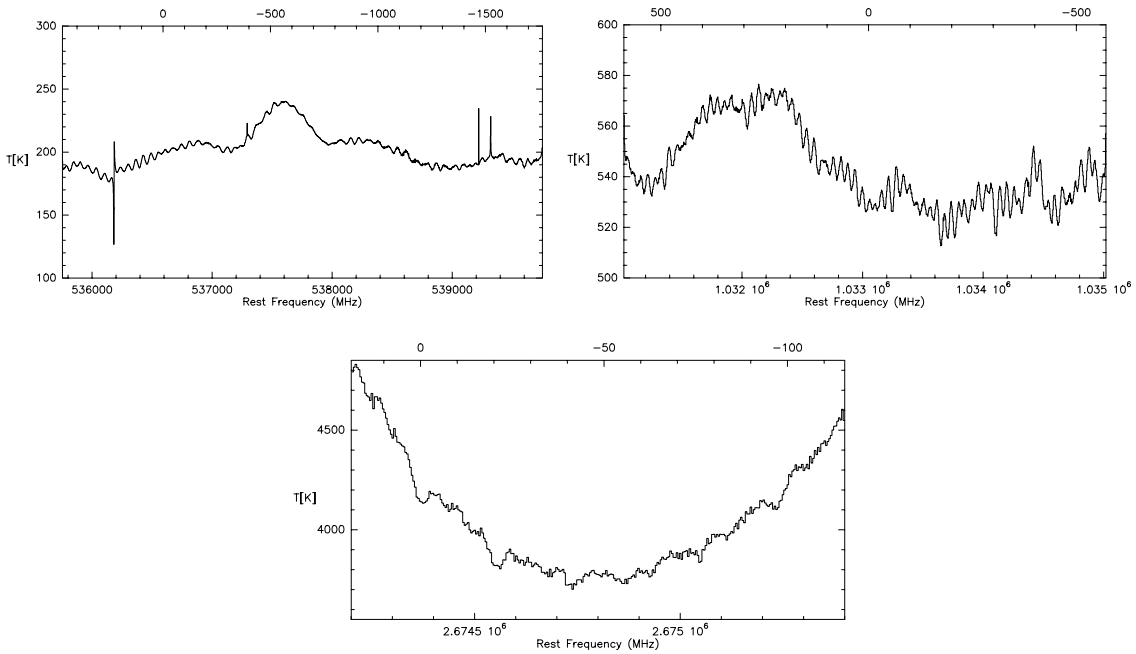

Figure 4.9: 4GREAT channels 1, 2 and 4 single side band receiver temperatures obtained with the flight configuration on board SOFIA.

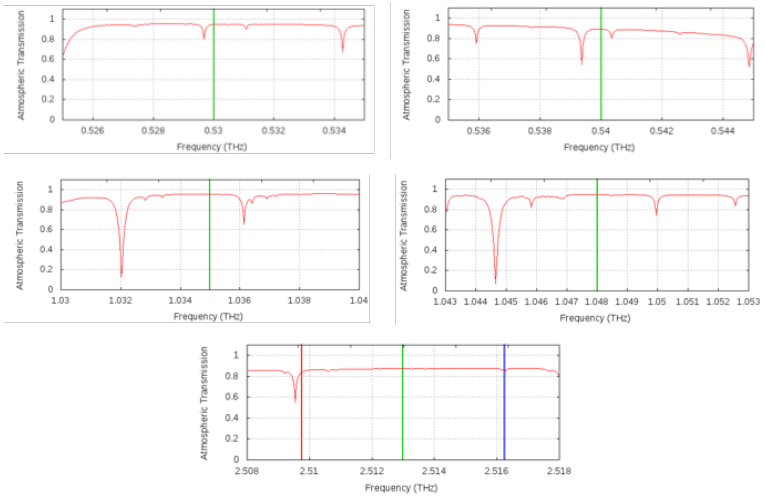

Figure 4.10: Atmospheric features that appear at the frequency used for the commissioning of 4G-1(top), 4G-2 (middle) and 4G-4 (lower)

instrument is removed and reinstalled the bore-sight changes slightly and has to be re-determined.

Jupiter has been used as target for the commissioning. On UT July 11 2017 Jupiter was extended with a 33.9” × 36.3” disk diameter at 24.5° CCW. The brightness temperature of Jupiter is modulated by strong atmospheric absorptions (Fig. 4.10). The 4 GHz wide IF (4-8 GHz) and the DSB response of the SIS mixers required careful selection of the RF band for calibration, folded with the planet-intrinsic spectral features. A good choice for 4G-1 has been to tune to 536 GHz LO (530 GHz rest frequency) while 4G-2 LO does it at 1043 GHz. Table 4.2 displays the setup frequencies used.

Table 4.2: Frequency setup for the commissioning run. T_{Rec} was estimated during pre-flight verification.

Channel	Source Name	Frequency [GHz]	Sideband	IF F_{center}[KHz]	$T_{Rec-SSB}$ [K]
4G-1	4G-1_Jupiter2	530.00000	USB	5600	220
4G-2	4G-2_Jupiter3	1038.5000	LSB	6400	430
4G-4	4G-4_Jupiter4	2513.0000	LSB	2000	–

Many scans were performed in order to establish an average on the beam and the measured temperatures. Table 4.3 lists 4 of them with their results. 4G-4 beam could not be well determined on extended Jupiter, but obtained numbers were consistent to estimations of 11", within 10%. Further measurements on this channel to be performed in June 2018.

Table 4.3: Measured and averaged values of beam and T_{obs} using Jupiter.

	4G-1		4G-2		4G-4	
Scan number	$2 \cdot T_{obs}$	θ_b["]	$2 \cdot T_{obs}$	θ_b["]	$2 \cdot T_{obs}$	θ_b["]
22911 (x)	46.33	52.1	102.55	28.1	124.9	n/a
22908 (x)	46.70	51.8	103.40	28.1	122.1	n/a
22905 (y)	45.95	52.7	99.45	25.9	127.8	n/a
22903 (x)	46.65	51.9	103.8	27.8	104.6	n/a
22900 (x)	46.53	51.7	105.2	28.0	114.3	n/a
22900 (y)				25.8		
Average	46.4	52.0	102.9	28.0×25.9	118.7	n/a

Measurements for beam sizes are compared to theoretical values given by equation A.8 and presented in table 4.4. The calculation of the theoretical values makes use of the effective taper which depends on the frequency, but underestimates the effective aperture.

Table 4.4: Measured and estimated channel beam sizes.

	4G-1	4G-2	4G-4	Remark
Frequency [GHz]	530	1038.5	2513	Comm. frequencies (Table 4.2).
Taper [dB]	13.14	14.95	14.27	Value at tuned frequency.
Estimated beam ["]	55.9	29.12	11.9	Using Eq. A.8
Measured beam ["]	52	26.9	10.5	

Efficiencies are calculated using the expected target planet temperature and geometry, the peak measured temperature and derived beam size. The coupling efficiency (η_c) is calculated taking into account target geometry by equation A.18, while the main beam efficiency (η_{mb}) uses the measured peak temperature and the main beam temperature derived using η_c and the forward efficiency ($\eta_f = 0.97$) as described by the equation A.20. Values are listed on table 4.5

Table 4.5: Jupiter temperatures and derived efficiencies per band.

Jupiter temperatures	4G-1	4G-2	4G-4
Predicted brightness temperature T_b	147.0	148.1	133.5
Predicted R-J temperature T_{RJ}	134.7	124.5	82.1
Coupling efficiency η_c (Eq. A.18 - diff. limited. Taper 14 dB)	0.27	0.69	0.999
Predicted RJ temperature, folded into beam $T_{RJ,G}$ ($\eta_c \cdot T_{RJ}$)	36.4	85.9	82
Observed RJ temperature T_{obs} (cal with η_f = 0.97)	23.2	51.5	59.3
Main beam efficiency η_{mb} (Eq. A.20 - ($T_{obs}/T_{RJ,G}$) $\cdot$ η_f)	0.62	0.58	0.70

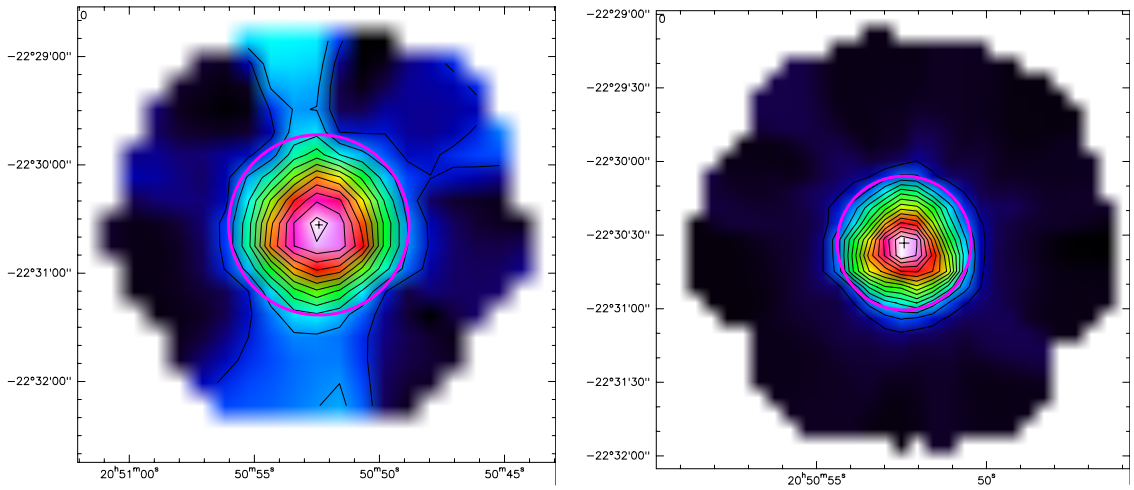

Figure 4.11: Cross scan maps of 4G-1 at 530 GHz and 4G-2 at 1038 GHz over Mars performed in June 2018. The estimated beams are 60" and and 30" however they have not been corrected by the corresponding efficiencies, that will lead to the numbers in table 4.4.

4.4 Findings

During laboratory tests and the instrument commissioning, some features or particular effects were found. Some of these could be solved or improved on the spot, while others required of a much more complex solution, even re-designing key components. These effects are summarized and described in this section.

4.4.1 Standing Waves

Standing waves were detected in the channels 1 and 2. The 4G-1 spectrum (Figure 4.12, top) shows a 16.9 MHz standing wave ($\lambda/2$ =8.85 m). This matches the distance between the subreflector and the mixer horn of 4G-1 mixer (7.242 meters between subreflector and focal plane, plus 1.605 meters in the optical path). Similarly, 4G-2 shows a 17.2 MHz feature ($\lambda/2$ = 8.72 m) corresponding to the distance between the subreflector and its mixer (7.242 m + 1.482 m).

The standing waves are more visible when single-phase chopped observations are carried out as the optical path between the two phases is slightly different.

Recent far field simulations show that the problem is caused by the diffraction due to the discontinuity (step) between the edge of the scattering cone and the sub-reflector surface and the perfect back reflection of the flat-head screws used to attach the cone. The first one is an unavoidable feature imposed by the

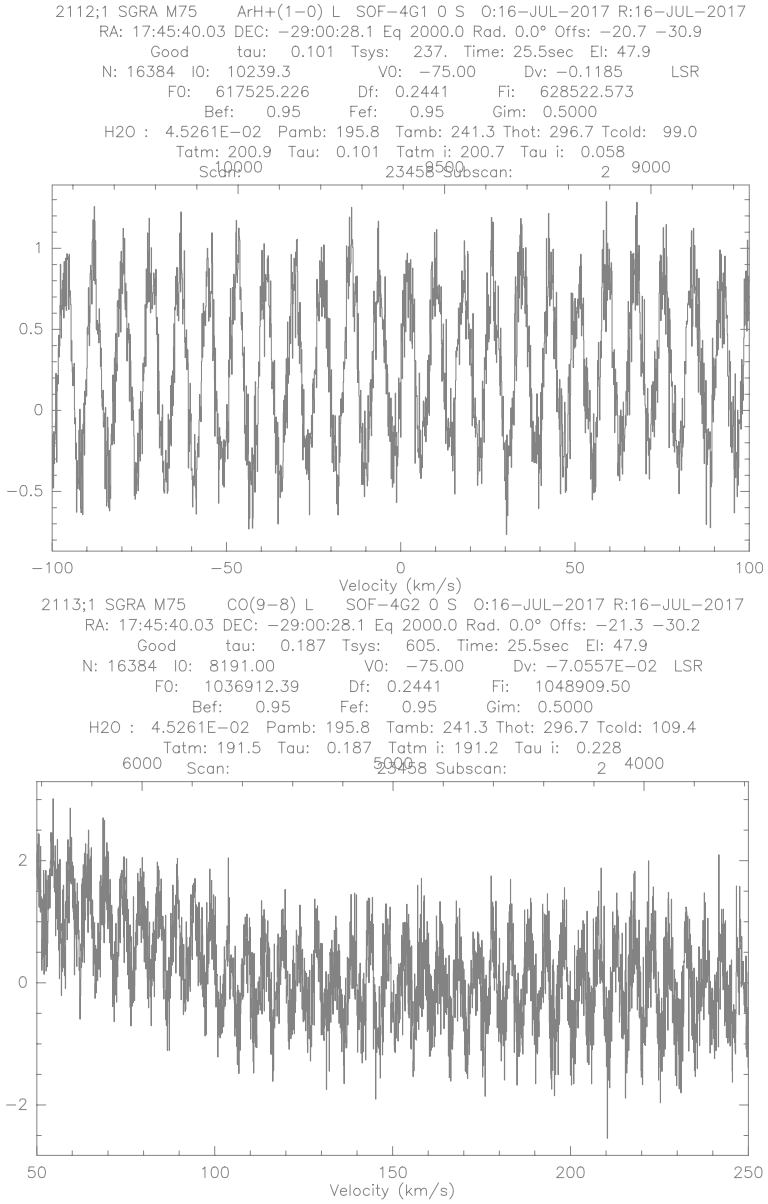

Figure 4.12: Sample single beam switch spectra of 4G-1 (top) and 4G-2 (bottom) showing the appearance of standing waves due to features mechanical discontinuities and flat-head attaching screws on the scattering cone of the subreflector. See text for details.

construction constraint to avoid scratching or stressing the surface of the secondary mirror. A promising solution comes from substituting the cone by a chirp edge (i.e. continuous sinuous non-periodic) cone, and use a different attaching method. The same simulations show that the net direct reflection effect near the propagation axis is significantly reduced (Figure 4.13) and with this the prominence of the standing waves due to LO back reflection (U. Graf 2017).

There is also a small effect on 4G-4, presumably coming from the alignment of the diplexer and its internal components.

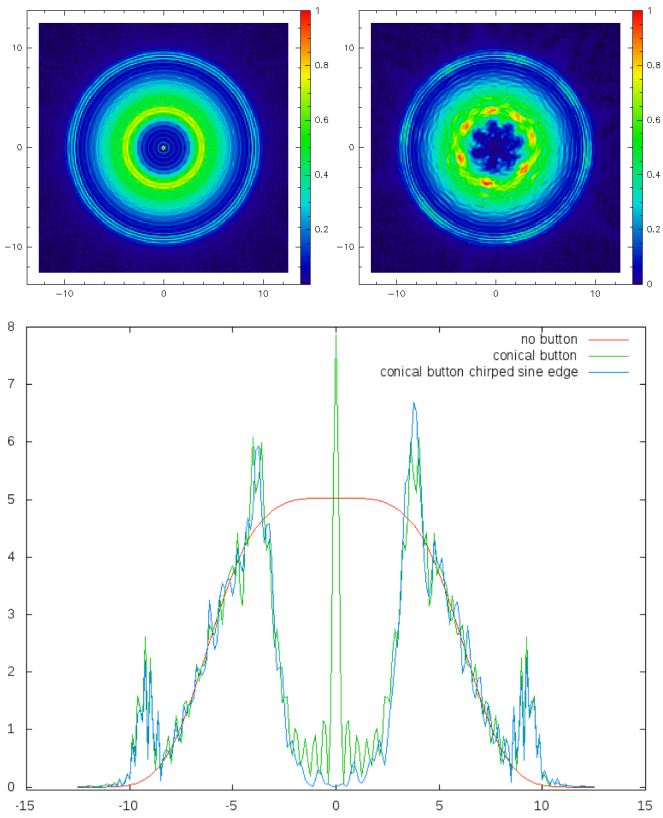

Figure 4.13: Standing waves and the scattering cone (button) effect. Top left, far field simulation of conical circular cone (U. Graf 2017). Top Right, far field for chirped edge. Down, comparison of continuous sub-reflector, scattering cone and chirped edge cone. Units in all plots are arbitrary.

4.4.2 Ground Loops

A feature on the I-V curves of the 4G-4 have been detected with the GREAT flight configuration. On the plot of the curve an abnormal modulation resembling a standing wave appeared. When performing tests at the laboratory such distortions disappeared. They were tracked down to come from *ground loops* (Rich 1983) on the bias modules for the mixers and a readout software artifact. This feature has been resolved to a large extent.

However, there are still some effects of other ground loops which can not be avoided given certain physical constructive constraints of discrete components, like coaxial cables ground looped with component chassis and mounting plates. Grounding is critical for every single stage of the receiver to ensure a low noise temperature, maximum sensibility and performance. This is an ongoing issue that is being currently addressed.

4.4.3 Spurious on the LO Signal

Spurious on the LO signal have been previously detected and are a known feature of solid state sources. Tests performed by the VDI and MPIfR teams showed that the source of some of the spurious comes from noise on the DC bias lines for multiplier stages. After different configurations tested, multistage commercial 10.7 MHz low pass filters from Minicircuits were installed in every single line, reducing

significantly the appearance of such unwanted signals on the output spectra from each 4G channel. A positive side-effect is that all the available power goes only to the main tone and therefore the LO chains are more efficient, meaning more LO signal is available. The same solution has been implemented in other LO sources equipped with such technology, as the upGREAT LFA LO.

4.4.4 The Effect of the HFA/4G Dichroic

Table 4.6: Dichroic D-HFA4G net effect over 4G bands. Additional receiver noise temperature comes from the direct element contribution at 300 K and element losses (transmission).

	4G-1	4G-2	4G-3	4G-4
Transmission: Min [%]	90.33	93.77	92.96	86.95
Transmission: Max [%]	97.99	92.96	96.63	90.26
Transmission: Average [%]	92.17	96.03	94.45	88.48
Direct contribution of D-HFA4G [K]	12.8	6.2	8.8	19.6
Additional loss by transmission [K]	6.2	9.9	49.6	164.8
Total contribution in T_{Rec} [%]	17.2	5.7	6.5	14.0

Operating five simultaneous receivers (a single frequency 7 pixel HFA and the 4 channels of 4G) has a penalty over the transmission on the signal path imposed by the dichroic filter used to separate the frequency ranges of the upGREAT HFA and 4G. This penalty is directly reflected on the T_{Rec}. Table 4.6 shows the average net effect of the dichroic over each 4G band. A strong cast on 4G-1 and 4G-4 can be seen on the lower panel of figure 4.14.

Based on the scientific program of every flight that would only include 4G observations the D-HFA4G could be removed, improving the transmission and therefore the receiver temperature, in particular for 4G-1 where the receiver temperature contribution from the D-HFA4G dichroic exceeds the 17%.

4.4.5 IF Processor Warmup Effect

When testing the whole GREAT system, 4G mixer currents remain stable, while total power output drifts as IF processor components warm up and then stabilize on a time scale of 90 minutes. During that time, gain changes directly affect the quality of data calibration processes. This effect has been successfully reproduced by laboratory tests, and taken into account during stability tests.

During observations campaigns, this problem is circumvented by the procedure of switching on the IF processor and electronics modules in general as early as possible and testing them on a *dry-run* before take off.

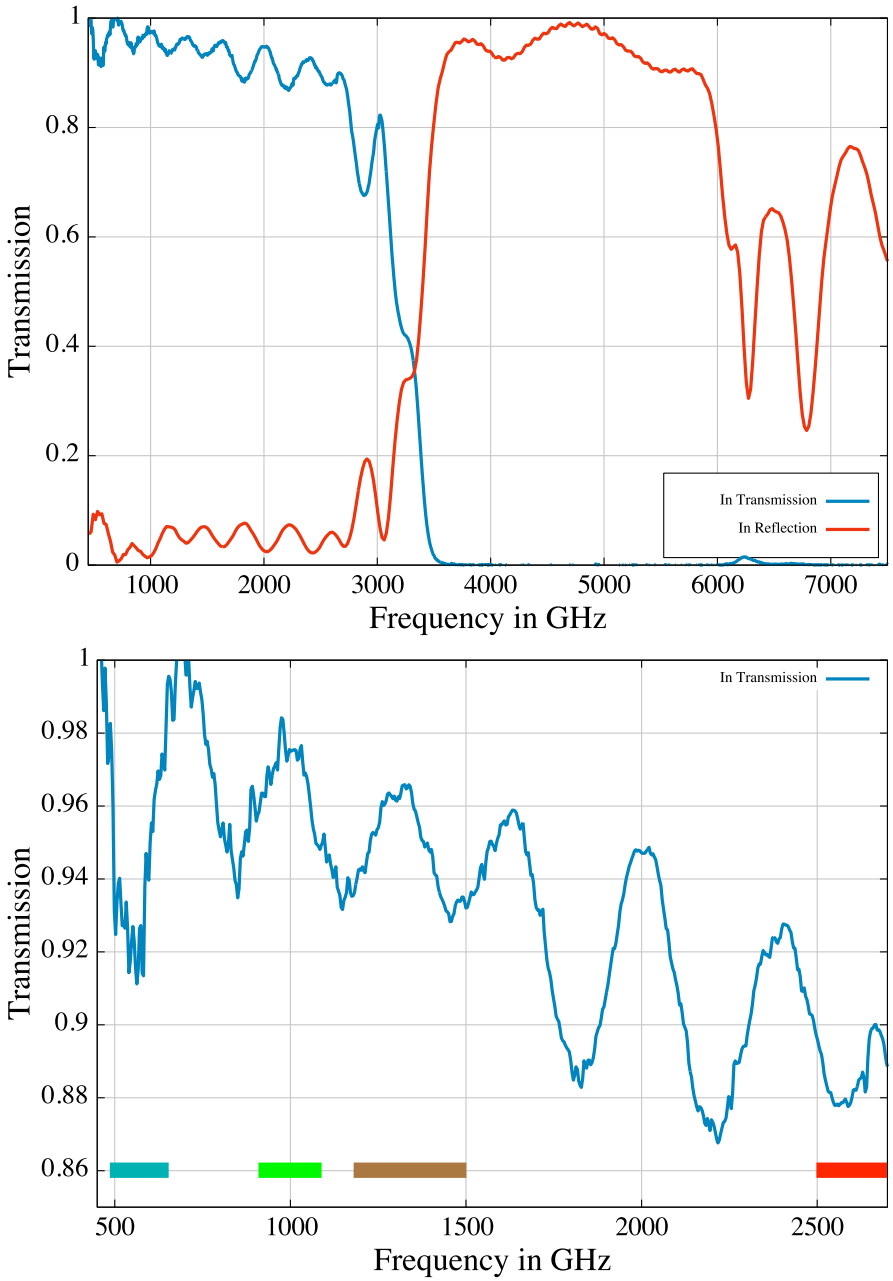

Figure 4.14: D-HFA4G. Top: transmission and reflection over the entire dichroic design band. Bottom: detail on the transmission over 4G channels, signalized by colored bars.

4.5 The new GREAT scenario

The design, construction and commissioning of 4GREAT, described in the previous chapters of this work, shows that GREAT is currently composed of the upGREAT LFA, with its dual polarization 7+7 pixels LO independent, the upGREAT HFA, with its 7 single frequency pixels, and 4GREAT, having 4 independent frequencies single pixel channels.

Table 4.7: GREAT receiver constellation after commissioning of 4G-1, 4G-2 and 4G-4. (*) Estimated values, as 4G-3 is expected to be commissioned by July 2018. Numbers in bracket represent the pixel separation for the arrays. Beam size for the 4GREAT channels are given for the commissioning frequencies, in Table 4.2. LFA beam size at 1.9 THz.

Receiver	Channel	# Pixels	Frequency [GHz]	Beam ["]	η_b	Configuration
4GREAT	4G-1	1	492 - 627	52	0.61	4G+HFA
	4G-2	1	893 - 1073	26.9	0.55	
	4G-3	1	1239 - 1515	22*	0.62*	
	4G-4	1	2495 - 2690	10.5	0.57	
upGREAT HFA	HFA	7	4745	6.3 (13.8)		4G+HFA LFA+HFA
upGREAT LFA	LFA-V	7	1810 - 1950	14.1 (34)	0.69	LFA+HFA
	LFA-H	7	1830 - 2070	14.1 (34)	0.70	

The three cryostats can be grouped in two valid combinations. The first combination, commissioned in June 2017, uses the LFA and HFA. As for the second combination, three of the four channels of 4GREAT, operated in parallel with the HFA, have been commissioned in July 2017. The table 4.7 presents the receivers beam FWHM, efficiencies and the valid combinations. The disposition of the pixels for the different frequency channels in the sky is sketched in the figure 4.15.

GREAT was already a very powerful high resolution instrument, however with 4GREAT not only two exclusive frequency windows have reopened, but also the scientific possibilities and the operational efficiency of GREAT have drastically increased.

The receiver sensitivity estimation tool, the *GREAT time estimator*, is used to determine the integration time needed to reach a requested signal-to-noise for a given brightness temperature, based on the noise performance of every GREAT channel. It is available at the USRA/SOFIA web page[1].

[1] https://great.sofia.usra.edu/cgi-bin/great/great.cgi

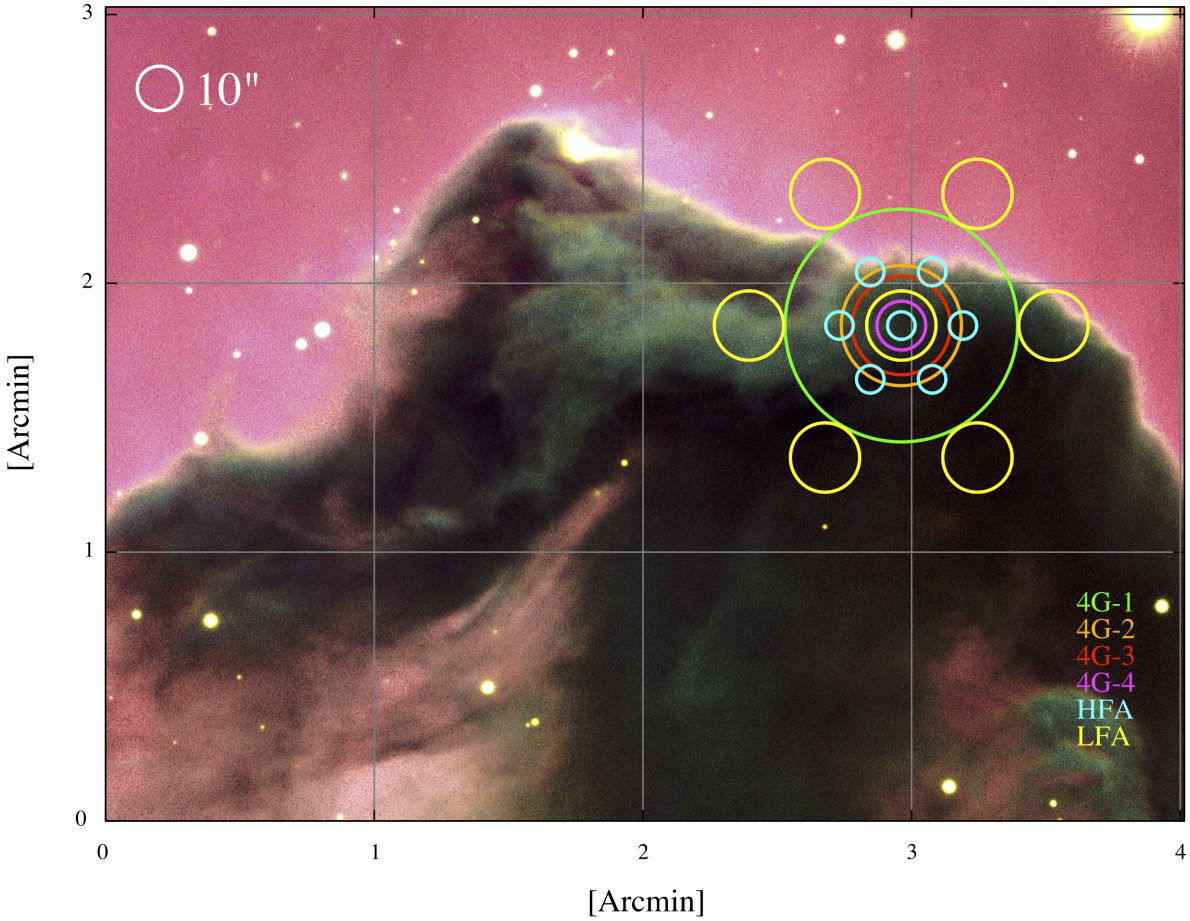

Figure 4.15: GREAT receivers 4G, HFA and LFA pixel beams on sky, identified by colors over a 3×4 arcmin image of the Horse Head nebula. Pixel sizes are on scale to the 10" circle in the upper left corner.

CHAPTER 5

A study of diffuse molecular gas on a sightline towards the fourth quadrant of the Galaxy, traced by CH

Molecular hydrogen is a symmetric and homo-nuclear molecule that does not have a permanent dipole moment, since its centers of mass and of electric charge coincide and therefore it has no allowed rotational transitions. Only the much higher excitation ro-vibrational transitions are observable in the infrared, however, they correspond to only a fraction of the total amount of H_2 in the ISM. The problem of detecting molecular hydrogen is tackled by using other species that are related to H_2 and serve as tracers or *surrogates*.

The prime tracer for dense clouds has historically been CO with its many transitions available in the submm regime as in the THz bands. However CO is under-abundant in diffuse clouds, because it shields itself less efficiently against disassociating UV radiation than H_2 (Snow and McCall 2006, further references therein). For the diffuse gas, hydrides like HF, OH and CH can be used as chemical tracers (Gerin et al. 2016). HF (Neufeld et al. 2005), and OH (Wiesemeyer et al. 2012) are used as a proxy for H_2 with the caveat that they suffer from saturation when they are observed in absorption. Methylidyne (CH) on the contrary does not suffer from saturation (Gerin et al. 2010; Wiesemeyer et al. 2018). It has been shown that the column density of CH is strongly correlated with that of H_2, with $N(CH)/N(H_2) = 3.5^{+2.1}_{-1.4}$ x 10^{-8}(Sheffer et al. 2008). This relationship has been established thanks to observations of CH and H_2 absorptions in the optical and UV, respectively. However, due to the dust extinction towards the background stars, this study is limited to a relatively nearby regions of the Galaxy. A similar correlation can be obtained from far-infrared and cm spectroscopy. The emission and absorption lines of CH in the radio domain arise from transitions between the hyperfine split levels of a given rotational state. However, like in the case of the OH molecule, their analysis is hampered by their uncertain excitation out of thermal equilibrium, unlike absorption line studies in the far-infrared, for which column density is an observable.

The sightline towards G330.95+0.18 (J2000 16:09:53.01, -51:54:55.0), a star forming region at 5.7 kpc distance (Wienen et al. 2015), and hereafter G330.95, crosses three spiral arms. It allows to study the diffuse gas in the inner Galaxy, which is generally characterized by a higher molecular gas fraction than the outer Galaxy. G330.95 offers a very bright background continuum source suitable for absorption studies.

The objective of the work described in this chapter is to estimate the column densities of H_2 of cold diffuse gas on this sightline, using CH. In order to understand why CH is a good surrogate for H_2, the underlying chemistry is introduced first.

5.1 A Light Hydride: Methylidyne and its Chemistry

CH, also know as *methylidyne radical*, is the simplest carbyne. Consisting of the combination of hydrogen and carbon with three unbounded electrons, via single bond, its highly reactive and gets quickly destroyed in normal terrestrial conditions, but in the low-density environment of the interstellar medium (ISM) it is abundant. It has a long history in astronomy and spectroscopy as it was the first gas-phase molecule detected in the ISM in the early 20^{th} century by Dunham (1937) and identified by Swings and Rosenfeld (1937). Since then it is among the most studied hydrides (Gerin et al. 2016).

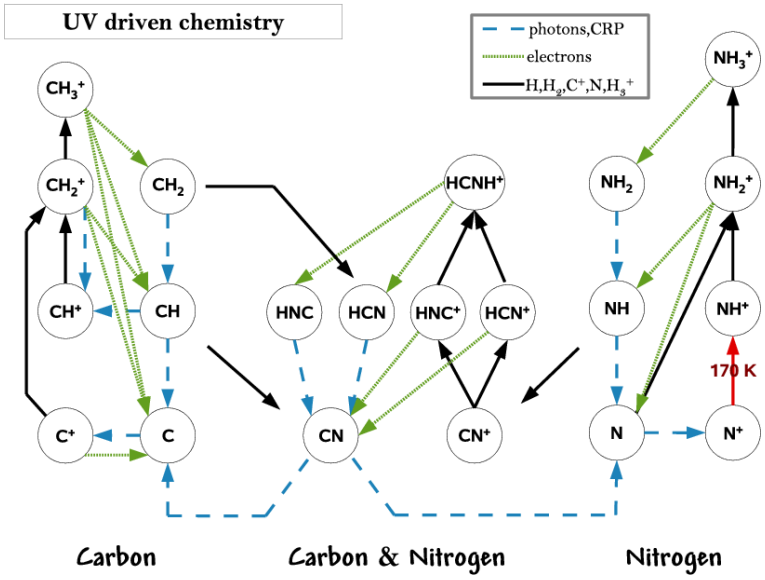

Figure 5.1: UV driven formation of different hydrides. Taken from Godard et al. (2010)

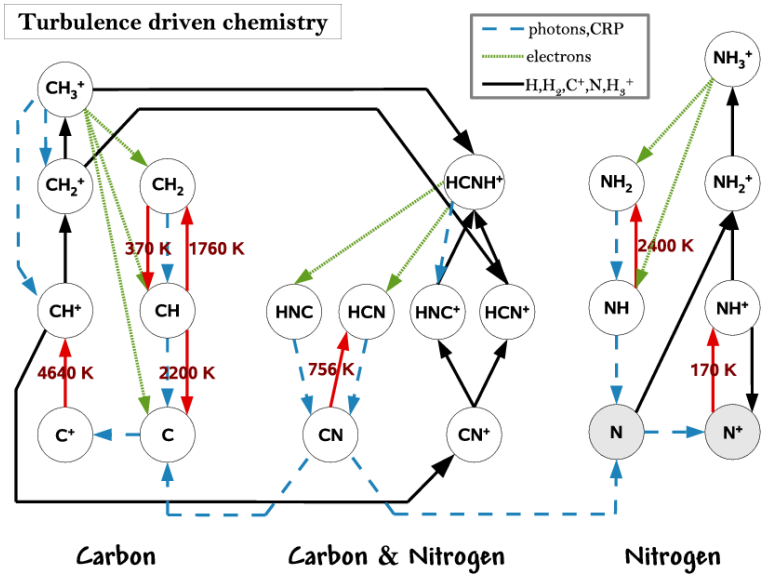

Figure 5.2: Turbulence driven chemistry for different ISM molecules. Energy barriers for endothermic reactions are shown in red. Taken from Godard et al. (2010).

CH can exist in high and low density regions in the ISM and its formation mechanism can be of different nature. On one hand the simplest and more direct formation path ($C + H_2 \rightarrow CH + H$) is highly endothermic making it very inefficient. On the other hand, conditions in which CH forms in the ISM require sufficient amount of C^+ (ionized carbon) interacting with vibrationally excited H_2.

Carbon is the fourth most abundant element in space. With an ionization potential (IP) of 11.26 eV it is easier to ionize than hydrogen, which has an IP of 13.60 eV. C^+ is therefore the natural form of atomic carbon throughout the warm ionized medium, but also in the cold neutral matter (CNM) phase of the ISM. Even in translucent clouds which are considered to be the precursors of molecular clouds, it is still present, then in atomic form before it is taken up in the formation of carbon bearing molecules. Moreover, due to its lower IP, it is a reservoir of free electrons, which are needed in the underlying network of chemical reactions.

The formation of CH is initiated by the slow radiative association of C^+ with vibrationally excited H_2, producing CH_2^+:

$$C^+ + H_2^* \rightarrow CH_2^+ + h\nu$$

The following reactions are exothermic, however, their production rates depends on temperature, and on the availability of the reaction partners. The CH_2^+ ion subsequently forms CH by the virtue of an exothermic dissociative recombination:

$$CH_2^+ + e^- \rightarrow CH + H$$

An alternative path is the fast hydrogen abstraction reaction:

$$CH_2^+ + H_2 \rightarrow CH_3^+ + H$$

followed by dissociative recombination:

$$CH_3^+ + e^- \rightarrow CH + H_2$$

The dependence of the methylidyne production on the availability of molecular hydrogen makes it such a reliable surrogate for the latter. So far only exothermic reactions were considered since endothermic reactions are inhibited by reaction barriers up to several thousands of Kelvins. However, the required energy may be provided by the turbulence taking place in slow shocks (Godard et al. 2014). Once turbulence is generated by supernova remnants expanding into the ISM, and by protostellar outflows and winds from young stars, it decays if it is not sustained by such an energy input, and the dissipated energy can drive the following reaction path:

a particular endothermic leg ($\Delta E / k = 4640$ K):

$$C^+ + H_2 \rightarrow CH^+ + H$$

two hydrogen abstraction reactions:

$$CH^+ + H_2 \rightarrow CH_2^+ + H$$

$$CH_2^+ + H_2 \rightarrow CH_3^+ + H$$

followed by the corresponding dissociative recombinations, forming CH, as above:

$$CH_2^+ + e^- \rightarrow CH + H$$

These two reaction sequences are shown in Figs 5.1 for the UV driven and 5.2, for the turbulence driven chemistry, respectively. In steady state chemistry, usually achieved after ∼10 Myr, the production of CH is in equilibrium with its destruction owing to photodissociation and photoionization by UV photons and cosmic ray particles.

In general, for diffuse (van Dishoeck and Black 1986) and translucent clouds (van Dishoeck and Black 1988), chemistry is controlled by UV radiation and cosmic ray flux.

5.1.1 CH Hyperfine Splitting

Hyperfine structure or HFS refers to small shifts and splittings in the energy levels of atoms, molecules and ions, due to the interaction between the state of the nucleus and the state of the electron clouds. These small differences are described by molecular quantum numbers (Draine 2010). The energy levels of CH (Figure 5.3) and the transitions between these levels lead to lines of hyper fine components (HFC) that occur over a wide range of frequencies starting as low as 0.7 GHz[1]. Transitions happening between energetic levels with small energy difference are associated with low frequency lines, typically observed in the radio regime.

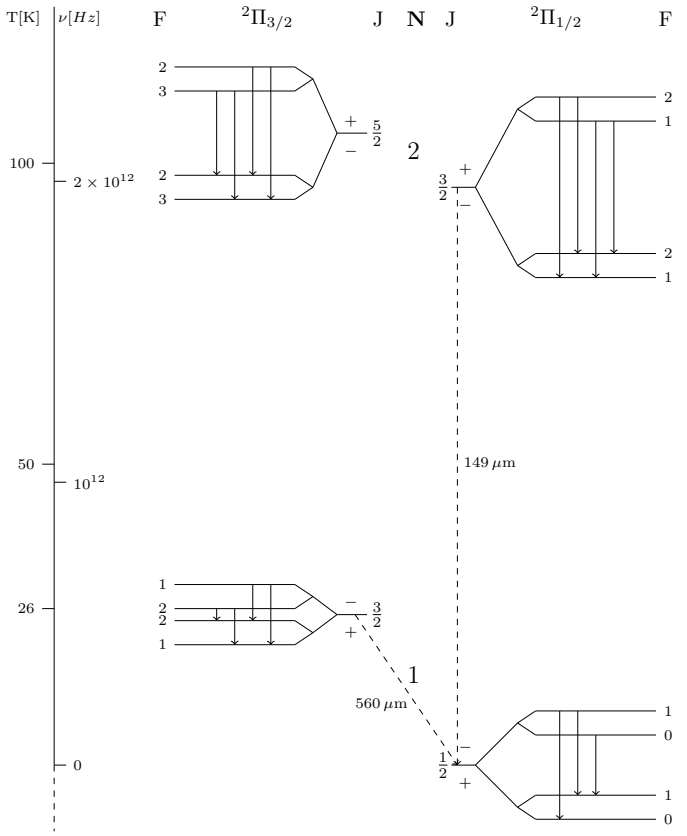

Figure 5.3: CH energy level diagram for the lowest 16 hyperfine levels. Dotted lines indicate the transitions at 532/536 GHz and 2006/2010 GHz. Taken from Wiesemeyer et al. (2018)

Exploiting the capabilities of the upGREAT LFA and 4GREAT, part of the GREAT instrument, the focus is set on the rotational ground state transitions at λ149 μm and the cross-ladder transition at λ560

[1] CDMS: https://www.astro.uni-koeln.de/cgi-bin/cdmssearch?file=c013502.cat

μm. At λ149 μm there are actually 6 HFC. Three of them are around 2006 GHz and the other three at 2010 GHz. This splitting arises from the uncoupling of the electronics orbital angular momentum from the C-H axis (Λ doubling, Hinkley et al. 1972). A similar situation happens at λ560 μm, with three transitions at 532 GHz and three at 536 GHz. The group of three HFC around a specific frequency are said to form a triplet. The frequency difference between the members of a triplet is in the order of a few tens of MHz.

Because of the frequency difference between the triplets, of the IF limitations of the GREAT instrument channels, and the atmospheric transmission features, usually only one triplet per band can be observed at the same time. Specific details of the triplets selected for this work are presented in Table 5.1

Table 5.1: Transition changes, frequencies, Einstein coefficients, energy levels, degeneracies and relative intensities for CH hyper fine components (HFC) of interest at 560 and 149 μm.

Transition	HFC F change	Frequency [GHz]	A_E [s^{-1}]	E_U [K]	E_L [K]	g_u	g_l	Δv_{HFS} [km/s]	r_{HFS}
N=1, J=/2 ← 1/2	$2^- \leftarrow 1^+$	536.7611	0.000638		0.0007	5	3	0	0.625
	$1^- \leftarrow 1^+$	536.7819	0.000213	25.76	0.0007	3	1	-11.6	0.125
	$1^- \leftarrow 0^+$	536.7956	0.000425		0.0000	3	3	-19.3	0.250
N=2 ← 1, J=3/2 ← 1/2	$1^- \leftarrow 1^+$	2006.74892	0.01117	96.31011	0.00072	3	3	7.5	0.125
	$1^- \leftarrow 0^+$	2006.76263	0.02234	96.31005	0.0000	3	1	5.45	0.250
	$2^- \leftarrow 1^+$	2006.79912	0.0335	96.3125	0.00072	5	3	0	0.625

5.2 Cold Diffuse Gas towards G330.95

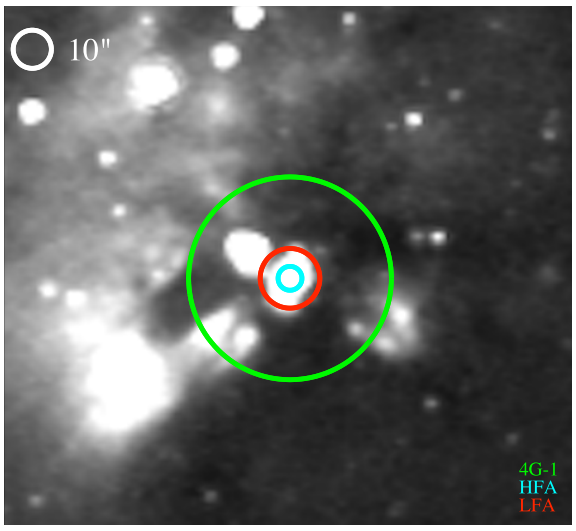

Figure 5.4: Overlay of 4G-1 (52"), LFA-px00 (15.5") and HFA-px00 (6.3") pixels on G330.95. Background image comes from Spitzer/IRAC 5.8 μm (Werner et al. 2004).

CH absorption lines at 2 THz (λ149 μm) and 536 GHz (λ560 μm) are investigated towards G330.95. The velocity range of interest is between -80 and -5 km/s, which includes the line of sight crossing of the

Carina, Crux and Norma spiral arms (Vallée 2008; Wiesemeyer et al. 2016), but excludes the local gas. Particular emphasis is put on the velocity ranges [-50, -30] and [-80, -50] km/s which include mainly the Crux and Norma arms.

5.2.1 Observations of the CH λ149 μm and λ560 μm lines

Table 5.2: GREAT Observation setup parameters for CH at 149 and 560 μm.

Receiver	Line setup	Frequency [GHz]	IF center [MHz]	Side band	Observing mode	Chopper amplitude ["]
LFA	CH_149	2006.762578	1900	USB	DBS	60
4G-1	CH_560	536.761046	5000	USB	DBS	90

G330.95 was observed using the upGREAT LFA and 4GREAT channel 1 on board SOFIA. Data at 2 THz using the upGREAT LFA was acquired during the GREAT Cycle 5-H flight #08 (Hagar) Flight ID: 2017/07/06 (#416) as part of the project called *The chemistry of interstellar CH* (ID: 83-0513). As for the observation at 536 GHz using 4G-1, it took place during the first light and commissioning of 4GREAT on the GREAT Cycle 5-H flight #09 Flight ID: 2017/07/11 (#418) under the same project. The observations were performed using double beam switch mode to reduce the effect of instrumental and atmospheric instabilities, and standing waves. Other specific details about the observation setup (SOFIA Science Center 2017) are summarized in Table 5.2.

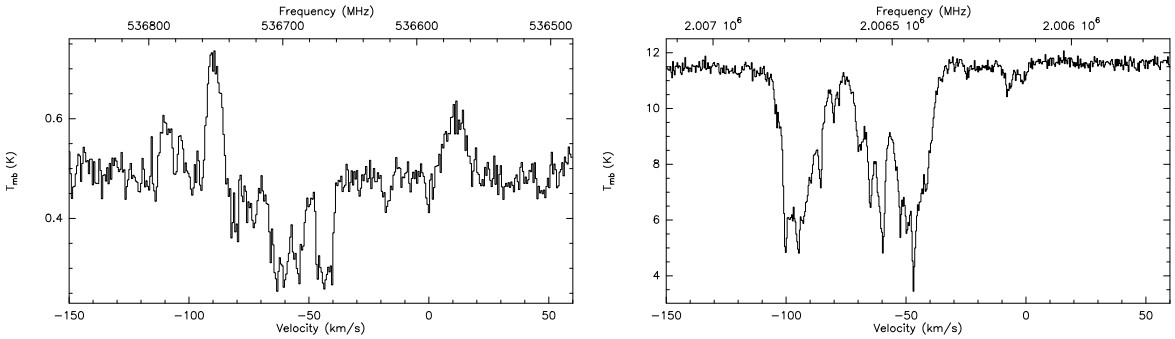

Figure 5.5: Left: CH λ560 μm spectrum towards G330.95, obtained with 4GREAT channel 1. Right: CH λ149 μm spectrum in the central pixel of the upGREAT LFA (horizontal polarization sub-array). Data has been calibrated and smoothed. The base line level has also been corrected for both cases.

5.2.2 Data Calibration and Preparation

During observations, the *Kosma-control* software controls, monitors and interacts with the GREAT instrument. One of the Kosma-control modules, named *kalibrate*, performs an on-line data calibration. *Kalibrate* uses the hot and cold loads of the GREAT onboard calibration unit (see 2.2.2) to determine the receiver performance, intrinsic noise and bandpass shape of the system, and to establish the count-to-Kelvin conversion ratio. These tasks are periodically performed during flight, usually every time a scan is loaded. The total power measured from the sky and the count-to-Kelvin ratio are used to calculate the Rayleigh-Jeans equivalent brightness temperature of the sky. From the atmospheric model, the estimated

atmospheric opacity that best matches the sky temperature is derived and used by *kalibrate* to compensate and correct for atmospheric attenuation and features (Guan et al. 2012). At this stage the data is said to be pre-calibrated and corresponds to *antenna temperature* T_A in Kelvins.

Data reduction and processing is performed using the *Continuum and Line Analysis Single-dish Software CLASS* [2].

After the observations, a second calibration step or *offline* calibration accounts for uncorrected frequency dependent atmospheric attenuation, in particular due to the dry constituents of the atmosphere, yielding post calibration antenna temperature or T_A^* (Eq. A.19). The spectra on T_A^* scale are then corrected for the main beam efficiency (η_b), obtaining the data in T_{mb} temperature scale (Eq. A.20). While the forward efficiency is the same for each GREAT channel ($\eta_f = 0.97$), main beam efficiencies are specific for each of them (Table 4.7).

Because of the DSB nature of all the GREAT detectors, the spectral continuum level has an equal contribution from the signal and the image band (assuming mixers side band ratio $G_{usb}/G_{lsb} = 1$). A dedicated DSB continuum calibration process can be used to correct for this effect.

GREAT, with 16384 spectral channels, resolves features down to a minimum of 0.0365 km/s for the 2 THz regime and 0.137 km/s for the 500 GHz range. By spectrally smoothing the data, high frequency noise is smeared out. This is achieved by binning adjacent channels together using a *sinc* function, a natural low pass filter. Although the net effect of the smoothing is a decrease in the spectral resolution, binned data still have a sufficiently high enough resolution of 0.54 km/s for the $\lambda 560$ μm data and 0.36 km/s for $\lambda 149$ μm.

A baseline correction step addresses for the insufficient or incorrect compensations of atmospheric features from the signal band and the image band. The base line correction also compensates non-linearities in the GREAT instrument response. Thanks to the good performance of the previous steps, corrections on the data used by this work for both bands required only a zero order polynomial. The final spectra are displayed in Fig, 5.5.

5.2.3 The Hybrid line Fitting Method

We have named *hybrid* the fitting method developed and used for this work, as it combines the capabilities of standard tools used to make automatic fittings, the flexibility of manual control over the fitting input parameters and the successive analysis of the results using customized scripts, as they evolve through the different parts of the fitting process. The initial step establishes the baseline, removes the continuum (T_C) from the data and estimates the noise on the line free channels (σ_{rms}). The double side band calibration done during the data preparation stage already accounted for contribution from both side bands in the baseline level, leading to the corrected continuum (T_C). Once T_C has been removed, the spectra contain absorption or emission lines.

The CH line analysis requires hyper fine structure (HFS) fitting. CLASS provides a HFS fitting method, but the HFS line parameter files are needed to be provided by the user. These line parameter files contain the relative velocities (Δv_{HFS} or v_i) and intensities (r_i) of each component of the triplet, and they are specific for each band. The sum of all intensities is normalized to one, while the strongest component is also used as the zero velocity reference for all the rest of the components of the triplet (see Table 5.1 and Figure 5.3). The HFS fitting tool works based on several assumptions (Bardeau et al. 2006):

1. Same excitation temperature for all the components of the multiplet.

2. Gaussian profiles for the opacity as a function of velocity.

[2] http://www.iram.fr/IRAMFR/GILDAS

3. The lines (HFS components) all have the same width.

4. The multiplet components do not overlap.

The last assumption is subjective as it depends on the line width that is estimated by the HFS method and partially on the presence of other HFS components at different velocities that might lead to line *blending*. Early attempts of fitting multiple detections proved CLASS to be able to reliably fit the three hyperfine components for one velocity component. It also showed that the most efficient and effective way of fitting lines is by supplying *line-guessing* files. The line-guessing files contain approximated values for the position, line-width, intensity and opacity of the velocity components which are used as starting point for the HFS tool. The tool was not always able to work for all of the suggested lines, yielding wrong fitting results, like line widths of hundreds of km/s. Those cases required user intervention and constraining of line-guessing parameters to specific values, limiting the degrees of freedom of the HFS solver.

Accounting for all these restrictions, the fitting process is performed iteratively: after every step, the fit calculated by the HFS tool is subtracted from the data and so the next fitting step works on the *residual*. This sequence repeats until a final residual is reached such that the result can not be distinguished from the fitting limit, chosen to be in the range of $\pm 3 \cdot \sigma_{rms}$. In the following, the index i refers to the hyperfine component ($i = 1, 2, 3$), while j denotes the velocity component ($j = 1, 2, 3, \ldots, N$). A total of N lines is said to constitute a detection set.

$$\sum_i \tau_{i,j} = p_{4,j} \tag{5.1}$$

$$\tau_{i,j}(v) = \tau_{i,j} \cdot \exp\left[-4 \ln 2 \cdot \left(\frac{v - v_{i,j} - p_{2,j}}{p_{3,j}} \right)^2 \right] \tag{5.2}$$

$$\tau_j(v) = p_{4,j} \cdot \sum_{i=1}^{I} r_i \cdot \exp\left[-4 \ln 2 \cdot \left(\frac{v - v_{i,j} - p_{2,j}}{p_{3,j}} \right)^2 \right] \tag{5.3}$$

$$\tau(v) = \sum_{j=1}^{J} \sum_{i=1}^{I} p_{4,j} \cdot r_i \cdot \exp\left[-4 \ln 2 \cdot \left(\frac{v - v_{i,j} - p_{2,j}}{p_{3,j}} \right)^2 \right] \tag{5.4}$$

$$\Delta T_{L,i,j}(v_{i,j} + p_{2,j}) = \frac{p_{1,j}}{p_{4,j}} \cdot \left(1 - e^{-p_{4,j} r_i} \right) \tag{5.5}$$

$$T_{synth}(v) = \sum_{j=1}^{J} \frac{p_{1,j}}{p_{4,j}} \cdot \left(1 - e^{-\tau_j(v)} \right) + T_C \tag{5.6}$$

$$\Delta_{Fit} = \frac{\sqrt{\sum_{c=1}^{n} \frac{(T_{data,c} - T_{synth,c})^2}{n}}}{\sigma_{rms}} \tag{5.7}$$

For each detection (j) of the set, the HFS method provides a group of four parameters named $T_{Ant} \cdot \tau$, V_{lsr}, ΔV and τ_{main}. These four parameters are also known as p_1, p_2, p_3 and p_4 (Bardeau et al. 2006). The FWHM of the detection corresponds to p_3 (ΔV) and p_2 (V_{lsr}) is the velocity of the strongest component (reference) of the triplet in km/s. The fourth parameter, p_4, corresponds to the sum of all the individual HFS opacities τ_i of the detection at their center lines (Eqns. 5.2, 5.1). Equation 5.5 relates the peak temperature of the i^{th} HFS component of the j^{th} detected line ($T_{L,i,j}$) with the corresponding parameters

$p_{1,j}$, $p_{4,j}$ and the relative intensity of the HFS component (r_i). The peak temperature of every hyperfine component is determined directly from this equation. Equation 5.3 presents the total opacity of the detection over the band, which is then used to compute the synthetic version of the spectra (eq. 5.6) using custom made scripts in HIPE (Herschel Science Ground Segment Consortium 2011; Panuzzo et al. 2012). The synthetic spectrum is constructed based on the assumptions of LTE conditions, lines do not saturate and beam filling factor equal to one. This is a simplification of the formalism presented by Bottinelli et al. (2014).

With the synthetic and the original spectrum, the quality of the fit can be calculated by using the Δ_{Fit} estimator, as defined by equation 5.7. A copy of the parameters set for the first *set* (J_1) of detections is stored and a new line fitting process is performed using slightly modified line-guessing file parameters from the first set. Similarly, a new set of detections (J_2), parameters and fit estimator are obtained and stored and the fitting process is repeated in the same way. In total m detection-sets are produced (J_1, J_2 ... J_m).

On one hand, this line fitting method presents the advantage of being able to fit even small intensity lines by setting line-guessing parameters based on the physical conditions expected. In general the detections of absorptions were constrained by setting the opacity to be optically thin ($\tau_{main} = 0.1$). The HFS tool accounts for this restriction over the other parameters. On the other hand, there is a considerable number of potentially valid solutions and the risk of introducing artifacts is inherent. This is reason for the process to be repeated and carried out systematically. The quality of the total fit depends on the amount of lines fitted, the amplitude of the artifacts introduced and the number of bins (velocity channels) taken into account. They are intrinsic to the Δ_{Fit} estimator.

The best fit that would correctly account for the noise gets a $\Delta_{Fit} = 1$, while values lower than one might mean overfitting, or a poor signal to noise spectra. Based on this, the best fit of the m iterations is finally selected.

5.2.4 HFS in the CH λ149 μm Line Regime

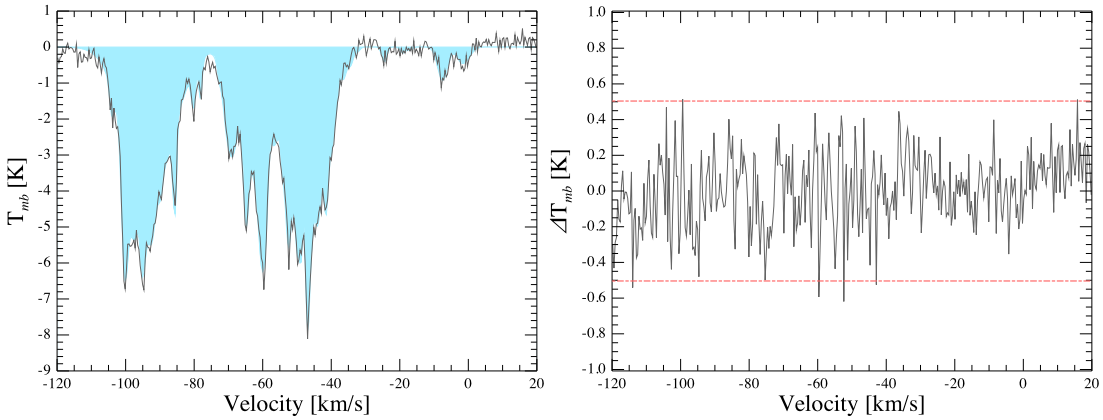

Figure 5.6: Left: λ149 μm spectrum (black line) and the synthetic spectrum using the HFS fit (shaded in blue). Right pane corresponds to the final residual and the noise thresholds. Note the different scales on the ordinates

A simple inspection of the spectrum as displayed in Figure 5.5 reveals only absorption features. The resolution and amount of details in the data allows fitting a large number of components. The rest

Table 5.3: Derived parameters for the CH λ149 μm line as listed by CLASS. Data was acquired using LFA central pixel (LFA-px00). T_C = 11.57 K, with σ_{rms} = 0.17 K

Detection ID #	$[p_1]$ $T_{Ant} \cdot \tau$	$[p_2]$ V_{lsr}	$[p_3]$ ΔV	$[p_4]$ τ_{main}
1	-1.37	-104.0	1.6	0.1
2	-6.7	-100.2	2.4	0.1
3	-2.99	-97.5	2.2	0.1
4	-4.6	-95.3	14.3	0.1
5	-1.51	-95.2	1.4	0.1
6	-3.5	-85.8	1.3	0.1
7	-1.29	-85.3	0.7	0.1
8	-0.85	-78.2	1.1	0.1
9	-4.95	-69.1	5.0	0.1
10	-5.5	-64.8	2.0	0.1
11	-1.2	-62.9	1.6	0.1
12	-7.5	-60.3	3.6	0.1
13	-1.1	-58.7	1.2	0.1
14	-1.64	-56.5	1.9	0.1
15	-1.2	-54.2	1.1	0.1
16	-6.65	-52.3	2.3	0.1
17	-8.65	-49.8	2.1	0.1
18	-2.72	-48.7	1.0	0.1
19	-9.85	-46.9	2.2	0.1
20	-2.85	-44.1	1.8	0.1
21	-1.38	-45.4	1.0	0.1
22	-1.95	-41.9	2.8	0.1
23	-0.75	-39.7	1.6	0.1
24	-0.68	-24.5	1.8	0.1
25	-1.53	-7.5	3.4	0.1

frequencies, relative intensities and velocities of the HFS components of the triplet for the λ149 μm line are listed in Table 5.1 in columns number 3, 9 and 10. The strongest component at 2006.79912 GHz is used as reference for the HFS profile fitting (zero velocity offset). This introduces an offset of 5.45 km/s due to the difference with respect to the used observing frequency (see Table 5.2) which is then compensated during the calculation of the column density.

The continuum level has been determined to be 11.56 K, with a σ_{rms} equals to 0.17 K. The fitting limit used ($3{\cdot}\sigma_{rms}$) is ± 0.5 K.

A total of 25 components were fitted using the method described in subsection 5.2.3 in the spectrum over the velocity range from -120 to 20 km/s. They are listed in Table 5.3. The original (in black) and the synthetic spectrum (shaded in blue) computed from the best fit and the residual (difference of both) are displayed on Figure 5.6, while some of the fitting steps of the process are displayed on Figure 5.7. For the velocity range of interest for this work (-80 to -5 km/s), 20 components of the best fit are taken into account, over 219 spectral channels, yielding a Δ_{Fit} = 1.186 in that band.

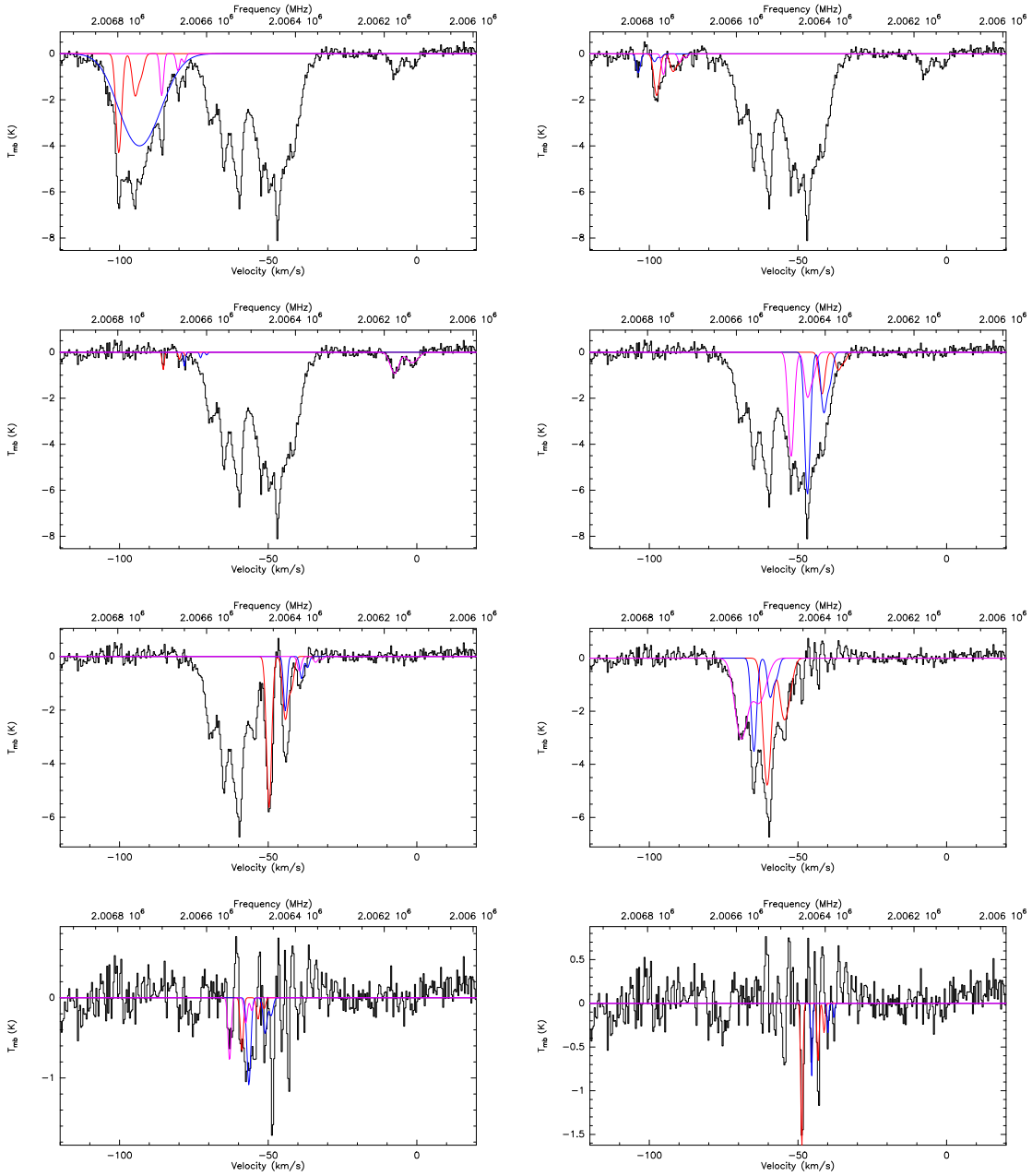

Figure 5.7: Hyper fine splitting fit to the G330.95 spectrum for the CH λ149 μm line. The continuum is removed before fitting. Note that the panels have different ordinate scales.

5.2.5 HFS in the CH λ560 μm Line Regime

The spectrum obtained for the CH λ560 μm line is more complex than that for the λ149 μm line. The continuum level measured T_C is 0.486 K, with σ_{rms} = 0.024 K and fitting limit in ± 0.07 K range.

In the spectrum there are emission features around the -95 km/s coming from a dense and hot molecular clump usually attributed to massive star formation regions. This source is known to be a *hot core* (Kurtz et al. 2000). In addition, absorptions from some of the same clouds depicted by the λ149 μm line and contamination from a different species are present. This last feature is centered at 536.781042 GHz and

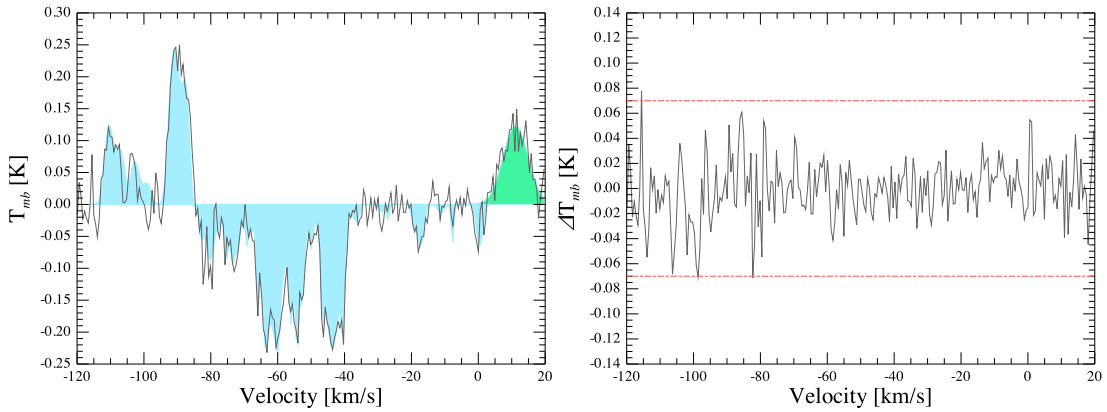

Figure 5.8: Left: CH λ560 μm line spectrum (black line), the synthetic spectrum using the HFS fit (shaded in blue) and the image band polluting line fitted with a single gaussian profile (shaded in green). The right panel corresponds to the final residual and the noise thresholds. Note the scale differences.

does not present the expected triplet profile. It may come as *image band contamination* from methanol line from the hot core (CH_3OH, v_t = 0, [19 317 1] – [19 218 1] with a rest frequency of 526.949841 GHz). Another methanol line -not shown in the figure- also appears at 536.35519 GHz (CH_3OH, v_t = 0, [15 313 1] – [15 214 1] with a rest frequency of 527.171462 GHz).

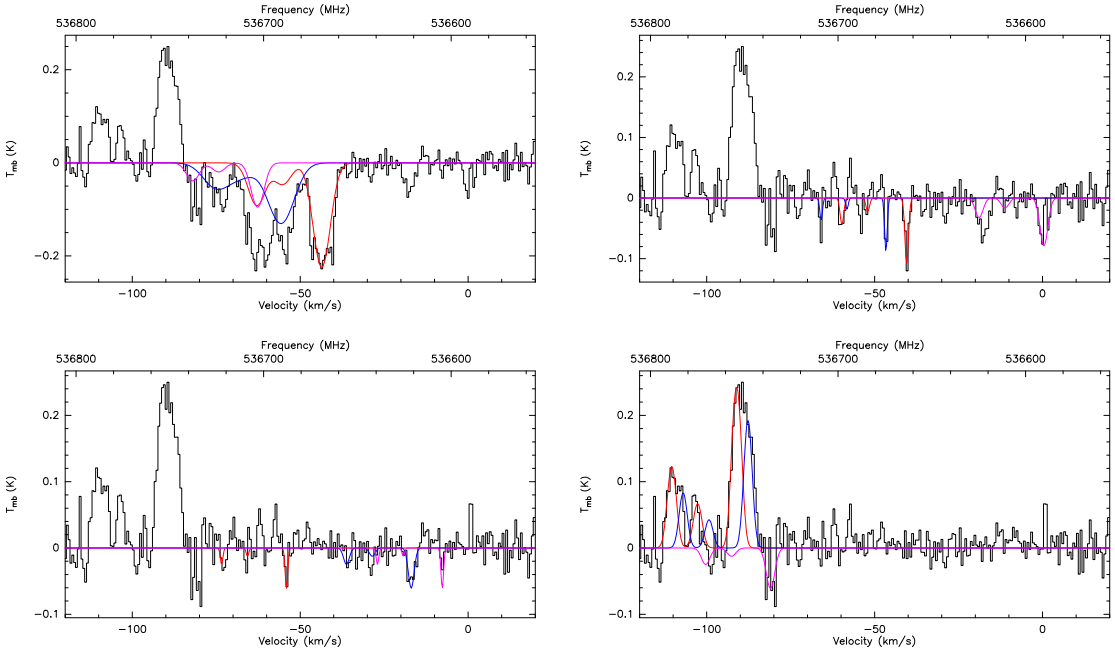

Figure 5.9: Successive hyper fine splitting fit on the G330.95 spectrum for CH559 line. Contamination from methanol is removed before line fitting.

After removing the continuum from the calibrated spectrum and the line contamination using a simple gaussian line fit, the fitting process is carried out in a similar way as for the spectrum at 2 THz (Fig. 5.9). Opacity is set to be thin for the case of absorptions. The result of the iterative process produces a total of

Table 5.4: Derived parameters for CH-λ560 μm line using 4G-1, as listed by CLASS. Continuum level of 0.486 K, with σ = 0.024 K. Detections sorted by velocity. Detections #1 and 2 correspond to emission.

Detection ID #	$[p_1]$ $T_{Ant} \cdot \tau$	$[p_2]$ V_{lsr}	$[p_3]$ ΔV	$[p_4]$ τ_{main}
1	0.58	-91.1	3.0	1.4
2	0.35	-87.7	2.8	0.4
3	-0.05	-80.5	2.2	0.1
4	-0.05	-69.0	1.0	0.1
5	-0.1	-66.0	1.0	0.1
6	-0.2	-63.5	1.8	0.1
7	-0.24	-60.4	3.2	0.1
8	-0.1	-50.1	1.5	0.1
9	-0.1	-56.1	1.0	0.1
10	-0.14	-55.7	3.3	0.1
11	-0.22	-54.2	1.1	0.1
12	-0.18	-52.8	1.5	0.1
13	-0.15	-46.6	0.9	0.1
14	-0.37	-43.6	5.5	0.1
15	-0.2	-40.4	1.3	0.1
16	-0.1	-17.1	2.0	0.1
17	-0.1	-7.7	0.9	0.1
18	-0.11	0.45	2.3	0.1

16 absorptions and two emissions over the range from -120 to 20 km/s. The original spectrum and the synthetic spectrum reconstructed from the best fit and calculated residual are displayed on Figure 5.8. As for the velocity range of interest of this work, only 15 absorptions are taken into account. The calculated Δ_{fit} value over 146 channels is 0.833.

5.2.6 Determination of the Column Densities and Analysis

For the determination of the column densities it is required to recall the key basic assumptions made:

- CH absorbs the photons from background continuum source.
- The hyperfine lines are in LTE.
- CH absorption does not saturate.

The opacity of a component in absorption can be derived from the group of parameters from CLASS. However the continuum level is not properly addressed by those parameters as prior to the line fitting T_C has been removed. When comparing equation 5.5 and the equation for absorption (5.8), two direct relationship are established (Eqns. 5.9 and 5.10). By inserting 5.9 into 5.10, the equation 5.11 is derived. This one reintroduces the continuum and provides an expression for the opacity at the central velocity of each component of the HFS triplet. The sign of $p_{1,j}$ is neglected as absorption fitting yields to negative values of this parameter.

$$\Delta T_L = T_L - T_C = T_C \cdot (1 - e^{-\tau}) \tag{5.8}$$

$$T_C = \frac{p_{1,j}}{p_{4,j}} \tag{5.9}$$

$$\tau = p_{4,j} \cdot r_{i,j} \tag{5.10}$$

$$\tau_{i,j}(v_{i,j} + p_{2,j}) = \frac{|p_{1,j}|}{T_C} \cdot r_i \tag{5.11}$$

$$\tau_{i,j} = \sqrt{\frac{\ln 2}{\pi}} \cdot \frac{A_{E,i}}{4\pi \cdot FWHM_j} \cdot \left(\frac{c}{\nu_{i,j}}\right)^3 \cdot \frac{g_{u,i}}{Q(T)} \cdot \exp\left[-\frac{E_{L,i}}{kT}\right] \cdot N_{TOT,j} \tag{5.12}$$

The HFC opacity ($\tau_{i,j}$) and the total column density for CH ($N_{TOT,j}$) are related by equation 5.12 (e.g., Wiesemeyer et al. 2016), where $A_{E,i}$ stands for the Einstein coefficient, $g_{u,i}$ the upper level degeneracy, $E_{L,i}$ the ground state energy level and $\nu_{i,j}$ the velocity shifted component frequency of the i^{th} hyper fine component. $Q(T)$ corresponds to the partition function and temperature (T) is the CMB temperature (2.73 K) (Winkel et al. 2017). The specific parameters for each HFS component are listed in Table 5.1.

Tables 5.5 and 5.6 display the estimated column densities for each velocity component. Columns 5 of each table displays the estimated molecular hydrogen column density, using the relation from Sheffer et al. (2008) ($[N(CH)]/[N(H_2)] = 3.5 \times 10^{-8}$).

In order to make the column densities from the different bands comparable, the column density profiles $N_v(CH_{\lambda 149 \mu m})$ and $N_v(CH_{\lambda 560 \mu m})$ are derived (Eq. 5.13), resampled to the same velocity resolution and presented in Figure 5.10. In addition, the N_v(OH) estimated by Wiesemeyer et al. (2016) on the same source using the GREAT M_a channel on board SOFIA in July 2013 has been conveniently scaled and overlaid in gray.

The beam size (Figure 5.4) difference between 4G-1 (52") and LFAH-px00 (15.5") requires careful analysis. The same foreground element seen at $\lambda 149$ μm, assuming a beam filling factor close to one, may not necessarily fill the beam of 4G-1. In addition, the 4G-1 beam could include other foreground clouds and even background elements which are not in the beam of LFAH-px00. This has implications for the way the spectra look in terms of emissions and absorptions, continuum level and noise.

The presence of contamination from the image band for the CH $\lambda 560$ μm line also prohibits the data processing and analysis of the 0 km/s vicinity range.

$$\frac{\mathrm{d}N}{\mathrm{d}v} = N_v = \sum_{j=1}^{m} N_{v,j} = \sum_{j=1}^{m} 2 \cdot \sqrt{\frac{\ln 2}{\pi}} \cdot \exp\left[-4 \cdot \log 2 \cdot \left(\frac{v - v_j}{FWHM_j}\right)^2\right] \cdot \frac{N_{TOT,j}}{FWHM_j} \tag{5.13}$$

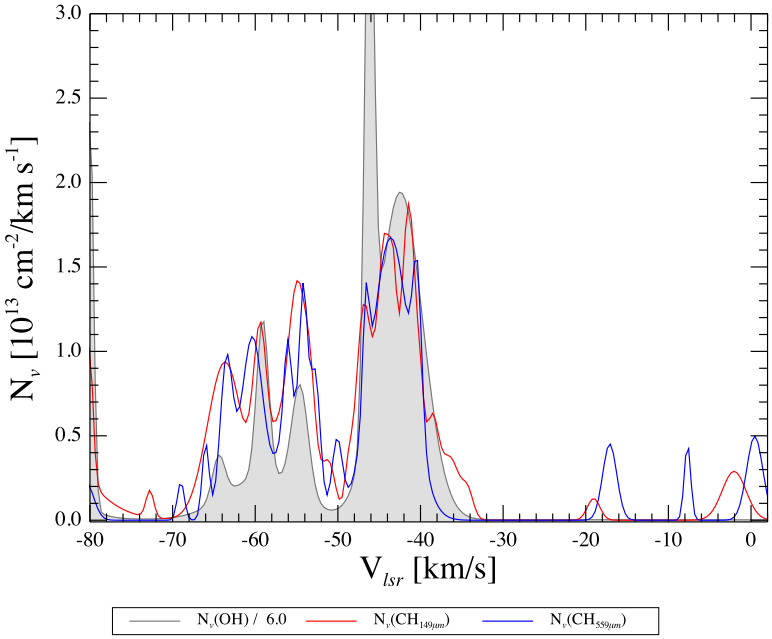

Figure 5.10: Column density profiles derived from the fitting. In red, CH λ149 μm, CH λ560 μm in blue. OH, in gray kindly provided by Wiesemeyer et al. (2016)

Table 5.5: Total column density of CH λ560 μm at different detection velocities in the range investigated

Detection ID #	V_{lsr} [km/s]	FWHM [km/s]	N($CH_{\lambda 560\mu m}$) [10^{12} / cm^2]	N(H_2) [10^{19} / cm^2]
3	-80.5	2.2	5.15	14.72
4	-69.0	1.0	2.34	6.69
5	-66.0	1.0	2.34	6.69
6	-63.5	1.8	4.21	12.04
7	-60.4	3.2	7.49	21.40
8	-50.1	1.5	3.51	10.03
9	-56.1	1.0	2.34	6.69
10	-55.7	3.3	7.72	22.07
11	-54.2	1.1	2.57	7.36
12	-52.8	1.5	3.51	10.03
13	-46.6	0.9	2.13	6.07
14	-43.6	5.5	12.87	36.77
15	-40.4	1.3	2.95	8.42
16	-17.1	2.0	4.68	13.37
17	-7.7	0.9	2.12	6.07

Table 5.6: Total column density for CH λ149 μm and H_2 at different velocity components.

Detection ID #	V_{lsr} [km/s]	FWHM [km/s]	N($CH_{\lambda 149 \mu m}$) [10^{12}/cm^2]	N(H_2) [10^{19}/cm^2]
6	-85.8	1.3	3.03	8.66
7	-85.3	0.7	1.63	4.66
8	-78.2	1.1	2.56	7.32
9	-69.1	5.0	11.65	33.28
10	-64.8	2.0	4.66	13.31
11	-62.9	1.6	3.61	10.36
12	-60.3	3.4	7.80	22.29
13	-58.7	1.2	2.80	7.99
14	-56.5	1.9	4.47	12.65
15	-54.2	1.1	2.45	6.99
16	-52.3	2.3	5.24	14.97
17	-49.8	2.1	4.89	13.98
18	-48.7	1.0	2.21	6.32
19	-46.9	2.2	5.12	14.64
20	-44.1	1.8	4.17	11.91
21	-45.4	0.9	2.14	6.12
22	-41.9	2.8	6.48	18.50
23	-39.7	1.6	3.61	10.31
24	-24.5	1.8	4.15	11.84
25	-7.5	3.4	7.89	22.55

5.3 Discussion and Conclusions

The hybrid analysis method developed and presented for this work has shown to be a good tradeoff between automatic fitting, by using the HFS tool from CLASS, and with the user controlling the parameters of the line fit *candidates* while working recursively. In addition, suggested amplitude values were also set in certain cases controlling in detail the fit. Although this whole process seems tedious at first sight, the ability of fitting weak and/or narrow lines pays-off.

The Monte-Carlo fit method used by Wiesemeyer et al. (2018) offers a good fitting, in a (semi) automatized way, but has many degrees of freedom and is very computing demanding. Based on the minimization (control) of the residuals, it has the advantage of being able to fit weak features. In the same way, fitting noise or *overfitting* is an inherent risk.

On the other hand, WEEDS (Maret et al. 2011), an extension for CLASS, follows a forward fitting approach by assuming that complex lines (like HFS) are the superposition of individual Gaussian line profiles. WEEDS also requires a set of (5) parameters for the fitting of each line independently and the fitting optimization algorithm convergence is biased by the signal to noise ratio.

The method used by Jacob (2017) is based on deconvolution and the use of a Wiener filter. It probed to be direct and *unbiased*, however is currently limited to spectra that do not present blending of emission and absorption nor strong saturation. The inherent use of an apodization window for the signal processing introduces features in the deconvolved data, like Gibbs distortions (Proakis 2007). This method looks very promising and is still evolving.

A fifth tool for fitting, XCLASS[3], is an extension for the Common Astronomy Software Applications CASA[4], the ALMA data pipeline tool. However no real experience has been made with it in this work.

Components of different spiral arms can be easily distinguished when plotting the column density profiles in both CH λ560 μm and CH λ149 μm (Figure 5.10). The range from -78 to -50 km/s corresponds to the Norma arm while Crux ranges from -50 to -30 km/s. The column density profiles in these velocity intervals reflect the different physical conditions encountered in these spiral arms and, eventually, various chemical regimes (Figs. 5.1 and 5.2). However some differences are possibly due to the dissimilar sensitivity. While CH λ149 μm has a continuum level of 11.8 K, CH λ560 μm falls to 0.488 K.

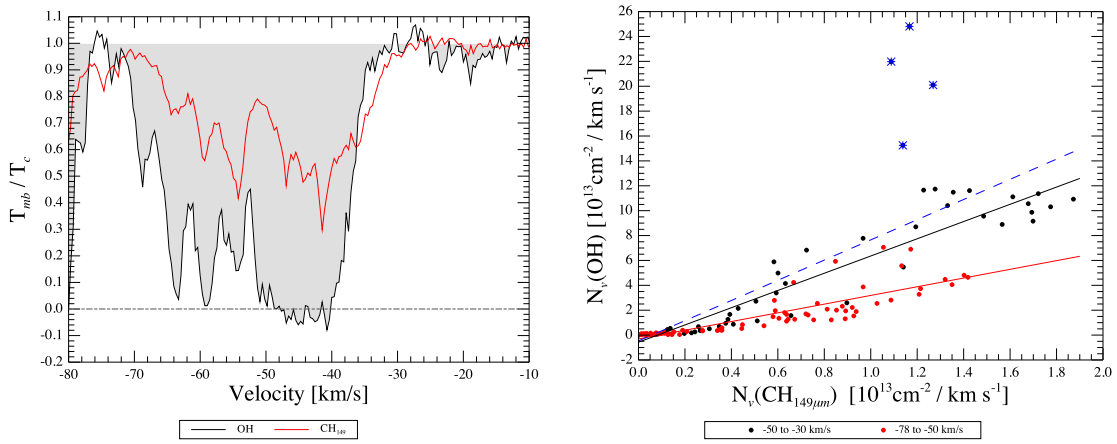

Figure 5.11: Left: Observed CH λ149 μm (red) and OH absorption (gray) spectra towards G330.95. Right: Correlation between column density profiles of OH and CH149 in the spiral arms regions (-80 to -30 km/s). There are two distinguishable data scattering areas, corresponding to different spiral arms. OH data kindly provided by Wiesemeyer et al. (2016)

The validity of methylidyne as a non-saturating H_2 tracer has been shown throughout this chapter. First by revising the chemical relation between them, and then by using two different CH hyperfine splitting lines observed towards a bright background source. The derived opacities and column densities using the hybrid fitting method, allowed the estimation of the N_{tot} for CH at λ560 μm and λ149 μm for two different velocity ranges. The total column density ratios (as defined in Table 5.7) only differ by a remarkable 1.7% between the two velocity ranges. This implies that both LFAH-px00 and 4G-1 beams are fully filled by the same low density clouds and both channels are complementary when making this kind of studies.

Table 5.7: Total column densities and ratios per arm and specie.

Spiral arm	(v_{min}, v_{max}) [km/s]	N($CH_{\lambda560\mu m}$) [10^{13} cm^{-2}]	N($CH_{\lambda149\mu m}$) [10^{13} cm^{-2}]	N(OH) [10^{14} cm^{-2}]	N($CH_{\lambda560\mu m}$)/ N($CH_{\lambda149\mu m}$)	N(OH)/ N($CH_{\lambda149\mu m}$)
Norma	(-78, -50)	11.76	14.02	4.03	1.19	2.88
Crux	(-50, -30)	11.94	14.49	10.83	1.214	7.47

Plotting the column density profiles of CH λ149 μm and OH (provided by Wiesemeyer et al. 2016),

[3] https://xclass.astro.uni-koeln.de
[4] https://casa.nrao.edu/

towards G330.95 (Fig. 5.11) reveals that data scatters in two different areas, depending on the velocity. Focusing only on the Norma arm (red dots) a line can be fit and a simple relation can be derived (Eq. 5.14). This implies that in absence of OH, CH could be present, and may be taken as a hint that in the low-density regime CH forms more efficiently than OH (Godard et al. 2014). The data for the Crux arm (represented by black and blue dots) shows a big dispersion as OH saturates, and a linear fit leads to a different relationship.

$$[N_v(OH)] = 3.496 \cdot [N_v(CH_{149\mu m})] - 0.308 \text{ , all in} \times 10^{13} \text{ cm}^{-2} \tag{5.14}$$

With more sightline studies it will be most interesting to confirm whether different spiral arms and galactocentric distance show different correlations, as suggested by the different slopes in Fig. 5.11. In the same manner, relationships between CH and other hydrides could be established.

The Herschel/HIFI instrument allowed remarkable ISM gas studies like the *PRobing the InterStellar medium Molecules with Absorption line Studies* or PRISMAS[5]. Given the lifespan of HIFI, PRISMAS was limited to 8 sources over 128 hours of guaranteed time. Studies of this kind are currently only possible by using GREAT aboard SOFIA with no other scientific instrument/platform in the close horizon.

[5] http://astro.ens.fr/index.cgi?exe=175&xar=PRISMAS

CHAPTER 6

Conclusions

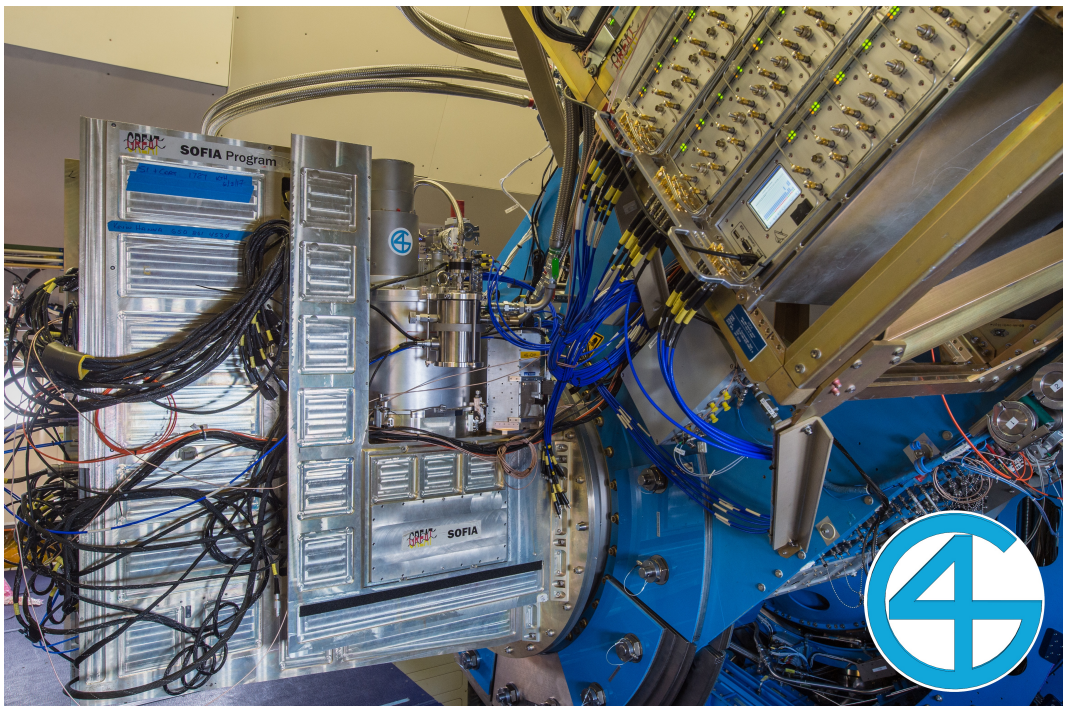

Figure 6.1: 4GREAT aboard SOFIA and ready for its first-light flight on July 11^{th}, 2017

GREAT, as a powerful wide band spectrometer has enabled very broad range of studies of the ISM. GREAT data have allowed to confirm and refine galactic (Tiwari et al. 2018; Pérez-Beaupuits et al. 2012) and extragalactic (Okada et al. 2015) PDR models, tracking the dynamics of outflows resulting from protostellar accretion processes (Leurini et al. 2014; Schneider et al. 2018) and of cloud formation mechanisms (Bisbas et al. 2018). Line of sight absorption studies of diffuse ISM chemistry (Wiesemeyer et al. 2018) have been an important area to which GREAT has already made important contributions, which will be significantly extended with 4GREAT as will be studies of denser gas (Wyrowski et al. 2016; Csengeri et al. 2012), fundamental for the star forming process.

4GREAT has brought new scientific opportunities to this highly demanding SOFIA/GREAT community. The frequency-multiplexing and simultaneous observations enabled by its four bands allows a more efficient use of the limited observing time on board SOFIA.

4GREAT targets molecular and atomic lines of unique importance. A particular scientific case presented in this thesis work describes the use of the methylidyne radical (CH), detectable in the 4G-1 (and 4G-3) and the upGREAT LFA bands, as a tracer of line-of-sight low density molecular gas in absorption, using a bright radio continuum background source. CH does not suffer from saturation, like other hydrides, and thanks to the high resolution of GREAT and a systematic and careful data analysis, a very precise column density profile could be determined. The profile ratios derived using the two CH transitions clearly distinguish between the Galactic arms and offer more details than previous studies using (the frequently saturated) OH as tracer. With similar studies towards different line of sights it will be possible to greatly enhance CH's capabilities as a diffuse ISM probe and allow comparison with other molecules.

With the addition of 4GREAT to GREAT, the number of cryostat configurations is now limited to two (LFA + HFA, 4GREAT + HFA), which has reduced significantly the technical overheads. All-closed-cycle operation does eliminate the need for daily cryogen service before flight and makes the system operation more robust, but more versatile.

The short time scale (15 months) over which 4GREAT was designed, built, commissioned and put in full service was possible because of the availability of key components, including the detectors and their basic interfaces, and the experience of the team involved in the development.

6.1 Synergy with other Instruments and Observatories

Although SOFIA/GREAT is rather unique, there are scientific and technical complementarities with other observatories and instruments around the globe.

Technical Synergy

A high degree of technical synergy between SOFIA/GREAT and other facilities facilities exists on different levels.

The specific experience used to design and build the components of GREAT has been gathered over years of constructing instrumentation by the different partner groups forming the GREAT consortium. Some noteworthy examples are:

* The SIS mixers, used in 4G-1 and 4G-2 are inherited from the HERSCHEL/HIFI instrument.
* Multi beam heterodyne receiver layout, like the one used by the APEX/CHAMP+ instrument[1], and the LO splitting by Fourier grating mirrors technique has been used on the GREAT arrays.
* The development of the FFTS started as experimental backends for APEX, improving and expanding their spectral capabilities generation after generation, maturing a design scheme that finally has seen now three generations installed (an updated) at SOFIA/GREAT.
* The bias electronics modules developed for SIS mixers and different LNA architectures matured at APEX. The second generation of them is in use at GREAT.

Much of the GREAT technology development has profited from synergy with APEX were analogous versions of many of its components could be tested and debugged.

In a reciprocal way, the use of solid state multiplication chains and synthesizers as LO sources permeated from GREAT/SOFIA to APEX, where they are now being used in current, but also in forthcoming instrumentation, making diplexers obsolete at the working frequencies of APEX.

[1] http://www.mpifr-bonn.mpg.de

Scientific Synergy

The scientific synergy offered by the overlapping and complementary frequency windows between GREAT and ground based facilities is obvious.

The 900-1000 GHz band is covered by both 4G-2 and the APEX/1THz receivers. The atmospheric transmission at SOFIA (~90 %) and therefore the sensibility of 4G-2 has no match; APEX's site on Chajnantor site has much worse transmission in this range. On the other hand, APEX, with its 12 m diameter telescope, has a ~6" beam size compared to the 26" of 4G-2, and its dish has a surface quality of ~ 10 μm, making it highly efficient. Similar synergy exists between SOFIA/4G-1 and APEX/nFLASH-2[2] for the [CI] line at 492 GHz. SOFIA/4G-1 offers a beam of 52", while APEX/nFLASH-2 has a theoretical value of 12.7 arcsec.

The CO ladder, starting at J=5-4, covered by GREAT (Table J.2) is complemented by the lower excitation lines of J=2-1 covered by nFLASH-1, J=3-2 by LASMA[3] (a 7 beam array) and J=4-3 with nFLASH-2, all of them newly on APEX.

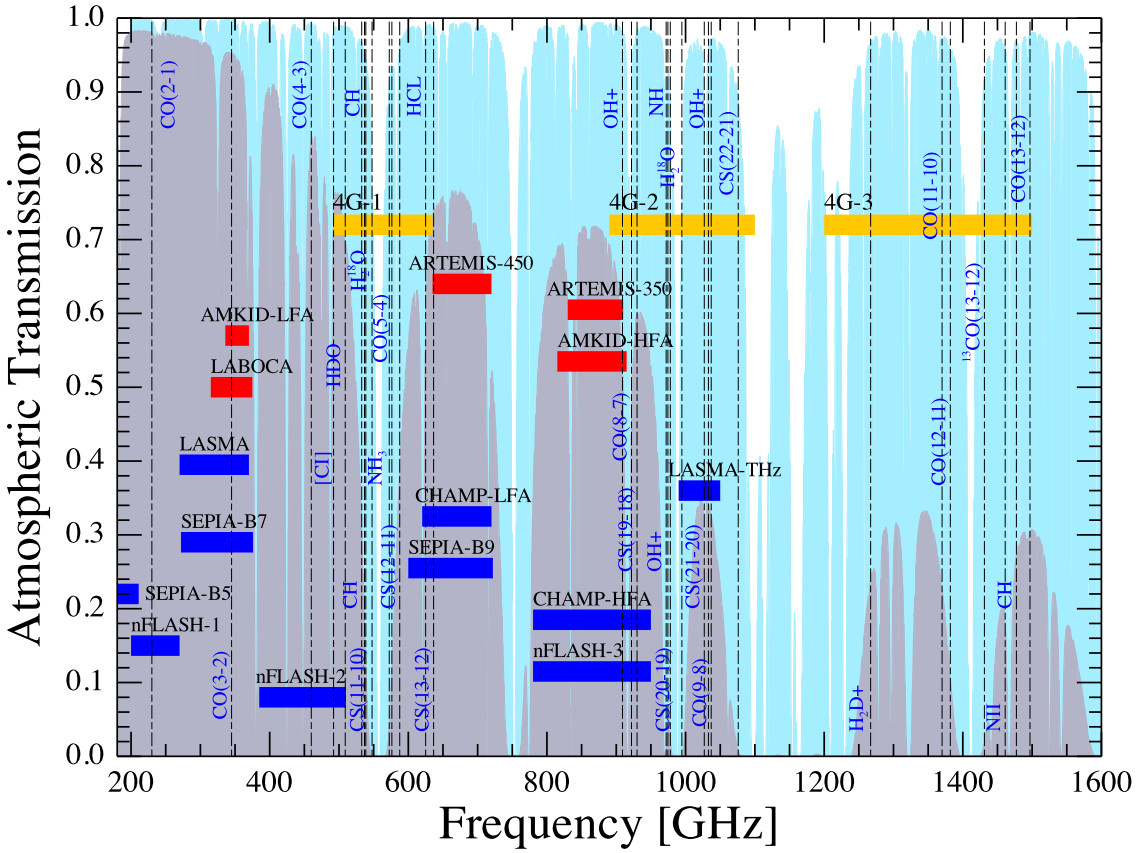

Figure 6.2: 4GREAT and the APEX instrumentation frequency coverage, including the planned extension to be installed between 2018–2022. The frequency ranges covered by APEX and SOFIA heterodyne receivers are indicated by bars colored blue and orange, respectively. Those covered by direct detection APEX receivers are shown in red. Some important spectral lines are marked.

[2] A new multicolor receiver facility instrument for APEX, expected to be commissioned in 2019 (Klein 2018)
[3] http://www.apex-telescope.org/instrumentation

6.2 Outlook

6.2.1 Improvements and upgrades

New Generation of Mixers

The HEB detectors developed by KOSMA have shown a remarkable performance. Different generations have been built for most of the bands, in a constant evolution process. The target specifications for a new generation would require less LO power, higher rolloff frequency and therefore wider effective IF band.

A More Powerful 4G-4LO Source

As the technology for solid state LO chains evolves, more power, spectrally clean and more stable sources become available. Once a better and stable chain with average power of more than 30 μW (significantly more than the current 5 μW) would be available, the diplexer used for the LO coupling of 4G-4 could be replaced by a coupling grid as it happens with the other 4GREAT channels. This comes with lower receiver temperature and a wider instantaneous IF bandwidth, allowing the detection of more and/or broader lines.

Expansion of the HFA

When designing the HFA array, adding a second polarization was considered as a potential future upgrade. This would imply seven new mixers with the corresponding upgrades in the optics plate. More detectors imply important changes for many subsystems of GREAT. The IF and bias controllers would need to accommodate seven additional new electronics modules and interface boxes or require a complete redesign. The current LO box would require a second LO source (QCL) to pump the second polarization and therefore a major redesign.

More Frequency Bands

The addition of new cryostat to the GREAT constellation, covering scientifically important lines from H_2 at λ28 μm and [OIII] at λ51 and λ88 μm. A system like this, needing 3 LO sources a 3.41, 5.2 and 10.74 THz will push the development of new wide-band flexibly tunable local oscillator sources, based either on photonics or QCLs. Some of the common optical elements of GREAT, as mirrors and grids, would require better manufacturing and precision. Moreover, the optics coupling method might need to change.

6.2.2 GREAT II: A Complete New Instrument

A more ambitious plan would consider the complete redesign of GREAT. While still keeping the successful modular approach as design philosophy, a totally different layout of the structure would save weight and make better use of the allowed instrument envelope.

A higher density array with several junctions (and horns), of wider IF bandwidth and requiring less LO power, all integrated in the same mixer block, will demand a major development, with the intrinsic benefit of better resolution on sky and mapping speed. Such a change would come with the use of improved optical quality of the already excellent components, including windows, optical filters, gratings, mirrors and grids. An expanded capabilities and temperature insensitive wide band IF processor modules would interface the frontend to the backend, and a new FFTS generation, which is certain to come, would cover 6.5 GHz (or more) of bandwidth and 128K spectral channels per pixel.

Bibliography

Ade, P. A. R., G. Pisano, C. Tucker and S. Weaver (2006), "A review of metal mesh filters", *Society of Photo-Optical Instrumentation Engineers (SPIE) Conference Series*, vol. 6275, Proc. SPIE 62750U (cit. on p. 32).

André, P., J. Di Francesco, D. Ward-Thompson, S.-I. Inutsuka, R. E. Pudritz and J. E. Pineda (2014), *From Filamentary Networks to Dense Cores in Molecular Clouds: Toward a New Paradigm for Star Formation*, Protostars and Planets VI 27, arXiv: 1312.6232 (cit. on p. 1).

Baars, J. W. M. (2007), *The paraboloidal reflector antenna in radio astronomy and communication: theory and practice*, Astrophysics and Space Science Library, Springer, URL: https://cds.cern.ch/record/1251572 (cit. on p. 6).

Bahner, K. (1967), "Teleskope", *Optische Instrumente / Optical Instruments*, ed. by S. Flügge, Springer Berlin Heidelberg 227, ISBN: 978-3-642-46077-7, URL: https://doi.org/10.1007/978-3-642-46077-7_6 (cit. on pp. 4, 29, 38).

Balanis, C. A. (2005), *Antenna theory : analysis and design* (cit. on p. 5).

Bardeau, S., J. Pety, P. Hily-Blant, S. Guilloteau, B. Delforge, T. Forveille and R. Lucas (2006), *CLASS: Continuum and Line Analysis Single-dish Software*, English, version Version 1.1, IRAM, November 21, 2006 (cit. on pp. 97, 98).

Behrens, G., W. Campbell, D. Williams and S. White (1997), *NRAO EDIR 306: Guidelines for the Design of Cryogenic Systems*, tech. rep., National Radio Astronomy Observatory - Electronics Division, URL: http://library.nrao.edu/edir.shtml (cit. on p. 67).

Belitsky, V. (1999), *ALMA Memo 264: Local Oscillator Power Requirements for ALMA SIS Mixers*, tech. rep., Atacama Large Millimeter Array, URL: https://library.nrao.edu/public/memos/alma/memo264.pdf (cit. on p. 17).

Benford, D. J., M. C. Gaidis and J. W. Kooi (2003), *Optical properties of Zitex in the infrared to submillimeter*, Appl. Opt. **42** 5118, URL: http://ao.osa.org/abstract.cfm?URI=ao-42-25-5118 (cit. on pp. 54, 67, 135, 136).

Best, R. (2003), *Phase-Locked Loops*, McGraw-Hill professional engineering, McGraw-Hill Education, ISBN: 9780071501231, URL: https://books.google.de/books?id=lasCAI23NBYC (cit. on p. 20).

Billot, N. et al. (2006), "The Herschel/PACS 2560 bolometers imaging camera", *Society of Photo-Optical Instrumentation Engineers (SPIE) Conference Series*, vol. 6265, Proc. SPIE 62650D, eprint: astro-ph/0606623 (cit. on p. 11).

Bisbas, T. G., J. C. Tan, T. Csengeri, B. Wu, W. Lim, P. Caselli, R. Güsten, O. Ricken and D. Riquelme (2018), *The inception of star cluster formation revealed by [C II] emission around an Infrared Dark Cloud*, MNRAS **478** L54, arXiv: 1803.00566 (cit. on p. 109).

Blundell, R. (2004), "The Submillimeter Array Antennas and Receivers",
Fifteenth International Symposium on Space Terahertz Technology, ed. by G. Narayanan 3
(cit. on p. 8).
Bottinelli, S., V. Wakelam, E. Caux, C. Vastel, Y. Aikawa and C. Ceccarelli (2014),
CH in absorption in IRAS 16293-2422, MNRAS **441** 1964, arXiv: 1405.0846 [astro-ph.SR]
(cit. on p. 99).
Büchel, D. et al. (2015), *4.7-THz Superconducting Hot Electron Bolometer Waveguide Mixer*,
IEEE Transactions on Terahertz Science and Technology **5** 207 (cit. on pp. 18, 35, 44).
Cámara Mayorga, I. (2008), *Photomixers as tunable terahertz local oscillators*,
PhD thesis: University of Bonn, Germany,
URL: http://hss.ulb.uni-bonn.de/2008/1570/1570.htm (cit. on p. 22).
Cámara Mayorga, I., A. Schmitz, T. Klein, C. Leinz and R. Gusten (2012),
First In-Field Application of a Full Photonic Local Oscillator to Terahertz Astronomy,
IEEE Transactions on Terahertz Science and Technology **2** 393 (cit. on pp. 21, 22).
Carlstrom, J. E., R. L. Plambeck and D. D. Thornton (1985),
A continuously tunable 65-115-GHz Gunn oscillator,
IEEE Transactions on Microwave Theory Techniques **33** 610 (cit. on p. 20).
Cherednichenko, S., V. Drakinskiy, T. Berg, E. L. Kollberg and I. Angelov (2007),
The Direct Detection Effect in the Hot-Electron Bolometer Mixer Sensitivity Calibration,
IEEE Transactions on Microwave Theory Techniques **55** 504 (cit. on p. 18).
Clarricoats, P. J. B. and A. D. Olver (1984),
Corrugated horns for microwave antennas / P.J.B. Clarricoats and A.D. Olver, English,
P. Peregrinus on behalf of the Institution of Electrical Engineers London, UK vii, 231 p. :
ISBN: 0863410030 (cit. on p. 131).
CMT, Caltech., URL: http://www.caltechmicrowave.org/amplifiers (cit. on pp. 32, 34, 48).
Cooley, J. and J. Tukey (1965), *An Algorithm for the Machine Calculation of Complex Fourier Series*,
Mathematics of Computation **19** 297 (cit. on p. 25).
Cotton, D. V., J. Bailey and L. Kedziora-Chudczer (2014),
Atmospheric modelling for the removal of telluric features from infrared planetary spectra,
MNRAS **439** 387, arXiv: 1312.5824 [astro-ph.EP] (cit. on p. 6).
Crill, B. P. et al. (2003), *BOOMERANG: A Balloon-borne Millimeter-Wave Telescope and Total Power
Receiver for Mapping Anisotropy in the Cosmic Microwave Background*, ApJS **148** 527,
eprint: astro-ph/0206254 (cit. on p. 9).
Crowe, T. W., J. L. Hesler, W. L. Bishop, G. S. Schoenthal and K. Hui (2009),
"Terahertz Local Oscillator Sources",
Twentieth International Symposium on Space Terahertz Technology,
ed. by E. Bryerton, A. Kerr and A. Lichtenberger 37 (cit. on pp. 20, 32, 49).
Cryomech, Cryomech, Inc., URL: http://www.cryomech.com/ (cit. on p. 62).
Cryovac, CryoVac Gesellschaft für Tieftemperaturtechnik mbH & Co. KG,
URL: http://www.cryovac.de/ (cit. on pp. 32, 37, 62).
Csengeri, T., K. M. Menten, F. Wyrowski, M. A. Requena-Torres, R. Güsten, H. Wiesemeyer,
H.-W. Hübers, P. Hartogh and K. Jacobs (2012), *SOFIA observations of far-infrared hydroxyl emission
toward classical ultracompact HII/OH maser regions*, A&A **542**, L8 L8, arXiv: 1203.4987
(cit. on p. 109).
Cuadrado-Calle, D. et al. (2017),
Broadband MMIC LNAs for ALMA Band 2+3 With Noise Temperature Below 28 K,
IEEE Transactions on Microwave Theory Techniques **65** 1589 (cit. on p. 16).

Cui, M., J. N. Hovenier, Y. Ren, N. Vercruyssen, J. R. Gao, T. Y. Kao, Q. Hu and J. L. Reno (2013), *Beam and phase distributions of a terahertz quantum cascade wire laser*, Applied Physics Letters **102**, 111113 111113 (cit. on p. 21).

de Graauw, T. et al. (2009), "The Herschel-Heterodyne Instrument for the Far-Infrared (HIFI)", *EAS Publications Series*, ed. by L. Pagani and M. Gerin, vol. 34, EAS Publications Series 3 (cit. on pp. 11, 25, 39).

de Graauw, T. et al. (2010), *The Herschel-Heterodyne Instrument for the Far-Infrared (HIFI)*, aap **518**, L6 L6 (cit. on p. 39).

De Lange, G. (2016), *HIFI 4 mixers sizes*, Personal communication by Email (cit. on p. 46).

de Lange, G., B. D. Jackson, M. Jochemsen, W. M. Laauwen, L. de Jong, M. Kroug, T. Zijlstra and T. M. Klapwijk (2006), "Performance of the flight model HIFI band 3 and 4 mixer units", *Society of Photo-Optical Instrumentation Engineers (SPIE) Conference Series*, vol. 6275, Proc. SPIE 627517 (cit. on p. 46).

de Lange, G. et al. (2003), "Development of the HIFI Band 3 and 4 Mixer Units", *Fourteenth International Symposium on Space Terahertz Technology*, ed. by C. Walker and J. Payne 447 (cit. on p. 46).

Delorme, Y. (2016), *Internal FS(M)02 Test Report*, tech. rep., LERMA (cit. on p. 44).

Draine, B. (2010), *Physics of the Interstellar and Intergalactic Medium*, Princeton Series in Astrophysics, Princeton University Press, ISBN: 9781400839087, URL: https://books.google.de/books?id=FycJvKHyiwsC (cit. on pp. 1, 94).

Duband, L., A. Lange and A. Ravex (1991), "A miniature adsorption He-3 refrigerator", *ESA, 4th European Symposium on Space Environmental Control Systems, Volume 1 p 407-409 (SEE N92-25828 16-18)* (cit. on p. 11).

Dunham Jr., T. (1937), *Interstellar Neutral Potassium and Neutral Calcium*, PASP **49** 26 (cit. on p. 92).

Durán, C. (2018), "Synergy between APEX and 4GREAT at SOFIA", "Science with the Atacama Pathfinder EXperiment. Schloss Ringberg, Germany.", URL: https://events.mpifr-bonn.mpg.de/indico/event/58/timetable/?ttLyt=room#all.detailed (cit. on p. 64).

Ekin, J. W. (2006), *Experimental techniques for low-temperature measurements*, Oxford University Press (cit. on pp. 67, 136).

Erickson, E. F. and A. W. Meyer (2013), *NASA's Kuiper Airborne Observatory, 1971-1995: An Operations Retrospective With a View to SOFIA*, tech. rep., NASA, URL: https://history.arc.nasa.gov/hist_pdfs/nasasp2013-216025.pdf (cit. on p. 8).

Faist, J., F. Capasso, D. L. Sivco, C. Sirtori, A. L. Hutchinson and A. Y. Cho (1994), *Quantum Cascade Laser*, Science **264** 553 (cit. on p. 21).

Ferrite-Quasar, Ferrite-Quasar, URL: http://www.ferrite-quasar.ru (cit. on p. 47).

Fissel, L. M. et al. (2010), "The balloon-borne large-aperture submillimeter telescope for polarimetry: BLAST-Pol", *Millimeter, Submillimeter, and Far-Infrared Detectors and Instrumentation for Astronomy V*, vol. 7741, Proc. SPIE, arXiv: 1007.1390 [astro-ph.IM] (cit. on p. 9).

Gardner, J. P. et al. (2006), *The James Webb Space Telescope*, Space Sci. Rev. **123** 485, eprint: astro-ph/0606175 (cit. on pp. 8, 11).

Gerin, M., D. A. Neufeld and J. R. Goicoechea (2016), *Interstellar Hydrides*, ARA&A **54** 181, arXiv: 1601.02985 (cit. on pp. 3, 91, 92).

Gerin, M. et al. (2010), *Interstellar CH absorption in the diffuse interstellar medium along the sight-lines to G10.6-0.4 (W31C), W49N, and W51*, A&A **521**, L16 L16 (cit. on p. 91).

Godard, B., E. Falgarone, M. Gerin, P. Hily-Blant and M. de Luca (2010), *Molecular absorption lines toward star-forming regions: a comparative study of HCO^+, HNC, HCN, and CN*, A&A **520**, A20 A20, arXiv: 1006.0582 (cit. on p. 92).

Godard, B., E. Falgarone and G. Pineau des Forêts (2014), *Chemical probes of turbulence in the diffuse medium: the TDR model*, A&A **570**, A27 A27, arXiv: 1408.3716 (cit. on pp. 93, 108).

Goldsmith, P. (1998), *Quasioptical Systems: Gaussian Beam Quasioptical Propogation and Applications*, IEEE Press Series on RF and Microwave Technology, Wiley, ISBN: 9780780334397, URL: https://books.google.de/books?id=q0uOQgAACAAJ (cit. on pp. 5, 57, 61, 67, 75, 125, 129, 131).

Graf, U. (2016), *Question about L1 and L2 horns.* Personal communication by Email (cit. on p. 52).

– (2017), *Button Simulation*, Personal communication by Email (cit. on pp. 85, 86).

Graf, U. U. and S. Heyminck (2001), *Fourier gratings as submillimeter beam splitters*, IEEE Transactions on Antennas and Propagation **49** 542 (cit. on p. 35).

Graf, U. U. (2016), *A Compact Beam Measurement Setup*, English, Journal of Infrared, Millimeter, and Terahertz Waves **37** 770 (cit. on p. 75).

Granet, C., G. L. James, R. Bolton and G. Moorey (2004), *A Smooth-Walled Spline-Profile Horn as an Alternative to the Corrugated Horn for Wide Band Millimeter-Wave Applications*, IEEE Transactions on Antennas and Propagation **52** 848 (cit. on pp. 34, 47).

Griffin, M. J. et al. (2010), *The Herschel-SPIRE instrument and its in-flight performance*, A&A **518**, L3 L3, arXiv: 1005.5123 [astro-ph.IM] (cit. on pp. 9, 11).

Gružinskis, V., J. H. Zhao, P. Shiktorov and E. Starikov (1998), "Gunn Effect and THz Frequency Power Generation in n+- n - n+ GaN Structures", *Ultrafast Phenomena in Semiconductors*, vol. 297, Materials Science Forum, Trans Tech Publications 341 (cit. on p. 20).

Guan, X., J. Stutzki, U. U. Graf, R. Güsten, Y. Okada, M. A. Requena-Torres, R. Simon and H. Wiesemeyer (2012), *GREAT/SOFIA atmospheric calibration*, A&A **542**, L4 L4, arXiv: 1203.1661 [astro-ph.IM] (cit. on pp. 6, 22, 97).

Guilloteau, S. (2002), *ALMA Memo 393: DSB versus SSB and Bandwidth/Sensitivity Tradeoff*, tech. rep., Atacama Large Millimeter Array, URL: http://library.nrao.edu/alma.shtml (cit. on p. 15).

Gunn, J. B. (1963), *Microwave oscillations of current in III V semiconductors*, Solid State Communications **1** 88 (cit. on p. 19).

Güsten, R. (2015), *Memo: First concept study of a low-frequency extension of the GREAT* (cit. on p. 39).

Güsten, R., L. Å. Nyman, P. Schilke, K. Menten, C. Cesarsky and R. Booth (2006), *The Atacama Pathfinder EXperiment (APEX) - a new submillimeter facility for southern skies -*, A&A **454** L13 (cit. on p. 6).

Heiter, C. (2017), *4GREAT frequency measurements on Zitex.* Personal communication by Email (cit. on pp. 54, 136).

Herschel Science Ground Segment Consortium (2011), *HIPE: Herschel Interactive Processing Environment*, Astrophysics Source Code Library, ascl: 1111.001 (cit. on p. 99).

Heyminck, S., U. U. Graf, R. Güsten, J. Stutzki, H. W. Hübers and P. Hartogh (2012), *GREAT: the SOFIA high-frequency heterodyne instrument*, A&A **542**, L1 L1, arXiv: 1203.2845 [astro-ph.IM] (cit. on pp. 30, 39, 63).

Higgins, R. et al. (2014), *The effect of sideband ratio on line intensity for Herschel/HIFI*, Experimental Astronomy **37** 433, arXiv: 1404.2806 [astro-ph.IM] (cit. on pp. 45, 46).

Hinkley, R. K., J. A. Hall, T. E. H. Walker and W. G. Richards (1972), *Λ doubling in $^2\Pi$ states of diatomic molecules*, Journal of Physics B Atomic Molecular Physics **5** 204 (cit. on p. 95).

Hollenbach, D. J. and A. G. G. M. Tielens (1997), *Dense Photodissociation Regions (PDRs)*, ARA&A **35** 179 (cit. on pp. 1, 4).

Horn, J., O. Siebertz, F. Schmülling, C. Kunz, R. Schieder and G. Winnewisser (1999), *A 4x1 GHz Array Acousto-Optical Spectrometer*, Experimental Astronomy **9** 17 (cit. on p. 33).

Huang, Y. D. (et al. (2016), "The Atacama Large Millimeter/sub-millimeter Array band-1 receiver", *Modeling, Systems Engineering, and Project Management for Astronomy VI*, vol. 9911, Proc. SPIE 99111V, arXiv: 1612.00893 [astro-ph.IM] (cit. on pp. 15, 16).

Jackson, B., J. Evers, W. Wild and G. de Lange (2002), *Mixer Unit Band 4 Specification*, tech. rep., Doc Id. FPSS-00062: SRON/HIFI (cit. on pp. 46, 49).

Jacob, A. (2017), *CH as a tracer for molecular hydrogen: Forming synergies between its far-infrared and radio fingerprints*, MA thesis: Mathematisch-Naturwissenschaftlichen Fakultät der Rheinischen Friedrich-Wilhelms-Universität Bonn (cit. on p. 106).

Jellema, W. (2015), *Optical design and performance verification of Herschel-HIFI*, PhD thesis: University of Groningen, ISBN: 978-90-367-7443-7 (cit. on pp. 39, 52, 131).

Johansson, J. F. (1995), "A Comparison of Some Feed Types", *Multi-Feed Systems for Radio Telescopes*, ed. by D. T. Emerson and J. M. Payne, vol. 75, Astronomical Society of the Pacific Conference Series 82 (cit. on p. 132).

Kadin, A. (1999), *Introduction to Superconducting Circuits*, A Wiley Interscience publication, Wiley, ISBN: 9780471314325, URL: https://books.google.de/books?id=kChTAAAAMAAJ (cit. on p. 17).

Kaper, L. (1998), "Winds in Ob-Type Stars", *Ultraviolet Astrophysics Beyond the IUE Final Archive*, ed. by W. Wamsteker, R. Gonzalez Riestra and B. Harris, vol. 413, ESA Special Publication 149, eprint: astro-ph/9712201 (cit. on p. 1).

Kessler, M. F. et al. (1996), *The Infrared Space Observatory (ISO) mission.*, A&A **315** L27 (cit. on p. 9).

Kidd, S. (1964), *Astronomical ballooning: the Stratoscope program*, New Scientist **409** 702, URL: https://books.google.com/books?id=3qpBF3BjFE4C&pg=PA702 (cit. on p. 9).

Klein, B. (2017), "A new Fast Fourier Transform Spectrometer for upGREAT and 4GREAT", "Spectroscopy with SOFIA: new results & future opportunities. Schloss Ringberg, Germany.", URL: https://events.mpifr-bonn.mpg.de/indico/event/16/session/1/contribution/6/material/slides/0.pdf (cit. on pp. 25, 36, 64).

– (2018), "MPIfR APEX instrumentation", "Science with the Atacama Pathfinder EXperiment. Schloss Ringberg, Germany.", URL: https://events.mpifr-bonn.mpg.de/indico/event/58/timetable/?ttLyt=room#all.detailed (cit. on p. 111).

Klein, B., S. Hochgürtel, I. Krämer, A. Bell, K. Meyer and R. Güsten (2012), *High-resolution wide-band fast Fourier transform spectrometers*, A&A **542**, L3 L3, arXiv: 1203.3972 [astro-ph.IM] (cit. on pp. 26, 33).

Klein, B., S. D. Philipp, I. Krämer, C. Kasemann, R. Güsten and K. M. Menten (2006), *The APEX digital Fast Fourier Transform Spectrometer*, A&A **454** L29 (cit. on pp. 33, 64).

Kooi, J. (2008), *Advanced Receivers for Submillimeter and Far Infrared Astronomy:* Rijksuniversiteit Groningen, ISBN: 9789036736534, URL: https://books.google.de/books?id=2xuhOwAACAAJ (cit. on p. 12).

Krabbe, A. (2000), "SOFIA telescope", *Airborne Telescope Systems*, ed. by R. K. Melugin and H.-P. Röser, vol. 4014, Proc. SPIE 276, eprint: astro-ph/0004253 (cit. on pp. 29, 38).
Krieg, B. M., M. Salez, J. Evers, W. Wild and J. M. Lamarre (2002), *Specification Mixer Unit Band 1*, tech. rep., Doc Id. FPSS-00006: P-LERMA/HIFI/SP/2002-001 (cit. on p. 44).
Kugler, Kugler GmbH, URL: https://www.kugler-precision.com/ (cit. on p. 36).
Kulesa, C. (2011), *Terahertz Spectroscopy for Astronomy: From Comets to Cosmology*, IEEE Transactions on Terahertz Science and Technology **1** 232 (cit. on p. 2).
Kurtz, S., R. Cesaroni, E. Churchwell, P. Hofner and C. M. Walmsley (2000), *Hot Molecular Cores and the Earliest Phases of High-Mass Star Formation*, Protostars and Planets IV 299 (cit. on p. 101).
LabView, National Instruments Corporation., URL: https://www.ni.com/ (cit. on p. 64).
Lakeshore, Lake Shore Cryotronics, Inc., URL: http://www.lakeshore.com (cit. on p. 49).
Lamb, J. W. (1992), *NRAO EDIR 290: Infrared Filters for Cryogenic Receivers*, tech. rep., National Radio Astronomy Observatory - Electronics Division, URL: http://library.nrao.edu/edir.shtml (cit. on pp. 54, 67, 135).
– (2000), *ALMA Memo 301: SSB vs. DSB for Submillimeter Receivers*, tech. rep., Atacama Large Millimeter Array, URL: http://library.nrao.edu/alma.shtml (cit. on p. 15).
Leinz, C., M. Caris, T. Klein, G. de Lange, T. Zijlstra, T. M. Klapwijk, H. J. Wunsch and R. Güsten (2010), "A 1THz Receiver System at APEX", *Twenty-First International Symposium on Space Terahertz Technology* 130 (cit. on p. 46).
Lemke, D. (1970), *Die astronomische Ballonsonde THISBE.*, Sterne und Weltraum **9** 29 (cit. on p. 9).
Lesurf, J. C. G. (1981), *Gaussian optics and the design of Martin-Puplett diplexers*, Infrared Physics **21** 383 (cit. on pp. 33, 50, 59).
Leurini, S., C. Codella, A. López-Sepulcre, A. Gusdorf, T. Csengeri and S. Anderl (2014), *SiO excitation from dense shocks in the earliest stages of massive star formation*, A&A **570**, A49 A49, arXiv: 1409.4181 (cit. on p. 109).
LNF, Low Noise Factory., URL: http://www.lownoisefactory.com (cit. on p. 48).
Lord, S. D. (1992), *A new software tool for computing Earth's atmospheric transmission of near- and far-infrared radiation*, tech. rep. (cit. on p. 6).
Maret, S., P. Hily-Blant, J. Pety, S. Bardeau and E. Reynier (2011), *Weeds: a CLASS extension for the analysis of millimeter and sub-millimeter spectral surveys*, A&A **526**, A47 A47, arXiv: 1012.1747 [astro-ph.IM] (cit. on p. 106).
Martin, C. L., Stratospheric TeraHertz Observatory (STO) Team and Gal/Xgal U/LDB Spectroscopic/Stratospheric THz Observatory (GUSSTO) Team (2012), "Terahertz Ballooning: STO And GUSSTO", *American Astronomical Society Meeting Abstracts #220*, vol. 220, American Astronomical Society Meeting Abstracts 134.09 (cit. on p. 9).
McGrath, W. R., B. Karasik, A. Skalare, I. Siddiqi and D. Prober (2002), "Superconductive Hot Electron Bolometer Mixers", *Far-IR, Sub-mm & MM Detector Technology Workshop* 69 (cit. on p. 18).
Mimura, T., S. Hiyamizu, T. Fujii and K. Nanbu (1980), *A New Field-Effect Transistor with Selectively Doped GaAs/n-$Al_xGa_{1-x}As$ Heterojunctions*, Japanese Journal of Applied Physics **19** L225 (cit. on p. 15).
Minicircuits, Mini-Circuits (Scientific Components Corp.), URL: http://www.minicircuits.com/ (cit. on p. 86).
Miteq, L3 Narda Miteq., URL: https://nardamiteq.com (cit. on pp. 34, 47).

Molinari, S. et al. (2014), *The Milky Way as a Star Formation Engine*, Protostars and Planets VI 125, arXiv: 1402.6196 (cit. on p. 1).

Muñoz, P., S. Bedorf, M. Brandt, T. Tils, N. Honingh and K. Jacobs (2004), "Fabrication and characterization of phonon-cooled hot-electron bolometers on freestanding 2-μm silicon nitride membranes for THz applications", *Z-Spec: a broadband millimeter-wave grating spectrometer: design, construction, and first cryogenic measurements*, ed. by C. M. Bradford et al., vol. 5498, Proc. SPIE 834 (cit. on p. 46).

Muñoz, P., S. Bedorf, M. Brandt, T. Tils, N. Honingh and K. . Jacobs (2006), *THz Waveguide Mixers With NbTiN HEBs on Silicon Nitride Membranes*, IEEE Microwave and Wireless Components Letters **16** 606 (cit. on p. 47).

Murakami, H. et al. (2007), *The Infrared Astronomical Mission AKARI**, PASJ **59** S369, arXiv: 0708.1796 (cit. on p. 10).

Neufeld, D. A., M. G. Wolfire and P. Schilke (2005), *The Chemistry of Fluorine-bearing Molecules in Diffuse and Dense Interstellar Gas Clouds*, ApJ **628** 260, eprint: astro-ph/0504304 (cit. on p. 91).

Neugebauer, G. et al. (1984), *The Infrared Astronomical Satellite (IRAS) mission*, ApJ **278** L1 (cit. on p. 9).

Okada, Y., M. A. Requena-Torres, R. Güsten, J. Stutzki, H. Wiesemeyer, P. Pütz and O. Ricken (2015), *Velocity resolved [C ii], [C i], and CO observations of the N159 star-forming region in the Large Magellanic Cloud: a complex velocity structure and variation of the column densities*, A&A **580**, A54 A54, arXiv: 1506.01860 (cit. on p. 109).

Ossenkopf, V. (2008), *The stability of spectroscopic instruments: a unified Allan variance computation scheme*, aap **479** 915, eprint: 0712.4335 (cit. on pp. 22, 79).

Otárola, A., M. Holdaway, L. Nyman, S. Radford and B. Butler (2005), *Atmospheric TRANSPARENCY AT CHAJNANTOR: 1973-2003*, tech. rep., Atacama Large Millimeter Array, URL: http://library.nrao.edu/alma.shtml (cit. on p. 6).

Paine, S. (2018), *The am atmospheric model*, URL: https://doi.org/10.5281/zenodo.1193646 (cit. on p. 6).

Panuzzo, P., J. Li and E. Caux (2012), "PlotXY: A High Quality Plotting System for the Herschel Interactive Processing Environment (HIPE) and the Astronomical Community", *Astronomical Data Analysis Software and Systems XXI*, ed. by P. Ballester, D. Egret and N. P. F. Lorente, vol. 461, Astronomical Society of the Pacific Conference Series 845, arXiv: 1207.3921 [cs.GR] (cit. on p. 99).

Pardo, J. R., J. Cernicharo and E. Serabyn (2001), *Atmospheric transmission at microwaves (ATM): an improved model for millimeter/submillimeter applications*, IEEE Transactions on Antennas and Propagation **49** 1683 (cit. on p. 6).

Pascale, E. et al. (2008), *The Balloon-borne Large Aperture Submillimeter Telescope: BLAST*, ApJ **681** 400, arXiv: 0711.3465 (cit. on p. 9).

Pearson, J. C. et al. (2011), *Demonstration of a room temperature 2.48-2.75 THz coherent spectroscopy source*, Review of Scientific Instruments **82**, 093105-093105-9 (cit. on p. 20).

Pérez-Beaupuits, J. P., H. Wiesemeyer, V. Ossenkopf, J. Stutzki, R. Güsten, R. Simon, H.-W. Hübers and O. Ricken (2012), *The ionized and hot gas in M17 SW. SOFIA/GREAT THz observations of [C II] and ^{12}CO J = 13-12*, A&A **542**, L13 L13, arXiv: 1203.1560 (cit. on p. 109).

Phillips, T. G., P. J. Huggins, T. B. H. Kuiper and R. E. Miller (1980),
Detection of the 610 micron /492 GHz/ line of interstellar atomic carbon, ApJ **238** L103 (cit. on p. 3).
Pilbratt, G. L. et al. (2010),
Herschel Space Observatory. An ESA facility for far-infrared and submillimetre astronomy,
A&A **518**, L1 L1, arXiv: 1005.5331 [astro-ph.IM] (cit. on p. 10).
Pozar, D. (2004), *Microwave Engineering*, Wiley, ISBN: 9780471448785,
URL: https://books.google.de/books?id=4wzpQwAACAAJ (cit. on pp. 15, 16, 23).
Proakis, J. (2007), *Digital Signal Processing: Principles, Algorithms, And Applications, 4/E*,
Pearson Education, ISBN: 9788131710005,
URL: https://books.google.de/books?id=CTw6GoBh-vkC (cit. on pp. 23, 106).
Pütz, P. (2016), *4GREAT: M Mixer general questions*, Personal communication by Email (cit. on p. 47).
Pütz, P., D. Büchel, K. Jacobs, M. Schultz and C. Honing (2015),
"1.9 THz Waveguide HEB Mixers for the upGREAT Low Frequency Array",
26Th International Symposium on Space Terahertz Technology (cit. on p. 34).
Pütz, P., C. E. Honingh, K. Jacobs, M. Justen, M. Schultz and J. Stutzki (2012),
Terahertz hot electron bolometer waveguide mixers for GREAT, A&A **542**, L2 L2,
arXiv: 1204.2381 [astro-ph.IM] (cit. on pp. 32, 44).
Pütz, P., K. Jacobs, M. Justen, F. Schomaker, M. Schultz, S. Wulff and C. E. Honingh (2011),
NbTiN Hot Electron Bolometer Waveguide Mixers on Si_3N_4 Membranes at THz Frequencies,
IEEE Transactions on Applied Superconductivity **21** 636 (cit. on p. 47).
QMC, QMC Instruments Ltd., URL: http://www.terahertz.co.uk/ (cit. on pp. 52, 54, 57, 62).
Rabanus, D., C. Granet, A. Murk and T. Tils (2006),
Measurement of properties of a smooth-walled spline-profile feed horn around 840 GHz,
Infrared Physics and Technology **48** 181 (cit. on pp. 47, 52, 132).
Radebaugh, R. (2000), "Pulse tube cryocoolers for cooling infrared sensors", vol. 4130,
URL: http://dx.doi.org/10.1117/12.409878 (cit. on p. 62).
Rich, A. (1983), *AN-347: Shielding and Guarding*, tech. rep., Analog Devices,
URL: http://www.analog.com/media/en/technical-documentation/application-notes/41727248AN_347.pdf?doc=CN0397.pdf (cit. on p. 86).
Richter, H., M. Wienold, L. Schrottke, K. Biermann, H. T. Grahn and H. W. H¸bers (2015),
4.7-THz Local Oscillator for the GREAT Heterodyne Spectrometer on SOFIA,
IEEE Transactions on Terahertz Science and Technology **5** 539, ISSN: 2156-342X (cit. on pp. 21, 32).
Richter, H., N. Rothbart, M. Wienold, L. Schrottke, H. T. Biermann Klaus und Grahn and H.-W. Hübers
(2017), "Local Oscillator for a 4.7-THz Multi-Pixel Heterodyne Receiver Based on a
Quantum-Cascade Laser." (cit. on p. 35).
Risacher, C. (2005), *Low noise SIS mixers and cryogenic amplifiers for sub-millimeter astronomy*,
PhD thesis: Chalmers Tekniska Hogskola, Sweden (cit. on p. 16).
Risacher, C. et al. (2016a),
First Supra-THz Heterodyne Array Receivers for Astronomy With the SOFIA Observatory,
IEEE Transactions on Terahertz Science and Technology **6** 199, arXiv: 1512.02908 [astro-ph.IM]
(cit. on pp. 20, 31, 35, 37, 39).
Risacher, C. et al. (2016b),
The upGREAT 1.9 THz multi-pixel high resolution spectrometer for the SOFIA Observatory,
A&A **595**, A34 A34, arXiv: 1607.04239 [astro-ph.IM] (cit. on pp. 34, 35, 62).
Roelfsema, P. R. et al. (2018),
SPICA - a large cryogenic infrared space telescope Unveiling the obscured Universe, ArXiv e-prints,
arXiv: 1803.10438 [astro-ph.IM] (cit. on p. 11).

RPG, RPG-Radiometer Physics GmbH, URL: http://www.radiometer-physics.de/ (cit. on pp. 34, 47).

Russell, R. W. (1985), "The Lear Jet Observatory - fifteen years of discovery and rebirth.", *NASA Conference Publication*, vol. 2353, NASA Conference Publication 26 (cit. on p. 8).

Ruze, J. (1966), *Antenna Tolerance Theory – A Review*, IEEE Proceedings **54** (cit. on pp. 5, 67, 129).

Schieder, R. T., O. Siebertz, C. Gal, M. Olbrich, F. Schloeder, R. Bieber, F. Schmuelling, V. Tolls and J. M. M. Horn (2003), "Toward very large bandwidth with acousto-optical spectrometers", *Millimeter and Submillimeter Detectors for Astronomy*, ed. by T. G. Phillips and J. Zmuidzinas, vol. 4855, Proc. SPIE 290 (cit. on p. 25).

Schneider, N. et al. (2018), *Anatomy of the massive star-forming region S106: The OI 63 micron line observed with GREAT/SOFIA as a versatile diagnostic tool for the evolution of massive stars*, ArXiv e-prints, arXiv: 1806.00991 (cit. on p. 109).

Sheffer, Y., M. Rogers, S. R. Federman, N. P. Abel, R. Gredel, D. L. Lambert and G. Shaw (2008), *Ultraviolet Survey of CO and H_2 in Diffuse Molecular Clouds: The Reflection of Two Photochemistry Regimes in Abundance Relationships*, ApJ **687**, 1075-1106 1075, arXiv: 0807.0940 (cit. on pp. 91, 104).

Siebertz, O., F. Schmülling, C. Gal, F. Schloeder, P. Hartogh, V. Natale and R. Schieder (2007), "The Wide-Band Spectrometer (WBS) for the HIFI instrument of Herschel", *Eighteenth International Symposium on Space Terahertz Technology*, ed. by A. Karpov 135 (cit. on p. 25).

Smith, E. C. et al. (2014), "SOFIA science instruments: commissioning, upgrades and future opportunities", *Ground-based and Airborne Instrumentation for Astronomy V*, vol. 9147, Proc. SPIE 914706 (cit. on p. 9).

Smith, W. (1966), *Modern optical engineering*, McGraw-Hill, URL: https://books.google.de/books?id=yelEAAAAIAAJ (cit. on p. 38).

Snow, T. P. and B. J. McCall (2006), *Diffuse Atomic and Molecular Clouds*, ARA&A **44** 367 (cit. on pp. 3, 91).

SOFIA Science Center, ed. (2017), *SOFIA Observer's Handbook for Cycle 6*, Universities Space Research Association (USRA), URL: https://www.sofia.usra.edu/science/proposing-and-observing/sofia-observers-handbook-cycle-6 (cit. on p. 96).

Stark, A. A. et al. (2001), *The Antarctic Submillimeter Telescope and Remote Observatory (AST/RO)*, PASP **113** 567, eprint: astro-ph/0008253 (cit. on p. 8).

Sumitomo, Sumitomo Heavy Insdustries, Ltd. - Cryogenic Group, URL: http://www.shicryogenics.com/products/compressors/ (cit. on pp. 37, 62).

Swings, P. and L. Rosenfeld (1937), *Considerations Regarding Interstellar Molecules*, ApJ **86** 483 (cit. on p. 92).

Tiwari, M., K. M. Menten, F. Wyrowski, J. P. Pérez-Beaupuits, H. Wiesemeyer, R. Güsten, B. Klein and C. Henkel (2018), *Unveiling the remarkable photodissociation region of M8*, ArXiv e-prints, arXiv: 1803.10164 (cit. on p. 109).

Transmit, TransMIT Gesellschaft für Technologietransfer mbH., URL: https://www.transmit.de/ (cit. on pp. 37, 62, 153).

Tydex, Tydex J.S.Co., URL: http://www.tydexoptics.com (cit. on p. 54).

Vallée, J. P. (2008), *New Velocimetry and Revised Cartography of the Spiral Arms in the Milky Way: A Consistent Symbiosis*, AJ **135**, 1301-1310 1301 (cit. on p. 96).

van Dishoeck, E. F. and J. H. Black (1986),
Comprehensive models of diffuse interstellar clouds - Physical conditions and molecular abundances,
ApJS **62** 109 (cit. on p. 94).
– (1988), *The photodissociation and chemistry of interstellar CO*, ApJ **334** 771 (cit. on p. 94).
Vanderveen, W. (1989), "The James Clerk Maxwell telescope", *Infrared Spectroscopy in Astronomy*,
ed. by E. Böhm-Vitense, vol. 290, ESA Special Publication (cit. on p. 8).
Vankka, J. and K. Halonen (2010), *Direct Digital Synthesizers: Theory, Design and Applications*,
The Springer International Series in Engineering and Computer Science, Springer US,
ISBN: 9781441948953, URL: https://books.google.de/books?id=XYdKcgAACAAJ (cit. on p. 20).
VDI, Virginia Diodes, Inc, URL: http://vadiodes.com/ (cit. on pp. 20, 21, 50, 52, 57).
Villanueva, G. (2004), *The High Resolution Spectrometer for SOFIA-GREAT: Instrumentation,
Atmospheric Modeling and Observations*,
PhD thesis: Max-Planck-Institut für Sonnensystemforschung (cit. on p. 26).
Villanueva, G. and P. Hartogh (2004),
The High Resolution Chirp Transform Spectrometer for the Sofia-Great Instrument,
Experimental Astronomy **18** 77 (cit. on p. 33).
Wagner-Gentner, A. (2007),
Aufbau, Optimierung und Charakterisierung der THz-Optik für GREAT auf SOFIA,
PhD thesis: University of Cologne, Germany (cit. on p. 33).
Wagner-Gentner, A., U. U. Graf, M. Philipp, D. Rabanus and J. Stutzki (2004), "GREAT optics",
*Z-Spec: a broadband millimeter-wave grating spectrometer: design, construction, and first cryogenic
measurements*, ed. by C. M. Bradford et al., vol. 5498, Proc. SPIE 464 (cit. on pp. 33, 37).
Walker, C. (2015), *Terahertz Astronomy*, CRC Press, ISBN: 9781466570436 (cit. on pp. 2–4, 132).
Walker, C. et al. (2018),
"GUSTO: Gal/Xgal U/LDB Spectroscopic-Stratospheric TeraHertz Observatory",
American Astronomical Society Meeting Abstracts #231, vol. 231,
American Astronomical Society Meeting Abstracts (cit. on p. 9).
Walker, C. et al. (2010), "The Stratospheric THz Observatory (STO)",
Ground-based and Airborne Telescopes III, vol. 7733, Proc. SPIE 77330N (cit. on p. 9).
Werner, M. W. et al. (2004), *The Spitzer Space Telescope Mission*, ApJS **154** 1,
eprint: astro-ph/0406223 (cit. on pp. 10, 95).
Whiting Dolci, W. (1997), *Milestones in Airborne Astronomy: From the 1920' to the Present*,
American Institute of Aeronautics and Astronautics, Inc. (cit. on p. 8).
Wieching, G. (2007), *CONDOR: A Heterodyne Receiver for Astronomical Observations at 1.5 THz*,
PhD thesis: University of Cologne, Germany (cit. on p. 47).
Wienen, M. et al. (2015),
ATLASGAL - Kinematic distances and the dense gas mass distribution of the inner Galaxy,
A&A **579**, A91 A91, arXiv: 1503.00007 [astro-ph.SR] (cit. on p. 91).
Wiesemeyer, H., R. Güsten, S. Heyminck, K. Jacobs, K. M. Menten, D. A. Neufeld,
M. A. Requena-Torres and J. Stutzki (2012),
High-resolution absorption spectroscopy of the OH $^2\Pi_{3/2}$ *ground state line*, A&A **542**, L7 L7,
arXiv: 1203.1744 [astro-ph.GA] (cit. on p. 91).
Wiesemeyer, H., R. Gusten, K. Menten, T. Durán C.A.and Csengeri, A. Jacob, R. Simon, J. Stutzki and
F. Wyrowski (2018),
Unveiling the chemistry of interstellar CH: Spectroscopy of the 2 THz N = 2 <- 1 ground state line,
A&A (cit. on pp. 91, 94, 106, 109).

Wiesemeyer, H. et al. (2016), *Far-infrared study of tracers of oxygen chemistry in diffuse clouds*, A&A **585**, A76 A76, arXiv: 1602.03472 (cit. on pp. 96, 104, 105, 107).

Wilson, T. L., K. Rohlfs and S. Hüttemeister (2009), *Tools of Radio Astronomy*, Springer-Verlag (cit. on pp. 4, 5, 16).

Winkel, B., H. Wiesemeyer, K. M. Menten, M. Sato, A. Brunthaler, F. Wyrowski, D. Neufeld, M. Gerin and N. Indriolo (2017), *Hydrogen in diffuse molecular clouds in the Milky Way. Atomic column densities and molecular fraction along prominent lines of sight*, A&A **600**, A2 A2, arXiv: 1702.05956 (cit. on p. 104).

Winnewisser, C., F. Lewen and H. Helm (1998), *Transmission characteristics of dichroic filters measured by THz time-domain spectroscopy*, Applied Physics A: Materials Science & Processing **66** 593 (cit. on pp. 28, 32).

Wootten, A. and A. R. Thompson (2009), *The Atacama Large Millimeter/Submillimeter Array*, IEEE Proceedings **97** 1463, arXiv: 0904.3739 [astro-ph.IM] (cit. on p. 8).

Wyrowski, F., R. Güsten, K. M. Menten, H. Wiesemeyer, T. Csengeri, S. Heyminck, B. Klein, C. König and J. S. Urquhart (2016), *Infall through the evolution of high-mass star-forming clumps*, A&A **585**, A149 A149, arXiv: 1510.08374 [astro-ph.SR] (cit. on p. 109).

Yoshii, Y. et al. (2010), "The University of Tokyo Atacama Observatory 6.5m telescope project", *Ground-based and Airborne Telescopes III*, vol. 7733, Proc. SPIE 773308 (cit. on p. 8).

Young, E. T. et al. (2012a), "Early science results from SOFIA", *Ground-based and Airborne Telescopes IV*, vol. 8444, Proc. SPIE 844410 (cit. on p. 28).

Young, E. T. et al. (2012b), *Early Science with SOFIA, the Stratospheric Observatory For Infrared Astronomy*, ApJ **749**, L17 L17, arXiv: 1205.0791 [astro-ph.IM] (cit. on p. 28).

Acknowledgements

It has been a long way since a friend -César Muñoz- convinced me to apply for a news paper announced position in Chile back in 2003. That was my first real approach into astronomy, working as electronics engineer for the freshly installed Atacama Pathfinder EXperiment; since then, 15 years have passed. For the almost 12 years I worked at APEX I met many people and to my surprise, I have crossed paths with some of them over and over even again. Some of them have been very influential on my career and motivated me to reach to this point.

Figure 6.1: The author at SOFIA in May 2016. Palmdale, California, USA.

Dr. Rolf Güsten, the real *driver* of APEX. I have been interacting with him in different levels for these 15 years. Sometimes I (we) suffered from his *requests*, but he also supported me when I was in need. Thanks to him, and to Prof. Dr. Karl Menten, who gave me the chance to pursuit a PhD at the MPIfR Division 4, developing instrumentation, is that this project has seen the light. *Don Rolf*, my eternal gratitude.

Dr. Timea Csengeri, my partner, encouraged and supported me to make this long time envision a reality. She advised me, explained concepts and ideas and review the manuscript many times, but most important, she had to deal with my absence at home taking care of our little daughter. Thanks a lot Timi, you are marvelous!

Dr. Christophe Risacher, a friend from the APEX old times, when he was a PhD student coming from

Onsala, becoming later a colleague at ESO and with whom I came across once more when I came to Germany in 2015. We struggled together a couple of times, and these anecdotes should make it into a book one day. He guided me on the technical and administrative matters, and worked side to side in the design, assembly and preparation of the instrument. Certainly without his experience and global view this project wound not been possible: *Gracias viejita!*

My good friend Juan C. Fluxá, senior engineer at APEX who guided me, mentored me and with whom I had the privilege to work for many years. Juan, many thanks for your help and your friendship.

Thanks to Dr. Oliver Ricken, Dr. Stefan Heyminck and Dr. Bernd Klein. They helped me to identify flaws and caveats in the early stage of the design and also review and improved part of the mechanical designs. Thanks to the MPIfR Div 4 team composed by Andreas Henseler, Gundula Lunderhausen, Andrej Görlitz, Stefan Kellner, Andreas Schmidt and Gert Schneider, and in particular to Achim Wunsch who helped me on learning about the *dark art* of the CAD design.

Dr. Urs Graf and Dr. Karl Jacobs from KOSMA; they kindly shared their knowledge always in a very open way. Working with them was synonym of hard but fun work. Thank you guys.

The scientific chapter of this work was developed with the help and patient guidance of Dr. Helmut Wiesemeyer. Thanks a lot Helmut.

I thank my father Carlos, mother Carol and siblings Pablo and Ximena who have supported me from the distance with their unconditional love and care.

Thanks to the APEX people: Panchito, Claudio, Jorge, Pato, Rodrigo, Thomas, Juan Pablo, JP. They were like my second family for a very long time. I had endless and enjoyable discussion with them about life and death, about morality and humanity and they gave me a supportive word more than once.

And finally, I thank to my little daughter Viktoria. In her innocent eyes I have found the strength and resilience to endure the hard times and go against all odds. I have learnt more from her than from anyone else in my life.

APPENDIX A

Quasi-optics Equations

A.1 Fundamental Quasi-optics Equations

The basic equations that govern quasi-optics (Goldsmith 1998) are those that define the beam width radius w (eq. A.1), waist radius size w_0 (Eq. A.2, A.3), position of the beam width z (Eq. A.4) and curvature radius R (Eq. A.5). Designing a quasi-optical system usually requires two known parameters, for example w_0 at distance z from a feed horn.

$$w = w_0 \cdot \sqrt{1 + \left(\frac{\lambda \cdot z}{\pi \cdot w_0^2}\right)^2} \tag{A.1}$$

$$w_0^2 = \frac{\lambda}{\pi} \cdot \sqrt{z \cdot (R - z)} \tag{A.2}$$

$$w_0^2 = \frac{w^2}{2} \cdot \left(1 \pm \sqrt{1 - \left(\frac{2 \cdot \lambda \cdot z}{\pi \cdot w^2}\right)^2}\right) \tag{A.3}$$

$$z = \frac{\pi \cdot w_0}{\lambda} \cdot \sqrt{w^2 - w_0^2} \tag{A.4}$$

$$R = z \cdot \left(1 + \left(\frac{\pi \cdot w_0^2}{\lambda \cdot z}\right)^2\right) \tag{A.5}$$

An additional parameter might constraint the system, for example the edge taper (T_e, Eq. A.6), measuring the illumination patter by the ratio of the power density P(r). For a fundamental mode Gaussian beam, equation A.7 presents the relation between taper (in dB), beam width radius and effective geometrical radius r_e of the telescope.

$$T_e = 10 \cdot \log\left(\frac{P_{center}}{P_{edge}}\right) \tag{A.6}$$

$$T_e = 8.686 \cdot \left(\frac{r_e}{w}\right)^2 \tag{A.7}$$

The full width to half maximum beam width of an in-focus, unblocked aperture with Gaussian

illumination is described by the equation A.8.

$$\Theta_{FWHM} = \left(1.02 + 0.0135 \cdot T_e\right) \cdot \frac{\lambda}{D} \tag{A.8}$$

The beam waist illuminating a Cassegrain telescope with diameter D, focal length f_e and edge taper T_e calculates to:

$$w_{cass} = 0.22 \cdot \lambda \cdot \left(\frac{f_e}{D}\right) \cdot \sqrt{T_e} \tag{A.9}$$

A.2 Instrument and Telescope Beam coupling

The antenna temperature T'_A for a source of brightness distribution T_b is given by the equation A.10, where $P(\vec{x})$ is the telescope radiation pattern.

$$T'_A(\vec{x}) = \frac{\int_{source} P(\vec{x} - \vec{x'}) \cdot T_b(\vec{x'}) d\vec{x'}}{\int_{4\pi} P(\vec{x}) d\vec{x}} \tag{A.10}$$

An uniformly radiating elliptical source of semi-axes a and $b = p \cdot a$ leads to:

$$x = a \cdot \cos(\alpha) \tag{A.11a}$$
$$y = b \cdot \sin(\alpha) = pa \cdot \sin(\alpha) \tag{A.11b}$$

The telescope beam area is defined as by the equation A.12:

$$\Omega_A = \int_{4\pi} P(\vec{x}) d\vec{x} \tag{A.12}$$

Using the Gaussian approximation, the main beam is area given by equation A.13

$$\Omega_{mb} = \frac{\pi \theta_b^2}{4 \ln(2)} \tag{A.13}$$

The peak antenna temperature of the elliptical source (Eq. A.11) can be calculated by:

$$T'_{A,Peak} = \frac{\int_0^{\frac{\pi}{2}} \int_0^a P(\xi, \alpha) \cdot T_b d\xi d\alpha\xi}{\int_{4\pi} P(\vec{x}) d\vec{x}} \tag{A.14a}$$
$$= \frac{\int_0^{\frac{\pi}{2}} \int_0^a P(\xi, \alpha) \cdot T_b d\xi d\alpha\xi}{\Omega_A} \tag{A.14b}$$
$$= \frac{1}{\Omega_A} \int_0^{\frac{\pi}{2}} \int_0^a P(\xi, \alpha) \cdot T_b d\xi d\alpha\xi \tag{A.14c}$$
$$= \frac{2pT_b\Omega_{mb}}{\pi\Omega_A} \int_0^{\frac{\pi}{2}} \frac{1 - e^{\frac{4 \ln 2 a^2}{\theta^2}(\cos^2(\alpha) + p^2 \sin^2(\alpha))}}{\cos^2(\alpha) + p^2 \sin^2(\alpha)} d\alpha \tag{A.14d}$$

The forward efficiency (η_f) and the main beam efficiency (η_{mb}) are defined by the equations A.15 and A.16 respectively.

$$\eta_f = \frac{T'_A}{T^*_A} \tag{A.15}$$

$$\eta_{mb} = \frac{\Omega_{mb}}{\Omega_A} \tag{A.16}$$

Combining the equations A.12, A.13 and A.14 the main beam efficiency can be also expressed by the equation A.17

$$\eta_{mb} = \frac{\pi \eta_f T^*_A}{2pT_b \int_0^{\frac{\pi}{2}} \frac{1 - e^{\frac{4\ln 2\alpha^2}{\theta_b^2}(\cos^2(\alpha)+p^2\sin^2(\alpha))}}{\cos^2(\alpha)+p^2\sin^2(\alpha)} d\alpha} \tag{A.17}$$

The coupling efficiency η_c relates the source brightness with the main beam temperature as:

$$T_{mb} = T_b \cdot \frac{2p}{\pi} \int_0^{\frac{\pi}{2}} \frac{1 - e^{\left(\frac{2a}{\theta_b \cdot e}\right)^2 e^2 \ln(2)(\cos^2(\alpha)+p^2\sin^2(\alpha))}}{\cos^2(\alpha)+p^2\sin^2(\alpha)} d\alpha \tag{A.18a}$$

$$T_{mb} = T_b \cdot \eta_c \tag{A.18b}$$

The corrected antenna temperature by the atmospheric opacity and the forward efficiency is defined as:

$$T^*_A = \frac{e^{\tau_{atm}(\nu)} \cdot T_A}{\eta_f} \tag{A.19}$$

The main beam efficiency, the forward efficiency, T^*_A and T_{mb} are related as:

$$\eta_b = \eta_f \cdot \frac{T^*_A}{T_{mb}} \tag{A.20}$$

A.3 The Gaussian Beam Telescope

When two active mirrors are separated by exactly the sum of their focal distances, as seen on figure A.1, the system becomes frequency independent. The magnification (M) of the input waist is given by the ratio between the focal distances of the two mirrors (eq A.21). Such system is know as Gaussian beam telescope (GT).

$$M = \frac{w_{0out}}{w_{0in}} = \frac{f_2}{f_1} \tag{A.21}$$

$$d_{out} = \frac{f_2}{f_1} \cdot \left(f_1 + f_2 - \frac{f_2}{f_1} \cdot d_{in}\right) \tag{A.22}$$

The position of the output waist (d_{out}) depends on the position of the input waist (d_{in}) scaled by focal distances of both elements as described by equation A.22. The simplest case happens when input and

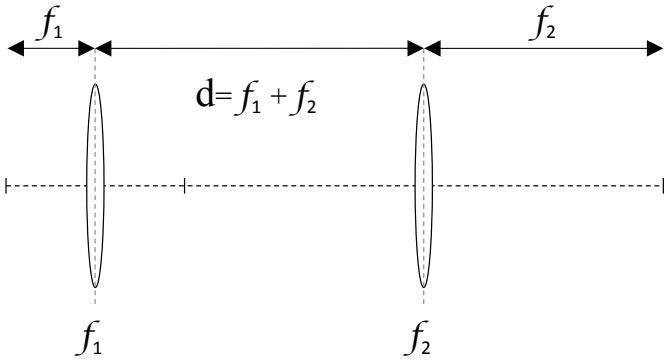

Figure A.1: Gaussian beam telescope formed by two active elements

ouput distances are equal to focal distances.

The Gaussian beam telescope is a powerful tool as a single system serves broad frequency ranges. By daisy chaining multiple Gaussian beam telescopes, the signal beams can be easily redirected and transformed (equation A.23).

$$M = \frac{w_{0out}}{w_{0in}} = \frac{f_2}{f_1} \cdot \frac{f_4}{f_3} \cdots \frac{f_{2n}}{f_{2n-1}} \tag{A.23}$$

When an odd number of active mirrors compose an optical system (2n+1), a similar analysis can be performed by virtually grouping mirrors in pairs and accounting for the additional mirror. This configuration is not frequency independent (Eq. A.24)

$$w_{0out} = \frac{\lambda}{\pi \cdot w_{0in}} \cdot \frac{f_1}{f_2} \cdot \frac{f_3}{f_4} \cdots \frac{f_{2n-1}}{f_{2n}} \cdot f_{2n+1} \tag{A.24}$$

APPENDIX B

Quasi-optical Elements

B.1 Mirrors

Different elements can be used to re-direct and focus a beam of radiation. The most typical ones are lenses and mirrors (Goldsmith 1998). There are two particular kind of mirrors often used in the optical design: the paraboloidal and the ellipsoidal mirrors. The surface quality and accuracy (Ruze 1966) is key when manufacturing the element.

B.1.1 Paraboloidal Mirror

Paraboloidal mirrors take their name from their pattern curve: A paraboloid. They are typically used in two applications. The first one is to focus a radiation field with $R \rightarrow \infty$ into a spot (waist) and second to transform a fast growing beam coming from a horn into a slower beam propagated through active elements. Equation B.1 relates the mirror focus (ρ) with the beam incidence angle (θ_i) and the focal point of the parent paraboloid.

$$\rho = \frac{f_p}{\cos^2 \theta_i} \tag{B.1}$$

B.1.2 Ellipsoidal Mirror

Ellipsoidal mirrors are constructed starting from a pattern ellipse (Fig. B.1). The geometry is calculated by using desired focal (f), wavelength (λ) and input (w_{01}) and output beam waist (w_{02}). The incidence angle (θ_i) defines then point where the parent ellipse intersects the axis of the beam and therefore its revolution axis. The equations B.4 and B.6 define the semi axes (a, b), while B.5 the eccentricity (e).

$$R_1 = f \cdot \left(1 + \left(\frac{\pi \cdot w_{01}^2}{f \cdot \lambda}\right)^2\right) \tag{B.2}$$

$$R_2 = f \cdot \left(1 + \left(\frac{\pi \cdot w_{02}^2}{f \cdot \lambda}\right)^2\right) \tag{B.3}$$

$$a = \frac{R_1 + R_2}{2} \tag{B.4}$$

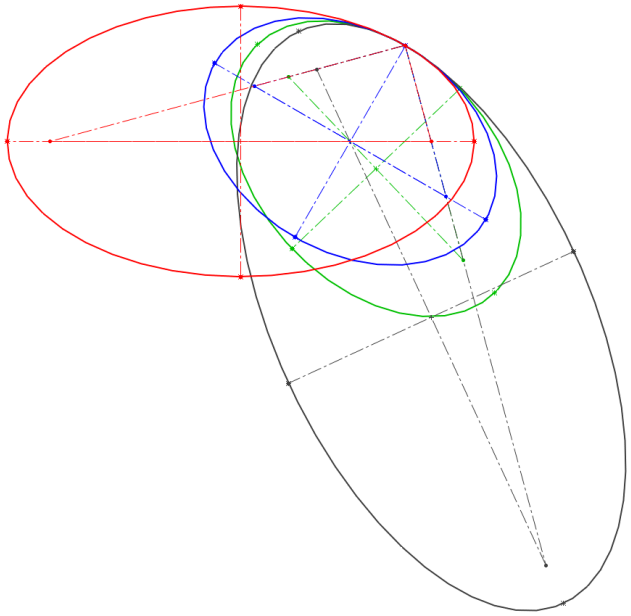

Figure B.1: Example of the M4-G (f = 195mm) pattern ellipsoids calculated for different frequencies: 4G-1 at 560 GHz (black), 4G-2 at 996 GHz (green), 4G-3 at 1350 GHz (blue) and 4G-4 at 2600 GHz (red).

$$e = \frac{(R_1^2 + R_2^2 - 2 \cdot R_1 \cdot R_2 \cdot \cos 2\theta_i)^2}{R_1 + R_2} \tag{B.5}$$

$$b = \sqrt{(1 - e^2) \cdot a^2} \tag{B.6}$$

$$A_0 = 2 \cdot e \cdot a \tag{B.7}$$

$$f_e = \frac{R_1 \cdot R_2}{R_1 + R_2} \tag{B.8}$$

B.2 Wire Grids

A wire grid, used for beam splitting or combining, is composed by many equal diameter constantly spaced conductors (wires) held by a frame, either free standing or on a substrate. There are four key geometrical parameters for a wire grid: Pitch (g), wire diameter (a), physical wire angle (θ) and effective wire angle (θ'). The pitch, defined as the spacing between the wires, is much smaller than half wavelength of the target frequency ($g << \lambda_{wg}/2$). When a signal beam reaches a wire grid, the component of the electric field parallel to the direction of the wires (of the grid) is fully reflected, while the orthogonal component is transmitted. In the same way two (orthogonal) beams can be combined. Signals with higher frequencies than the design frequency of the wire grid ($\lambda < \lambda_{wg}$) are fully transmitted, regardless its polarization (neglecting the effect of the grid mounting substrate). To fully work as combiner, the pitch must be at least the double of the wires diameter ($2a < g$).

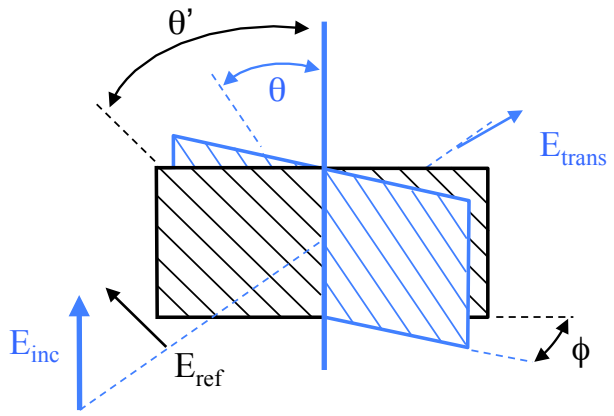

Figure B.2: Wire grid as power splitter/combiner. The effective angle of the wires (θ') changes with the physical angle of the frame respect to the perpendicular projection (ϕ)

$$\theta' = \tan^{-1}(\tan\theta \cdot \cos\phi) \tag{B.9}$$

When a wire grid is rotated around a selected axis (in its own plane) by an angle of ϕ degrees (Fig. B.2), the physical angle of the wires (θ) remains constant, while the angle of projection of the wires on the plane perpendicular to the propagation of the incident beam, θ', changes (Eq. B.9) The reflected and transmitted components of the signal are $|E_{trans}| = |E_{inc}| \sin\theta'$ and $|E_{ref}| = |E_{inc}| \cos\theta'$. A detailed description of the equations governing grids can be found in Goldsmith (1998), including the estimation of the ohmic losses.

B.3 Feed Horns

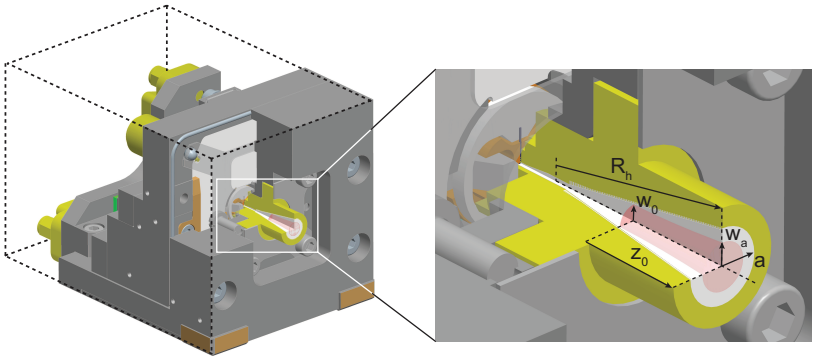

Figure B.3: The Herschel/HIFI SIS mixer band 3 corrugated horn. Some of the key dimensions of the horn are clearly marked. Image taken from Jellema (2015)

Feed horns are used as interface elements between the quasi-optics (free space propagation) and the junction of a signal detector or emitter. The golden standard for feed horns is the corrugated (Clarricoats and Olver 1984). However, when going to higher frequencies (>1.5 THz) the constructibility of the

Table B.1: Different types of horns and their specific parameters.

Horn type	η_{horn}	Bandwidth [%]	Reference
Corrugated	0.644	35	From Johansson (1995)
Pickett-Potter	0.556	20	From Walker (2015)
Diagonal	0.60	55	"
Neilson	0.62	20	"
Smooth-walled	0.74	n/a	Derived from Rabanus et al. (2006)

internal corrugations is limited by machining techniques. 4GREAT channels 1, 2 and 3 use a corrugated horn, while 4G-4 employs an smooth walled. Diagonal horns are much simpler to build and have a wide bandwidth that makes them suitable for LO sources, however they have strong side lobes.

Different simulations have been carried out confirming the horn waist (Eq. A.2), its position (Eq. A.4) and the beam width radius (Eq. A.1), using the physical dimensions (Fig B.3) of aperture (a), the horn slant (R_h) and the η_{horn} parameter (Table B.1). The curvature radius is assumed to be the horn slant while the position of the waist is measured from the aperture, inside the horn. The parameter η_{horn} is defined as the ratio between the beam waist and the horn aperture (ω/a).

APPENDIX C

Equations Related to Heterodyne Systems

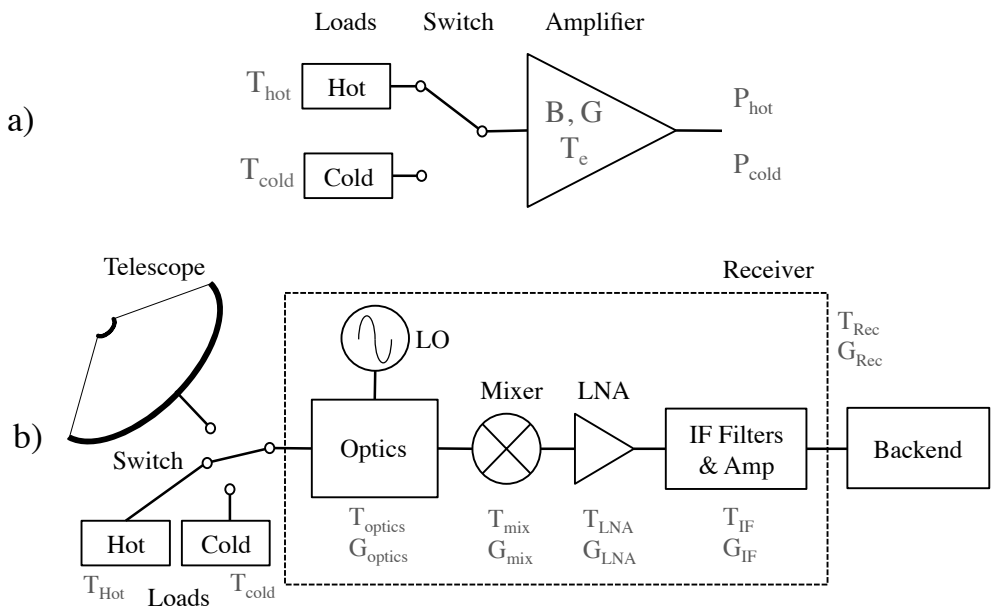

Figure C.1: Scheme of the receiver temperature estimation method by Y factor. The upper image depicts a simplified way to determine the noise temperature of an individual component.

The receiver temperature can be derived by using the Y factor method. This is a general way to estimate the noise equivalent temperature for any system, based on thermal noise estimation. It consist of measuring the output power of the device-under-test while its input is connected to two different loads (Eq. C.1). The noise equivalent temperature is then calculated using the Y parameter and the physical temperatures of the loads (Eq. C.2).

$$Y = \frac{P_{hot}}{P_{cold}} = \frac{T_{hot} + T_e}{T_{cold} + T_e} > 1 \tag{C.1}$$

$$T_e = \frac{T_{hot} - Y \cdot T_{cold}}{Y - 1} \tag{C.2}$$

For an optical element, the noise equivalent temperature is derived using its transmission and its

physical temperature.

$$T_e = \left(\frac{1}{\text{Transmission}} - 1\right) \cdot T_{\text{Physical}} \tag{C.3}$$

The receiver noise temperature can be estimated by accounting the contribution from the individual components of the system (Eq. C.4).

$$T_{Rec} = T_{Optics} + \frac{1}{G_{Optics}} \cdot \left(T_{Mixer} + \frac{T_{LNA}}{G_{Mixer}} + \frac{T_{IF}}{G_{Mixer} \cdot G_{LNA}} + \cdots\right) \tag{C.4}$$

When estimating the double side band receiver temperature, the effect of the optics must be properly addressed (Eq. C.5)

$$T_{Rec-DSB} = \frac{T_{Optics}}{2} + \frac{1}{G_{Optics}} \cdot \left(T_{Mixer-DSB} + \frac{T_{LNA}}{G_{Mixer}} + \frac{T_{IF}}{G_{Mixer} \cdot G_{LNA}} + \cdots\right) \tag{C.5}$$

The continuous Fourier transform, convolution and correlation functions are defined as:

$$\mathfrak{F}(g_s(t)) = \int_{-\infty}^{\infty} g_s(t) \cdot \exp^{-j \cdot t 2\pi \cdot \nu} \, dt = G_s(\nu) \tag{C.6}$$

$$f(t) * g(t) = \int_{-\infty}^{\infty} f(\tau) \cdot g(t - \tau) d\tau \tag{C.7}$$

$$R_{f,g}(t) = \int_{-\infty}^{\infty} f(\tau) \cdot g(\tau - t) d\tau \tag{C.8}$$

APPENDIX D

Heat Load and Infrared Filter

D.1 Infrared Filter Effect and Temperature Profile

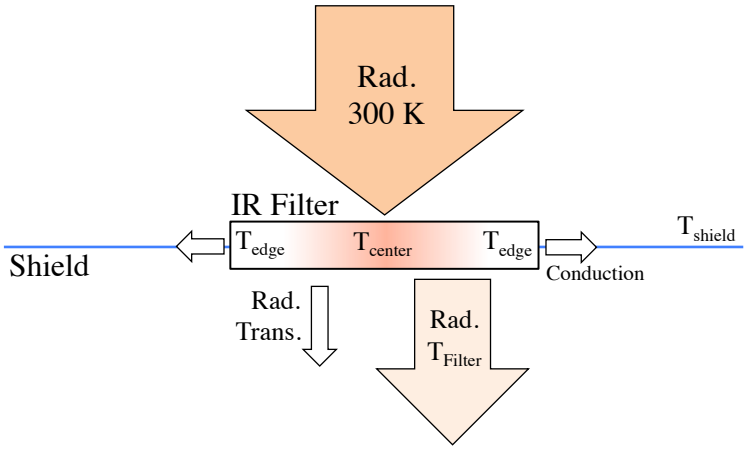

Figure D.1: Infrared filter temperatures. Incident radiation into the IR filter can be modeled as a coming from a black body at room temperature. There is a small fraction of heat that passes the filter while most of it is absorbed.

Located inside the cryostat, infrared filters block most of the (black body) radiation coming from the previous stage, which is usually at 300 K. A small fraction is still transmitted, as the filter has (to have) a high transmission for the response frequency band of the instrument.

The radiation (heat) absorbed by the filter (Fig. D.2 left) needs to be dissipated. Some of the heat is removed by conduction to the edges of the IR filter, that are thermally connected to a cold shield (77 K or 4 K), while another portion is re-emitted as a black body (Fig. D.1), establishing a temperature distribution profile across the filter. Intuitively a Gaussian profile can be expected, however some works (Lamb 1992) suggest a parabolic profile. In both cases, the filter presents a central *hot spot* (T_{center}) and for small diameter filters the differences between both profile models can be neglected. The temperature profile is used to establish the equivalent physical temperature and estimate the re-emitted radiation from the filter (Fig. D.2 right.). By simply balancing the net heat transfer the IR filter central temperature can be calculated. 4GREAT uses one Zitex G-104 IR filter (layer) at the 77 K radiation shield stage, per band. All the simulations performed were based on data obtained by Benford et al. (2003) or extrapolated

Table D.1: 4G IR filter simulation results. The power transmitted and dissipated have been calculated using the data from Benford et al. (2003)

Filter Material	Zitex-G104
IR Cutoff Freq.	3.3 THz
% Energy transmitted by IR filter	0.759 %
Power transmitted through filter	1.556 mW
% Energy blocked (dissipated) by IR filter	99.241%
Power to be dissipated	203.313 mW
300.0 K black body peak freq.	17.64 THz

from it. They tested different materials, covering the band from the infrared to the submillimeter regime. However, Zitex G-104 was not characterized in the whole sub-mm range.

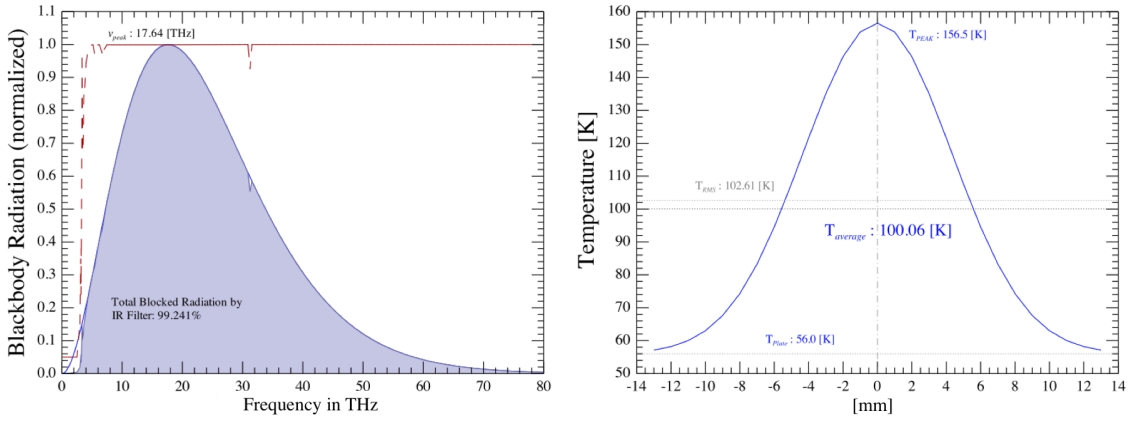

Figure D.2: IR filter. Left: absorbed radiation. The line in red represents the filter absorption, while line un blue is the black body radiation coming from 300 K. Right: Derived temperature profile for a 26 mm diameter IR filter.

Recent measurements for the specific bands (Fig. D.3) of 4GREAT were performed at the MPIfR (Heiter 2017). The values obtained for the 4G-1 band were casted by the presence of standing waves due to physical limitations in the FTS measurement, leading to unrealistic numbers. However, some parts of the data set were usable and have been considered to estimate a very conservative transmission average value of 91.73%.

D.2 Heat Conduction

In order to calculate the effects of heat contribution by conduction, its important to estimate correctly the conductivity of the material (Fig D.4), as it depends on the actual temperature (Ekin 2006). Each material conductivity is modeled by a polynomial (Eq. D.1) with specific terms that are listed on table D.2.

$$k = 10^{\frac{a+c\cdot T^{0.5}+e\cdot T+g\cdot T^{1.5}+i\cdot T^2}{1+b\cdot T^{0.5}+d\cdot T+f\cdot T^{1.5}+h\cdot T^2}} \tag{D.1}$$

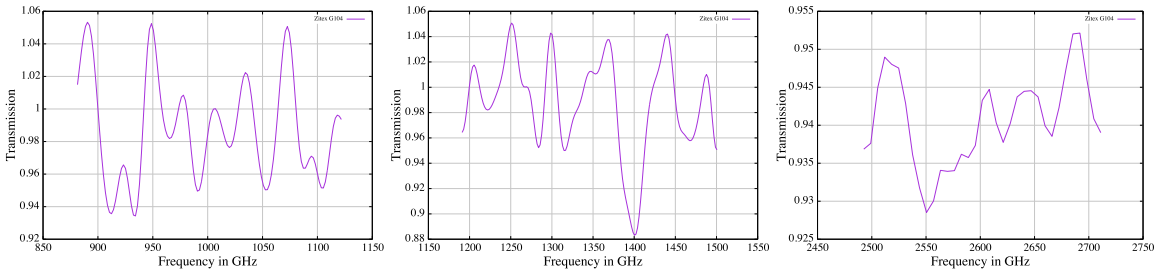

Figure D.3: Zitex G104 transmission for all 4G-2, 4G-3 and 4G-4. Measurements of the transmission over 1.0 and bellow 0.8 have been omitted for calculations as they are features introduced by the FTS limitations.

Table D.2: Conductivity polynomial factors for different materials

	CuBe	G10	Stainless Steel	Cu
a	-0.50015	-4.1236	-1.4087	2.2154
b	1.93190	13.788	1.3982	-0.47461
c	-1.69540	-26.068	0.2543	-0.88068
d	0.71218	26.272	-0.6260	0.13871
e	1.27880	-14.663	0.2334	0.29505
f	-1.61450	4.4954	0.4256	-0.02043
g	0.68722	-0.6905	-0.4658	-0.04831
h	-0.10501	0.0397	0.1650	0.001281
i	0	0	-0.0199	0.003207

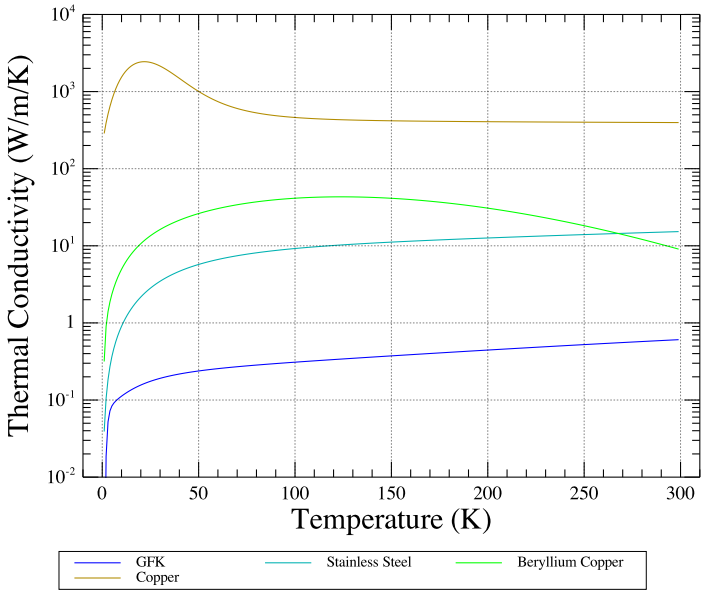

Figure D.4: Curves of conductivity as a function of temperature for different materials typically used in cryostats.

APPENDIX E

4GREAT Optical Elements Details per Band

This appendix contains tables listing the different characteristics of all the optical components used in the 4GREAT optics. The tables E.1, E.2 and E.3 show the result of the estimated distortion introduced by the active mirrors in the signal path for 4G-2, 4G-3 and 4G-4, as defined in section 3.9.3. The coupling of the Gaussian main mode has been also estimated. Tables E.4, E.5, E.6 and E.7 list the optical characteristics of all the components of the signal path for every channel. Analogously, tables E.8, E.9, E.10 and E.11 contain the details of the elements present in the local oscillator beam path. Some of those elements are shared between signal and LO beams.

Table E.1: 4G-2 active mirrors distortion and Gaussian main mode coupling, calculated at 996 GHz.

Mirror	f [mm]	U	K_f [%]	f/D
M0-2	20.1	0.0332	99.8898	1.3310
M1-2	200.0	0.0012	99.9999	6.45
M2-2	190.75	0.0112	99.9874	6.288
M3-2	155.0	0.0013	99.9998	5.69
M4-2	195.0	0.0013	99.9872	6.239

Table E.2: 4G-3 Active mirrors distortion and Gaussian main mode coupling, calculated at 1350 GHz.

Mirror	f [mm]	U	K_f [%]	f/D
M0-3	18.29	0.0418	99.8249	0.9756
M1-3	272.53	0.0007	100.0	8.645
M2-3	160.0	0.0107	99.9885	6.607
M3-3	154.0	0.0033	99.9989	6.513
M4-3	195.0	0.0095	99.909	7.429

Table E.3: 4G-4 Active mirrors distortion and Gaussian main mode coupling, calculated at 2600 GHz.

Mirror	f [mm]	U	K_f [%]	f/D
M0-4	11.94	0.0346	99.8798	1.3246
M1-4	310.0	0.0005	100.0	12.095
M2-4	185.5	0.0089	99.992	7.918
M3-4	155.0	0.001	99.9999	7.723
M4-4	195.0	0.0076	99.9943	9.328

Table E.4: 4G-1 beam path optical elements specifications, with total bouncing angle $\measuredangle = 2\theta_i$.

Element	Name	f [mm]	$\measuredangle$ [°]	ϕ [mm]	Comment
Corrugated horn	Horn1	-	-	-	Cold Tower 1 / Table 3.12
Paraboloidal mirror	M0-1	47.65	60	50	Cold Tower 1 / ρ = 63.533 mm
Flat mirror	F1-1	-	52	52	Cold tower 1
Ellipsoidal mirror	M1-1	250	15.5	54	Cold Tower 1
IR filter	IR-1	-	(6)	26	77K. See section 3.5.1
Vacuum window	W-1	-	(6)	26.4	See section 3.5.1
Wire-grid	CWG-1	-	-	30	Cryostat / Pol. Cleaning Grid
Wire-grid	WG-LO1	-	-	38	Opt. Plate / See Sec. 3.5.2
Ellipsoidal mirror	M2-1	188.85	90	45	Opt. Plate / Adj. Group 1
Flat mirror	F2-1	-	60	39	Opt. Plate / Adj. Group 1
Dichroic Filter	D-13	-	-	46	Opt. Plate / Trans. Fig. 3.22
Ellipsoidal mirror	M3-13	154	34	43	Opt. Plate / Comm. ch. 1 & 3
Wire-grid	WG-VH	-	(90)	46	Opt. Plate / Horiz. Pol.
Ellipsoidal mirror	M4G	195	90	52	Opt. Plate / Comm. All channels

Table E.5: 4G-2 beam path optical elements specifications, with $\measuredangle = 2\theta_i$

Element	Name	f [mm]	$\measuredangle$ [°]	ϕ [mm]	Comment
Corrugated horn	Horn2	-	-	-	Cold Tower 2 / Table 3.12
Paraboloidal mirror	M0-2	17.83	74	22	Cold Tower 2 / ρ = 27.949 mm
Flat mirror	F1-2	-	38	30.5	Cold Tower 2
Ellipsoidal mirror	M1-2	200	22	37	Cold Tower 2
IR filter	IR-2	-	(6)	26	See section 3.5.1
Vacuum window	W-2	-	(6)	26.4	See section 3.5.1
Wire-grid	CWG-2	-	-	30	Cryostat / Pol. Cleaning Grid
Wire-grid	WG-LO2	-	-	38	Optics Plate / See Sec. 3.5.2
Ellipsoidal mirror	M2-2	190.75	90	32.2	Opt. Plate / Adj. Group 2
Flat mirror	F2-2	-	102	26	Opt. Plate / Adj. Group 2
Dichroic Filter	D-24	-	-	30	Opt. Plate / Trans. Fig. 3.22
Ellipsoidal mirror	M3-24	155	12	29.5	Opt. Plate / Comm. ch. 2 & 4
Wire-grid	WG-VH	-	-	46	Opt. Plate / Vert. Pol.
Ellipsoidal mirror	M4G	195	90	52	Opt. Plate / Comm. All channels

Table E.6: 4G-3 beam path optical elements specifications, with $\measuredangle = 2\theta_i$

Element	Name	f [mm]	$\measuredangle$ [°]	ϕ [mm]	Comment
Corrugated horn	Horn3	-	-	-	Cold Tower 3 / Table 3.12
Paraboloidal mirror	M0-3	18.179	60	30.9	Cold Tower 3/ ρ = 27.949 mm
Flat mirror	F1-3	-	42	33.6	Cold Tower 3
Ellipsoidal mirror	M1-3	272.5	18	34	Cold Tower 3
IR filter	IR-3	-	(6)	24	See section 3.5.1
Vacuum window	W-3	-	(6)	25	See section 3.5.1
Wire-grid	CWG-3	-	-	30	Cryostat / Pol. Cleaning Grid
Wire-grid	WG-LO3	-	-	25	Opt. Plate / See section 3.5.2
Ellipsoidal mirror	M2-3	160	90	26	Opt. Plate / Adj. Group 3
Flat mirror	F2-3	-	102	26	Opt. Plate / Adj. Group 3
Dichroic Filter	D-13	-	26	46	Opt. Plate / Refl. Figure 3.22
Ellipsoidal mirror	M3-13	155	34	43	Opt. Plate / Comm. ch. 1 & 3
Wire-grid	WG-VH	-	90	46	Opt. Plate / Hor. Pol.
Ellipsoidal mirror	M4G	195	90	52	Opt. Plate / Comm. All channels

Table E.7: 4G-4 beam path optical elements specifications, with $\measuredangle = 2\theta_i$

Element	Name	f [mm]	$\measuredangle$ [°]	ϕ [mm]	Comment
Smooth Walled Horn	Horn4	-	-	-	Cold Tower 4 / Table 3.12
Paraboloidal mirror	M0-4	12.732	60	15	Cold Tower 4 / ρ = 16.975 mm
Flat mirror	F1-4	-	14	25.5	Cold Tower 4
Ellipsoidal mirror	M1-4	310	12	29	Cold Tower 4
IR filter	IR-4	-	(6)	24	See section 3.5.1
Vacuum window	W-4	-	(6)	25	See section 3.5.1
Wire-grid	CWG-4	-	-	30	Cryostat / Pol. Cleaning Grid
M-P Diplexer	DIPLX-4	-	-	-	Opt. Plate / See Table 3.16
Ellipsoidal mirror	M2-4	185.5	90	38	Opt. Plate / Adj. Group 4
Flat mirror	F2-4	-	90	24	Opt. Plate / Adj. Group 4
Wire-grid	WG-LO4	-	74	25	Opt. Plate / Refl. See Sec. 3.5.2
Dichroic Filter	D-24	-	-	30	Opt. Plate / Refl. See Fig. 3.22
Ellipsoidal mirror	M3-24	155	12	29.5	Opt. Plate / Comm. ch. 2 & 4
Wire-grid	WG-VH	-	-	46	Opt. Plate / Vert. Pol.
Ellipsoidal mirror	M4G	195	90	52	Opt. Plate / Comm. All channels

Table E.8: 4G-1LO path optical elements specifications

Element	Name	f [mm]	$\measuredangle$ [°]	ϕ [mm]	Comment
Diagonal horn	Horn-LO1	-	-	-	See Table 3.14
Attenuator	Attn-LO1	-	-	-	Ying-Yang Wheel.
Paraboloidal mirror	P1-LO1	16.2	85	29	
Ellipsoidal mirror	M4-LO1	75	85	31.1	Adj 1
Vacuum window	W-LO1	-	-	33	See text and 3.5.1
Flat mirror	F4-LO1	-	70	33	
Ellipsoidal mirror	M3-LO1	130	70	54	
Flat mirror	F3-LO1	-	90	53	Tip/Tilt/Displ - Adj 2
Flat mirror	F2-LO1	-	60	53	Optics Plate
Ellipsoidal mirror	M2-LO1	230	71	53	"
Wire-grid	WG-LO1	-	-	38	"/ See text.
Wire-grid	CWG-1	-	-	30	Cryostat / Pol. Cleaning Grid
Vacuum window	W-1	-	(6)	26.4	Cryostat. See section 3.5.1
IR filter	IR-1	-	(6)	26	"
Ellipsoidal mirror	M1-1	250	15.5	54	Cold optics in cryostat
Flat mirror	F1-1	-	52	52	"
Paraboloidal mirror	M0-1	47.65	60	50	"
Corrugated horn	Horn1	-	-	-	See Table 3.12

Table E.9: 4G-2LO path optical elements specifications

Element	Name	f [mm]	$\measuredangle$ [°]	ϕ [mm]	Comment
Diagonal horn	Horn-LO2	-	-	-	See Tablen 3.14
Paraboloidal mirror	P1-LO2	15.1	85	22	
Attenuator	Attn-LO2	-	-	-	Rotary grid.
Ellipsoidal mirror	M4-LO2	87.5	85	24	Adj 1
Vacuum window	W-LO2	-	-	33	See text and 3.5.1
Flat mirror	F5-LO2	-	90	15.5	
Ellipsoidal mirror	M3-LO2	128.5	90	36	
Flat mirror	F4-LO2	-	90	35	Tip/Tilt/Displ - Adj 2
Flat mirror	F3-LO2	-	77.5	33.6	Optics Plate
Ellipsoidal mirror	M2-LO2	280	96.893	40	"
Flat mirror	F2-LO2	-	82.607	32	"
Wire-grid	WG-LO2	-	-	38	"/ See text.
Wire-grid	CWG-2	-	-	30	Cryostat / Pol. Cleaning Grid
Vacuum window	W-2	-	(6)	26.4	Cryostat. See section 3.5.1
IR filter	IR-2	-	(6)	26	"
Ellipsoidal mirror	M1-2	200	22	37	Cold optics in cryostat
Flat mirror	F1-2	-	38	30.5	"
Paraboloidal mirror	M0-2	17.83	74	22	"
Corrugated horn	Horn1	-	-	-	See Table 3.12

Table E.10: 4G-3LO path optical elements specifications. Note that there are only 3 ellipsoidal (active) mirrors.

Element	Name	f [mm]	$\measuredangle$ [°]	ϕ [mm]	Comment
Diagonal horn	Horn-LO3	-	-	-	See Table 3.14
Paraboloidal mirror	P1-LO3	24	60	33	
Flat mirror	F7-LO3	-	60	36	
Attenuator	Attn-LO3	-	(22)	38	Rotary grid.
Flat mirror	F6-LO3	-	90	37	
Flat mirror	F5-LO3	-	90	38	
Ellipsoidal mirror	M3-LO3	315	90	44	Displ. - Adj 1
Flat mirror	F4-LO3	-	90	35	Circular Tip/Tilt/Displ - Adj 2
Vacuum window	W-LO3	-	(6)	35	See text and 3.5.1
Flat mirror	F3-LO3	-	79.16	45	LO Head
Flat mirror	F2-LO3	-	90	28	Optics Plate
Ellipsoidal mirror	M2-LO3	230	90	30.2	"
Wire-grid	WG-LO3	-	-	25	"/ See text.
Wire-grid	CWG-3	-	-	30	Cryostat / Pol. Cleaning Grid
Vacuum window	W-3	-	(6)	25	Cryostat. See section 3.5.1
IR filter	IR-3	-	(6)	24	"
Ellipsoidal mirror	M1-3	272.5	18	34	Cold optics in cryostat
Flat mirror	F1-3	-	42	33.6	"
Paraboloidal mirror	M0-3	18.179	60	30.9	"
Corrugated horn	Horn3	-	-	-	See Table 3.12

Table E.11: 4G-4LO path optical elements specifications.

Element	Name	f [mm]	$\measuredangle$ [$^\circ$]	ϕ [mm]	Comment
Diagonal horn	Horn-LO4	-	-	-	See Table 3.14
Paraboloidal mirror	P1-LO4	17.9	60	25.5	LOD
Flat mirror	F9-LO4	-	60	22	"
Attenuator	Attn-LO4	-	(17.5)	30	Rotary grid. LOD
Flat mirror	F8-LO4	-	30	24	LOD
Flat mirror	F7-LO4	-	30	27.5	"
Ellipsoidal mirror	M4-LO4	480	90	33	Displ. - Adj 1
Flat mirror	F6-LO4	-	90	28	Tip/Tilt/Displ - Adj 2. LOD
Vacuum window	W-LO4	-	(6)	35	See text and 3.5.1
Flat mirror	F5-LO4	-	90	45	LO Head
Flat mirror	F4-LO4	-	94.78	21	Optics Plate
Ellipsoidal mirror	M3-LO4	180	97.169	25	"
Flat mirror	F3-LO4	-	41.614	20	"
Wire-grid	WG-LO4	-	(53)	25	"/ See text.
Flat mirror	F2-4	-	90	24	Optics Plate "
Ellipsoidal mirror	M2-4	185.5	90	38	"
MP-Diplexer	DIPLX-4				See Table 3.16
Wire-grid	CWG-1	-	-	30	Cryostat / Pol. Cleaning grid
Vacuum window	W-4	-	(6)	25	Cryostat. See section 3.5.1
IR filter	IR-4	-	(6)	24	"
Ellipsoidal mirror	M1-4	310	12	29	Cold optics in cryostat
Flat mirror	F1-4	-	14	25.5	"
Paraboloidal mirror	M0-4	12.732	60	15	"
Corrugated horn	Horn4	-	-	-	See Table 3.12

APPENDIX F

4GREAT Unfolded Optics Plots

The unfolded plot is a way to display how the Gaussian beam propagates through the path defined by the optics of each channel, using the Eq. A.1. The plot excludes changes in the direction of the beam and focuses on the shape and the beam width modifications due to active elements. Such plots are particularly useful to determine beam waists and the relative position of critical elements like vacuum windows and infra red filters respect to the position of those waists. They have been used to refine the design of the optics of 4GREAT.

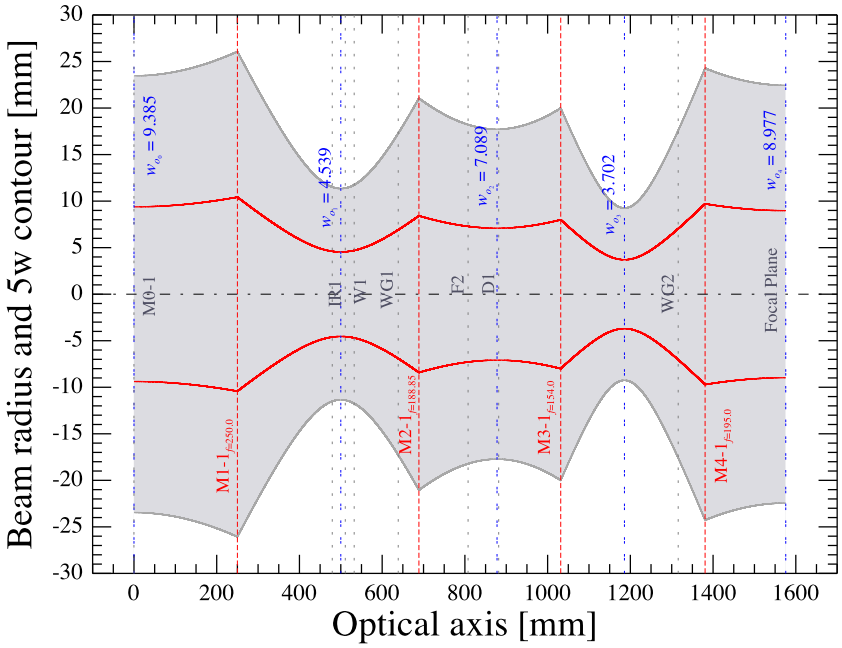

Figure F.1: 4G-1 unfolded optics diagram: beam width radius (red line) and contour of 5w at 560 GHz. The details of every optical element can be seen in table E.4

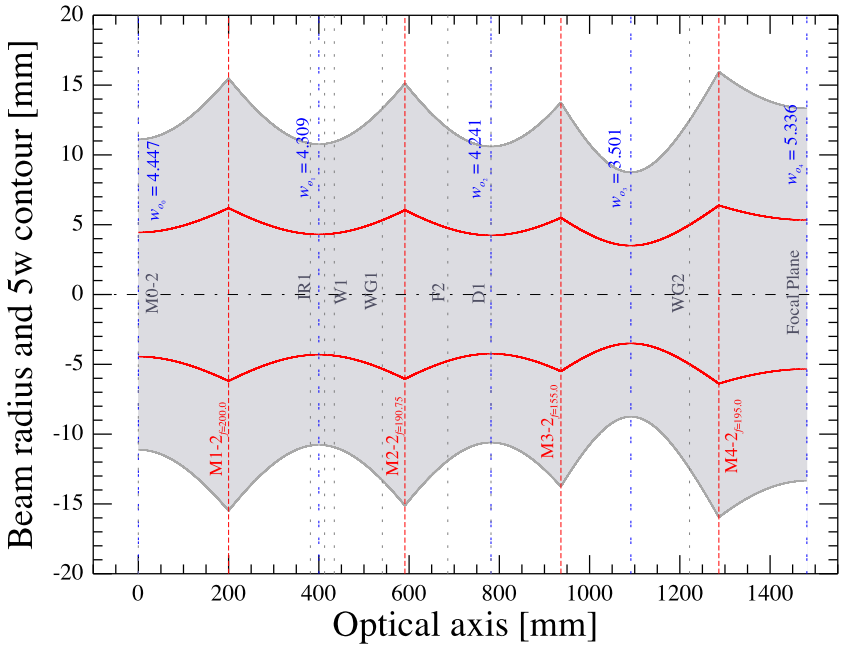

Figure F.2: 4G-2 unfolded optics diagram: beam width radius (red line) and contour of 5w at 996 GHz. The details of every optical element can be seen in table E.5

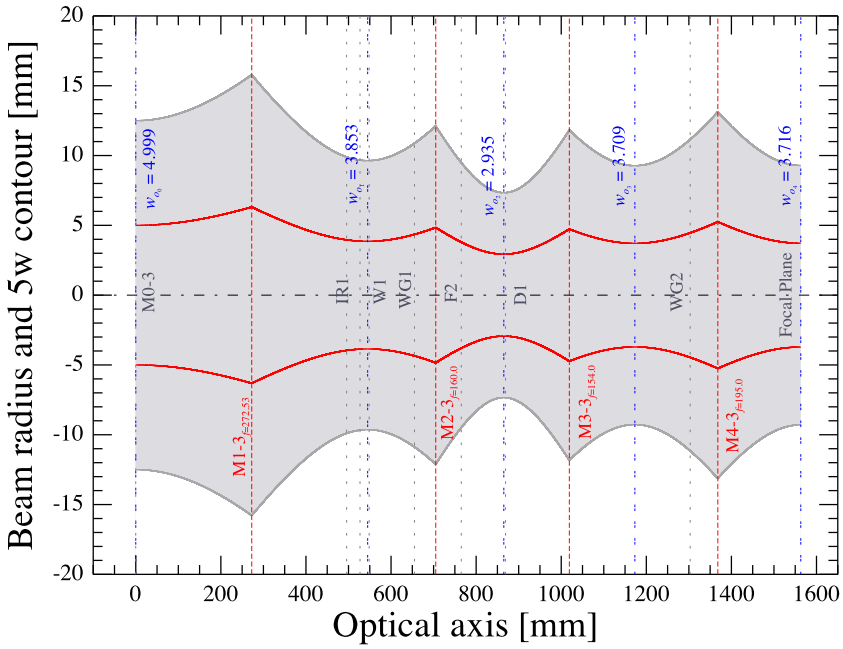

Figure F.3: 4G-3 unfolded optics diagram: beam width radius (red line) and contour of 5w at 1350 GHz. The details of every optical element can be seen in table E.6

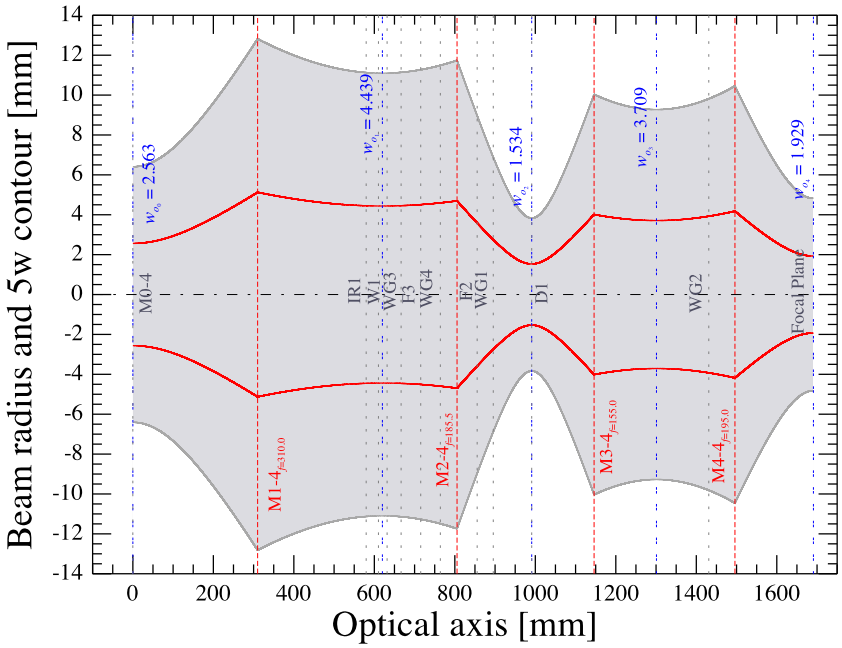

Figure F.4: 4G-4 unfolded optics diagram: beam width radius (red line) and contour of 5w at 2600 GHz. The details of every optical element can be seen in table E.4. Note that the diplexer grid appears as signalized as two elements: WG3, WG4.

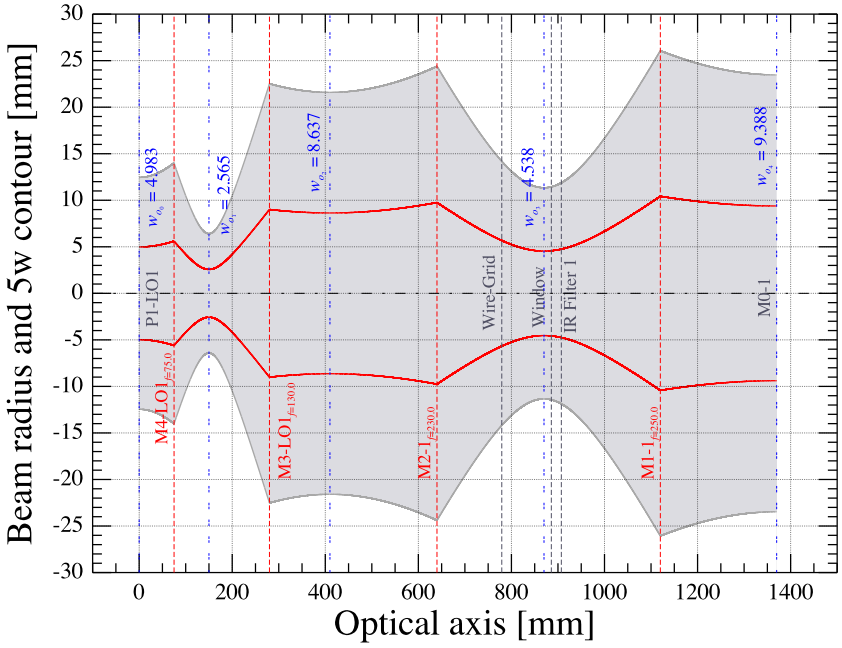

Figure F.5: 4G1-LO unfolded optics diagram: beam width radius (red line) and contour of 5w at 560 GHz. The details of every optical element can be seen in table E.8.

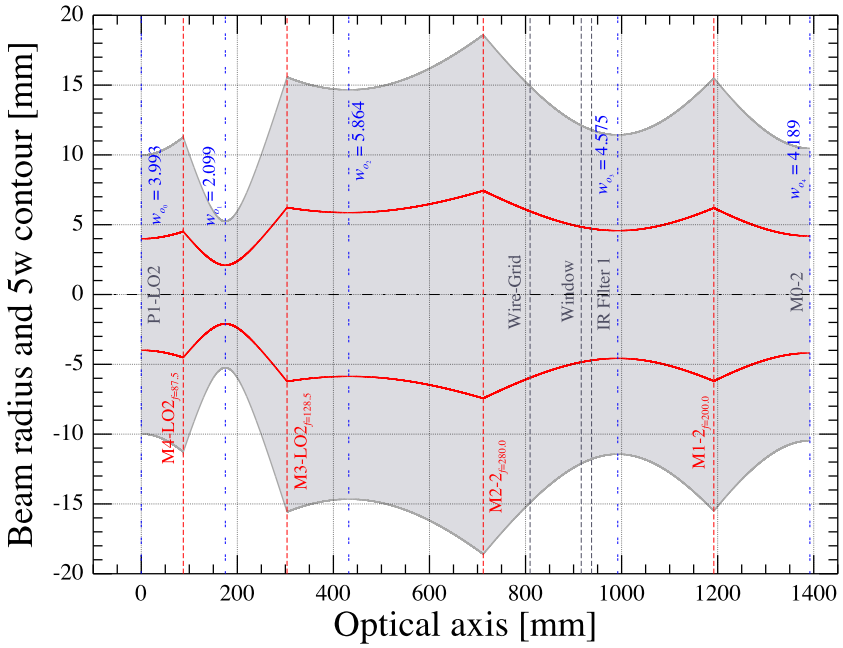

Figure F.6: 4G2-LO unfolded optics diagram: beam width radius (red line) and contour of 5w at 996 GHz. The details of every optical element can be seen in table E.9.

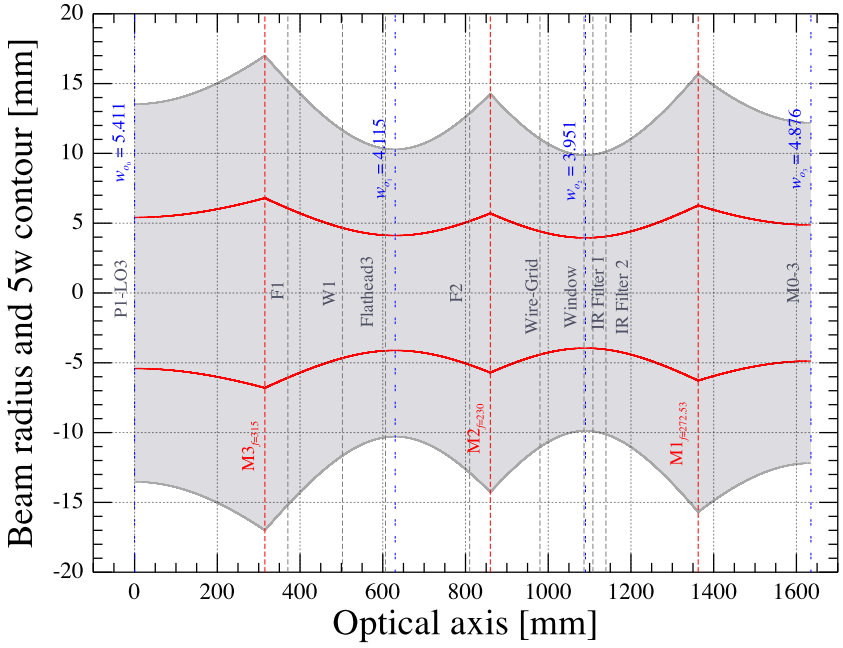

Figure F.7: 4G3-LO unfolded optics diagram: beam width radius (red line) and contour of 5w at 1350 GHz. The details of every optical element can be seen in table E.10. Note that the optics is realized using only three active mirrors.

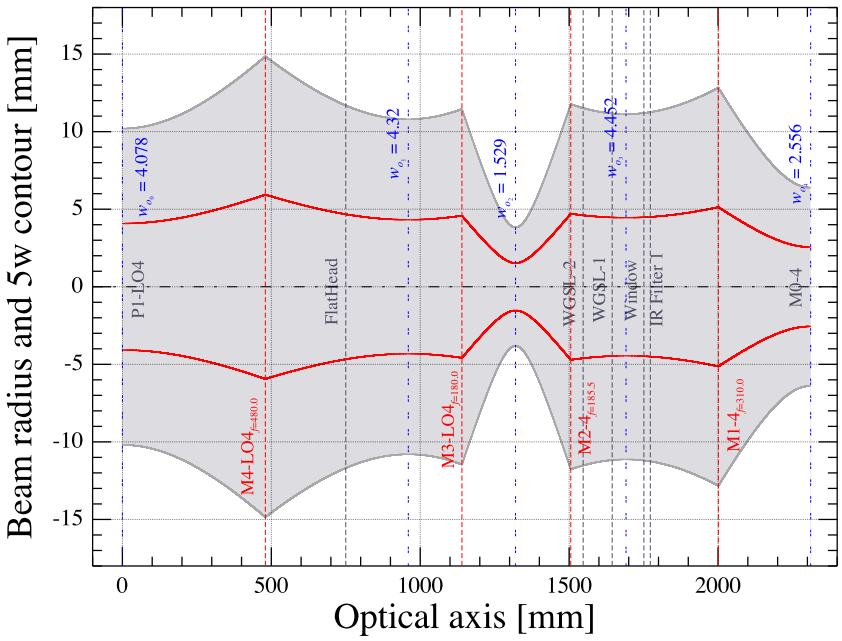

Figure F.8: 4G4-LO unfolded optics diagram: beam width radius (red line) and contour of 5w at 2600 GHz. The details of every optical element can be seen in table E.11. The diplexer is signalized here by WGSL1 and WGSL 2.

APPENDIX G

4GREAT Optical components noise temperature contributions

The noise contributions to the receiver temperature from the various optical components of each channel are listed in the following tables. The equivalent infrared filter temperature has been calculated according to the method described in the appendix D. The components and their specific features are listed in the tables of the appendix E. The transmission and reflection characteristics (curve) of the dichroic filter that separates de beam between HFA and 4G, named D-HFA4G, can be seen in the subsection 4.4.4.

Table G.1: Receiver temperature contribution of the individual optical elements in the signal path of 4G-1. The table is separated between the elements in the cryostat and those in the warm optics.

Warm	D-HFA4G	M4-G	WG-VH	M3-13	D13	F2-1	M2-1	WG-LO1
T [K]	300	300	300	300	300	300	300	300
Transm. (%)	92.17	99.00	99.00	99.00	97.89	99.00	99.00	90.5
T_e [K]	25.47	3.03	3.03	3.03	6.47	3.03	3.03	31.49
Cryostat	CWG-1	W1	IR1	M1-1	F1-1	M0-1		
T [K]	300	300	100	4	4	4		
Transm. (%)	99.00	96.74	91.73	99.00	99.00	99.00		
T_e [K]	3.03	10.11	9.016	0.04	0.04	0.04		

Table G.2: Receiver temperature contribution of the individual optical elements in the signal path of 4G-2. The table is separated between the elements in the cryostat and those in the warm optics

Warm	D-HFA4G	M4-G	WG-VH	M3-24	D24	F2-2	M2-2	WG-LO2
T [K]	300	300	300	300	300	300	300	300
Transm. (%)	96.03	99.00	99.00	99.00	95.86	99.00	99.00	90.60
T_e [K]	12.40	3.03	3.03	3.03	12.96	3.03	3.03	31.17
Cryostat	CWG-2	W2	IR2	M1-2	F1-2	M0-2		
T [K]	300	300	100	4	4	4		
Transm. (%)	99.00	94.72	97.95	99.00	99.00	99.00		
T_e [K]	3.03	16.72	2.09	0.040	0.04	0.04		

Table G.3: Receiver temperature contribution of the individual optical elements in the signal path of 4G-3. The table is separated between the elements in the cryostat and those in the warm optics

Warm	D-HFA4G	M4-G	WG-VH	M3-13	D13	F2-3	M2-3	WG-LO1
T [K]	300	300	300	300	300	300	300	300
Transm. (%)	94.45	99.00	99.00	99.00	93.33	99.00	99.00	92.50
T_e [K]	17.63	3.03	3.03	3.03	21.44	3.03	3.03	24.32
Cryostat	CWG-3	W3	IR3	M1-3	F1-3	M0-3		
T [K]	300	300	100	4	4	4		
Transm. (%)	99.00	85.25	98.15	99.00	99.00	99.00		
T_e [K]	3.03	51.91	1.89	0.04	0.04	0.04		

Table G.4: Receiver temperature contribution of the individual optical elements in the signal path of 4G-4. The table is separated between the elements in the cryostat and those in the warm optics

Warm	D-HFA4G	M4-G	WG-VH	M3-24	D24	WG-LO4	F2-4	M2-4	DIPLX
T [K]	300	300	300	300	300	300	300	300	300
Transm. (%)	88.48	99.00	99.00	99.00	91.50	99.00	99.00	99.00	96.06
T_e [K]	39.06	3.03	3.03	3.03	27.87	3.03	3.03	3.03	12.18
Cryostat	CWG-4	W4	IR4	M1-4	F1-4	M0-4			
T [K]	300	300	100	4	4	4			
Transm. (%)	99.00	90.01	94.73	99.00	99.00	99.00			
T_e [K]	3.03	33.3	5.56	0.04	0.04	0.04			

APPENDIX H

Pulse Tube Load Map

The pulse tube load map presents the different thermal load configurations that the pulse the cryo cooler can handle and the operational temperatures of the different stages under these conditions. The system has been optimazed for the second stage at 4 K.

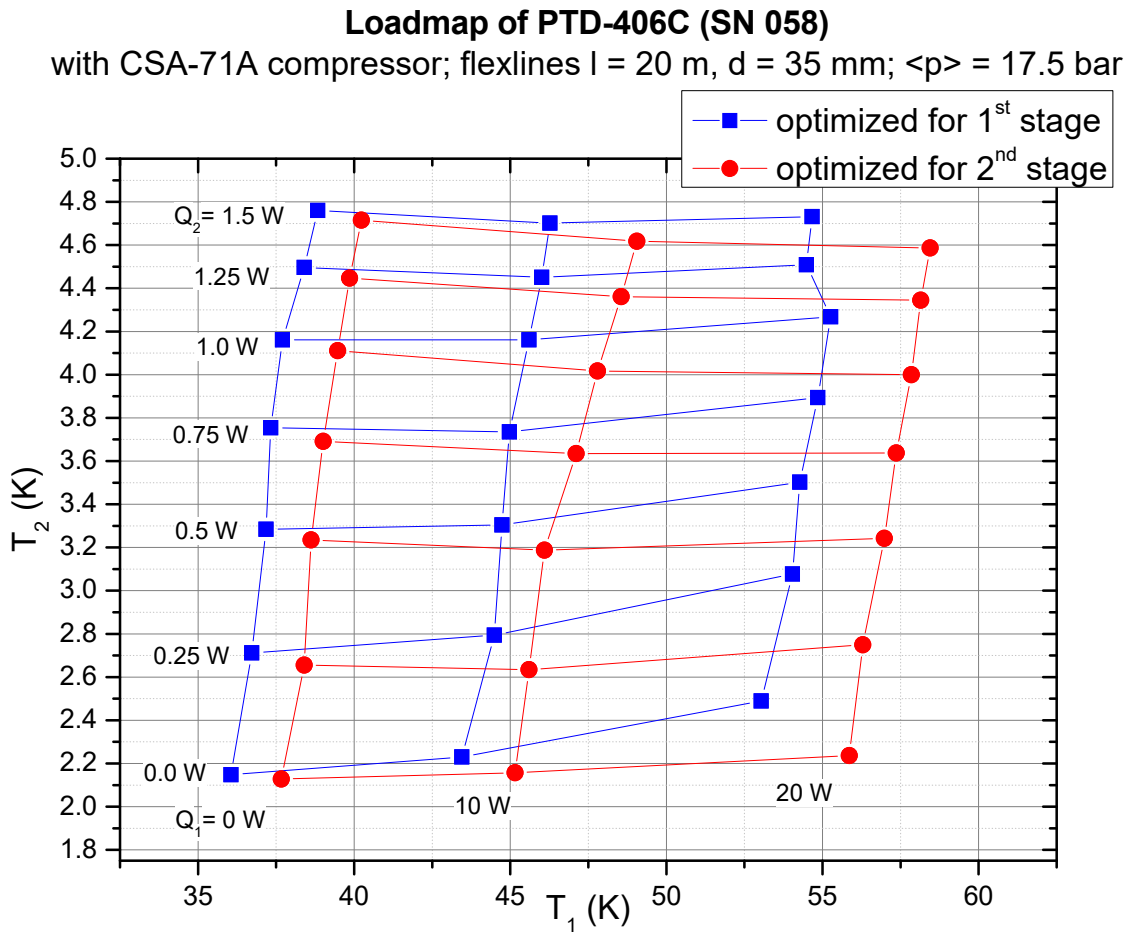

Figure H.1: PTD-406C pulse tube closed-cycle cooler load map, as provided by Transmit

APPENDIX I

4GREAT Allan Variance test plots per channel

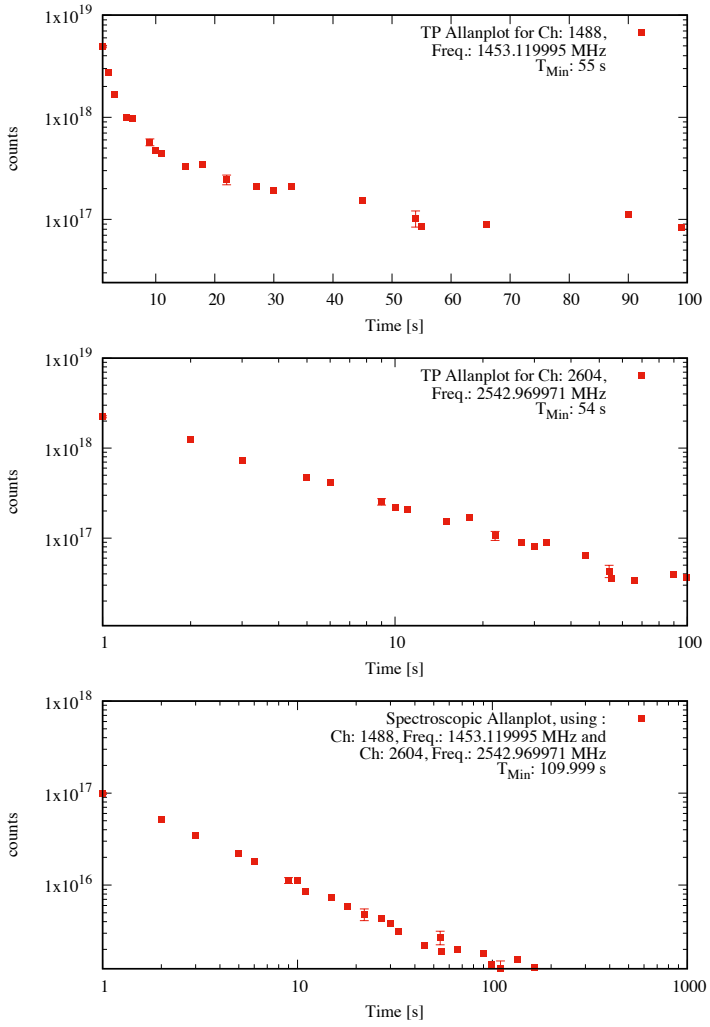

Figure I.1: 4G-1 total power and spectroscopic Allan variance test performed with the LO frequency set at 520 GHz.

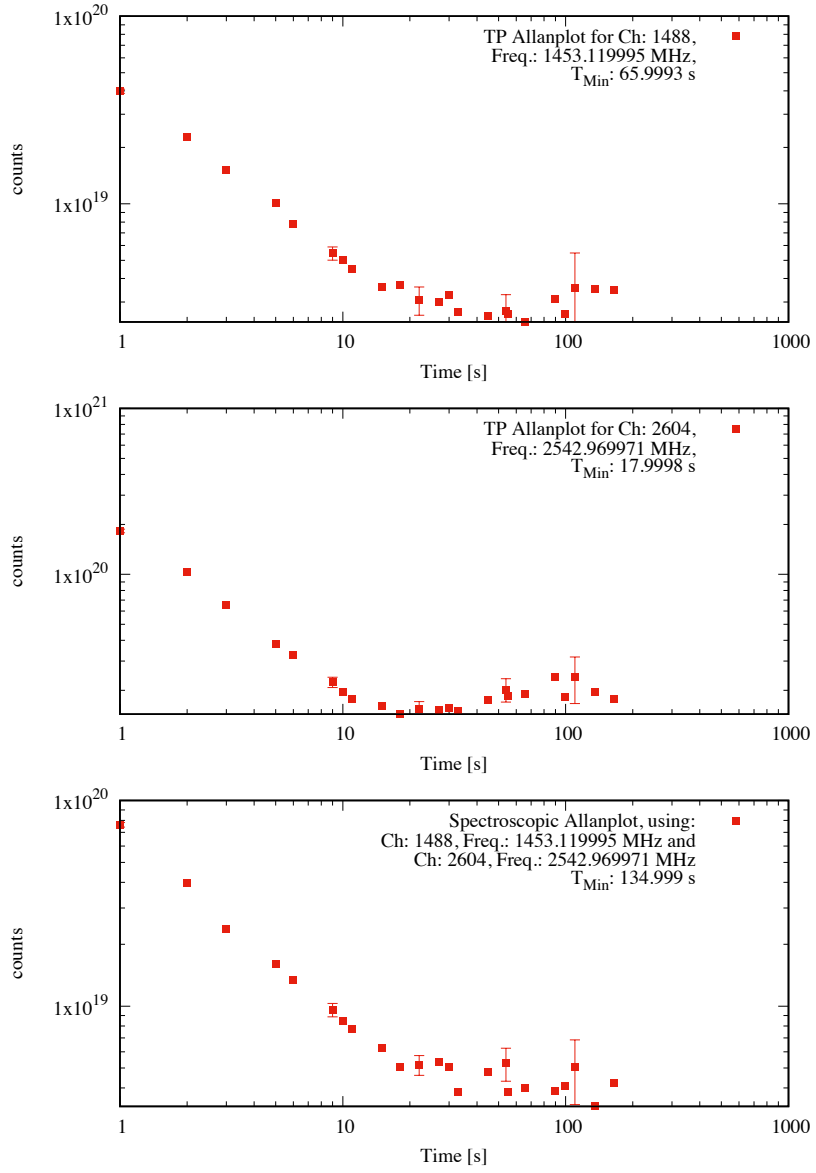

Figure I.2: 4G-2 total power and spectroscopic Allan variance test performed with the LO frequency set at 920 GHz.

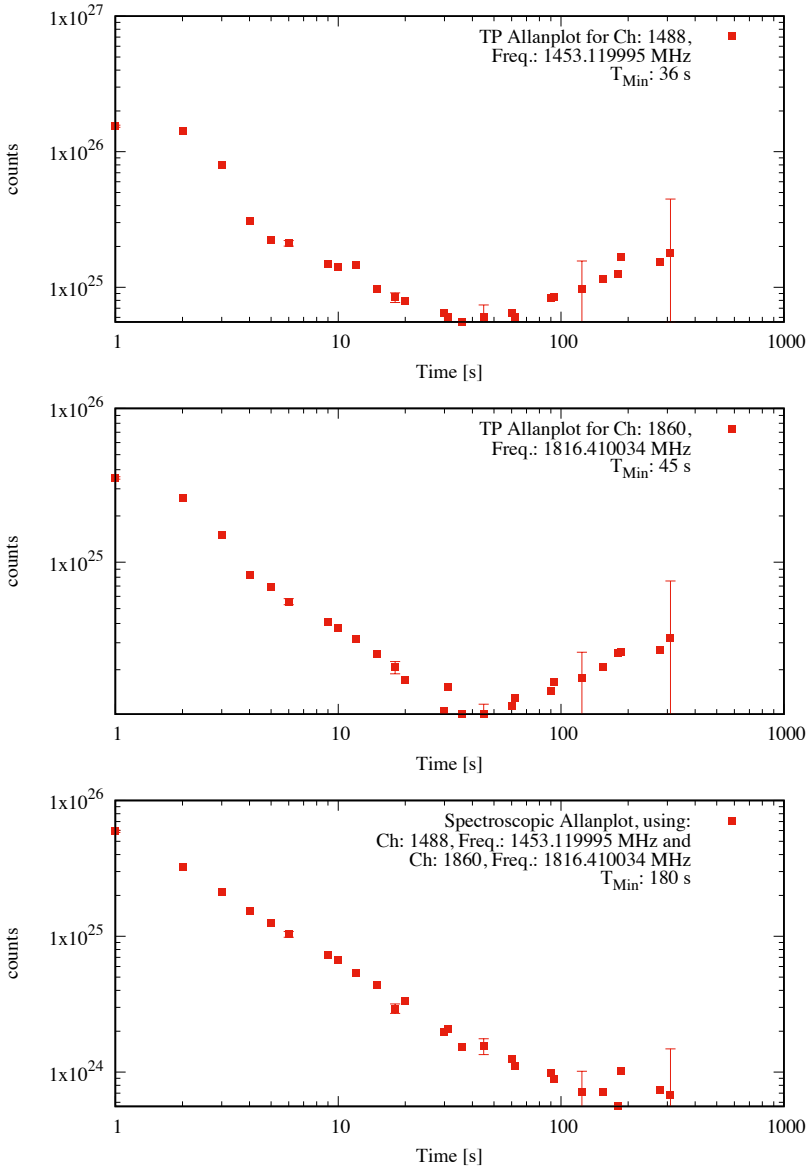

Figure I.3: 4G-3 total power and spectroscopic Allan variance test performed with the LO frequency set at 1300 GHz.

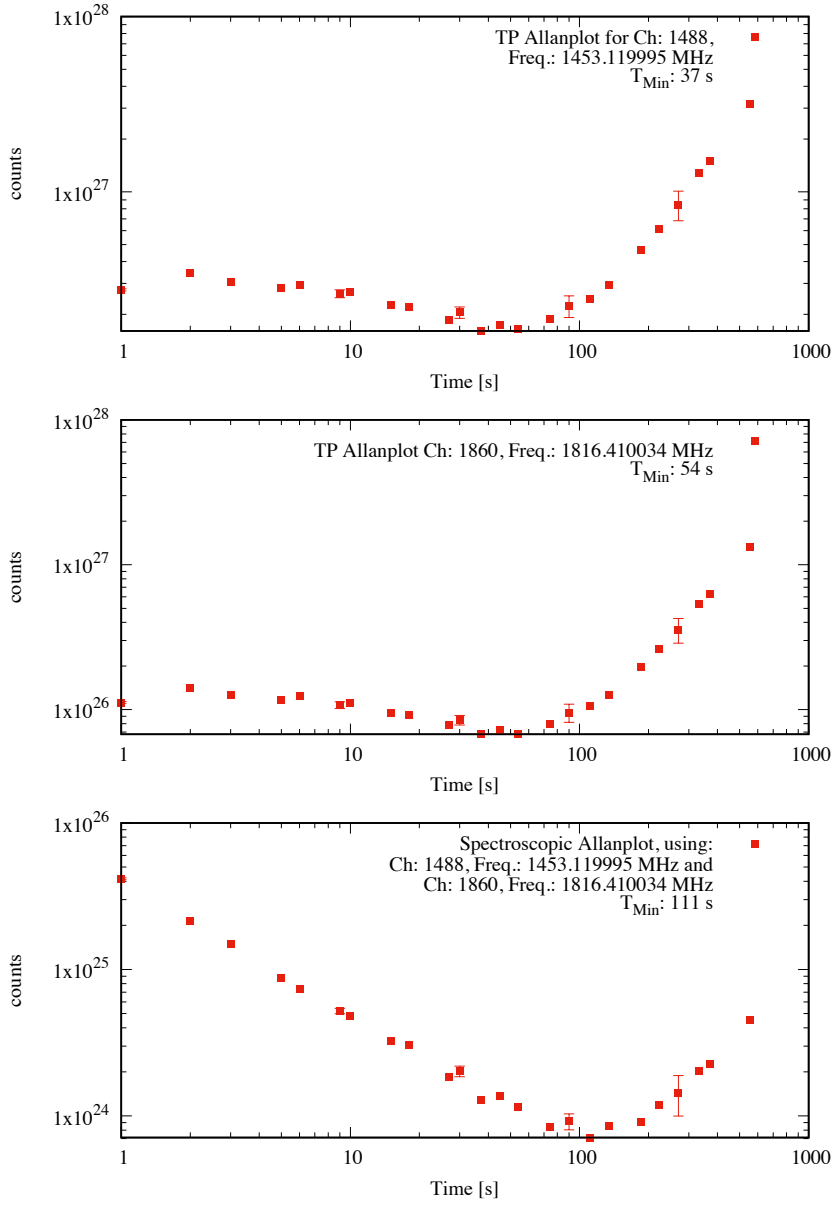

Figure I.4: 4G-4 total power and spectroscopic Allan variance test, performed with the LO frequency set at 2673 GHz and diplexer tuned at 15.023 mm.

APPENDIX J

The GREAT line catalog

The Table J.1 lists the species and transitions rest frequencies detectable by GREAT, as May 2018. The specific frequency shift given by the source velocity is accounted by the LO tuning. The effect of the atmospheric windows and technical boundaries and restrictions of the instrument have been taken into consideration.

Some selected species transitions, like CO, are highlighted in Tables J.2, J.3 and J.4.

Table J.1: The GREAT line catalog as May 2018. The upGREAT LFA and HFA lines are also included.

Specie	Transition (QNs)	Frequency [GHz]	Receiver	Remark
C	$^3P_0$-$^3P_1$	492.160651	4G-1	[CI]
HDO	1(1,0) - 1(0,1)	509.29242	4G-1	
CH	J = 3/2-3/2, Ω= 3/2, F = 5/2- -3/2+	536.761	4G-1	
$H_2^{18}O$	1(1,0)-1(0,1)	547.67644	4G-1	
NH_3	1(0)0s- 0(0)0a	572.4981599	4G-1	
CO	J=5-4	576.26793	4G-1	
HCl	J=1-0, (F_1=5/2-3/2)	625.918756	4G-1	
HDO	1(1,1) - 0(0,0)	893.638666	4G-2	
HCNO	7(1,6)- 7(0,7)	903.6	4G-2	Many lines
OH+	N=0-1, J=1-0, F=1/2-3/2	909.1588	4G-2	
CO	J=8-7	921.7997	4G-2	
OH+	N = 2 - 1, J = 1 - 0, F = 5/2 - 3/2	971.8038	4G-2	
NH	N= 1-0, J= 0-1, F1=1/2-3/2, F=3/2-5/2	974.478612	4G-2	Multiplets
H_3O+ v=0,1	0(0)-1(0), 0- - 0+	984.711907	4G-2	
^{13}CO	J=9-8	991.329348	4G-2	
$H_2{}^{18}O$	2(0, 2)-1(1, 1)	994.675129	4G-2	
OH+	N=1-1, J=1-0, F=3/2-3/2	1033.1186	4G-2	
CO	J=9-8	1036.912393	4G-2	
H_2S	2(2,1) - 1(1,0)	1072.836548	4G-2	
HCN	J=14-13	1239.89	4G-3	
HCO+	J=14-13	1247.735047	4G-3	
HCl	J=2-1, F_1=7/2-5/2	1251.45193	4G-3	HFS
CO	J=11-10	1267.014486	4G-3	
H_2O_2	12(1,11),τ=3,4 - 11(0,11)τ=1,2	1274.577045	4G-3	
HDO	2(1,2)-1(0,1)	1277.97	4G-3	Shifted

H_2O	7(4,3) - 6(5,2)	1278.265	4G-3	
H_2O	8(2,7) - 7(3,4)	1296.41106	4G-3	
H_2F+	1(1,1)- 0(0,0)	1305.31496	4G-3	
HCN	J=15-14	1328.302232	4G-3	
^{7}LiH	J=3-2	1329.414	4G-3	
PH_3	5(-3)- 4(3)	1333.2	4G-3	multiplets
HCO+	J=15-14	1336.714924	4G-3	
^{6}LiH	J=3-2	1356.928	4G-3	
H_2D+	1(0,1) - 0(0,0)	1370.08488	4G-3	
CO	J=12-11	1381.995105	4G-3	
SH	J=5/2-3/2, Ω=3/2, F= 3+- 2-	1382.9101	4G-3	
OD	J=5/2-3/2, Ω=3/2,F=7/2+-5/2-	1390.613966	4G-3	
OD	J=5/2-3/2, Ω=3/2,F=7/2–5/2+	1391.494707	4G-3	
HCO+	J=16-15	1425.665008	4G-3	
^{13}CO	J=13-12	1431.153037	4G-3	
H_2O	7(2,6) - 6(3,3)	1440.78167	4G-3	
HCL+	N=2-1, J=5/2-3/2, p=1- -1, F=1/2-1/2	1444.3	4G-3	multiplets
N+	$^3P_0$-$^3P_1$	1461.1338	4G-3	[NII] 205 μm
CH	J = 3/2 - 1/2, Ω = 1/2, F = 1/2+ - 3/2-	1477.313022	4G-3	
CO	$J = 13 - 12$	1496.922909	4G-3	
HCN	J=17-16	1505.029918	4G-3	
HCO+	J=16-15	1514.583317	4G-3	
^{18}OH	J=5/2-3/2, Ω=3/2,F= 3+- 2-	2494.695072	4G-4	
^{18}OH	J=5/2-3/2, Ω=3/2,F= 3– 2+	2498.994533	4G-4	
OH	N = 2- - 1+, J = 5/2 - 3/2, F = 3 - 2	2509.94901	4G-4	
OH	N = 2+ - 1-, J = 5/2 - 3/2, F = 3 - 2	2514.316705	4G-4	
CO	$J = 22 - 21$	2528.17206	4G-4	
HD	J=1-0	2674.986094	4G-4	
NH_3	3(1)0a- 2(1)0s	1808.934565	LFA	
NH_3	3(2)0a- 2(2)0s	1810.379971	LFA	
^{13}CCC		1816.685589	LFA	
^{13}CCC		1820.797	LFA	
^{18}OH	J=3/2-1/2, Ω=1/2,F= 2– 1+	1821.948866	LFA	
^{18}OH	J=3/2-1/2, Ω=1/2,F= 2+- 1-	1825.030512	LFA	
^{13}CCC		1825.72	LFA	
^{13}CCC		1831.448	LFA	
OH	N=2+ - 1-, J=3/2-1/2, F= 2-1	1834.74735	LFA	
OH	N=2- - 1+, J=3/2-1/2, F= 2-1	1837.81634	LFA	
^{13}CCC		1837.975	LFA	
CO	$J = 16 - 15$	1841.345506	LFA	
H_2F+	2(1,2)-1(0,1)	1850.0917	LFA	
HCN	J=21-20	1858.042221	LFA	
HCL	J=3-2	1876.2275	LFA	HFS
HCO+	J=21-20	1869.899192	LFA	
CH_4		1881.98031	LFA	

^{13}CCC		1882.638269	LFA	
H_2O	8(4,5) - 7(5,2)	1884.888	LFA	
^{13}CCC		1888.50188	LFA	
C_3	J= 2-2, v2=1-0, l= 1-0	1890.558	LFA	
H_2O	3(3,1) - 4(0,4)	1893.68651	LFA	
$H_2{}^{18}O$	3(2,2)- 3(1,3)	1894.323823	LFA	
C_3	J= 4-4, v2= 1-0, l= 1-0	1896.707	LFA	
H_2O_2	5(3,3),v=0,τ=3,4 - 6(4,3),v=0,τ=1,2	1898.126105	LFA	multiplets
H_3O+ v=0,1	11(11)-11(11), 0- - 0+	1898.982998	LFA	
C+	$^2P_{3/2}$-$^2P_{1/2}$	1900.5369	LFA	[CII] 157 μm
CH_2	1(1,0)-1(0,1), J= 1-1, I_{tot}=0, F=1-1	1902.654373	LFA	
CH_2	1(1,0)-1(0,1), J= 2-1, I_{tot}= 0, F=2-1	1907.986693	LFA	
C_3	J= 6- 6, v2= 1- 0, l= 1- 0	1906.3379	LFA	
LiH		1906.60932	LFA	
CH	J=3/2-1/2,Ω =1/2, F=1/2- - -1/2+	2006.762578	LFA	
HeH+	J=1-0	2010.183873	LFA	
O	$^3P_0$-$^3P_1$	2060.06886	LFA	[OI] 145 μm
CO	$J = 18 - 17$	2070.615993	LFA	
O	$^3P_1$-$^3P_2$	4744.77749	HFA	[OI] 63 μm

Table J.2: CO ladder transitions covered by GREAT

Transition (J)	Frequency [GHz]	E_L [K]	Receiver
5 – 4	576.2679305	55.3179	4G-1
8 – 7	921.7997000	154.8725	4G-2
9 – 8	1036.9123930	199.1118	4G-2
11 – 10	1267.0144860	304.1616	4G-3
12 – 11	1381.9951050	364.9684	4G-3
13 – 12	1496.9229090	431.2934	4G-3
16 – 15	1841.3455060	663.3508	LFA
17 – 16	1956.0181390	751.7208	LFA
18 – 17	2070.6159930	845.5944	LFA
22 – 21	2528.1720600	1276.0474	4G-4
23 – 22	2642.33034590	1397.3799	4G-4

Table J.3: GREAT detectable lines (frequencies) for C, N and O.

Line	Transition	Frequency [GHz]	E_L [K]	Receiver
[CI]	$^3P_1 - ^3P_0$	492.160	0	4G-1
[CII]	$^2P_{3/2} - ^2P_{1/2}$	1900.537	0	LFA
[OI]	$^3P_1 - ^3P_0$	2060.068	0	LFA
[OI]	$^3P_2 - ^3P_1$	4745.804	0	HFA
[NII]	$^3P_2 - ^3P_1$	1461.131	0	4G-3

Table J.4: GREAT detectable lines of carbon monosulfide and silicon monoxide

Specie	Transition (J)	Frequency [GHz]	Receiver
CS	11 – 10	538.68899720	4G-1
	12 – 11	587.61648500	4G-1
	13 – 12	636.53246000	4G-1
	18 – 17	880.90557920	4G-2
	20 – 19	978.54043290	4G-2
	21 – 20	1027.32950360	4G-2
	22 – 21	1076.09838950	4G-2
	26 – 25	1270.95287790	4G-3
	27 – 26	1319.60643530	4G-3
	28 – 27	1368.23404700	4G-3
	30 – 29	1465.40759400	4G-3
	38 – 37	1852.87207030	LFA
	39 – 38	1901.15096650	LFA
	40 – 39	1949.39240980	LFA
	41 – 40	1997.59544230	LFA
	42 – 41	2045.75910630	LFA
	52 – 51	2525.01994000	4G-4
	53 – 52	2572.68740410	4G-4
	54 – 53	2620.30402420	4G-4
	55 – 54	2667.86884560	4G-4
SiO	12 – 11	520.87820390	4G-1
	13 – 12	564.24396200	4G-1
	14 – 13	607.59942070	4G-1
	21 – 20	910.71001720	4G-2
	22 – 21	953.94328510	4G-2
	23 – 22	997.15547560	4G-2
	24 – 23	1040.34508600	4G-2
	25 – 24	1083.51054080	4G-2
	29 – 28	1255.89657620	4G-3
	30 – 29	1298.91485810	4G-3
	31 – 30	1341.89782950	4G-3

List of Figures

List of Tables